Technical Physics, Vol. 45, No. 5, 2000, pp. 521–527. Translated from Zhurnal Tekhnicheskoĭ Fiziki, Vol. 70, No. 5, 2000, pp. 1–7.

REVIEW

Development Prospects of the Commercial Production of Fullerenes

A. A. Bogdanov[1], D. Deininger[2], and G. A. Dyuzhev[1]

[1] *Ioffe Physicotechnical Institute, Russian Academy of Sciences, St. Petersburg, 194021 Russia*

[2] *Institut für Innovative Technologien GmbH, Am Holländer Weg 11, D-06366 Kéthen, Germany*

Received July 8, 1999

Abstract—The review gives a description of the various modern methods of fullerene production. Reasons of the high cost of fullerenes are discussed, and development prospects of commercial production of fullerenes we analyzed. © *2000 MAIK "Nauka/Interperiodica".*

INTRODUCTION

First discovered in 1985 in experiments on laser vaporization of graphite [1], the new allotropic form of carbon—fullerenes—attracted great interest in the scientific community. After the invention of the method of producing macroscopic quantities of fullerenes [2] in 1990, a flood of works dealing with fullerenes followed [3]. Already at that time, numerous possible application areas for fullerenes had been discussed [4].

In recent years, intensive research of fullerene properties has been underway involving their formation mechanisms, and applications in most varied fields. Considerable progress has been achieved in many directions and analysis of fullerene applications in different fields can be found in recent reviews [5, 6]. However, in none of these fields is the achieved development level high enough to warrant the start of commercial scale production of fullerenes. This is largely due to the marked slowdown in the decline of the price of fullerenes after 1994 [6, 7] (Fig. 1).

An analysis of the marginal cost of fullerenes that could bring about their wide application in various branches of industry has been made in [7]. In Fig. 2, some data from this work are presented. It can be seen that the first application fields for fullerenes might be the pharmaceutical industry and production of diamonds and catalysts. But even in these fields, for fullerenes to become competitive, their prices should be brought down by a factor of 10. The high fullerene price stems from high costs of production involving the use of an arc discharge [8], which is, at the moment, the major source of fullerenes in the market [5]. In order to find out what makes fullerenes so costly and outline possible ways of reducing the costs, we consider, below, the results of investigations of the arc discharge method and other methods of fullerene production.

ARC DISCHARGE METHOD OF FULLERENE PRODUCTION

The mechanism of highly efficient formation of fullerenes from chaotic carbon vapors in arc discharge, despite a large number of works on the subject, still remains unclear in many of its aspects [9, 10]. However, this circumstance did not prevent researchers from undertaking detailed phenomenological studies of fullerene formation in an arc discharge with graphite electrodes.

The most comprehensive investigations have been carried out in [11], [12], and [13], where graphite anode erosion, the growth rate of cathode carbon deposit, and fullerene content α in the carbon soot were studied as functions of arc current, kind of gas and its pressure, and the interelectrode separation. For a graphite anode 6 mm in diameter, maximum α values, 10–15%, are

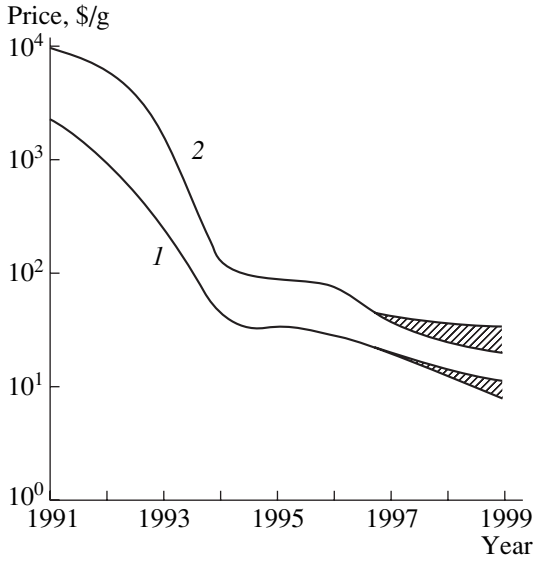

Fig. 1. World prices for (*1*) a mixture of fullerenes and (*2*) the pure C_{60} fullerene.

1063-7842/00/4505-0521$20.00 © 2000 MAIK "Nauka/Interperiodica"

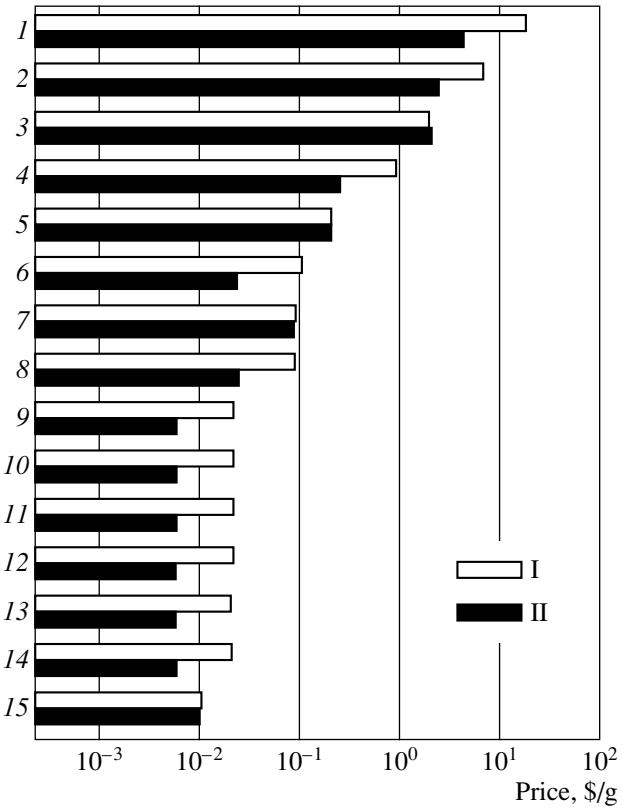

Fig. 2. (*I*) Price of available products and materials in some potential application fields for fullerenes and (*II*) the maximum price for fullerenes to be competitive in some fields. The application fields of fullerenes: *1*—pharmaceutical industry; *2*—diamonds; *3*—catalysts; *4*—non-linear absorbers; *5*—optical materials; *6*—coats for electronics; *7*—carbon filaments; *8*—composites; *9*—antifriction additives; *10*—rubber components; *11*—detergent additives; *12*—dyes; *13*—plasticizers; *14*—high-quantity polymers; and *15*—adsorbents.

found for a current of 80 A, helium pressure 100 torr, and the interelectrode separation of 3–5 mm. At optimum interelectrode separation, α diminishes as current and pressure are either increased or reduced (Fig. 3).

Fullerenes are then extracted from the carbon soot with organic solvents and separated into homologues, either by means of crystallization in solution, or by chromatography. Extraction and separation methods are common to all methods of production of fullerene-containing soot. The efficiency of these processes should also be increased in order to lower the market price of pure fullerenes [8], but this aspect of production will not be considered here.

The low economic efficiency of fullerene production is due in a large degree to the fact that only 30–40% of the sublimated carbon is converted into soot [8, 12]. The remainder deposits on the cathode as large blocks of baked carbon material containing no fullerenes. At present, this carbon material, as well as the residue after soot extraction, represent the waste of fullerene production. So, with $\alpha = 10\%$, fullerenes constitute only 3–4% of the spent anode material, which obviously makes fullerenes highly expensive. It is clear, therefore, that recycling of the carbon waste could reduce the expenditure of raw materials in fullerene production and, thus, reduce the cost of fullerenes [8].

Another way of increasing the efficiency of an arc discharge process could be the raising of the fullerene content α in the soot. Fullerenes are produced in an expanding carbon vapor by way of gradual growth of carbon clusters. In this growth process, the clusters are annealed in the buffer gas. The efficiency of fullerene formation is determined by the carbon concentration, gas temperature, and the velocity of the gas flow out of the interelectrode gap or, more precisely, by the radial distribution of these quantities. It is evident that for efficient fullerene formation, the combination of these three parameters should be optimal. But in an arc discharge, this optimum relationship is almost impossible to attain, because any change of the arc current will affect all three of the above parameters. Therefore, it is hard to expect that α can be considerably increased (above 10–15%) in standard arc discharge reactors, especially considering the fact that thorough optimization work has already been carried out.

Thus, the conventional arc discharge method of fullerene production has, apparently, exhausted all its reserves of efficiency increase. Higher fullerene production efficiency ought to be pursued with systems employing disperse carbon feed, especially those using low-cost starting materials, and also with hybrid discharge systems, in which the feed of carbon material, gas temperature, and the flow rate can be controlled independently.

HYBRID SYSTEMS AND CARBON POWDER FEED SYSTEMS

Very few works on hybrid fullerene production schemes have been published so far. In [14] the use in fullerene production of a hybrid plasma generator is described (Fig. 4). This generator had been developed for application in plasma chemistry and studied in detail in [15]. The generator consists of two stages: a dc arc plasmatron and an rf discharge (4 MHz); the operating pressure is 260–760 torr; power ratings of the first and second stages are 5 and 20 kW, respectively. Soot consisting of particles less than 10 μm in size was introduced into the first stage with a flow of argon. The rate of carbon feed was 0.05–0.5 g/min. The yield of fullerenes was 7% of the collected soot, which is a rather good result. However, optimization of this installation has not been undertaken, and for unknown reasons, this work was not pursued further, at least, not published.

In [16], a three-phase plasmatron of rather high power (50–100 kW) was used in fullerene production. The experiments were carried out under atmospheric

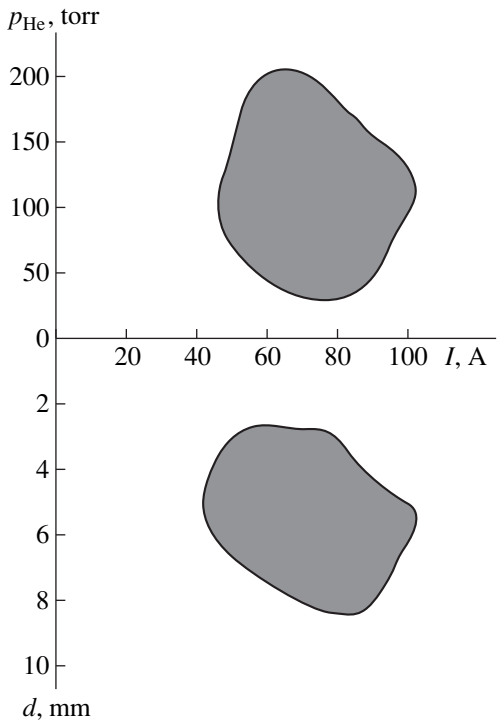

Fig. 3. Limits of the arc discharge parameters (current, helium pressure, and interelectrode separation) for which the fullerene content in the soot α exceeds 10%. The diameter of electrodes is 6 mm.

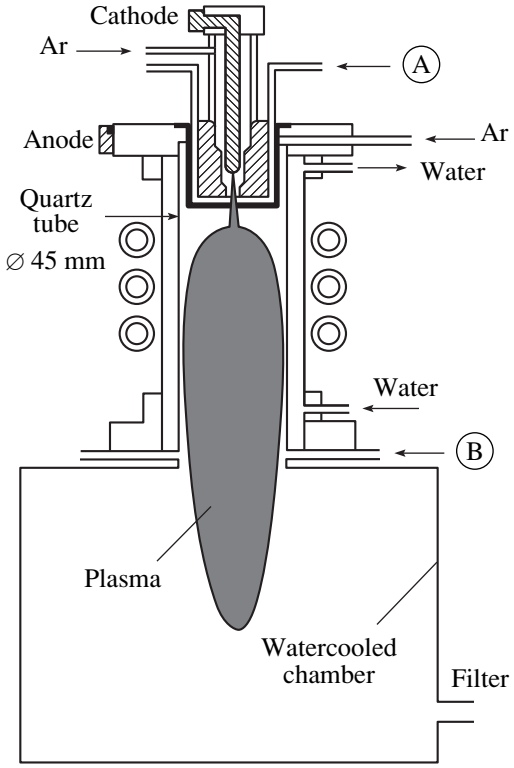

Fig. 4. Schematic of the hybrid plasma generator. A—introduction of fine graphite particles into the gas flow; B—inlet of argon for cooling the reaction zone.

pressure. As plasma-forming gases, nitrogen, argon, and helium were used. The best results have been obtained with helium. The carbon powder was introduced into the reactor through the plasma zone, where it evaporated. The smaller the carbon particles introduced, the faster they evaporated. Fullerene formation was adversely affected if the carbon particles contained hydrogen. The authors estimated their first results as promising, as they were able to produce a few kilograms of soot per hour with a fullerene yield of 1 and 0.2 per cent of C_{60} and C_{70}, respectively.

FULLERENE PRODUCTION IN A FLAME

Soon after the discovery of fullerenes in laser vaporization of graphite, research on production of fullerenes in the flame of a gas burner was started [17]. Alongside the scientific interest, these investigations had a distinct practical aspect, aiming at the development of a new method of fullerene production. From the very beginning, it was understood that the production of fullerenes by burning a hydrocarbon material is more technological and an easier controlled process than the synthesis in an arc discharge. In addition to, this method is especially attractive, because of the possibility of it being easily scaled up. Still, it was necessary to identify an optimum fuel, appropriate mixture composition, combustion regimes, and burner design that would provide efficiency and acceptable rate of production.

Since then, quite a few results have been obtained.[1] Combustion processes of various hydrocarbons (benzene, acetylene [18–21], naphthalene [22], and others) were studied for a range of operating parameters. Mass-spectra of the combustion products formed at various heights above the burner have been obtained [21]. Fullerene formation in similar processes as a result of thermal decomposition (pyrolysis) of hydrocarbons in oxygen-free atmosphere was studied [23]. In [24], the chemistry of C_{60} and C_{70} fullerene formation in a flame was considered. It was soon discovered that in a flame, apart from the soot and fullerenes, nanotubes are formed [25]. It has been shown that flames can be more efficient as a source of higher fullerenes than an arc discharge [26].

In one of the most comprehensive and thorough investigations [20], formation of fullerenes by burning a benzene–oxygen–argon (helium/nitrogen) mixture was studied. As a fuel, acetylene was tried as well. The flame parameters were varied in the following ranges: pressure in the chamber from 12 to 100 torr, C/O atomic ratio from 0.717 to 1.082, molar content of

[1] In a recent review [38], the results obtained in fullerene production with the plasma method have been summarized and the prospects of this method considered.

Ar (He, N_2) from 0 to 50%, and the velocity of gas over the burner from 14.6 to 75.4 cm/s. The combustion in many regimes lasted for 1–3 h. The combustion products contained soot, polycyclic aromatic hydrocarbons (PAH), and fullerenes. In the above parameter ranges, the fullerene content in the soot was measured as a function of C/O ratio, gas velocity, chamber pressure, the kind and concentration of dilution gas, and other parameters (Fig. 5).

The authors of [20] elucidated the differences between synthesis in a flame and in an arc discharge: (1) in a flame, the C_{70}/C_{60} ratio is greater and can be varied by changing the regime; (2) in a flame metastable C_{60} and C_{70} isomers, oxidized $C_{60}O$ and $C_{70}O$ fullerenes, and hydrogenated fullerenes are formed; and (3) in the region of fullerene formation, oxygen and hydrogen are present.

Also, differences in the behavior in the flame of the soot and the fullerenes were noted: (1) surface curvature and strain of the fullerene precursors are the factors slowing down the growth of fullerenes compared to soot. Therefore, in some regimes, fullerenes are formed farther away from the burner than soot; (2) the highest fullerene content is found in soot not produced in the most smoky regimes; and (3) because oxygen and hydrogen are present in the flame, the formed fullerenes, as more inert structures, survive in areas where the soot is destroyed.

An important practical result of the work was the establishment of the ranges of fullerene content in the soot in different regimes, the total range being 0.0026–20%, and of the yield of fullerenes per quantity of carbon fed to the discharge, 0.002–0.5%. The highest achieved rate of fullerene production ($C_{60} + C_{70}$) was 0.45 g/h in the following regime: pressure was 69 torr; C/O was 0.989; velocity was 38 cm/s, and helium content was 25%. Under these conditions, fullerenes accounted for 12.2% of the weight of soot. The highest content of fullerenes in the soot (20%) was obtained in the following regime: pressure was 37.5 torr; C/O was 0.959; velocity was 40 cm/s, and helium content was 25%.

Relying on the obtained results, the authors of [20] arrived at the conclusion that "… flame synthesis offers not only an alternative method for large scale fullerenes production, but an ability to control the distribution of products (e.g., the C_{70}/C_{60} ratio) over a larger range than has been realized in the graphite vaporization method." In 1992, when the cost of C_{60} fullerenes was $5000 per g, this conclusion looked very realistic. Nowadays, as regards the economic efficiency of fullerene production, the flame method is far behind the arc discharge method. For example, the highest yield of fullerenes produced in flame is 0.5% of the carbon introduced into the flame [20], which is an order of magnitude less than for the arc discharge. Maximum yield of fullerenes in the flame is obtained at low pressures (40–79 torr) and small velocity of the gas flow over the burner (30–50 cm/s). This means that the rate of fullerene formation in these regimes must be very low. The maximum rate amounted, in fact, to a mere 0.5 g/h in an experimental burner 100 mm in diameter. This is considerably less than the quantities produced in modern plasma reactors.

However, in order to get an assessment of the future development of fullerene production by the plasma method, let us consider in more detail those mechanisms of fullerene formation in a flame, which can be considered sufficiently well founded [19, 24]. The formation of fullerenes in a flame occurs not as a result of free carbon coagulation reactions, beginning with small C_n molecules, but via reactions involving polyaromatic hydrocarbons (PAH).

In fuel-enriched flames, the growth process of large hydrocarbon molecules takes place in a region immediately following the oxidation zone. Taking part in this process are rather small aromatic molecules (benzene, naphthalene, and others), as well as C_2H_2 and H_2 molecules, and H atoms, which, similar to the aromatic molecules, represent primary products of the oxidation reaction. The fullerene formation process can be considered as a branching of the dominant growth process of a planar PAH occurring when a considerable curvature has been induced in the growing molecule by a pentagon in its interior part. However, because of the low velocity of intramolecular transformations in a flame at $T = 2000$ K (compared with an arc) and the short time spent by a molecule in the reaction zone, only an insignificant fraction of the coagulations of large PAH molecules ends in structures that then can develop into fullerenes. The bulk of coagulated PAHs takes the path leading to soot formation. Note also that calculations [24] predict a dramatic enhancement of fullerene formation at higher C_2H_2 concentrations and lower concentration of H_2.

There is an optimum temperature for the fullerene formation in a flame. With rising pressure up to atmospheric pressure, the yield of fullerenes decreases, because the relation of competing processes of fullerene and soot formation shifts towards more intensive soot formation.

So, the process of fullerene formation in a flame consists of a very complicated sequence of reactions competing with soot formation process. Naturally, this process depends on the concentration of reactants, temperature, and the flow velocity. The aforementioned parameter determines the time spent in a region where soot and fullerenes are produced. In conventional flames, it is possible to control, independently, the mixture composition (C/O ratio), the mass flow rate, or the pressure in the chamber. Each of these three process parameters influences the overall characteristics of the flame, i.e., in some measure affects each of the above three variables. This situation is similar to that occurring in the arc. It is, therefore, unlikely that a considerable increase in the fullerene formation efficiency can be achieved with known flame types.

To significantly raise the efficiency of fullerene formation in a flame, the following improved methods can be proposed:

The use of fuels with considerably higher C/H atomic ratio than that of benzene and acetylene. If such a fuel happens to be unstable or unfit for storage, it could be prepared in an additional stage immediately preceding the burner.

The introduction of additional reagents, e.g., C_2H_2, into the anteregion of the fullerene formation zone, with preliminary heating.

The development of combination flame-discharge schemes for independent temperature control in the fullerene formation zone. The term "discharge" is construed in a general sense, as glow-, arc-, or rf-discharge, or a discharge with injection of an easy-to-ionize additive. It should be noted that any discharge raises not only the temperature, but also the concentration of charged particles, which can also have a significant effect on fullerene generation [27].

In addition to the above ways of modernizing the flame method, one more method of fullerene production from hydrocarbons can be suggested, which does not involve the combustion process. A flow of hydrocarbons (or their mixture with a buffer gas) can be passed through the volume of plasma in the discharge zone, where excitation, ionization, and dissociation of hydrocarbons takes place. In the discharge zone and at its exit, there will occur an association of the starting hydrocarbons with formation of large PAHs, fullerenes, and soot. An advantage of this method is the possibility of independent control of the concentration of hydrocarbon molecules, the electronic temperature, and the time spent by the reacting mix in the discharge zone. In addition, this method eliminates the unrecoverable loss of fuel as a result of full oxidation taking place in the flame.

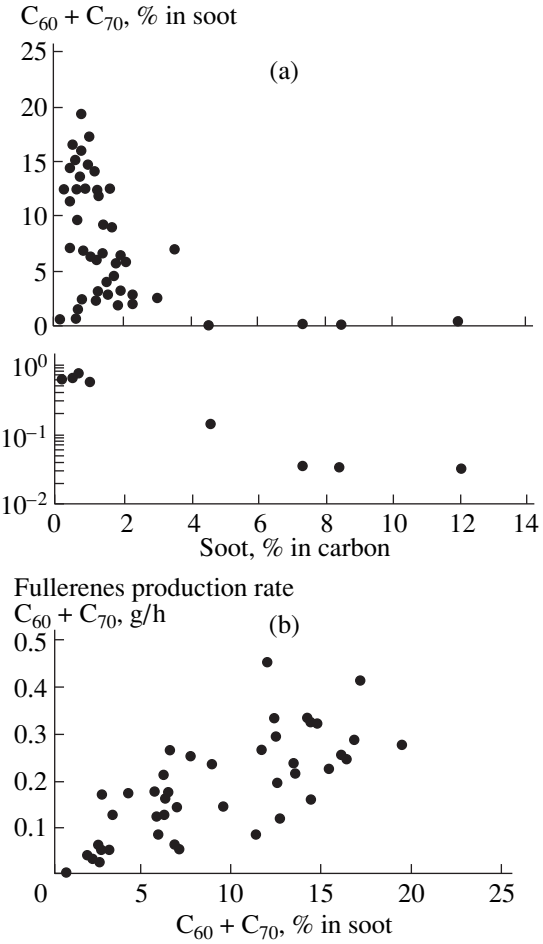

Fig. 5. Formation of fullerenes in the combustion of benzene: (a) fullerene content ($C_{60} + C_{70}$) in the soot as a function of soot yield (in % of the spent carbon); (b) the rate of fullerene production as a function of fullerene content in the soot.

FORMATION OF FULLERENES UNDER LASER HEATING

First, fullerenes have been produced by laser vaporization of graphite. A pulsed laser was used that generated short pulses of high power density [1], and the quantity of fullerenes, thus, produced measured in milligrams. To our knowledge, the use of a continuous wave laser for obtaining visible quantities of fullerenes has not yet been reported. In our opinion, production of fullerenes by laser vaporization of graphite could hardly become technologically viable in the near future. Of course, laser vaporization does not involve formation of the cathode deposit and most of the evaporated graphite will be converted to soot, but the cost of the "unit" of laser beam power will always be considerably higher than corresponding power units in other methods; in addition, the efficiency and the very feasibility of fullerenes production by continuous laser vaporization of graphite need to be experimentally verified.

FORMATION OF FULLERENES BY VAPORIZATION OF GRAPHITE UNDER CONCENTRATED SOLAR IRRADIATION

This method of fullerene production was proposed and implemented in [28] and [29]. The authors of [28] took the view that the main reason of a rather low yield of fullerenes in an arc discharge could be the intense UV radiation of the arc stimulating conversion of fullerenes into insoluble particles. The use of concentrated solar radiation eliminates the harmful effect of UV radiation produced in the arc. In [28] and [29], only small quantities (milligrams) of fullerenes were produced. The authors declared their intention to continue the work, but no further investigations have been reported.

METHODS OF CHEMICAL SYNTHESIS OF FULLERENES

The controlled chemical synthesis of fullerenes can be of considerable interest for two reasons. In this synthesis, it is hoped only molecules of a specified size C_n and, in addition, of a particular C_n isomer will be produced. This will eliminate the step of separation of synthesized fullerenes. In addition, the chemical synthesis can prove very efficient in producing higher fullerenes, which in the standard arc synthesis are produced in very small quantities.

The discovery of fullerenes stimulated numerous works on the synthesis of molecules and structures consisting either exclusively, or, for the most part, of carbon atoms [30, 31]. One of the directions in these works was the synthesis of polycyclic aromatic hydrocarbons (PAH), with one or several pentagons included in the planar network of benzene rings. The first to be synthesized (prior to the discovery of fullerenes) was corannulene, $C_{20}C_{10}$ [32], then followed isomers $C_{30}H_{12}$ [33] and $C_{36}C_{12}$ [34]. As the carbon skeleton of some $C_{30}H_{12}$ isomers is identical to a half of the C_{60} molecule, such an isomer was termed semi-buckminsterfullerene (SBF). Even setting aside the fact that, so far, the existing methods of SBF synthesis yield only milligrams of pure substance [35], dimerization of the obtained SBF's to produce C_{60} will require some rearrangement of bonds [33], which makes the prospects of such a process appear bleak.

FULLERENES AND SCHUNGITES

In 1992, sensational news came from the University of Arizona (USA) [36] of the discovery of fullerenes in schungites of Karelia. Because natural deposits of schungites are very large, this news inspired hopes of producing large quantities of inexpensive fullerenes. In [37], it was reported that the concentration of fullerenes in schungites is as low as 1–10 ppm. The researchers detecting considerable quantities of fullerenes in schungites were experimenting, as a rule, with mass-spectrometers, in which a schungite sample was laser-evaporated and the formation of fullerenes was to be expected.

CONCLUSION

The application prospects of fullerenes as a material of the future for many branches of science and technology depend on the availability of large quantities of low-cost fullerenes. Mass media, including the Internet, regularly report "discoveries" from many countries of new fullerene production methods. As a rule, the authors shroud their essence in a veil of commercial know-how and the excitement settles down without any consequences. In our opinion, the prospects for reducing the cost of fullerenes are realistic and the path leads to hybrid methods of producing fullerene-containing soot. However, the scaling of these methods to commercial quantities will require extensive scientific research.

ACKNOWLEDGMENTS

This work was supported under the Russian science and technology program "Fullerenes and Atomic Clusters" (project no. 98056).

REFERENCES

1. H. W. Kroto, J. R. Heath, S. C. O'Brien, *et al.*, Nature **318**, 162 (1985).
2. W. Kraetschmer, L. D. Lamb, K. Fostiropoulos, and D. Huffman, Nature **347**, 354 (1990).
3. T. Braun and E. Osawa, Fullerene Sci. Technol. **5** (1) (1997).
4. *Fullerene* (Technologie-Analyse) VDL Technologienzentrum, Ed. by H. Eickenbusch, P. Hartwich, Physikalische Technologien, 1993.
5. J. C. Withers, R. O. Loutfy, and T. P. Lowe, Fullerene Sci. Technol. **5** (1), 1 (1997).
6. A. Ya. Vul' and D. R. Huffman, Mol. Mater. **10**, 37 (1998).
7. T. Yadav, in *Proceedings of the Symposium on Recent Advances in Chemistry and Phsyics of Fullerenes and Related Materials, 1994*, Ed. by R. Ruoff and K. Kadish [Proc. Electrochem. Soc. **PV94-24**, 111 (1994)].
8. T. Yadav, in *Proceedings of the Symposium on Recent Advances in Chemistry and Phsyics of Fullerenes and Related Materials, 1994*, Ed. by R. Ruoff and K. Kadish [Proc. Electrochem. Soc. **PV94-24**, 120 (1994)].
9. G. Dyuzhev, Mol. Mater. **7**, 61 (1996).
10. N. S. Goroff, Acc. Chem. Res. **29** (2), 77 (1996).
11. D. H. Parker, P. Wurz, K. Chatterjee, *et al.*, J. Am. Chem. Soc. **113**, 7499 (1991).
12. D. Afanas'ev, I. Blinov, A. Bogdanov, *et al.*, Zh. Tekh. Fiz. **64** (10), 76 (1994) [Tech. Phys. **39**, 1017 (1994)].
13. T. Belz, J. Find, D. Herein, *et al.*, Ber. Bunsenges. Phys. Chem. **101**, 712 (1997).
14. K. Yoshie, Sh. Kasuya, K. Eguchi, and T. Yoshida, Appl. Phys. Lett. **61** (23), 2782 (1992).
15. T. Yoshida, T. Tani, H. Nishimura, and K. Akashi, J. Appl. Phys. **54**, 640 (1983).
16. L. Fulcheri, Y. Schwob, F. Fabry, and G. Flamant, in *Proceedings of the 5th European Conference on Thermal Plasma Process, St. Petersburg, 1998*, p. 216.
17. Ph. Gerhardt, S. Loeffer, and K.-H. Homann, Chem. Phys. Lett. **137**, 306 (1987).
18. J. B. Howard, J. T. McKinnon, Y. Makarovsky, *et al.*, Nature **352**, 139 (1991).
19. J. B. Howard, J. T. McKinnon, M. T. Johnson, *et al.*, J. Phys. Chem. **96**, 6657 (1992).
20. J. B. Howard, A. L. Lafleur, Y. Makarovsky, *et al.*, Carbon **30** (8), 1183 (1992).
21. Th. Baum, S. Loeffler, Ph. Loeffler, *et al.*, Ber. Bunsenges. Phys. Chem. **96** (7), 841 (1992).
22. M. Bachman, J. Griesheimer, and K.-H. Homann, Chem. Phys. Lett. **223**, 506 (1994).

23. R. Tailor, G. J. Langley, H. W. Kroto, and D. R. M. Walton, Nature **366**, 728 (1993).
24. Ch. J. Pope, J. A. Marr, and J. B. Howard, J. Phys. Chem. **97**, 11001 (1993).
25. H. M. Duan and J. T. McKinnon, J. Phys. Chem. **98** (49), 12815 (1994).
26. H. Richter, A. J. Labrocca, W. J. Grieco, *et al*., J. Phys. Chem. B **101**, 1556 (1997).
27. D. V. Afanas'ev, G. A. Dyuzhev, and V. I. Karataev, Pis'ma Zh. Tekh. Fiz. **25** (5), 35 (1999) [Tech. Phys. Lett. **25**, 182 (1999)].
28. L. P. F. Chibante, A. Thess, J. M. Alford, *et al.*, J. Phys. Chem. **97**, 8696 (1993).
29. C. L. Field, J. R. Pitts, M. J. Hale, *et al*., J. Phys. Chem. **97**, 8701 (1993).
30. F. Diederich and J. Rubin, Angew. Chem. Int. Ed. Engl. **31** (9), 1101 (1992).
31. F. Diederich, Nature **369**, 199 (1994).
32. W. E. Barth and R. G. Lawton, J. Am. Chem. Soc. **88** (2), 380 (1966).
33. P. W. Rabideau, A. Y. Abdourazak, H. E. Folsom, *et al*., J. Am. Chem. Soc. **116** (17), 7891 (1994).
34. L. T. Scott, M. S. Bratcher, and S. Hagen, J. Am. Chem. Soc. **118** (36), 8743 (1996).
35. S. Hagen, M. S. Bratcher, M. S. Erickson, *et al*., Angew. Chem. Int. Ed. Engl. **36** (4), 406 (1997).
36. P. R. Buseck, S. J. Tsipurski, and R. Hettich, Science **257** (5067), 215 (1992).
37. E. Ozawa, Fullerene Sci. Technol. **7** (4), 637 (1999).

Translated by B. Kalinin

Technical Physics, Vol. 45, No. 5, 2000, pp. 528–531. Translated from Zhurnal Tekhnicheskoĭ Fiziki, Vol. 70, No. 5, 2000, pp. 8–11.

Resonant Frequencies of Azimuthal-Homogeneous Oscillations of an Anisotropic Sphere

Yu. F. Filippov and Z. E. Eremenko

Usikov Institute of Radiophysics and Electronics, National Academy of Sciences of Ukraine, Kharkov, 310085 Ukraine

Received December 1, 1998

Abstract—The anisotropy of parameters is an intrinsic characteristic feature of dielectrics employed in production of high-*Q* resonators. A theory of azimuthal-homogeneous resonant oscillations in a single-crystal sphere is developed. It is demonstrated that the anisotropy gives rise to *TM* oscillations of two orders at different frequencies. Oscillations with large polar indices are numerically investigated. © *2000 MAIK "Nauka/Interperiodica".*

Spectral characteristics of resonant oscillations are investigated for an isotropic sphere only [1, 2]. The lower order oscillation modes in a spherical resonator that is manufactured of a single crystal bounded with a perfectly conducting surface are studied in [3].

The anisotropy of parameters is an intrinsic characteristic feature of dielectrics employed in production of high-*Q* resonators. Investigations of this anisotropy are necessary for studying deformations accompanied by a rise of the electric field intensity and for evaluating the degree of ordering of the domain structure. These factors should be analyzed when designing integrated circuits of millimeter and submillimeter wavelength bands. The foregoing indicates that investigations of the anisotropy effect on the resonant frequencies are of considerable importance.

Ruby, leucosapphire, and quartz single crystals, which are characterized by low dielectric losses, are widely used in technology. Their electric parameters are described by the permittivity dyadic

$$\hat{\varepsilon} = \varepsilon_{ik}\delta_{ik} \quad \text{for} \quad \varepsilon_{xx} = \varepsilon_{yy} \neq \varepsilon_{zz}, \tag{1}$$

where ε_{zz} and ε_{xx} are the permittivities measured in the directions parallel and perpendicular to the anisotropy axis.

In the spherical coordinate system (r, θ, φ), dyadic $\hat{\varepsilon}$ is reduced to the form

$$\hat{\varepsilon} = \begin{pmatrix} \varepsilon_{rr} & -\varepsilon_{r\theta} & 0 \\ -\varepsilon_{r\theta} & \varepsilon_{\theta\theta} & 0 \\ 0 & 0 & \varepsilon_{xx} \end{pmatrix}, \tag{2}$$

where $\varepsilon_{rr} = \varepsilon_+ + \varepsilon_-\cos 2\theta$, $\varepsilon_{\theta\theta} = \varepsilon_+ - \varepsilon_-\cos 2\theta$, $\varepsilon_{r\theta} = \varepsilon_-\sin 2\theta$, and $2\varepsilon_\pm = \varepsilon_{zz} \pm \varepsilon_{xx}$.

In this paper, we investigate azimuthal-homogeneous oscillations ($\partial E/\partial\varphi = \partial H/\partial\varphi = 0$) of a uniaxial single-crystal sphere. The system of Maxwell equations describing these oscillations is split into two independent subsystems for *TE* ($E_r = E_\theta = H_\varphi = 0$) and *TM* ($H_r = H_\theta = E_\varphi = 0$) modes. The solution of these subsystems reduces to the solution of the differential equations

$$\left(\frac{\partial^2}{\partial r^2} + \frac{1}{r^2\sin\theta}\frac{\partial}{\partial\theta}\sin\theta\frac{\partial}{\partial\theta} - \frac{\varepsilon_{xx}}{c^2}\frac{\partial^2}{\partial t^2}\right)V = 0, \tag{3}$$

$$\left(\varepsilon_{rr}\frac{\partial^2}{\partial r^2} + \frac{1}{r^2\sin\theta}\frac{\partial}{\partial\theta}\sin\theta\left(\frac{\partial}{\partial\theta}\varepsilon_{\theta\theta} - \varepsilon_{r\theta}\left(1 + r\frac{\partial}{\partial r}\right)\right)\right.$$
$$\left. - \frac{\varepsilon_{r\theta}}{r}\frac{\partial^2}{\partial r\partial\theta} - \frac{\varepsilon_{xx}\varepsilon_{zz}}{c^2}\frac{\partial^2}{\partial t^2}\right)U = 0. \tag{4}$$

The field components of the resonant oscillations are expressed through potential functions U and V by

$$H_r = \left(\frac{\partial^2}{\partial r^2} + \frac{\varepsilon_{xx}}{c^2}\frac{\partial^2}{\partial t^2}\right)V; \quad rcE_\varphi = \varepsilon_{xx}\frac{\partial^2}{\partial t\partial\theta}V;$$
$$rH_\theta = \frac{\partial^2}{\partial r\partial\theta}V; \tag{5}$$

and

$$E_r = \left(\frac{\partial^2}{\partial r^2} + \frac{\varepsilon_{\theta\theta}}{c^2}\frac{\partial^2}{\partial t^2}\right)U; \quad rE_\theta = \left(\frac{\partial^2}{\partial t\partial\theta} - \frac{\varepsilon_{r\theta}r}{c^2}\frac{\partial^2}{\partial t^2}\right)U;$$
$$rcH_\theta = \frac{\partial}{\partial t}\left(\varepsilon_{r\theta}\left(1 + r\frac{\partial}{\partial r}\right) - \frac{\partial}{\partial\theta}\varepsilon_{\theta\theta}\right)U \tag{6}$$

for the *TE* and *TM* modes, respectively.

A solution to system (3) and (4), which is finite at $r = 0$ and satisfies the radiation condition at $r \longrightarrow \infty$,

1063-7842/00/4505-0528$20.00

can be represented in the form

$$\{S\} = \sum_n \exp(-i\omega t) P_n(\cos\theta) \begin{cases} A_{S,n} j_n(qsr), & r \le r_0 \\ B_{S,n} h_n^{(1)}(kr), & r \ge r_0, \end{cases} \quad (7)$$

where ($S = U, V$), $A_{S,n}$ and $B_{S,n}$ are constants; r_0 is the radius of the sphere; $k = \omega/c$; n is the polar index; q_S is the radial component of the wave vector inside the sphere; $j_n(x) = \sqrt{\frac{\pi x}{2}} J_{n+\frac{1}{2}}(x)$, $h_n^{(1)}(x) = \sqrt{\frac{\pi x}{2}} H^{(1)}_{n+\frac{1}{2}}(x)$, $J_\nu(x)$, and $H_\nu^{(1)}(x)$ are the cylinder Bessel and Hankel functions of the first kind; and $P_n(\cos\theta)$ are the Legendre polynomials. Functions $j_n(x)$ and $P_n \equiv P_n(\cos\theta)$ satisfy the recurrence correlations

$$\sin\theta \frac{\partial P_n}{d\theta} = n(P_n \cos\theta - P_{n-1}) = (n+1)(P_{n+1} - P_n \cos\theta), \quad (8)$$

$$x \frac{d j_n(x)}{dx} = (n+1) j_n(x) - x j_{n+1}(x) = x j_{n-1}(x) - n j_n(x).$$

The substitution of expansion (7) into (3) yields the radial components of the *TE*-mode wave vector. For the azimuthal-homogeneous oscillations in isotropic and anisotropic resonators, they are identical and equal to $q_V = k\sqrt{\varepsilon_{xx}}$.

The anisotropy affects only the *TM* mode. Substituting (7) into (4), using recurrence correlations (8), and equating coefficients at $j_n(qr)P_n(\cos\theta)$, we obtain the system of algebraic equations for coefficients $A_{U,n}$ of expansion (7)

$$\left(\varepsilon_{xx}\varepsilon_{zz}k^2 - \left(\varepsilon_+ - \frac{\varepsilon_-}{(2n-1)(2n+3)}\right)q_U^2\right)A_{U,n} + \frac{\varepsilon_- q_U^2}{2}\left(\left(1 + \frac{4n-3}{(2n-1)(2n-3)}\right)A_{U,n-2} + \left(1 - \frac{4n+7}{(2n+3)(2n+5)}\right)A_{U,n+2}\right) = 0. \quad (9)$$

One can see from (9) that the anisotropy effect initiates the interaction of partial oscillations with different polar indices n. After some algebra, system (9) reduces to the form

$$\left(\alpha_n - \frac{\gamma_{n-2}\beta_n}{Q_n} - \frac{\gamma_n \beta_{n+2}}{T_n}\right)A_n = 0, \quad (10)$$

$$A_{n+2} = -\rho_n A_n, \quad A_{n-2} = -g_n A_n, \quad (11)$$

where

$$\alpha_n = \alpha + \frac{\varepsilon_- q_U^2}{(2n-1)(2n+3)},$$

$$\beta_n = \beta\left(1 + \frac{4n-3}{(2n-1)(2n-3)}\right),$$

$$\gamma_n = \beta\left(1 - \frac{4n+7}{(2n+3)(2n+5)}\right),$$

$$\alpha = \varepsilon_{xx}\varepsilon_{zz}k^2 - \varepsilon_+ q_U^2, \quad \beta = \frac{\varepsilon_- q_U^2}{2},$$

$$\rho_n = \frac{\beta_{n+2}}{Q_n}, \quad g_n = \frac{\gamma_{n-2}}{T_n},$$

$$Q_n = \alpha_{n-2} - \cfrac{\beta_{n-2}\gamma_{n-4}}{\alpha_{n-4} - \cfrac{\beta_{n-4}\gamma_{n-6}}{\alpha_{n-6} - \cfrac{\beta_{n-6}\gamma_{n-8}}{\ldots R}}},$$

$$T_n = \alpha_{n+2} - \cfrac{\beta_{n+4}\gamma_{n+2}}{\alpha_{n+4} - \cfrac{\beta_{n+6}\gamma_{n+4}}{\alpha_{n+6} - \ldots}}.$$

At $n = 0$ and $n = 1$, parameter β_n is equal to zero. Hence, in the expression for Q_n,

$$R = \alpha_2 - \frac{\beta_2\gamma_0}{\alpha_0}$$

and

$$R = \alpha_3 - \frac{\beta_3\gamma_5}{\alpha_1}$$

for even and odd n, respectively. The fraction involved in the expression for T_n can be represented in a more compact form. Indeed, when $(n+s) \gg 1$, one can ignore the index dependence of α_{n+s}, β_{n+s}, and γ_{n+s}. In this case,

$$\Omega \equiv \alpha_{n+s} - \frac{\gamma_{n+s}\beta_{n+s+2}}{\alpha_{n+s+2} - \ldots} = \alpha - \frac{\beta^2}{\alpha - \ldots} = \alpha - \frac{\beta^2}{\Omega}. \quad (12)$$

Solving (12) with respect to Ω yields

$$2\Omega_\pm = \alpha \pm \sqrt{\alpha^2 - 4\beta^2}. \quad (13)$$

Then, T_n is modified to the form

$$T_n = \alpha_{n+2} - \cfrac{\gamma_{n+2}\beta_{n+4}}{\alpha_{n+4} - \ldots - \cfrac{\gamma_{n+s-2}\beta_{n+s}}{\Omega_\pm}}. \quad (14)$$

A nontrivial solution to (10) exists when the following functional relationship holds:

$$\alpha_n - \frac{\gamma_{n-2}\beta_n}{\Omega_n} - \frac{\gamma_n\beta_{n+2}}{T_n} = 0. \quad (15)$$

The tangential field components E_θ and H_φ of the resonant oscillations must be continuous on the surface

of the sphere ($r = r_0$). Taking into account this condition, we obtain the equation for the *TE* modes, which coincides with the dispersion equation for the isotropic sphere,

$$y_V j_{n-1}(y_V) h_n^{(1)}(y_0) = y_0 j_n(y_V) h_{n-1}^{(1)}(y_0), \qquad (16)$$

where $y_s = q_s r_0$ and $y_0 = kr_0$.

Now, consider the *TM* modes. Taking into account the continuity condition for tangential components E_θ and H_φ at $r = r_0$ yields the relationships

$$\sum_n \Big((y_U j_{n-1}(y_U) - n j_n(y_U)) \frac{dP_n}{d\theta} - \varepsilon_- y_0^2 \sin 2\theta\, j_n(y_U) P_n \Big) A_n$$

$$= \sum_n (y_0 h_{n-1}^{(1)}(y_0) - n h_n^{(1)}(y_0)) \frac{dP_n}{d\theta} B_n,$$

$$\sum_n \Big(j_n(y_U) \frac{d}{d\theta} (\varepsilon_+ - \varepsilon_- \cos 2\theta) P_n + \varepsilon_- \sin 2\theta ((n+1) j_n(y_U) + y_U j_{n-1}(y_U)) \Big) A_n \qquad (17)$$

$$= \sum_n h_n^{(1)}(y_0) \frac{dP_n}{d\theta} B_n.$$

Using recurrence correlations (8), one can show that

$$\sin 2\theta P_n = \frac{2}{2n+1} \frac{d}{d\theta} \Big(\frac{n}{2n-1} P_{n-2} - \frac{n+1}{2n+3} P_{n+2} - \frac{2n+1}{(2n-1)(2n+3) P_n} \Big),$$

$$\cos 2\theta P_n = \frac{2}{2n+1} \Big(\frac{n(n-1)}{2n+1} P_{n-2} + \frac{(n+1)(n+2)}{2n+3} P_{n+2} - \frac{2n+1}{(2n-1)(2n+3) P_n} \Big). \qquad (18)$$

Substituting (18) into (17) and equating the coefficients at $dP_n/d\theta$, we obtain a system of algebraic equations for A_n and B_n. Nontrivial solutions to this system exist when the following functional equation is satisfied:

$$y_0 h_n^{(1)}(y_0) F_{U,n} = (y_0 h_{n-1}^{(1)}(y_0) - n h_n^{(1)}(y_0)) G_{U,n}, \qquad (19)$$

where

$$F_{U,n} = y_U j_{n-1}(y_U) - n j_n(y_U) + 2\varepsilon_- y_0^2 \Big(\frac{(n+2)\rho_n j_{n+2}(y_U)}{(2n+3)(2n+5)} - \frac{(n-1) g_n j_{n-2}(y_U)}{(2n-1)(2n-3)} - \frac{j_n(y_U)}{(2n-1)(2n-3)} \Big),$$

$$G_{U,n} = \Big[\varepsilon_+ - \frac{\varepsilon_-}{2n+3} \Big] j_n(y_U) + 2\varepsilon_- \Big(\frac{y_U j_{n-1}(y_U)}{2(2n-1)(2n+3)} + \frac{n R_{1,n} g_n}{(2n-1)(2n-3)} + \frac{(n+1) R_{2,n} \rho_n}{(2n+3)(2n+5)} \Big),$$

$$R_{1,n} = \Big(\frac{(2n-1)^2}{y_U} - y_U \Big) j_{n-1}(y_U) - (2n-1) j_n(y_U),$$

$$R_{2,n} = \Big(\frac{(2n+3)^2}{y_U} - y_U \Big) j_{n+1}(y_U) - (2n+3) j_n(y_U).$$

Solving simultaneously (15) and (19), we obtain the radial component of the wave vector and resonant frequency of the *TM*-mode oscillations in the single-crystal sphere for an arbitrary polar index.

In the isotropic sphere, there exist high-*Q* oscillations characterized by high polar indices. The main characteristic feature of these oscillations is that the energy of the field is concentrated in the region adjacent to the sphere surface [4]. A high *Q*-factor and the presence of regions with concentrated energy provide a possibility to design a number of devices with novel unique properties and to measure extremely low losses in crystals and liquids [5–8].

When $n \gg 1$, expressions (11) and (15) can be simplified as follows:

$$A_{n+1} \approx \zeta A_{n-1}, \quad \zeta = \pm 1,$$
$$[\varepsilon_+ - \zeta \varepsilon_-] q_U^2 \approx \varepsilon_{xx} \varepsilon_{zz} k^2. \qquad (20)$$

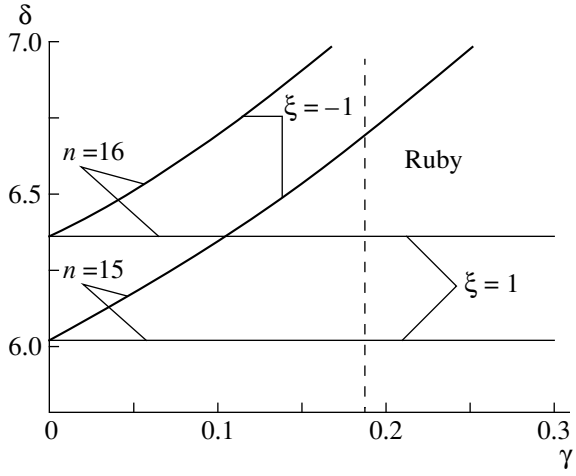

Fig. 1. Dimensionless resonant frequency δ of the *TM* mode excited in an anisotropic sphere vs. parameter γ for ε_{zz} = 11.53.

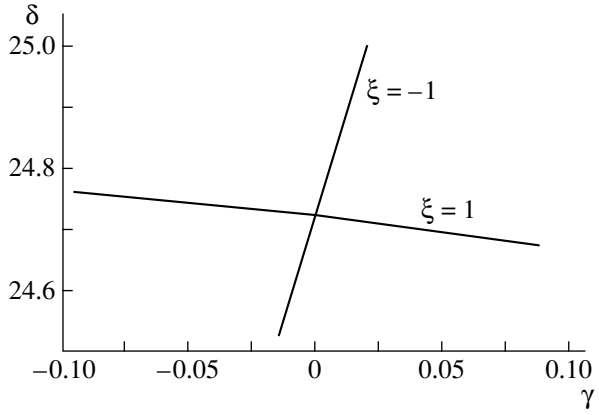

Fig. 2. Dimensionless resonant frequency δ of the *TM* mode excited in an anisotropic sphere vs. parameter γ for ε_{zz} = 2.04.

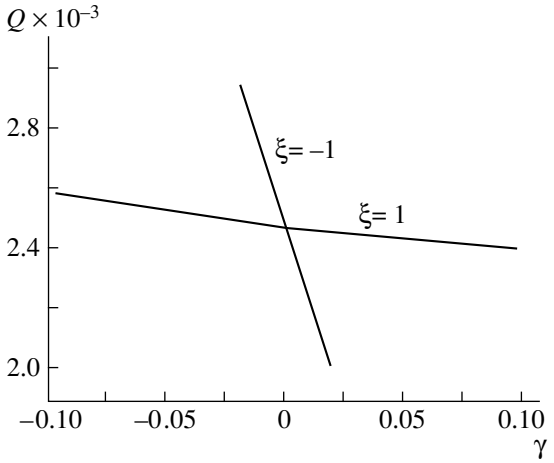

Fig. 3. *Q*-factor of the resonant *TM* oscillations excited in an anisotropic sphere vs. parameter γ for ε_{zz} = 2.04.

The latter relationship determines the component of the wave vector for the *TM* modes,

$$q_U = k\sqrt{\frac{\varepsilon_{xx}\varepsilon_{zz}}{\varepsilon_+ - \zeta\varepsilon_-}}. \qquad (21)$$

Relationship (19) is reduced to the form

$$\begin{aligned}&((y_V^2 - 2\varepsilon_- y_0^2) j_{n-1}(y_V) - n y_V j_n(y_V)) h_n^{(1)}(y_0)\\ &= (\varepsilon_+ - \zeta\varepsilon_-) y_V j_n(y_V)(y_0 h_{n-1}^{(1)}(y_0) - n h_n^{(1)}(y_0)).\end{aligned} \qquad (22)$$

The dispersion equation (22) involves parameter ζ taking the values +1 and –1, which correspond to the fact that the anisotropy effect initiates two independent *TM* oscillations with different frequencies.

Figure 1 shows the reduced resonant frequency $\delta = r_0\omega/c$ versus the parameter $\gamma = (\varepsilon_{zz} - \varepsilon_{xx})/\varepsilon_{xx}$ for *n* equal to 15 and 16, r_0 = 1 cm, ε_{zz} = 11.53, and $\tan\delta = 10^{-4}$. In the isotropic sphere (γ = 0), there exists one *TE* and one *TM* oscillations. The anisotropy effect (γ ≠ 0) splits the *TM* mode into two oscillations with different frequencies and radial components of the wave vector. In particular, for the ruby sphere, these frequencies are 28.7 and 32.3 GHz (*n* = 15).

Figures 2 and 3 present dimensionless frequency δ and *Q* versus parameter γ of the anisotropic sphere for ε_{zz} = 2.08 (teflon), r_0 = 3.9 cm, *n* = 30, and tan = 1.786×10^{-4}. Teflon is known to be an isotropic material. The anisotropy appears during the manufacturing process and causes the splitting of the resonant frequencies of the *TM* oscillations. This effect can be used in practice.

REFERENCES

1. J. A. Stratton, *Electromagnetic Theory* (McGraw-Hill, New York, 1941).
2. Babak Makkinejad and G. W. Ford, Phys. Rev. B **44**, 8536 (1991).
3. M. Gastine, L. Gourtois, and J. Dormann, IEEE Trans. Microwave Theory Tech. **MTT-15** (12), 694 (1967).
4. L. A. Vaĭnshteĭn, *Open Cavities and Open Waveguides* (Sov. Radio, Moscow, 1966).
5. V. V. Braginskiĭ and V. S. Il'chenko, Dokl. Akad. Nauk SSSR **293** (6), 1358 (1987) [Sov. Phys. Dokl. **32**, 306 (1987)].
6. S. Sottini, E. Giorgetti, and C. Marcellino, Pure Appl. Opt. **1** (6), 359 (1992).
7. E. M. Ganapol'skiĭ, A. V. Golik, and A. P. Korolyuk, Fiz. Nizk. Temp. **19** (11), 1255 (1993) [Low Temp. Phys. **19**, 892 (1993)].
8. S. N. Khar'kovskiĭ, A. E. Kogut, and V. V. Kutuzov, Pis'ma Zh. Tekh. Fiz. **23** (15), 25 (1997) [Tech. Phys. Lett. **23**, 584 (1997)].

Translated by I. Efimova

Technical Physics, Vol. 45, No. 5, 2000, pp. 532–537. Translated from Zhurnal Tekhnicheskoĭ Fiziki, Vol. 70, No. 5, 2000, pp. 12–16.

Temperature Dependence of an Electron Attachment to Chlorine Molecules

A. P. Golovitskiĭ

St. Petersburg State Technical University, ul. Politekhnicheskaya 29, St. Petersburg, 195251 Russia

Received February 19, 1999; in final form, May 24, 1999

Abstract—The cross section of electron attachment to chlorine molecules was calculated with the Condon reflection method for various populations of vibrational levels of the ground molecule state. The populations are defined by a prescribed vibrational temperature. The vibrational wave functions were obtained by numerically solving the Schrödinger equation, and required parameters of the potentials of upper ion states were taken, so as to minimize the deviation between calculated and room-temperature experimental data on the cross section of electron attachment. © *2000 MAIK "Nauka/Interperiodica".*

Recently, interest in modeling processes in a low-pressure plasma of electronegative gases, in particular, in a chlorine-containing plasma [1–4], has grown. The processes of fundamental importance for negative-ion generation in such plasmas are dissociative attachment (DA) of electrons

$$Cl_2 + e \longrightarrow Cl^- + Cl \qquad (1)$$

with the zero energy threshold and ion-pair formation (IPF)

$$Cl_2 + e \longrightarrow Cl^- + Cl^+ + e, \qquad (2)$$

which occurs at elevated electron energies. All discharge models employ experimental data on the cross sections of reactions (1) and (2) that were obtained in [5]. Although [5] was published more than twenty years ago, the subsequent revisions confirmed the validity of its results (see, e.g., [6]). However, they hold only for gases at room temperature, when the populations of vibrational states with $v > 0$ in Cl_2 do not exceed 7% (v is the vibrational quantum number). Data on a temperature dependence of electron attachment to Cl_2 molecules are lacking in the literature, however, it is known for other halogens. For example, the rate of electron attachment to I_2 molecules increased by almost threefold as the temperature rises from 290 to 460 K [7]. This fact is associated with a change in the populations of vibrational states of iodine molecule. In real-gas plasmas, the gas temperature may substantially exceed room temperature [1, 2, 8]. This may noticeably change the rate of attachment to chlorine as well, which should be taken into account in modeling.

The aim of this paper is to evaluate the cross section and the rate of electron attachment to chlorine molecules as a function of the populations of the vibrational molecule states. The populations are defined by vibrational temperature T_v.

According to [9], the process of electron attachment can be represented as the absorption of the energy W_e of an incident electron, which is accompanied by an upward transition from the vibrational levels of the ground state of Cl_2 molecule to one of the upper states either of a Cl_2^- molecular ion or of a Cl^-Cl^+ ion pair with subsequent dissociation into Cl^- + Cl (DA) or Cl^- + Cl^+ (IPF). Since the potential curves of the final states are repulsive (or the case in point is the repulsive branch of the $^2\Sigma_u^+Cl_2^-$ state), i.e., having a continuous energy spectrum, one can use the Condon reflection method [10] to calculate the cross sections of such transitions. Following this method, the cross section (prob-

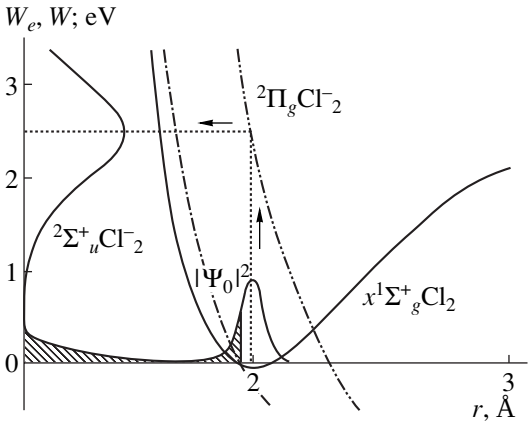

Fig. 1. Illustration of the Condon reflection method. Are shown potential curves for the Cl_2 ground state ($X^1\Sigma_g^+$) and two lower states of a Cl_2^- ion, as well as the results of reflection of $|\Psi_0|^2$ from the potentials of the $^2\Sigma_u^+$ (hatched) and $^2\Pi_g$ states.

1063-7842/00/4505-0532$20.00 © 2000 MAIK "Nauka/Interperiodica"

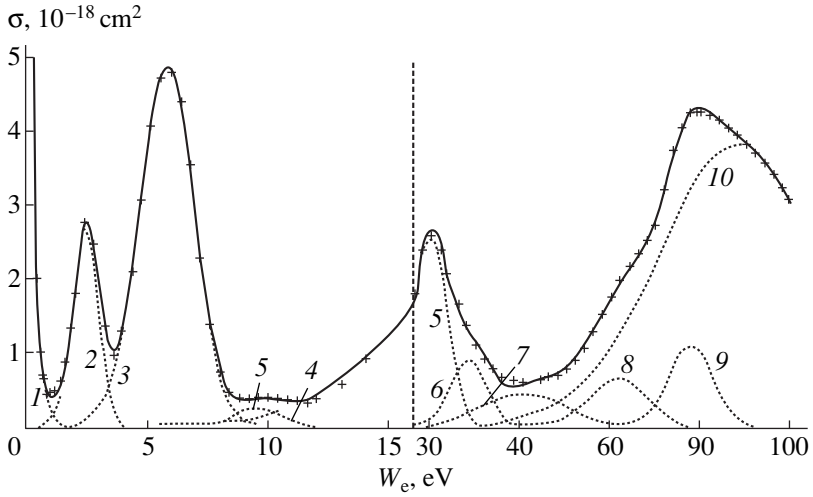

Fig. 2. Calculated total (solid line) and partial (dotted lines) attachment cross sections at 300 K. The partial cross sections are obtained by reflection from the potentials of the (*1*) $^2\Sigma_u^+$, (*2*) $^2\Pi_g$, (*3*) $^2\Pi_u$, and (*4*) $^2\Sigma_g^-$ states (all for Cl_2^-); (*5*)–(*10*) unknown states. The crosses refer to the experimental data [5]. The vertical dotted line separates different energy scales.

ability) for a corresponding transition is found by reflecting the squared magnitudes of the vibrational wave functions $|\Psi_v|^2$ for the ground electron state $X^1\Sigma_g^+$ of a molecule from the upper potential curve (in view of its curvature) onto an energy scale reckoned from the lower vibrational level (Fig. 1). If $v > 0$, both potentials should be lowered by the energy of the vth vibrational level on reflection. As a result, the scale of potential energy W will coincide with that of the incident electron energy W_e for any v. The reflected values of $|\Psi_v|^2$ are summed over v on the energy scale, their weights corresponding to the relative populations of the vibrational levels at a prescribed temperature T_v. The rotational excitation of molecules can be neglected in this case, since the centrifugal energy is almost equally shared by the upper and lower states due to the conservation of total angular momentum of a molecule in Frank–Condon transitions.

Basically, the reflection method is not an *ab initio* method. It gives an idea of only the shape of an energy dependence of the attachment cross section. In order to obtain the magnitude of the cross section, one should normalize the result by comparing with experimental data. It is worth noting, however, that, because of the lack of data on the run and arrangement of the potential curves for molecular terms and a low accuracy of their construction, most modern methods for calculating the attachment cross sections virtually are not *ab initio*, since their results should be brought into correspondence with experimental data.

DA involves transitions to at least four potential curves for Cl_2^- molecular ion states: $^2\Sigma_u^+$, $^2\Pi_g$, $^2\Pi_u$, and $^2\Sigma_g^+$ [5], whereas IPF implies transitions to a wide set of Cl^-Cl^+ possible ion states [11]. A cross section obtained by reflection from any potential curve will be referred to as a partial cross section. The total cross section is the sum of partial ones.

In our work, the vibrational wave functions Ψ_v for the ground state $X^1\Sigma_g^+$ of a Cl_2 molecule were calculated by numerically solving the Schrödinger equation with the use of the expression for interatomic potential taken from [12]. This expression is sufficiently accurate and provides the coincidence of calculated and measured vibrational level energies with a precision of three significant figures. Unfortunately, the accuracy of potential curves for a Cl_2^- ion available in the literature

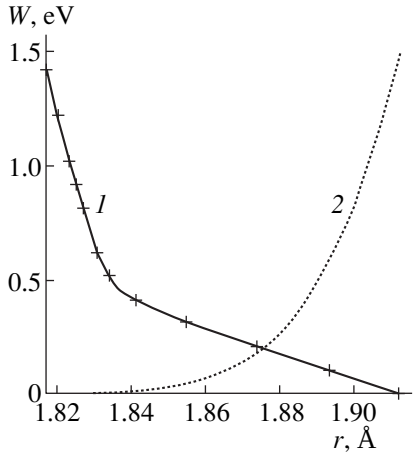

Fig. 3. Potential curve for the $^2\Sigma_u^+$ state of a Cl_2^- ion in the reflection region. Crosses, values restored by the data taken from [5]; (*1*) our approximation, and (*2*) $\sum_v |\Psi_v|^2$ at 300 K.

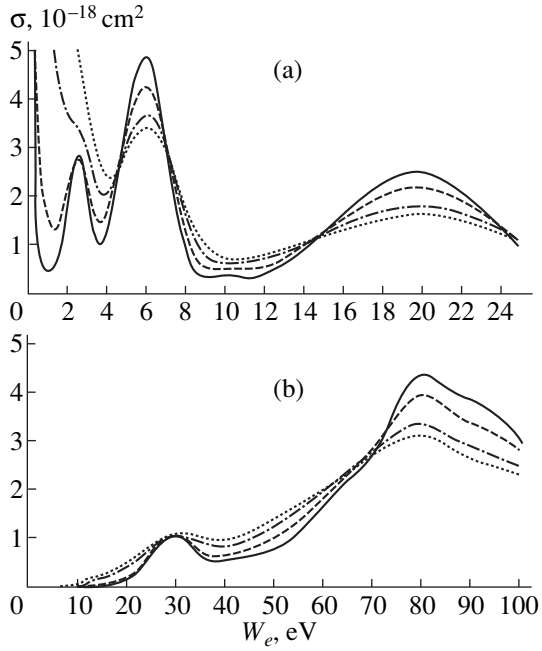

Fig. 4. Cross sections of (a) dissociative attachment and (b) ion-pair formation at (*1*) 300, (*2*) 500, (*3*) 800, and (*4*) 1000 K.

[11, 13, 14] is too poor for calculations with the reflection method to be done; moreover, the potentials of Cl^-Cl^+ ion states are unknown at all for energies above 16 eV. Therefore, we first refined available information on the run of the potential curves for the final states. True curves were represented by simple expressions with variables. The latter were selected such that the residual between calculated and experimentally found [5] room-temperature attachment cross sections was the smallest (Fig. 2).

In the domain of vibrational wave functions for a Cl_2 molecule (r = 1.6–2.6 Å), the potentials of the states $^2\Pi_g$, $^2\Pi_u$, and $^2\Sigma_g^+$ of a Cl_2^- molecule ion (reflection from these potentials yields to DA cross sections) were approximated by asymptotic expressions of type $a + b/r^6$ according to [13]. The same approximation was applied to the potential curve that presumably [5] corresponds to some Cl_2^- higher state responsible for the peak in the attachment cross section curve at $W_e \simeq$ 20 eV (Fig. 2). Since the threshold of this partial cross section <9 eV at T_v = 300 K, one should assign it to DA rather than to IPF, since the IPF threshold should be ≈11.48 eV at 300 K.

When calculating DA cross sections, we first varied parameters of partial cross section *3* in Fig. 2 (which corresponds to the upper potential of the $^2\Pi_u$ state). A comparison with the experiment was made in the range of electron energies where this partial cross section does not overlap with neighboring ones. Then we subtracted this value from experimentally found, varied parameters of cross section *2* (which corresponds to the potential of the $^2\Pi_g$ state), and so on.

The shape of the potential for the lower state $^2\Sigma_g^+$ of a $Cl_2^{-2}\Sigma_u^+$ ion is worth another look, since none of the approximations like $a + b/r^6$, $a + b/r^c$, or $a + b\exp(-c^r)$ did not lead to a satisfactory agreement between the result of reflection and the experimental data reported in [5]. This potential cuts the potential $X^1\Sigma_g^+$ of the ground state of Cl_2 molecule near its minimum more to the left of the coordinate of equilibrium interatomic distance (1.998 Å). Thus, only the left-hand side of $|\Psi_v|^2$ is reflected to the energy range $W_e \geq 0$ (Fig. 1). Using the shapes of $|\Psi_v|^2$ and the attachment cross sections near $W_e \approx 0$ [5], one can restore the potential curve for the $^2\Sigma_u^+$ state that provides adequate reflection. This curve, shown in Fig. 3, has a bend. The bend probably reflects the changed character of interaction between the components of a Cl_2^- molecular ion due to electron-impact-induced excitation of a Cl atom from the ground state $3p^2P^0_{3/2}$ to the $3p^2P^0_{1/2}$ state (the excitation thresh-

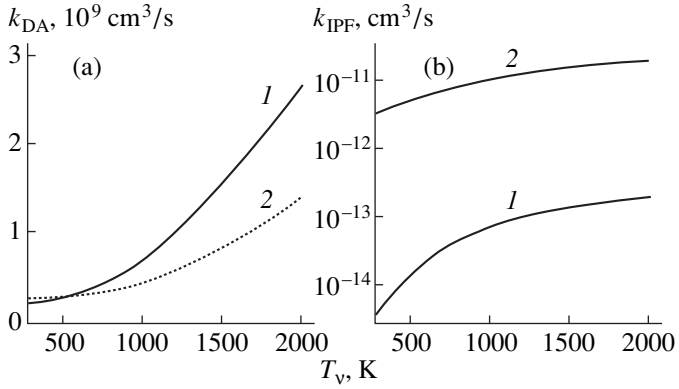

Fig. 5. Rate coefficients of electron attachment for (a) dissociative attachment and (b) ion-pair formation. T_e = (*1*) 1.5 and (*2*) 4 eV.

old $W_e \approx 0.11$ eV). The potential curve for the $^2\Sigma_u^+$ state was satisfactorily approximated by a hyperbola with inclined axes (Fig. 3).

Due to the considerable overlap of the IPF partial cross sections (Fig. 2), the parameters of the potential curves for the Cl^-Cl^+ ion states were estimated in a different way. First, we represented the experimental data obtained in [5] as the sum of Gaussian curves (the residual between $\sum_v |\Psi_v|^2$ and a Gaussian curve does not exceed 4% at 300 K). In such a way, we roughly estimated the positions and the magnitudes of the peaks of the partial cross sections. The potential curves for the ion states were approximated by linear functions in the form $a - b \times r$ bounded below at 11.48 eV (the difference between the ionization and affinity energies of a Cl atom plus the energy of dissociation of a Cl_2 molecule). Knowing the position of the cross section peak, one can relate the potential parameters between each other and vary only one parameter for everyone of the potentials. Then the refined approximations of the partial cross sections were obtained by means of reflections of $|\Psi_v|^2$ and variations of the potential parameters. Finally, we varied the positions and the magnitude of the peaks separately in order to minimize the discrepancy between the calculated and experimental total cross sections. This procedure was repeated several times.

Eventually, we determined the parameters of ten potential curves. The integral discrepancy between the DA total cross section calculated by reflection from these curves and experimental data at 300 K turned out to be no more than 3% for electron energies from 0 to 100 eV (Fig. 2).

Subsequently, we calculated the cross sections for DA and IPF at $T_v > 300$ K by the above method of reflection with the use of the obtained potential parameters. The results of calculations are presented in Fig. 4, as well as in Tables 1 and 2. Figure 4 shows that the peaks of the DA cross sections become smeared with increasing T_v because of an increase in the populations of vibrational levels with $v > 0$ and an upward extension of the potential well of the $X^1\Sigma_g^+$ state. The DA cross section grows largely at W_e's from 0 to 3 eV. This results from an increase in or, more precisely, rightward smearing of the first partial cross section due to transitions to the $^2\Sigma_u^+$ state of a Cl_2^- molecular ion. In Fig. 5, the temperature dependences of the rate coefficients k for electron attachment are shown separately for DA and IPF. They were calculated by integrating the obtained cross sections over the Maxwell energy distribution of electrons with temperatures T_e equal to 1.5 and 4 eV. The DA rate grows faster at smaller values of T_e, because the temperature affects the DA cross section most strongly just in the range of low electron energies.

Table 1. Cross section of dissociative attachment

W_e, eV	$\sigma \times 10^{18}$ cm^2 for T_v, K				
	300 [5]	300	500	800	1000
0	201.6	202	238	292	322
0.2	24.5	21.7	29.5	46.7	60.8
0.4	2.0	1.73	4.18	13.7	23.8
0.6	0.68	0.76	2.54	10.1	18.7
0.8	0.50	0.55	1.93	8.15	15.5
1	0.42	0.45	1.56	6.68	13.0
1.4	0.59	0.61	1.36	4.79	9.34
1.8	1.32	1.35	1.76	3.90	7.04
2.2	2.42	2.43	2.45	3.59	5.66
2.6	2.79	2.78	2.73	3.38	4.72
3	1.92	1.95	2.23	2.90	3.86
3.4	1.06	1.13	1.56	2.29	3.03
3.8	1.05	1.13	1.50	2.01	2.50
4.2	1.69	1.73	1.98	2.21	2.45
4.6	2.57	2.67	2.69	2.65	2.69
5	3.63	3.66	3.41	3.10	3.00
5.4	4.46	4.48	3.99	3.47	3.26
5.8	4.48	4.77	4.29	3.67	3.41
6.2	4.62	4.67	4.19	3.65	3.41
6.6	3.99	3.94	3.71	3.40	3.23
7	3.01	2.92	2.97	2.95	2.90
7.4	1.78	1.84	2.15	2.39	2.47
7.8	1.00	1.07	1.42	1.82	1.99
8.2	0.51	0.56	0.90	1.33	1.55
8.6	0.41	0.40	0.61	0.99	1.19
9	0.40	0.37	0.50	0.77	0.94
10	0.38	0.39	0.49	0.65	0.73
12	0.37	0.41	9.58	0.74	0.80
14	0.90	0.92	1.02	1.07	1.07
16	1.80	1.66	1.57	1.44	1.36
18	2.30	2.29	2.04	1.73	1.58
20	2.46	2.40	2.22	1.84	1.67
25	1.04	1.03	1.12	1.15	1.13

In Fig. 6, the available experimental data on the temperature dependence of the rate of electron attachment to iodine molecules [7] in an equilibrium plasma (due to the lack of corresponding data for chlorine) are com-

Table 2. Cross section of ion-pair formation

W_e, eV	$\sigma \times 10^{18}$ cm^2 for T_v, K				
	300 [5]	300	500	800	1000
12	<0.1	<0.1	<0.1	0.10	0.17
16	<0.1	<0.1	0.10	0.20	0.29
20	0.12	0.14	0.24	0.41	0.51
24	0.65	0.58	0.64	0.74	0.81
28	1.10	1.07	1.02	1.03	1.06
32	0.89	0.90	0.95	1.05	1.11
36	0.57	0.63	0.68	0.89	1.00
40	0.60	0.57	0.66	0.86	0.98
44	0.62	0.64	0.79	1.00	1.11
48	0.69	0.72	0.94	1.20	1.31
52	0.88	0.92	1.18	1.44	1.53
56	1.28	1.29	1.52	1.72	1.78
60	1.76	1.75	1.91	2.02	2.04
64	2.18	2.15	2.26	2.31	2.30
68	2.52	2.55	2.64	2.63	2.57
72	3.18	3.23	3.17	2.98	2.84
76	4.06	4.08	3.73	3.29	3.06
80	4.25	4.30	3.94	3.38	3.11
84	4.13	4.16	3.73	3.22	2.96
88	3.94	3.91	3.47	2.97	2.74
92	3.70	3.74	3.30	2.79	2.56
96	3.40	3.43	3.09	2.64	2.42
100	3.07	3.00	2.78	2.45	2.28

pared with the values calculated by the reflection method under the same conditions. The wave functions for the $X^1\Sigma_g^+$ state of I_2 were evaluated using the Morse potential, and the shape of the attachment cross section at 298 K was taken from [15]. Because of the extremely large spread in the literature data on the magnitudes of the attachment cross section for iodine (which runs as great as two orders of magnitude), we performed the calculation in arbitrary units, and the final data for the attachment rate were then correlated with the experimental data for room temperature. Figure 6 indicates that the calculation satisfactorily reproduces the behavior of the temperature dependence curve.

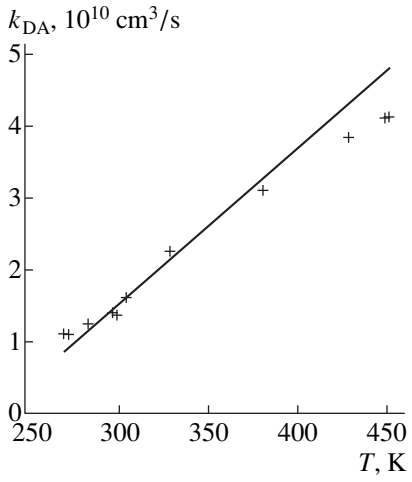

Fig. 6. Temperature dependence of the rate coefficient of electron attachment to an iodine molecule in an equilibrium plasma. Crosses, results obtained in [7]; solid line, this work.

The relative changes in the DA rate for chlorine turned out to be smaller than those for iodine. In particular, the threefold increase in the DA rate in chlorine corresponds to T_v varying from 300 to 1000 K at T_e = 1.5 eV and from 300 to 1300 K at T_e = 4 eV. The shapes of the DA cross sections at $W_e \approx 0$ are similar for chlorine and iodine; hence, so is the behavior of the potential curves for the molecular state $X^1\Sigma_g^+$ and the $^2\Sigma_u^+$ state of a negative molecular ion [15]. These facts make it possible to argue that mechanisms behind temperature dependences of DA in these halogens are similar. However, the potential well of the ground state $X^1\Sigma_g^+$ for a chlorine molecule is narrower than that for iodine, and the spacing between vibrational levels for chlorine (0.07 eV) is larger than that for iodine (0.0266 eV). Therefore, the population of upper vibrational levels and associated smearing of the first partial cross section for chlorine should be smaller than those for iodine at the same values of T_v.

Comparing the values of the DA and IPF cross sections one can conclude that, in chlorine, IPF is a less efficient process for generating negative ions than DA at T_e on the order of several electronvolts. A temperature dependence of electron attachment in chlorine is insignificant for $T_e \geq 4$ eV and temperatures of heavy particles to 1000 K. One should take into account, however, that vibrational temperature T_v in real-gas discharges may far exceed the gas temperature. In this case, a temperature dependence of electron attachment should be taken into consideration.

ACKNOWLEDGMENTS

This work was supported by the Ministry of Education of the Russin Federation, grant no. 97-0-5.3-34.

REFERENCES

1. G. I. Font and I. D. Boyd, J. Vac. Sci. Technol. A **15**, 313 (1997).
2. J. D. Bukowski and D. B. Graves, J. Appl. Phys. **80**, 2614 (1996).
3. N. L. Basset and D. J. Economou, J. Appl. Phys. **75**, 1931 (1994).
4. G. L. Rogoff *et al.*, IEEE Trans. Plasma Sci. **14**, 103 (1986).

5. M. V. Kurepa and D. S. Belić, J. Phys. B **11**, 3719 (1978).
6. N. Pinhão and A. Chouki, in *Proc. ICPIG XXII, Hoboken, 1995*, Pt. II, pp. 5–6.
7. F. K. Truby, Phys. Rev. **188**, 508 (1969).
8. A. P. Golovitskiĭ and S. V. Lebedev, Opt. Spektrosk. **82**, 251 (1997) [Opt. Spectrosc. **82**, 227 (1997)].
9. H. S. W. Massey, *Negative Ions* (Cambridge University Press, Cambridge, 1976; Mir, Moscow, 1979).
10. E. U. Condon, Phys. Rev. **32**, 858 (1928).
11. S. D. Peyerimhoff and R. J. Buenker, Chem. Phys. **57**, 279 (1981).
12. Th. Möller *et al.*, Chem. Phys. **76**, 295 (1983).
13. T. L. Gilbert and A. C. Wahl, J. Chem. Phys. **55**, 5247 (1971).
14. P. W. Tasker *et al.*, Mol. Phys. **32**, 1651 (1976).
15. J. B. Hasted, *Physics of Atomic Collisions* (Butterworths, London, 1964; Mir, Moscow, 1965).

Translated by M.S. Fofanov

Technical Physics, Vol. 45, No. 5, 2000, pp. 538–542. Translated from Zhurnal Tekhnicheskoĭ Fiziki, Vol. 70, No. 5, 2000, pp. 17–21.

Optimization of the Gas Outflow from a Ballistic Plasmatron Barrel

V. T. Volov, D. B. Volov, and V. M. Shmelev

Samara State Institute of Railway Transport Engineers, Samara, 443066 Russia

Received December 22, 1998

Abstract—A set of nonlinear differential equations for calculation of the gas flow parameters in a plasmatron barrel is derived. Comparison between the data obtained by integrating this set and a numerical solution of the corresponding 2D problem of the radiation gas dynamics revealed an agreement acceptable in technical applications. The investigation makes it possible to considerably reduce the time of calculation of the gas parameters. It is established that there is an optimum initial temperature for each particular setup configuration. © *2000 MAIK "Nauka/Interperiodica".*

INTRODUCTION

This paper considers the laws of radiating gas flow from a ballistic plasmatron barrel [1–5]. The working gas compressed by a piston up to high temperatures (~10000 K) and pressures (~500 atm) flows out from the plasmatron barrel channel with the length L and diameter D through an outlet nozzle with the diameter $\varnothing d$ (Fig. 1), with the gas volume inside the barrel during the outflow being virtually constant [6].

It was noted [6] that the gas flow parameters in the barrel at any given time instant are nearly constant throughout the barrel channel volume, and influence of a transition vortex zone on the flow character is negligible. Except for the hemisphere of radius $r = L/6$ with its center at point O (Fig. 1), the gas parameters inside the barrel differ from point to point by no more than 5.3% for the density, 6.4% for the temperature, and 2.3% for the pressure [6]. This suggests that an approximation is reasonable in which the gas parameters inside the barrel are assumed to be constant and equal to their average values. In other words, we turn to thermodynamic parameters defined by formulas of the type

$$f = \frac{1}{N}\sum_{i=1}^{N} f_i, \quad f = T, p, \rho,$$

where f_i are the gas parameters at ith point; N is the number of points in the initial numerical problem [6]; T, p, and ρ are the average gas temperature, pressure, and density, respectively.

Inasmuch as the actual gas parameters differ from their average values by no more than 5%, we can determine the gas parameters over the whole barrel volume to within the accuracy sufficient for engineering calculations.

GAS OUTFLOW FROM PLASMATRON BARREL

At high pressures and temperatures developed in a plasmatron, in the first stage of the process we deal with a surface radiator [7]. Therefore, the radiation losses may be evaluated in terms of the radiative loss power e_{rad} as follows:

$$e_{\text{rad}} = \sigma S_\sigma T^4, \quad E_{\text{rad}} = \int_0^\tau e_{\text{rad}} dt,$$

where E_{rad} is the radiation energy in the barrel, $S_\sigma = \pi DL + \pi D^2/2$ is the radiating surface area, and σ is the Stefan–Boltzmann constant.

According to the first principle of thermodynamics,

$$\begin{aligned} \delta Q &= \delta A + dU, \\ -e_{\text{rad}} &= pdV + d(\rho c_v VT), \end{aligned} \tag{1}$$

where c_v is the gas heat capacity at constant volume, δA is the elementary work performed by the gas, dU is the internal energy variation of the gas, and δQ is the heat supplied to the system.

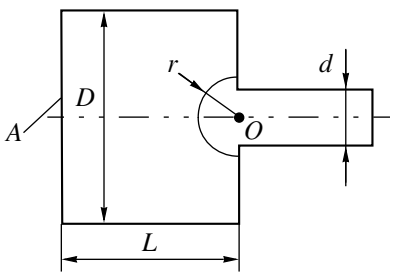

Fig. 1. A schematic diagram of the ballistic plasmatron (A is the piston surface).

1063-7842/00/4505-0538$20.00

Under the conditions considered, the gas undergoes both radiative and dynamic cooling, the latter is due to the gas outflow from a constant volume *V*. The gas density at each point of the barrel channel varies with time as $\rho = \rho(t)$ due to decreasing gas mass $M(t)$ in the barrel volume with $V = \text{const}$. Let us consider an equivalent problem of radiating gas cooled on expanding at a certain velocity. In this problem, the gas density varies as $\rho(t)$, because the volume $V = V(t)$ increases under the condition that the gas mass remains constant:

$$\rho(t) = \frac{M_0}{V(t)}, \quad M_0 = \text{const}$$

here and below, index 0 refers to the initial values of the gas parameters.

Then, under condition $c_v = \text{const}$, it follows from equation (1) that

$$-\sigma S_\sigma T^4 dt = \frac{M_0}{V(t)} RT dV + M_0 c_v dT, \qquad (2)$$

where *R* is the gas constant. As is shown in [6] for the approximation of a constant speed of sound ($a = \text{const}$), the volume $V(t)$ is defined as follows:

$$V(t) = \frac{M_0}{\rho(t)} = V \exp\left(\left(\frac{kd}{D}\right)^2 \frac{\sqrt{\gamma RT_0}}{L}(t - t_0)\right),$$

where γ is the adiabatic exponent and *k* is the nozzle constriction factor.

For the sake of simplicity, let us consider the case when the gas is perfect, that is, $\gamma = \text{const}$. Then (2) can be reduced to a solution for the gas temperature,

$$T_2(t) = \left[\exp(3A(t - t_0))\left(\frac{1}{T_0^3} + \frac{B}{A}\right) - \frac{B}{A}\right]^{-\frac{1}{3}},$$
$$A = (\gamma - 1)\left(\frac{kd}{D}\right)^2 \frac{\sqrt{\gamma RT_0}}{L}, \quad B = \frac{\sigma S_\sigma}{M_0 c_v}. \qquad (3)$$

If the radiative losses are small, that is, $\sigma T^4 \longrightarrow 0$ (or $B \longrightarrow 0$), then equation (3) describes a purely dynamic gas flow process. If the gas does not flow out, that is, $d/D \longrightarrow 0$ (or $A \longrightarrow 0$) we have

$$T_2(t) \longrightarrow \left[\frac{1}{T_0^3} + 3\frac{\sigma S_\sigma (t - t_0)}{\rho_0 c_v V_0}\right]^{-\frac{1}{3}},$$

which corresponds to solution of the equation

$$E_{\text{rad}} = \int_{t_0}^{t} \sigma S_\sigma T^4 d\tau = V\rho_0 c_v (T_0 - T(t)) = -\Delta U,$$

where ΔU is the internal energy variation of the gas during the time interval $(t - t_0)$.

In the case when the sound speed is not constant $a \neq \text{const}$ ($a = \sqrt{\gamma RT}$), the solution can be obtained in quadratures; however, the final formula is clumsy and inconvenient for calculations. Intrinsically, the solution reduces to integration in the formula

$$t(T_3) = t_0 - \int_{T_0}^{T_3} \frac{dT}{BT^4 + AT^{3/2}}.$$

As the gas is cooling, the surface radiation source transforms into the volume one, and formula (3) fails to be valid from a certain time instant $t \approx 0.5$ ms (Fig. 2). Transformation of the source from surface into volume can be taken into account by representing, as proposed

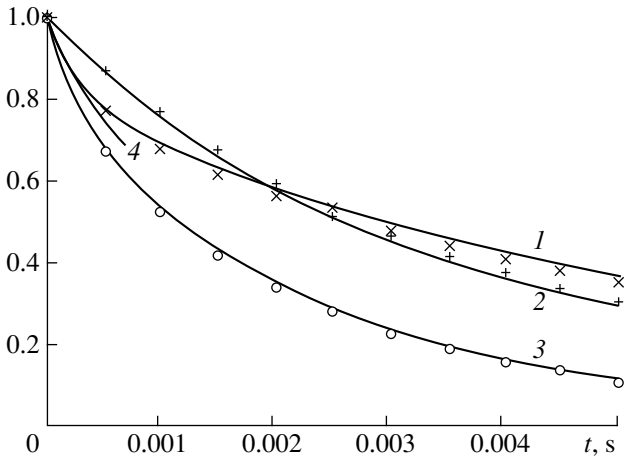

Fig. 2. The results of calculation of the gas flow parameters with an allowance for the radiative losses using a solution of equations (4): (*1*) $T_4(t)/T_0$, (*2*) $\rho_4(t)/\rho_0$, (*3*) $p_4(t)/p_0$. The same parameters derived from the 2D problem solution are depicted by symbols *T* (×), ρ (+), and *p* (○), respectively. Curve *4* is the analytical solution $T_2(t)/T_0$ for the radiating surface calculated according to formula (3).

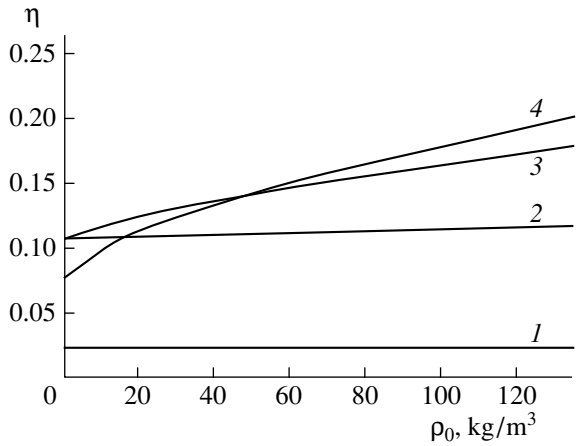

Fig. 3. The setup efficiency as function of the initial gas density ρ_0 at various initial temperatures T_0 = 7000 (*1*), 8000 (*2*), 10 000 (*3*), 12 000 K (*4*).

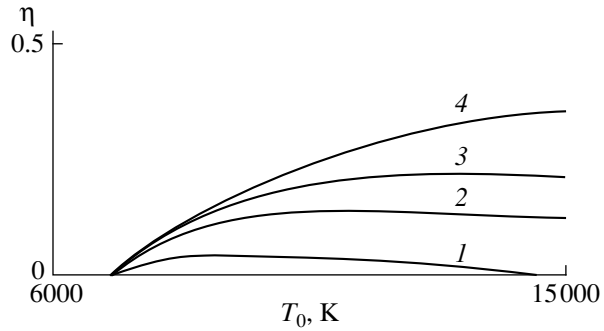

Fig. 4. The setup efficiency as function of the initial gas temperature T_0 for various nozzle diameters d = 5 (*1*), 12 (*2*), 20 (*3*), 52 mm (*4*).

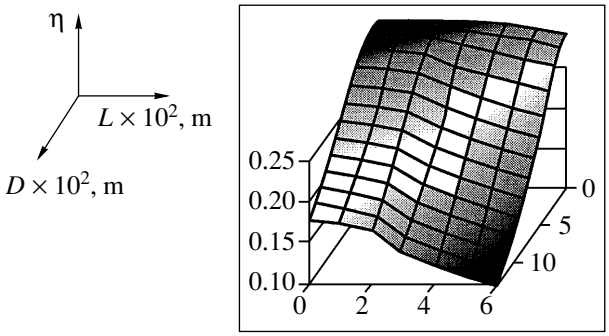

Fig. 5. The setup efficiency as function of the linear sizes L and D.

in [8], the radiative losses in the form

$$e_{\text{rad}} = \frac{4\sigma T^4}{a_1}\left(1 - \exp\left(-\frac{a_1 J}{4\sigma T^4}\right)\right)V,$$

where $a_1 = D/(1 + D/2L)$ is the characteristic size of the system [6]; J is the volume radiative loss power consisting of the continuous braking, recombination, and linear components [7].

Differences between the results of calculations carried out using equations (4) and a numerical solution of the 2D gas dynamics problem for a radiating gas outflow

t, ms	ε_ρ	ε_T	ε_p
0.5	0.010	0.012	0.001
1.0	0.019	0.018	0.002
1.5	0.025	0.022	0.004
2.0	0.028	0.022	0.007
2.5	0.030	0.024	0.010
3.0	0.034	0.027	0.009
3.5	0.037	0.030	0.009
4.0	0.040	0.032	0.006
4.5	0.040	0.036	0.008
5.0	0.043	0.038	0.005

In the problem being considered, the main contribution to the radiation is due to the free-bound transitions [8]; therefore, the calculation of J may be carried out using the formula

$$J \approx G\rho T \exp\left(-\frac{I}{T}\right),$$

where G and I are some constants depending on the particular gas kind only.

After some transformations, formula (1) can be represented as

$$\frac{dT}{dt} = -\frac{e_{\text{rad}}}{c_v M_0} - (\gamma - 1)\frac{S}{V}\sqrt{\gamma R}T^{3/2},$$

where S is the nozzle cross section area. Then a mathematical model of the gas outflow can be written in the form of a set of equations

$$\frac{d\rho}{dt} = -\rho\frac{S}{V}\sqrt{\gamma RT},$$

$$\frac{dT}{dt} = -\frac{4\sigma T^4 V}{c_v M_0 a_1}\left[1 - \exp\left(-\frac{a_1 G\rho T \exp(-I/T)}{4\sigma T^4}\right)\right] \quad (4)$$

$$-(\gamma - 1)\frac{S}{V}\sqrt{\gamma R}T^{3/2}.$$

Equations (4) are easily generalized to the case when $\gamma \neq$ const, $c_v \neq$ const, and even S, $V \neq$ const. Numerical solutions of set (4) are presented in Fig. 2 in comparison with a numerical solution of the 2D gas dynamics problem. Maximum differences between these solutions over a time interval of 5 ms are $\varepsilon_\rho < 0.043$ for the gas density, $\varepsilon_T < 0.038$ for the gas temperature, and $\varepsilon_p < 0.010$ for the gas pressures, the values of ε_t and ε_ρ increasing with time t (see table). To all appearances, the larger differences for the gas density and temperature are caused by the vortex zone formation affecting the flow more and more as the gas flows out.

OPTIMIZATION OF THE SYSTEM PARAMETERS

Reduction of the complicated 2D problem in radiation gas dynamics to the determination of the thermodynamic parameters T, ρ, and p using the set of differential equations allows us to turn to optimization of the system parameters. Now the calculations for a particular plasmatron take much less computing time. The optimization problem is complicated to some extent only by the fact that the equation set (4) cannot be reduced to a dimensionless form. Therefore, it is necessary to analyze how the system efficiency depends on each of the parameters T, ρ, L, D, and d for a particular gas, as well as on γ, R, G, and I for gases of various kinds.

The energy accumulated in the barrel is

$$E_0 = \frac{p_0 V}{\gamma - 1} = \rho_0 c_v V T_0.$$

The intensive radiation heat transfer involving emission in the visible range occurs at temperatures higher than a certain threshold value T_t. For example, in xenon this value is about 6800 K. Therefore, the radiation energy in the barrel and chamber is

$$E_r = \rho_0 V c_v (T_0 - T_t).$$

A fraction of the radiation energy transferred to the chamber is the difference between the total radiation energy and the radiation energy released in the barrel:

$$E_c = E_r - \int_{t_0}^{\tau} e_{\text{rad}} dt. \qquad (5)$$

If set (4) is solved numerically, the integral in (5) is replaced by an approximate sum

$$\int_{t_0}^{\tau} e_{\text{rad}} dt \approx V \Delta t \sum_{n=0}^{N_1} (e_{\text{rad}})_n,$$

where Δt is the step of integration over time and N_1 is the number of time steps in the numerical integration of set (4).

The efficiency of the energy transfer into the chamber is

$$\eta = \frac{E_c}{E_0} = \frac{\rho_0 V c_v (T_0 - T_t) - V \Delta t \sum_{n=0}^{N_1} (e_{\text{rad}})_n}{\rho_0 V c_v T_0}$$

$$= 1 - \frac{T_t}{T_0} - \frac{\Delta t}{\rho_0 c_v T_0} \sum_{n=0}^{N_1} (e_{\text{rad}})_n.$$

Let us study how the efficiency η depends on the dynamic gas parameters T and ρ, as well as on the geometric parameters L, D, d, and the scale factor ξ indicating how much the linear dimensions differ from the corresponding initial values. Let us carry out the calculation for xenon characterized by $R = 63.4$ J/kgK, $\gamma = 1.67$, $G = 1.12 \times 10^{12}$ m^3/kgK, and $I = 140602$ K and for a system with $d = 0.012$ m, $D = 0.076$ m, and $L = 0.05$ m. For the given initial geometry of the system and not too high initial temperatures (7000–8000 K), the initial gas density increase does not practically influence the efficiency η (see Fig. 3). This is explained by the volume character of the gas radiation at the given parameters. At temperatures $T_0 \geq 9000$ K, the efficiency η increases with the initial gas density (Fig. 3), which is characteristic of the surface radiator. While the efficiency η increases monotonically with increasing ρ_0 and T_0, the function $\eta(T_0)$ exhibits a maximum whose position depends on the nozzle diameter d (Fig. 4).

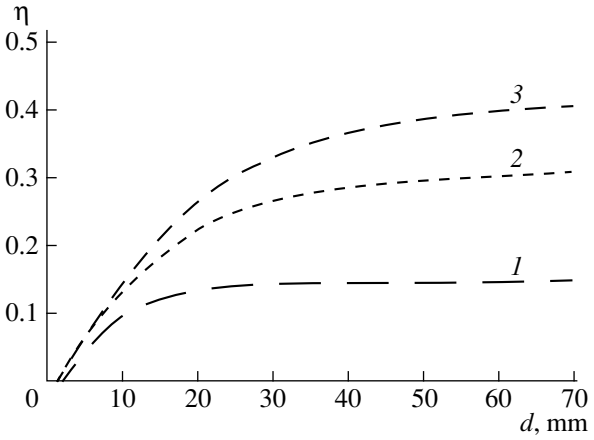

Fig. 6. The setup efficiency as a function of the nozzle diameter d at various initial gas temperatures T_0 = 8000 (*1*), 10 000 (*2*), 12 000 K (*3*).

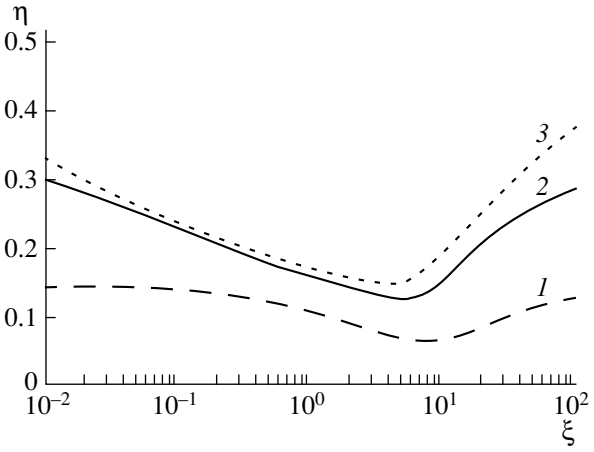

Fig. 7. Influence of the scale factor ξ on the setup efficiency at various initial gas temperatures T_0 = 8000 (*1*), 10 000 (*2*), 12 000 K (*3*).

From this it follows that, for each particular configuration specified by d, D, and L, there is the optimal initial temperature at which the efficiency η reaches its maximum.

The efficiency grows with decreasing length L and diameter D of the barrel (Fig. 5) and with increasing the nozzle diameter (Fig. 6).

At low initial temperatures T_0 and small ξ, when the radiation occurs from the gas volume, the efficiency does not depend on the geometric parameters. For example, at $T_0 = 8000$ K, the efficiency is practically constant up to $\xi = 0.1$ (Fig. 7). As ξ increases further, the efficiency η initially decreases and then, at a certain value of ξ, starts to increase. At high initial temperatures T_0, when the radiation is of the surface character, the function $\eta(\xi)$ exhibits a minimum (Fig. 7).

Such a behavior of the function $\eta(\xi)$ is explained by the influence of two conflicting factors. The first of

these consists in the ratio of the body surface to volume (S_σ/V) decreasing with increasing ξ. Under the surface radiation conditions, this leads to lowering radiative losses in the barrel and, consequently, to growing efficiency. On the other hand, as the scale factor ξ grows, the gas volume inside the barrel increases as the cubic function of ξ^3, while its surface is proportional only to the square of $\sim\xi^2$. According to the first formula of set (4), this must lead to an increase in the dwell time of gas particles in the barrel and, consequently, to higher radiative losses in the barrel. At small values of ξ, the radiation occurs intensively from the large surface and the second factor is dominating: the efficiency lowers with increasing ξ. As ξ increases, the first factor becomes more important: cooling of the massive body slows down, and the efficiency grows. However, this growth is still restricted by the second factor.

CONCLUSIONS

The set of nonlinear differential equations derived allows one to calculate the gas parameters in the plasmatron barrel. Comparison between the data obtained by integrating this system and the results of numerical solution of a 2D problem in radiation gas dynamics revealed a good agreement (the difference is not exceeding 5%). This allows us to recommend the mathematical model created for application in engineering calculations of the thermodynamic gas parameters in plasmatrons.

Reduction of a 2D problem in plasma dynamics to integrating the set of differential equations provided shorter computing time for particular parameters of the setup, which allows one to turn to the setup optimization problems. It was found that there is an optimum initial gas temperature for each configuration of the setup.

REFERENCES

1. N. A. Zlatin and G. I. Mishin, *Ballistic Setups and Their Use in Experimental Investigations* (Nauka, Moscow, 1974).
2. A. D. Margolin, N. Ya. Vasilik, V. M. Shmelev, *et al.*, in *Proceedings of the 1st All-Union Symposium on Radiation Plasma Dynamics* (Énergoatomizdat, Moscow, 1989), p. 33.
3. J. A. Dowling, J. Shumsky, J. Eckerman, and R. E. Schelier, Appl. Phys. Lett. **12** (5), 184 (1968).
4. V. M. Shmelev, A. D. Margolin, N. Ya. Vasilik, *et al.*, Zh. Tekh. Fiz. **68** (9), 67 (1998) [Tech. Phys. **43**, 1069 (1998)].
5. V. M. Shmelev, A. D. Margolin, N. Ya. Vasilik, *et al.*, Teplofiz. Vys. Temp. **36** (4), 548 (1998).
6. D. B. Volov, Candidate's Dissertation (Moscow, 1998).
7. Ya. B. Zel'dovich and Yu. P. Raizer, *Physics of Shock Waves and High-Temperature Hydrodynamic Phenomena* (Nauka, Moscow, 1966; Academic Press, New York, 1966).
8. S. V. Makarychev, G. V. Smekhov, and M. S. Yalovik, Izv. Ross. Akad. Nauk, Mekh. Zhidk. Gaza, No. 1, 155 (1992).

Translated by N. Mende

Technical Physics, Vol. 45, No. 5, 2000, pp. 543–548. Translated from Zhurnal Tekhnicheskoĭ Fiziki, Vol. 70, No. 5, 2000, pp. 22–27.

GASES AND LIQUIDS

Electric Dispersion of Fluid under the Oscillatory Instability of Its Free Surface

A. I. Grigor'ev

Demidov State University, Yaroslavl, 150000 Russia

Received December 23, 1998

Abstract—A semiphenomenological analysis is performed of possible modes of electric dispersion of drops and menisci at the end of the capillary used to deliver the liquid into the discharge system under an oscillatory instability of the charged liquid surface. The instability is assumed to be induced by a time-dependent external force acting on the liquid surface, a finite rate of charge redistribution over the surface under virtual deformations, and tangential discontinuity of the velocity field across the interface. *© 2000 MAIK "Nauka/Interperiodica".*

INTRODUCTION

Calculation of parameters characterizing the electric dispersion of finite charged liquid volumes in external electric fields (drops and menisci at the end of the capillary through which the liquid is supplied to the discharge system) is a very important problem arising in a variety of physical, geophysical, technical, and technological situations when a liquid surface is unstable with respect to its own or induced charges (e.g., see [1–3] and references therein). Physically adequate analytical and numerical methods have been found, and calculations have been made, to analyze some particular cases. These cases include mono- and polydispersion of a liquid from the top of the liquid meniscus at the end of the capillary through which the liquid is supplied to the discharge system by a constant electric field [4–7], the breakup of charged drops that are free or settled on objects in external uniform or nonuniform electrostatic fields [2, 3, 8–10], the breakup of a thin liquid layer on a solid substrate in external electrostatic field [11], and spray of electrode material in heavy-current arc discharges [12, 13]. However, no attempts of theoretical analysis of breakup mechanisms have been made yet for charged and uncharged drops in time-dependent electric fields in the case of an oscillatory instability of the charged liquid surface. At the same time, experimental studies of the phenomenon, though not numerous, have been conducted [14–18].

The laws that govern oscillatory instabilities of the surface of a charged drop induced by its motion relative to the ambient medium (i.e., by the tangential discontinuity of the velocity field across the surface) or by charge relaxation at the interface have been poorly studied [19–22]. The role played by time-dependent electric fields in changing the mechanisms of electric dispersion of liquid from the meniscus at the end of the capillary through which the liquid is supplied to the discharge system has also been investigated very little theoretically and experimentally [23, 24]. The effect of the oscillatory instability induced by charge relaxation on the mechanism of electric dispersion of fluid from the meniscus at the end of the capillary has never been studied theoretically. The experimental studies of such instability and its contribution to the phenomenology of electric dispersion of fluid do not go beyond numerous observations of intense chaotic oscillations of the meniscus at high values of voltage applied to the discharge gap [23, 25–31].

The aim of the paper is to analyze and classify fragmentary theoretical and experimental studies in order to fill the aforementioned gap in the current knowledge of electric dispersion of fluid.

1. As shown in [32, 33], a drop of a conducting fluid placed in external time-dependent electric field can exhibit resonance and parametric instabilities. The resonance instability is caused by forced capillary oscillations of the drop when the double frequency of the force (the external field strength) coincides with one of the eigenfrequencies of capillary oscillation of the drop, which in turn depend on the field strength [34, 35]. The parametric instability occurs when the external electric field frequency is in one of the resonance bands in the neighborhood of an eigenfrequency of capillary drop oscillation, which also depend on the external field strength [33, 36–38]. The parametric instability also develops as a result of stochastic variation of the drop charge or external field strength [39, 40].

Depending on the fluid viscosity, there are at least two different possible channels of the breakup of an isolated, heavily charged drop or a drop placed in a strong external electric field.

When the fluid viscosity is low, an instability makes the drop stretch and take a shape similar to a spheroid of revolution. At the apexes of the spheroid, emitting bulges develop as a result of a superposition of high-

1063-7842/00/4505-0543$20.00 © 2000 MAIK "Nauka/Interperiodica"

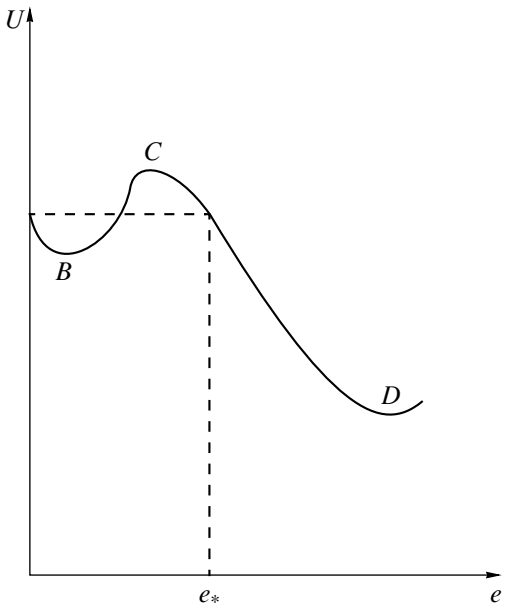

Fig. 1. Qualitative dependence of the spheroidal-drop energy in uniform electric field on its eccentricity.

order modes, which become unstable as the drop stretches into a spheroid and the apical charge surface density increases. The apexes of the bulges begin to lose charge through emission of numerous heavily charged, highly disperse secondary droplets (from a few hundreds during the heavily charged drop breakup to several thousands during the breakup of an uncharged drop in external electrostatic field) [2, 7, 8]. During the breakup of a heavily charged, low-viscosity fluid drop having the critical charge, the drop loses about 23% of its initial charge and 0.5% of its initial mass and then recovers its original spherical shape [2].

When the viscosity of the drop is high, a different breakup channel plays a dominant role: as the instability of the fundamental mode of capillary oscillation develops, in which case the drop stretches into a spheroid, the bulges cannot appear at the apexes because the increments of high-order unstable modes are reduced by the stronger influence of viscosity on them as compared to the fundamental mode, and the severely stretched drop breaks into two, three, or four fragments of comparable size [3, 4, 41–43].

The role of viscosity in the excitation of capillary drop oscillation and development of its instability can be characterized by the dimensionless parameter $\mu \equiv \nu(\rho/R\sigma)^{1/2}$, where ν is the kinematic viscosity, σ is the surface tension, ρ is the fluid density, and R is the drop radius [2, 3]. When the influence of viscosity is weak, the breakup of an unstable drop proceeds via the first channel ($\mu \ll 1$). When $\mu \geq 1$, viscosity plays a key role in the mechanism of instability of the charged drop surface. The breakup of an unstable drop proceeds via the second channel.

2. Let us analyze the general laws that govern the breakup of low-viscosity drops that are unstable in time-dependent electric fields via the first channel ($\mu \ll 1$).

(a) Forced resonance oscillations. Resonant growth of the fundamental mode of capillary oscillation driven by the uniform periodic external electric field $\mathbf{E} = \mathbf{E}_0 \cos\omega_0 t$ takes place when $2\omega_0$ approaches the fundamental frequency ω_2 of capillary oscillation. Assume that the resonance is reached. The drop will then oscillate with a large amplitude determined by the fluid viscosity and the forcing amplitude (proportional to $w^2 = 9E_0^2 R/4\pi\sigma$).

The graph of the potential energy of a drop placed in the field $\mathbf{E}$ as the function $U = U(e)$ of its eccentricity is qualitatively illustrated by Fig. 1 [44]. It is obvious that the drop becomes unstable when the amplitude of resonance oscillation of its fundamental mode exceeds a certain critical value associated with the eccentricity e_*. This means that the eccentricity rapidly increases with time, growing faster than any exponential $\sim e^{\alpha t}$ [45]. Concurrently, emitting bulges develop at the apexes of the spheroid as superpositions of high-order modes whose instability is triggered by the increase in surface charge density, starting to lose the polarization charge (Fig. 2) [2, 3, 8].

Since the polarity of an external field is assumed to vary with the frequency ω_0, the drop remains unstable during a time period $\tau \approx (1/4)\omega_0$, emitting several secondary droplets. During the next quarter of the period of the external field, as the polarization charge decreases with $\sim E_0 \cos\omega t$, the unstable drop recovers its spherical shape.

The drop then goes through the process of resonance growth and instability development again. If, during the first cycle of secondary-droplet emission, the radius R of the parental drop has substantially decreased, the value of u^2 will decrease for the residual drop, and so will the resonance oscillation amplitude. If the eccentricity e of the spheroidal drop becomes smaller than e_* at the maximum of the capillary oscillation amplitude, the next cycle of instability will not take place. Instead, the drop will merely oscillate with a large amplitude.

It may happen that the time τ_p of hydrodynamic drop relaxation from an unstable state characterized by a highly stretched spheroidal shape to the state with the eccentricity e_* is longer than the half-period of the external field oscillation:

$$\tau_p \ll \frac{1}{\omega_0}.$$

In this case, after the reversal of the polarity of $\mathbf{E}$, the drop cannot recover its spherical shape and, still having the eccentricity $e \geq e_*$, moves again along the

line *CD* in Fig. 1, i.e., becomes unstable once again, but the signs of the charges lost at *L* and *M* reverse (Fig. 2).

If the field **E** is nonuniform, then, depending on the degree of the nonuniformity, a linear (in time) resonance can be reached not only by the fundamental mode, but also by higher modes: 3, 4, 5th, etc., as it has been shown in [10, 32].

If the parental drop charge is *Q*, then in a single instability cycle, its charge may decrease so that the drop eigenfrequencies change substantially and the drop leaves the resonance band and remains stable.

(b) Parametrically induced oscillations. The parametric resonance of an uncharged drop placed in the electric field $E_0\cos\omega_0 t$ occurs when the frequency ω_0 of the external field falls within a small neighborhood of an eigenfrequency ω_n of capillary drop oscillation while the field amplitude E_0 is so large that the amount of energy gained by the drop during the field period is greater than that lost through viscous dissipation. A parametric resonance is characterized by the following form of the *n*th-mode amplitude dependence on time:

$$a_n(t) = a_{n_0}\exp(\gamma t)\cos(\omega_0 t).$$

In the case of an instability of the fundamental mode, when the drop geometry oscillates between oblate and prolate spheroids, the instability develops as described in the preceding subsection: as soon as the oscillation amplitude becomes such that the eccentricity *e* of the drop exceeds the critical value e_* (Fig. 1), the drop amplitude increases aperiodically in time and faster than any exponential. If the polarity of the external field does not change ($t_* \gg (1/4\omega_0^{-1})$) and its strength does not decrease much as compared to E_0 during the period t_* when the drop amplitude increases and emitting bulges form at its apexes, the parental drop will emit several secondary droplets. The emission will continue during a time period less than a quarter of the period of the electric field until the field strength $E(t) = E_0\cos\omega_0 t$ becomes low enough for the emitting bulges to disappear and for the drop to recover its spherical shape. Whether the drop will go through another cycle of parametrically forced oscillation depends on the shifts its fundamental frequencies caused by the loss of mass in the first cycle. Generally, it is clear that, as compared to the case of linear resonance, parametric instability would result in a loss of a smaller number of secondary droplets under equal conditions, because the time required for the field to reverse, thus, stopping the secondary-droplet emission, is shorter by a factor of 2 in the latter case.

When the characteristic time τ_p of hydrodynamic drop relaxation to its initial spherical shape is much longer than the period $1/\omega_0$ of electric-field oscillation, i.e., when $\tau_p \gg 1/\omega_0$, repeated cycles of secondary-droplet emission should be expected to occur, with the charge of secondary droplets alternating from cycle to cycle.

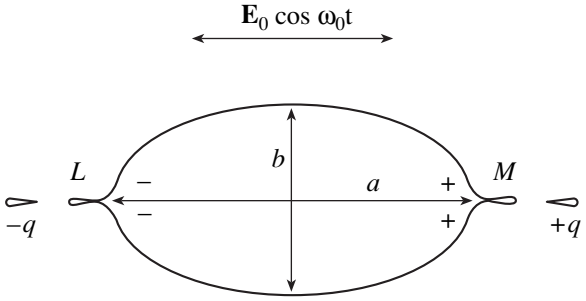

Fig. 2. Schematic of an unstable drop in an alternating electric field.

The time τ_p can be estimated as that required for a stretched spheroidal drop to recover its spherical form under the action of surface tension. The Laplacian force F_σ acting on a half drop is $F_\sigma = \int_s P_\sigma dS$, where *S* is a surface area of the half-drop and P_σ is the Laplacian pressure. Under the action of this force, the center of mass of the half-drop of mass $(2/3)\pi R^3\rho$ moves with an acceleration *a*. The deviation ξ of the drop surface from spherical shape that builds up during the time τ_p is $\xi = \int a\,\tau_p d\tau_p$. For P_σ = const, F_σ = const, and *a* = const, τ_p is estimated by an order of magnitude as

$$\tau_p = \sqrt{\frac{2\xi}{a}} = \sqrt{\frac{4\xi\pi R^3\rho}{3SP_\sigma}}.$$

Setting $\xi \approx R$, $S \approx 2\pi R^2$, and $P_0 \approx 2\sigma/R$, one obtains the following restriction on the drop parameters for which the condition $\tau_p \gg \omega_0^{-1}$ holds:

$$\tau_p \cong \sqrt{\frac{1}{3}\frac{R^3\rho}{\sigma}} \gg \frac{1}{\omega_0}. \qquad (1)$$

Thus, for *R*, σ, and ρ satisfying (1), one should expect multiple cycles of secondary-droplet emission to occur since the hydrodynamic motion is much slower than the inertia-free polarization charge reversal with the vector $\mathbf{E}(t)$ in a perfectly conducting fluid.

3. The breakup of a drop into fragments of comparable size via the resonance or parametric mechanism in an alternating electric field can occur for the same reasons as in the case of an aperiodically developing instability. Such a breakup can proceed in the following five modes:

1. The amplitude of a virtual (e.g., spheroidal) deformation of a drop with a subcritical charge exceeds a critical value, which depends on the drop charge, its size, and the surface tension of the fluid [46]. Such a breakup may have been detected in [47].

2. The fluid is dielectric and carries a volume charge while the drop has a supercritical charge with respect to its instability [41, 42].

3. Two fragments of comparable sizes result from the breakup of both a charged and an uncharged drop placed in a time-dependent electric field of high amplitude when the fluid viscosity is large enough for the inequality $\mu \equiv \nu(\rho/R\sigma)^{1/2} \geq 1$ to be valid. In this case, the increments of unstable high-order modes are much smaller than the increment of the fundamental mode instability and the emitting bulges cannot appear during the time required for the polarity of the external field to reverse [2]. The fundamental-mode amplitude increases (i.e., the spheroidal deformation grows) over several periods of polarity reversal if the characteristic time of hydrodynamic relaxation from a spheroidal fundamental-mode deformation to the spherical shape, which is driven by surface tension and impeded by viscosity, is longer than the period of the field polarity reversal (see (1)). Apparently, this is the breakup channel observed in the experiments reported in [48].

4. The drop can break up into several fragments of comparable size when the virtual spheroidal deformation of a perfectly conducting drop of a low-viscosity fluid grows so rapidly that the fundamental-mode increment exceeds some critical value, i.e., via an inertial mechanism [43]. Apparently, this breakup channel was the case in the experiments described in [15], where charged drops of radius ~100 μm broke into two, three, or four secondary droplets during a rapid deceleration of a drop in a nonuniform electric field. This breakup mode is unlikely to be important for a high-viscosity drop ($\mu > 1$), because high-speed deformation growth would hardly be expected to occur.

5. In a high-frequency external electric field of large amplitude, charged fluid fragments can be torn off the apexes of a high-viscosity, high-conductivity, weakly deformed drop when the negative pressure of the electric field on the free surface exceeds the strength limit of the fluid.

The fourth mode of drop breakup can take place when a heavily charged drop of a low-viscosity fluid (characterized by a small time of hydrodynamic relaxation) moves in a high-frequency alternating field of large amplitude at a sufficiently high speed. When the amplitude of resonance oscillation grows linearly with time, this breakup channel is unlikely to be important for the fundamental mode of capillary oscillation. However, this channel is quite feasible when the amplitude of capillary oscillation increases exponentially in the case of a parametrically induced instability.

The dimensionless criterion characterizing the capability of a drop for breaking up into a finite number of fragments of comparable size when the speed V of deformation growth is high has the following qualitative form:

$$\frac{V}{\zeta}\left[\frac{\rho R^3}{\sigma}\right]^{1/2} \ln\left(\frac{\sigma R^2}{kT}\right) \geq \text{const},$$

where ζ is the amplitude of deformation; ρ and σ are the density and surface tension of the fluid, respectively; k is the Boltzmann constant; T is the absolute temperature; and R is the radius of the drop [43].

4. Between the extreme modes of breakup considered in Sections 2 and 3, intermediate emission regimes can occur.

5. The oscillatory instability of the free drop surface also takes place during the translational motion of the drop relative to the ambient medium (e.g., while a drop falls down in the atmosphere). The instability develops because of the tangential discontinuity of the velocity field across the drop surface; i.e., by analogy with the Kelvin–Helmholtz instability (which is of oscillatory nature) [21, 22]. If a drop has an intrinsic charge or falls in an external electrostatic or time-dependent electric field, then the development of the capillary instability of its surface results in the emission of individual charged secondary droplets [16, 17]. The drop breakup described in [16], where a simultaneous emission of two secondary droplets from the opposite apexes of a parental drop, was apparently caused by a developing instability of a high-order capillary oscillation eigenmode or by a cooperative growth of several modes (this can be inferred from the sequence of the movie pictures of breakup presented in [16]). Intense oscillations of falling drops just before the breakup were recorded in [16, 18]. In the experiments described in [14], a water drop of radius ~1 mm placed in a flow of a dielectric fluid in a uniform electrostatic field was observed to break up into two fragments of equal size whose charges were equal in absolute value, but had opposite signs. This breakup mode may be explained by the large values of the drop and medium viscosities.

As shown in [22, 49], both the aperiodic instability of the surface with respect to the drop charge and the oscillatory instability with respect to the tangential discontinuity of velocity field across the interface can simultaneously develop when a charged drop moves relative to the ambient medium. The critical thresholds of both instabilities are lowered when they develop concurrently, which is also confirmed by experimental data [16, 50, 51]. The oscillatory instability of a drop moving relative to the medium involves a strong interaction between various modes of its capillary oscillation, and several modes contribute to the development of the instability.

6. Another feasible mechanism behind the oscillatory instability of a free charged fluid surface is the charge relaxation associated with a finite rate of redistribution of free-surface electric potential during virtual deformations for a real fluid. Instability of this type takes place when the electrical conductivity of the

ambient medium (a liquid or plasma that does not mix with the fluid in the drop) is higher than the electrical conductivity of the fluid in the drop [19, 20]. The threshold of this oscillatory instability is higher than that of the aperiodic instability (i.e., the Tonks–Frenkel instability in the planar case and Rayleigh instability in the case of a heavily charged drop [19, 20]). This means that the oscillatory instability develops when the surface charge is supercritical with regard to the aperiodic instability. In other words, it should be observed against an already developing background aperiodic instability. In all likelihood, this phenomenon was observed in [25–28] in the study of electric-charge loss from the apex of a liquid meniscus at the end of the capillary through which the liquid was supplied to the discharge system. As the voltage between the liquid meniscus and a plane counter-electrode was increased, a flat diffusion discharge ignited first at the meniscus top as a result of a surface instability of the charge meniscus and emission of highly disperse, heavily charged drops. With a subsequent increase in voltage, intense oscillation of the meniscus developed, and large drops were emitted, which can be interpreted as the development of an oscillatory instability of the meniscus.

In the experimental study of regimes of electrostatic monodispersion fluid reported in [23], two monodispersion regimes were observed in which the size and charge of droplets vary in different ways with the voltage applied. These two regimes exist in different ranges of applied voltage and are separated by an interval where the meniscus chaotically oscillates and the monodispersion regime does not take place. The existence of this interval between different regimes may also be explained by an oscillatory instability of the meniscus surrounded by a gas-discharge plasma cloud. The occurrence of monodispersion regimes that differ qualitatively by the dependence of the characteristics of the emitted drops on the applied voltage should be explained by the fact that, as shown in [20], different fluid-to-ambient-medium electrical conductivity ratios, in the case of a gas-discharge plasma, correspond to distinct regions of substantially different dependence of the capillary instability increment on this ratio, while the plasma electrical conductivity in a neighborhood of the liquid meniscus depends on the discharge intensity and varies with the voltage applied.

Note that, at large values of applied voltage, the intense oscillation of the meniscus at the end of the capillary through which the liquid is supplied to the discharge system has been observed in many experimental studies of the regimes of both electrostatic and electrohydrodynamic poly- and monodispersion of fluid (in addition to the papers cited above, see, for example, [29–31]).

The oscillatory instability of a liquid–metal film at the top of the emitter needle in a liquid–metal source of ions is probably associated with the charge relaxation effect on the liquid metal–discharge plasma interface. In all likelihood, it must be the cause of the ion-beam intensity oscillation with frequencies up to 100 MHz experimentally observed at high values of the voltage applied to the discharge gap, which have not been given any adequate physical interpretation to this day [52–54].

CONCLUSIONS

The analysis of mechanisms of electric dispersion of fluid under oscillatory instabilities presented in this paper is a qualitative and semiphenomenological kind, because of the lack of experimental studies focused on the phenomenon and its insufficient theoretical treatment. However, the phenomenon exists, considerably affects the operation of various analytical and technical devices, contributes to the phenomenology of processes in thunderclouds, and, hence, deserves a more accurate study.

REFERENCES

1. V. I. Kozhenkov and N. A. Fuks, Usp. Khim. **45** (12), 2274 (1976).
2. A. I. Grigor'ev and S. O. Shiryaeva, Zh. Tekh. Fiz. **61** (3), 19 (1991) [Sov. Phys. Tech. Phys. **36**, 258 (1991)].
3. A. I. Grigor'ev and S. O. Shiryaeva, Izv. Ross. Akad. Nauk, Mekh. Zhidk. Gaza, No. 3, 3 (1994).
4. A. A. Zemakov, S. O. Shiryaeva, and A. I. Grigor'ev, J. Colloid Interface Sci. **158**, 54 (1993).
5. A. I. Grigor'ev and S. O. Shiryaeva, J. Aerosol Sci. **25** (6), 1079 (1994).
6. S. O. Shiryaeva and A. I. Grigor'ev, J. Electrost. **34** (1), 51 (1995).
7. S. O. Shiryaeva and A. I. Grigor'ev, Zh. Tekh. Fiz. **65** (9), 46 (1995) [Tech. Phys. **40**, 889 (1995)].
8. A. I. Grigor'ev and S. O. Shiryaeva, J. Phys. D **23** (11), 1361 (1990).
9. I. D. Grigor'eva and S. O. Shiryaeva, Zh. Tekh. Fiz. **64** (9), 202 (1994) [Tech. Phys. **39**, 973 (1994)].
10. S. O. Shiryaeva and A. I. Grigor'ev, Zh. Tekh. Fiz. **62** (11), 49 (1992) [Sov. Phys. Tech. Phys. **37**, 1071 (1992)].
11. A. I. Grigor'ev, M. I. Munichev, and S. O. Shiryaeva, J. Colloid Interface Sci. **166**, 267 (1994).
12. V. A. Nevrovskiĭ, Izv. Ross. Akad. Nauk, Mekh. Zhidk. Gaza, No. 4, 20 (1977).
13. S. O. Shiryaeva and A. I. Grigor'ev, Pis'ma Zh. Tekh. Fiz. **19** (14), 24 (1993) [Tech. Phys. Lett. **19**, 443 (1993)].
14. R. S. Allan and S. G. Mason, Proc. R. Soc. London, Ser. A **267** (1), 45 (1962).
15. T. G. O. Berg, R. J. Trainor, and U. Vaughan, J. Atmos. Sci. **27** (11), 1173 (1970).
16. J. J. Bellinga and D. G. Holland, J. Geophys. Res. **74** (28), 6881 (1969).
17. C. N. Richards and C. A. Dawson, J. Geophys. Res. **76** (15), 3445 (1971).
18. A. K. Kamra, R. V. Bhalwankar, and A. B. Sathe, J. Geophys. Res. **96** (D10), 17159 (1991).

19. D. F. Belonozhko, Pis'ma Zh. Tekh. Fiz. **23** (22), 18 (1997) [Tech. Phys. Lett. **23**, 865 (1997)].
20. D. F. Belonozhko, A. I. Grigor'ev, and S. O. Shiryaeva, Zh. Tekh. Fiz. **68** (9), 13 (1998) [Tech. Phys. **43**, 1023 (1998)].
21. S. O. Shiryaeva, O. A. Grigor'ev, and A. I. Grigor'ev, Pis'ma Zh. Tekh. Fiz. **19** (8), 73 (1993) [Tech. Phys. Lett. **19**, 354 (1993)].
22. S. O. Shiryaeva, V. A. Koromyslov, and O. A. Grigor'ev, Pis'ma Zh. Tekh. Fiz. **24** (13), 54 (1998) [Tech. Phys. Lett. **24**, 523 (1998)].
23. S. B. Sample and R. Bollini, J. Colloid Interface Sci. **41** (2), 185 (1972).
24. A. I. Grigor'ev, V. I. Bezrukov, A. A. Zemskov, *et al*., Zh. Tekh. Fiz. **62** (2), 9 (1992) [Sov. Phys. Tech. Phys. **37**, 118 (1992)].
25. J. Zeleny, Phys. Rev. **3** (2), 69 (1914).
26. W. N. English, Phys. Rev. **74** (2), 179 (1948).
27. M. Cloupeau and B. Prunet-Foch, J. Electrost. **25**, 165 (1990).
28. A. I. Grigor'ev, I. D. Grigor'eva, and S. O. Shiryaeva, J. Sci. Expl. **5** (2), 163 (1991).
29. R. S. Carson and C. D. Hendrics, AIAA J. **3** (6), 1072 (1965).
30. A. G. Bailey and E. Borzabadi, IEEE Trans. Ind. Appl. **14** (2), 162 (1978).
31. I. Hayati, A. I. Bailey, and Th. F. Tadros, J. Colloid Interface Sci. **117** (1), 205 (1987).
32. A. I. Grigor'ev, Izv. Akad. Nauk SSSR, Mekh. Zhidk. Gaza, No. 1, 50 (1989).
33. S. O. Shiryaeva, A. I. Grigor'ev, and V. A. Koromyslov, Zh. Tekh. Fiz. **66** (5), 35 (1996) [Tech. Phys. **41**, 425 (1996)].
34. V. I. Kalechits, I. E. Nakhutin, and P. P. Poluéktov, Dokl. Akad. Nauk SSSR **262** (6), 1344 (1982).
35. Yu. A. Bykovskiĭ, É. A. Manykin, P. P. Poluéktov, *et al.*, Kvantovaya Élektron. (Moscow) **3** (1), 157 (1976).
36. G. N. Ionides, Can. J. Phys. **51**, 1443 (1973).
37. S. V. Nesterov, Izv. Akad. Nauk SSSR, Mekh. Zhidk. Gaza, No. 5, 170 (1986).
38. A. I. Grigor'ev and A. É. Lazaryants, Élektrokhim. Obrab. Met., No. 3, 45 (1990).
39. A. É. Lazaryants and A. I. Grigor'ev, Zh. Tekh. Fiz. **62** (3), 40 (1992).
40. A. I. Grigor'ev and A. É. Lazaryants, Izv. Akad. Nauk SSSR, Mekh. Zhidk. Gaza, No. 5, 52 (1990).
41. S. O. Shiryaeva, A. I. Grigor'ev, and I. D. Grigor'eva, Zh. Tekh. Fiz. **65** (2), 1 (1995) [Tech. Phys. **40**, 117 (1995)].
42. V. A. Koromyslov, A. I. Grigor'ev, and S. O. Shiryaeva, Zh. Tekh. Fiz. **68** (8), 31 (1998) [Tech. Phys. **43**, 904 (1998)].
43. A. A. Zemskov, A. I. Grigor'ev, and S. O. Shiryaeva, Élektrokhim. Obrab. Met., No. 2, 34 (1993).
44. S. I. Shchukin and A. I. Grigor'ev, Zh. Tekh. Fiz. **69** (7), 23 (1999) [Tech. Phys. **44**, 758 (1999)].
45. A. I. Grigor'ev, Pis'ma Zh. Tekh. Fiz. **24** (24), 35 (1998) [Tech. Phys. Lett. **24**, 962 (1998)].
46. S. I. Shchukin and A. I. Grigor'ev, Pis'ma Zh. Tekh. Fiz. **24** (7), 73 (1998) [Tech. Phys. Lett. **24**, 277 (1998)].
47. V. I. Krasnitskiĭ, A. M. Apasov, and S. M. Kontush, Pis'ma Zh. Tekh. Fiz. **16** (18), 77 (1990) [Sov. Tech. Phys. Lett. **16**, 717 (1990)].
48. S. Torza, R. Cox, and S. Mason, in *Reologiya suspenziĭ* (TRANS) (Mir, Moscow, 1975), pp. 285–332.
49. A. I. Grigor'ev, I. D. Grigor'eva, V. F. Koromyslov, and S. O. Shiryaeva, J. Mosc. Phys. Soc., No. 8, 1 (1998).
50. A. E. Cerkanowicz, IEEE–IAC Conf. Proc. 1981, pp. 1161–1165.
51. V. A. Dyachuk and V. M. Muchnik, Dokl. Akad. Nauk SSSR **248** (1), 60 (1979).
52. G. L. R. Mair, J. Phys. D **21**, 1654 (1988).
53. V. G. Dudnikov and A. L. Shabalin, Preprint No. 90-31, IyaF SO AN SSSR (Budker Institute of Nuclear Physics, Siberian Division, Russian Academy of Sciences, Novosibirsk, 1990).
54. A. I. Grigor'ev and S. O. Shiryaeva, Zh. Tekh. Fiz. **62** (12), 9 (1992) [Sov. Phys. Tech. Phys. **37**, 1136 (1992)].

Translated by V. Gurskiĭ

Technical Physics, Vol. 45, No. 5, 2000, pp. 549–553. Translated from Zhurnal Tekhnicheskoĭ Fiziki, Vol. 70, No. 5, 2000, pp. 28–31.

GASES AND LIQUIDS

The Theory of Droplet Diffusiophoresis for Concentrated Solutions

Yu. I. Yalamov and E. Yu. Terekhina

Moscow Pedagogical University, ul. Radio 10a, Moscow, 107005 Russia

Received January 28, 1999

Abstract—The theoretical diffusiophoresis velocity is obtained for a droplet of a concentrated solution suspended in a binary gaseous mixture. The droplet is characterized by a high thermal conductivity. The droplet radius is assumed to be much greater than the mean free path for gaseous-mixture molecules. One of the gaseous-mixture molecular components is the vapor of the droplet solvent. According to the formula obtained in this study, the droplet is driven toward lower concentration of the volatile gaseous-mixture component by diffusive slip and in the opposite direction by phase transition. An increase in the relative mass concentration of the volatile solvent in the droplet enhances effects associated with the dependence of surface tension on the volatile-component concentration and the reactive transport due to the surface nonuniformity of phase transition. As the relative mass concentration of the volatile solvent in the droplet approaches unity, the effect of diffusive slip tends to vanish. © *2000 MAIK "Nauka/Interperiodica".*

Consider a spherical droplet of radius R of a binary solution with an arbitrary solute concentration. The solvent undergoes a phase transition on the droplet surface. The solute is not volatile: it can neither evaporate nor condense on the droplet surface. The droplet is suspended in a binary gaseous mixture with nonuniform component concentrations. One of its molecular components is the vapor of the droplet solvent. The droplet surface is impermeable for the other gaseous-mixture component. The thermal conductivity of the droplet is assumed to be much higher than that of the gaseous mixture. Accordingly, the change in solvent temperature associated with the phase transition on the droplet surface is neglected.

In view of the droplet's geometry, the analysis is performed in spherical coordinates r, Θ, and φ with the origin at the droplet center. At a relatively large distance from the droplet ($r \gg R$), the gaseous mixture is characterized by constant gradients of the relative concentrations of its components, $(\nabla C_{1e})_\infty$ and $(\nabla C_{2e})_\infty$:

$$C_{1e} = \frac{n_{1e}}{n_{1e} + n_{2e}}, \tag{1}$$

$$C_{2e} = \frac{n_{2e}}{n_{1e} + n_{2e}}, \tag{2}$$

where n_{1e} and n_{2e} are the molecular concentrations of the mixture components and the total number density of molecules is

$$n_e = n_{1e} + n_{2e}. \tag{3}$$

It follows from (1)–(3) that

$$C_{1e} + C_{2e} = 1, \tag{4}$$

$$(\nabla C_{1e})_\infty = -(\nabla C_{2e})_\infty. \tag{5}$$

The vector $(\nabla C_{1e})_\infty$ is assumed to be aligned with the polar axis:

$$Z = r\cos\Theta. \tag{6}$$

With the present choice of the coordinate origin, it is convenient to consider a stationary droplet in a moving ambient gas whose velocity tends to $\mathbf{u}$ as $r \longrightarrow \infty$. The ambient gas is characterized by the average viscosity η_{0e}, density ρ_{0e}, temperature T_{0e}, and relative component concentrations C_{01e} and C_{02e}. The droplet is characterized by the average viscosity η_{0i}, density ρ_{0i}, temperature T_{0i}, and relative mass concentrations C_{01i} and C_{03i} of its components. The droplet is assumed to retain its spherical geometry in the moving gas. This assumption is valid when the force due to the surface tension at the droplet–gas phase boundary is much stronger than the viscous drag forces that tend to distort the spherical shape [1]:

$$\sigma \gg \eta_{0e}|\mathbf{u}_D|, \tag{7}$$

where σ is the surface tension and $\mathbf{u}_D$ is the diffusiophoresis velocity for the droplet, whose estimated magnitude is (see [2–4])

$$|\mathbf{u}_D| \approx \left|K_{sl}^{(e)} D_{12}^{(e)} (\nabla C_{1e})_\infty\right|. \tag{8}$$

In (8), $K_{sl}^{(e)}$ is the diffusive-slip coefficient and $D_{12}^{(e)}$ is the binary diffusivity of the gaseous mixture. Combining (7) with (8), we obtain the following constraint for $|(\nabla C_{1e})_\infty|$:

$$\left|(\nabla C_{1e})_\infty\right| \ll \frac{\sigma}{n_{0e} D_{12}^{(e)} \left|K_{sl}^{(e)}\right|}. \tag{9}$$

1063-7842/00/4505-0549$20.00

Substituting $\sigma = 10^{-1}$ N m^{-1}, $\eta_{0e} = 2 \times 10^{-5}$ N s m^{-2}, $D_{12}^{(e)} = 5 \times 10^{-5}$ m^2 s^{-1}, and $|K_{sl}^{(e)} = 0.3|$, which are characteristic of liquid droplets in gaseous mixtures, we obtain

$$\left|(\nabla C_{1e})_\infty\right| \ll 3 \times 10^8 \text{ m}^{-1}. \quad (10)$$

This estimate holds a fortiori, because the gradient of a relative concentration cannot exceed 10^3–10^4 m^{-1} in real systems.

It was shown in [1] that, when the condition

$$\left|K_{sl}^{(e)} R\right|(\nabla C_{1e})_\infty\left| \ll 1, \right. \quad (11)$$

is satisfied, the velocity, pressure, temperature, and concentration distributions inside and outside an individual droplet obey the following set of linear differential equations:

$$\eta_{0e}\nabla^2 \mathbf{V}^{(e)} = \nabla p^{(e)}, \quad (12)$$

$$\operatorname{div} \mathbf{V}^{(e)} = 0, \quad (13)$$

$$\nabla^2 T_e = 0, \quad (14)$$

$$\eta_{0i}\nabla^2 \mathbf{V}^{(i)} = \nabla p^{(i)}, \quad (15)$$

$$\operatorname{div} \mathbf{V}^{(i)} = 0, \quad (16)$$

$$\nabla^2 T_i = 0, \quad (17)$$

$$\nabla^2 C_{1e} = 0, \quad (18)$$

$$\nabla^2 C_{1i} = 0. \quad (19)$$

In (12), (13), (15), (16), and (19), $\mathbf{V}^{(e)}$ and $\mathbf{V}^{(i)}$ are the mass-average velocities outside and inside the droplet, respectively; $p^{(e)}$ and $p^{(i)}$ are the corresponding pressures; and

$$C_{1i} = \frac{m_1 n_{1i}}{\rho_i}. \quad (20)$$

The relative mass concentrations of the solvent and solute, C_{1i} and $C_{3i} = m_3 n_{3i}$, are related by the equation

$$C_{1i} + C_{3i} = 1, \quad (21)$$

because $\rho_i = n_{1i}m_1 + n_{3i}m_3$ is the average droplet density. The boundary conditions far from the surface and on the surface that allow for the effects due to the existence of a Knudsen layer were formulated in [1] in the case of thermophoresis of a large droplet of a concentrated solution. Similar conditions were used in the theory of diffusiophoresis of such a droplet proposed in [5], but the boundary conditions and the resulting velocity were presented for $C_{1e} \ll C_{2e}$. In this paper, we use boundary conditions consistent with those used in [1] to derive the diffusiophoresis velocity in a more general form than in [5].

Since the mathematical form of the boundary conditions is too cumbersome to be written out here, we restrict ourselves to describing their physical meaning as follows. The isothermal and diffusive slip conditions are set, with surface-curvature and Barnett effects taken into account by introducing corrections that are linear in the Knudsen number. The radial and tangential components of the viscous stress are continuous across the droplet surface. The concentration of the volatile gaseous-mixture component is continuous across the droplet surface while an impermeability condition is set for the concentration of the other gaseous-mixture component. The droplet surface is assumed to be impermeable for the solute. The distributions of temperature and relative concentration of the volatile component of the gaseous mixture have jumps across the Knudsen layer.

Henceforth, our calculation of the diffusiophoresis velocity follows that described in [1, 2, 5]. As a result, we analytically express the diffusiophoresis velocity for a large droplet of a concentrated binary solution characterized by a high thermal conductivity and suspended in a binary gaseous mixture,

$$\mathbf{U}_D = -2K_{DSl}D_{12}^{(e)}\Psi(\nabla C_{1e})_\infty. \quad (22)$$

Here,

$$\Psi = \Psi_{DSl} + \Psi_\sigma + \Psi_\nu + \Psi_p. \quad (23)$$

In (23),

$$\Psi_{DSl} = \left(1 + \frac{\beta_R'^{(D)}}{R}\right)g_1 + \frac{\beta_R^{(D)}}{R}g_2 - \frac{\beta_B^{(D)}}{R}g_3, \quad (24)$$

$$\Psi_\sigma = \frac{1}{K_{DSl}D_{12}^{(e)}}\frac{R}{3\eta_{0i}}\frac{\partial\sigma}{\partial C_{1i}}\bigg|_{C_{1i}=C_{01i}} g_4, \quad (25)$$

$$\Psi_\nu = -\frac{n_{0e}^2 m_1}{K_{DSl}\rho_{0e}n_{02e}}\left(1 + \frac{2\eta_{0e}}{\eta_{0i}} + \frac{\rho_{0e}}{\rho_{0i}} + 6\frac{C_m^*}{R}\right)g_2, \quad (26)$$

$$\Psi_p = -\frac{1}{K_{DSl}}\left[\frac{C_\nu^{(D)}}{R}\left(1 + \frac{2\eta_{0e}}{\eta_{0i}} + \frac{6C_m^*}{R}\right)\right. \quad (27)$$
$$\left. + \frac{C_D^{(D)}}{R}\frac{n_{0e}^2 m_1}{\rho_{0e}n_{02e}}\left(1 + \frac{2\eta_{0e}}{\eta_{0i}} + \frac{2\rho_{0e}}{\rho_{0i}} + \frac{6C_m^*}{R}\right)\right]g_4,$$

$$g_1 = \frac{1}{\alpha_{C_m}\Delta}\left(1 + \gamma\frac{k_n^{(n)}}{R}\right), \quad (28)$$

$$g_2 = \frac{1}{\alpha_{C_m}\Delta}\left(\gamma - 2\frac{C_D^{(D)}}{R}\right), \quad (29)$$

$$g_3 = \frac{1}{\alpha_{C_m}\Delta}\left[\left(-1 + \frac{K_n^{(n)}}{R}\right)\gamma + \left(1 + \frac{2C_D^{(D)}}{R}\right)\right], \quad (30)$$

$$g_4 = \frac{\gamma}{\alpha_{C_m}\Delta}, \tag{31}$$

$$\gamma = \frac{n_{01e}n_{02e}\rho_{0i}^2 D_{13}^{(i)}}{n_{0e}^2\rho_{01e}\rho_{03i}D_{12}^{(e)}\left.\frac{\partial\Phi}{\partial C_{1i}}\right|_{C_{1i}=C_{01i}}}, \tag{32}$$

$$\Delta = \left(1+\frac{2K_n^{(n)}}{R}\right)\gamma + 2\left(1-\frac{C_D^{(D)}}{R}\right), \tag{33}$$

$$\alpha_{C_m} = \left(1+\frac{2}{3}\frac{\eta_{0e}}{\eta_{0i}}+\frac{2C_m^*}{R}\right). \tag{34}$$

The following notation is used in (22)–(34): K_{DSl} is the diffusive-slip coefficient for a binary gaseous mixture [1, 2]; $D_{12}^{(e)}$ is the binary diffusivity of the gaseous mixture; σ is the surface tension at the droplet–gas phase boundary; C_m^*, $\beta_R^{\prime(D)}$, $\beta_R^{(D)}$, $\beta_B^{(D)}$, $K_n^{(n)}$, $C_v^{(D)}$, and $C_D^{(D)}$ are coefficients characterizing a two-component gaseous mixture with arbitrary component masses and concentrations, for which analytical expressions and methods of calculation were described in [1, 6–21]; Φ is an empirical function introduced to allow for the dependence of the saturating relative concentration of the solvent vapor in the gaseous mixture on the relative solvent concentration C_{1i} in the droplet.

Let us compare the contributions of Ψ_σ, Ψ_V, and Ψ_p to the velocity given by (22) with that of the diffusive-slip term Ψ_{DSl}.

To clarify our analysis, we consider the case of a very large droplet, when the Knudsen number $K_n = \bar{\lambda}/R$ tends to zero. Here, $\bar{\lambda}$ denotes the mean free path of gas molecules in the binary gaseous mixture. It is obvious that the kinetic coefficients that involve the factor $1/R$ in (24)–(31), (33), and (34) are proportional to $\bar{\lambda}$. Accordingly, as $\bar{\lambda}/K \longrightarrow 0$, (24)–(31), (33), and (34) yield

$$\Psi_{DSl} = \frac{1}{\alpha_0\Delta_0}, \tag{35}$$

$$\Psi_\sigma = \frac{1}{K_{DSl}D_{12}^{(e)}}\frac{R}{n_{0e}}\left.\frac{\partial\sigma}{\partial C_{1i}}\right|_{C_{1i}=C_{01i}}\frac{\gamma}{\alpha_0\Delta_0}, \tag{36}$$

$$\Psi_v = -\frac{n_{0e}^2 m_1}{2K_{DSl}\rho_{0e}n_{02e}}\left(1+\frac{2\eta_{0e}}{\eta_{0i}}+\frac{\rho_{0e}}{\rho_{0i}}\right)\frac{\gamma}{\alpha_0\Delta_0}, \tag{37}$$

$$\Psi_P = 0, \quad \Delta_0 = 2+\gamma, \quad \alpha_0 = 1+\frac{2}{3}\frac{\eta_{0e}}{\eta_{0i}}. \tag{38}$$

Now, we consider the following ratios:

$$E_{21} = \frac{\Psi_\sigma}{\Psi_{DSl}} = \frac{R\left.\frac{\partial\sigma}{\partial C_{1i}}\right|_{C_{1i}=C_{01i}}\gamma}{3\eta_{0i}K_{DSl}D_{12}^{(e)}}, \tag{39}$$

$$E_{31} = \frac{\Psi_v}{\Psi_{DSl}} = -\frac{n_{0e}^2 m_1\gamma}{2K_{DSl}n_{02e}\rho_{0e}}\left(1+\frac{\eta_{0e}}{\eta_{0i}}+\frac{\rho_{0e}}{\rho_{0i}}\right), \tag{40}$$

$$E_{41} = \frac{\Psi_P}{\Psi_{DSl}} = 0. \tag{41}$$

As an example, we present numerical estimates based on (39) and (40) for a droplet of the aqueous solution of glycerol in a water-vapor–air mixture at the temperature $T_{0e} = 239$ K and atmospheric pressure. Our calculations were performed for the following values of quantities contained in (32) and (39)–(41): $n_{01e} = 3.0\times10^{23}$ m^{-3}; $n_{02e} = 2.7\times10^{25}$ m^{-3}; $n_{0e} = 2.7\times10^{25}$ m^{-3}; $m_1 = 18\times1.7\times10^{-27}$ kg; $m_2 = 29\times1.7\times10^{-27}$ kg; $m_3 = 92\times1.7\times10^{-27}$ kg; $\rho_{0e} = 1.3$ kg m^{-3}; $\eta_{0e} = 1.8\times10^{-5}$ kg m^{-1} s^{-1}; $K_{DSl} = 0.3$, and $D_{12}^{(e)} = 2.5\times10^{-5}$ m^2 s^{-1}. The values depending on the concentration C_{01i} are shown in Table 1.

We used the average value of $\partial\sigma/\partial C_{1i}|_{C_{1i}=C_{01i}}$ equal to 7×10^{-3} N m^{-1}. Using the fact that $\eta_{0e}/\eta_{0i} \ll 1$ and $\rho_{0e}/\rho_{0i} \ll 1$, we obtained the values of E_{21} and E_{31} shown in Table 2.

Table 1

C_{01i}	1	0.8	0.5	0.1	0
$\frac{\partial\Phi}{\partial C_{1i}}$	9.75×10^{-3}	2.3×10^{-3}	18.3×10^{-3}	38.9×10^{-3}	51.2×10^{-3}
η_{0i} kg m^{-1} s^{-1}	1×10^{-3}	1.7×10^{-3}	6×10^{-3}	2.3×10^{-1}	1.48
ρ_{0i} kg m^{-3}	1×10^{3}	1.06×10^{3}	1.18×10^{3}	1.24×10^{3}	1.26×10^{3}
$D_{13}^{(i)}$ m^2 s^{-1}	$D_{11}^{(i)}$	4.1×10^{-10}	3.9×10^{-10}	3×10^{-10}	0
n_{0i} m^{-3}	3.4×10^{28}	2.8×10^{28}	2.1×10^{28}	9.9×10^{27}	8.5×10^{27}

Table 2

C_{01i}	E_{21}	E_{31}
0	0	0
0.1	$1.3\times10^{3}R$	–0.93
0.5	$1.3\times10^{5}R$	–2.5
0.8	$6.3\times10^{5}R$	–3.46
1	∞	–∞

Table 3

C_{01i}	$U_D^{(1)}$, m^2 s^{-1}	$U_D^{(2)}$, m^2 s^{-1}	$U_D^{(3)}$, m^2 s^{-1}	$U_D^{(4)}$, m^2 s^{-1}
0	-7.5×10^{-6}	0	0	0
0.1	-5.1×10^{-6}	$-6.6\times10^{-3}R$	4.7×10^{-6}	0
0.5	-3.3×10^{-6}	$-4.3\times10^{-1}R$	8.3×10^{-6}	0
0.8	-2.75×10^{-6}	$-1.7\times R$	9.5×10^{-6}	0
1	0	$-4.6\times R$	1.6×10^{-5}	0

Table 2 demonstrates that an increase in the relative mass concentration C_{01i} of the volatile solvent in the droplet enhances the effects associated with the dependence of surface tension on C_{01i} and the reactive transport due to the surface nonuniformity of the phase transition.

When $C_{01i} = 0$, (36) and (37) yield $\Psi_\sigma = 0$ and $\Psi_\nu = 0$ (since $\gamma = 0$). Then, substituting (35) into (22), we obtain

$$\mathbf{U}_D^{(\text{nonvolatile})} = -K_{DSl}D_{12}^{(e)}\frac{(\nabla C_{1e})_\infty}{\alpha_0}. \tag{42}$$

When $C_{01i} = 1$, the droplet does not contain any nonvolatile solute, so that γ tends to be infinitely large. In this case, (39) and (40) yield infinitely large E_{21} and E_{31}, and the velocity is expressed as

$$\mathbf{U}_D^{(\text{volatile})} = \frac{R}{3\eta_{0i}\alpha_0}\frac{\partial\sigma}{\partial C_{1i}}\bigg|_{C_{1i}=C_{01i}}(\nabla C_{1e}) + \frac{n_{0e}^2 m_1 D_{12}^{(e)}}{\rho_{0e}n_{02e}\alpha_0}\left(1+\frac{2\eta_{0e}}{\eta_{0i}}+\frac{\rho_{0e}}{\rho_{0i}}\right)(\nabla C_{1e})_\infty. \tag{43}$$

The limit formulas (42) and (43) obtained for nonvolatile and purely volatile droplets, respectively, agree with the corresponding results presented in [1, 3, 5]. Let us represent the velocity $\mathbf{U}_D$ given by (22) as

$$\mathbf{U}_D = (U_D^{(1)} + U_D^{(2)} + U_D^{(3)} + U_D^{(4)})(\nabla C_{1e})_\infty, \tag{44}$$

When $\bar{\lambda}/R = 0$,

$$U_D^{(1)} = -2\frac{K_{DSl}D_{12}^{(e)}}{\alpha_0\Delta_0}, \tag{45}$$

$$U_D^{(2)} = -\frac{2R\gamma}{3\eta_{0i}\alpha_0\Delta_0}\frac{\partial\sigma}{\partial C_{1i}}\bigg|_{C_{1i}=C_{01i}}, \tag{46}$$

$$U_D^{(3)} = \frac{n_{0e}^2 m_1\gamma}{\rho_{0e}n_{02e}\alpha_0\Delta_0}\left(1+\frac{2\eta_{0e}}{\eta_{0i}}+\frac{\rho_{0e}}{\rho_{0i}}\right), \tag{47}$$

$$U_D^{(4)} = 0. \tag{48}$$

Table 3 shows the numerical values of the quantities given by (45)–(48) for a droplet of aqueous solution of glycerol in a water-vapor–air gaseous mixture. These values were calculated for C_{01i} and varied from 0 to 1, with the gaseous-mixture and droplet parameters used in compiling Tables 1 and 2. The droplet radius R in Table 3 is measured in meters.

As the concentration C_{01i} of the volatile component (water) in the droplet is increased and the concentration C_{03i} of the nonvolatile component (glycerol) decreases correspondingly, the velocity $U_D^{(1)}$ associated with the diffusive slip proportional to K_{DSl} tends to vanish. Simultaneously, the terms $U_D^{(2)}$ and $U_D^{(3)}$ representing the contributions of variable surface tension (cf. $\partial\sigma/\partial C_{1i}|_{C_{1i}=C_{01i}}$) and phase transition (evaporation or condensation) increase with C_{01i}.

REFERENCES

1. Yu. I. Yalamov and V. S. Galoyan, *Droplet Dynamics in Inhomogeneous Viscous Media* (Luĭs, Yerevan, 1985).
2. Yu. I. Yalamov, Doctoral Dissertation, Moscow (1968).
3. Yu. I. Yalamov and B. A. Obukhov, Zh. Tekh. Fiz. **42**, 1064 (1972) [Sov. Phys. Tech. Phys. **17**, 844 (1972)].
4. Yu. I. Yalamov, B. A. Obukhov, and B. V. Deryagin, Dokl. Akad. Nauk SSSR **207**, 824 (1972) [Sov. Phys. Dokl. **17**, 1168 (1972)].
5. N. Ya. Ushakova and Yu. I. Yalamov, Thermo- and Diffusiophoretic Transport of Droplets in Binary Solutions [in Russian], Available from VINITI, no. 5958-B89 (Moscow, 1989).
6. S. A. Savkov, A. A. Yushkanov, and Yu. I. Yalamov, Physical Kinetics and Fluid Mechanics of Disperse Systems, Available from VINITI, no. 5321-B86 (Moscow, 1986), pp. 110–127.
7. Yu. I. Yalamov, A. A. Yushkanov, and S. A. Savkov, Dokl. Akad. Nauk SSSR **296**, 1107 (1987) [Sov. Phys. Dokl. **32**, 837 (1987)].
8. Yu. I. Yalamov, A. A. Yushkanov, and S. A. Savkov, Dokl. Akad. Nauk SSSR **301**, 1111 (1988) [Sov. Phys. Dokl. **33**, 615 (1988)].
9. J. R. Brock, J. Catal. **2**, 248 (1963).
10. M. N. Gaĭdukov, I. N. Ivchenko, and Yu. I. Yalamov, Izv. Akad. Nauk SSSR, Ser. Mekh. Zhidk. Gaza, No. 2, 199 (1972).
11. E. V. Metelkin and Yu. I. Yalamov, Izv. Akad. Nauk SSSR, Ser. Mekh. Zhidk. Gaza, No. 4, 142 (1973).
12. Y. Sone and I. Onishi, J. Phys. Soc. Jpn. **2** (3), 248 (1973).

13. Yu. I. Yalamov and M. N. Gaĭdukov, in *Physics of Air Suspensions and Physical Kinetics* (Kalinin, 1973), pp. 49–57.
14. Yu. I. Yalamov, E. R. Shchukin, and E. I. Alekhin, Topical Problems in Physics and Mechanics of Air Suspensions, Available from VINITI, no. 580-B89 (Moscow, 1989), pp. 43–77.
15. E. I. Alekhin and Yu. I. Yalamov, Selected Topics in Aerosol Physics, Available from VINITI, no. 862-B89 (Moscow, 1989), pp. 3–9.
16. Yu. I. Yalamov, E. R. Shchukin, and E. I. Alekhin, Teplofiz. Vys. Temp. **28**, 256 (1990).
17. E. I. Alekhin and Yu. I. Yalamov, Kinetic Effects at the Phase Boundary between a Liquid and a Multicomponent Gaseous Mixture, Available from VINITI, no. 4119-B90 (Moscow, 1990).
18. E. I. Alekhin and Yu. I. Yalamov, *Mathematical Foundations of Solution of Boundary Value Problems in the Kinetic Theory of Multicomponent Gases in the Vicinity of the Condensed State* (Mosk. Obl. Inst. im. N.K. Krupskoĭ, Moscow, 1991).
19. Yu. I. Yalamov and A. A. Yushkanov, Physics of Air Suspensions and Physical Kinetics, Available from VINITI, no. 3014-79 (Moscow, 1979), pp. 149–174.
20. Yu. I. Yalamov, M. N. Gaĭdukov, V. S. Galoyan, and M. A. Melkumyan, Physics of Air Suspensions and Physical Kinetics, vol. 5, Available from VINITI, no. 3865-81 (Moscow, 1981), pp. 7–78.
21. Yu. I. Yalamov, M. A. Melkumyan, and M. N. Gaĭdukov, Dokl. Akad. Nauk SSSR **250**, 1384 (1983) [Sov. Phys. Dokl. **28**, 499 (1983)].

Translated by A. S. Betev

Technical Physics, Vol. 45, No. 5, 2000, pp. 554–562. Translated from Zhurnal Tekhnicheskoĭ Fiziki, Vol. 70, No. 5, 2000, pp. 32–39.

GASES AND LIQUIDS

Parametric Identification of a Model for Hydrogen Transfer through Double-Layer Membranes

Yu. V. Zaĭka

Petrozavodsk State University, pr. Lenina 33, Petrozavodsk, Karelia, 185640 Russia

Received February 16, 1999

Abstract—A nonlinear inverse problem of determining the hydrogen permeability of double-layer membranes from experimental data is considered. The model includes both diffusion and adsorption/desorption processes. An identification algorithm is suggested. © *2000 MAIK "Nauka/Interperiodica".*

INTRODUCTION

The interaction of hydrogen and its isotopes with materials is of great interest in power engineering, chemical machine building, rocket manufacturing, and vacuum technology [1–7]. Considerable attention is given to the role of various alloys, oxide films, protective coatings, and multilayer composite materials. In what follows, we will be oriented to the capabilities of the setup described in [8]. A certain difficulty is posed by the fact that strong membranes are impossible to prepare from some materials to be tested. In [6, 7], the hydrogen permeability of semiconductors and beryllium was examined as follows: A substrate from a well-studied metal (e.g., nickel) was coated by a material under test, and its interaction with hydrogen was judged from a change in the hydrogen permeability. For composite materials, where direct measurements at the interfaces are impossible, the problem becomes much more involved.

In this work, we adopted the model that includes both diffusion in the bulk and physicochemical processes on the surface ([3, pp. 177–206]). The applicability limits of the model will not be discussed. We will demonstrate the basic possibility of parameter determination from experimental data and suggest a computational identification algorithm. Mathematical difficulties in solving such nonlinear inverse problems of mathematical physics are well known. In [9], a reference list of related numerical methods is available. In the general case, however, the application of, for example, gradient techniques at each iteration step implies numerical integration of partial differential equations on condition that approximated values of parameters to be evaluated are defined. Our algorithm, taking into account the specific of a model, uses only quadrature formulas to take several integrals. Measurements taken during hydrogen desorption from the outer surface of a double-layer membrane appear only under the integral sign, which makes the algorithm to a certain extent noise-immune. Its implementation does not require dedicated software.

The mathematical grounds for the adopted diffusion model with dynamic boundary conditions including surface-related processes have been given in [10]. The idea of using conjugate equations was borrowed from [11].

MATHEMATICAL MODEL

Let us consider a double-layer membrane. Let the first (input) layer be made of a well-studied metal. Parameters to be found are those of the interface and the second (output) layer. According to the experimental method of permeability, the hydrogen pressure in the gas phase on the input side of the membrane (the partition of a vacuum chamber) predehydrogenated and preheated to a fixed temperature $T(t) = \bar{T}$ is sharply raised and then kept constant: $p(t) = \bar{p}$. On the output side, the gas is continuously pumped off with a vacuum system. In experiments, we determine the output flux density of the desorbed hydrogen. For definiteness, we will refer to the capabilities of the setup described in [8].

The mathematical model for the first layer looks as

$$\frac{\partial c}{\partial t} = D(T)\frac{\partial^2 c}{\partial x^2}, \quad (t, x) \in (0, t^+) \times (0, l), \tag{1}$$

$$c(0, x) = \varphi(x), \quad x \in [0, l], \tag{2}$$

$$c_0(t) = c(t, 0) = g(T)q(t), \tag{3}$$

$$\frac{d}{dt}q(t) = \mu s(T)p(t) - b(T)q^2(t) + D(T)\frac{\partial c}{\partial x}(t, 0), \tag{4}$$

$$g(T(0))q(0) = c_0(0) = \varphi(0). \tag{5}$$

Here, $c(t, x)$ is the concentration of the diffusing (atomic) hydrogen, $q(t)$ is the hydrogen concentration at the input surface ($x = 0$), $D(T)$ is the diffusion coefficient, $g(T)$ is the coefficient matching the concentrations on the surface and in the near-surface volume of the membrane, μ is the kinetic constant, $s(T)$ is the adherence of the hydrogen falling on the surface from

the gas phase, and $b(T)$ is the desorption coefficient. If the membrane is dehydrogenated at the initial time instant $t = 0$, then $\varphi(x) = 0$. Differential equation (4) is the flux balance equation. The higher $p(t)$, the more hydrogen atoms strike unit area per unit time. The flow rate of the hydrogen desorbed from the surface backward to the chamber is approximated by a quadratic dependence. For other gases, the dependence may differ. Its form is of minor importance, as will be seen below. The last term in (4) describes the hydrogen flow to or from the surface due to volume diffusion in the membrane. Initial and boundary conditions are matched via (5).

For the second layer (we will use two reference points),

$$\frac{\partial c_*}{\partial t} = D_*(T)\frac{\partial^2 c_*}{\partial x^2}, \quad (t, x) \in (0, t^+) \times (0, l_*), \quad (6)$$

$$c_*(0, x) = \varphi_*(x), \quad x \in [0, l_*], \quad (7)$$

$$c_{*l_*}(t) = c_*(t, l_*) = g_*(T)q_*(t), \quad (8)$$

$$\frac{d}{dt}q_*(t) = \mu s_*(T)p_*(t) - b_*(T)q_*^2(t) + D_*(T)\frac{\partial c_*}{\partial x}(t, l_*), \quad (9)$$

$$g_*(T(0))q_*(0) = c_{*l_*}(0) = \varphi_*(l_*). \quad (10)$$

The output surface of the second layer is given by $x = l_*$. On evacuation, $\mu s_* p_* \approx 0$ in (9), since a high-capacity pump provides a very low hydrogen pressure $p_*(t)$ at the output. Hence, the probability that the desorbed hydrogen will return to the surface is negligibly small.

Assume the following matching conditions at the interfaces:

$$D(T)\frac{\partial c}{\partial x}(t, l) = D_*(T)\frac{\partial c_*}{\partial x}(t, 0), \quad (11)$$

$$k(T)c_l(t) - k_*(T)c_{*0}(t) = -D(T)\frac{\partial c}{\partial x}(t, l), \quad c_l(t) = c(t, l), \quad c_{*0}(t) = c_*(t, 0), \quad (12)$$

Condition (11) (the continuity equation for the diffusion flux at the interface) means that hydrogen during diffusion is not accumulated between the layers of the membrane. The layers exchange hydrogen atoms. The rates of these oppositely directed fluxes are proportional to related concentrations, and a difference in the rates is a diffusion flux. We arrive at the second condition in (12) [the second-order form for equations (1) and (6)]. Hereafter, by fluxes, we mean flux densities, or fluxes per unit area (surface areas can be taken as unit without loss in generality).

Suppose that the parameters $D_*(T)$, $g_*(T)$, $s_*(T)$, $b_*(T)$, $k(T)$, and $k_*(T)$, involved in the expression for the output desorption flux density

$$J(t) = b_*(T)q_*^2(t) = b_*(T)q_*^{-2}(T)c_{*l_*}^2(t), \quad T = T(t), \quad t \in [0, t_*], \quad (13)$$

must be found for a particular material of the second layer. Let D, g, b, and s for the first layer be known. Otherwise, they can be determined by the method that follows. For subsequent calculations, it is sufficient to know D, s, and the product $gb^{-1/2}$.

The experiment was considered to be completed (the time t_*) when the flux became steady-state: $J(t) \approx \bar{J} = \text{const}$, $t \geq t_*$ ($t_* < t^+$, $p(t) = \bar{p} = \text{const}$). To hydrogen, the Arrhenius law is usually applied:

$$D = D_{*0}\exp(-E_{D_*}/[RT(t)]), \ldots, b = b_{*0}\exp(-E_{b_*}/[RT(t)]), \ldots.$$

Other dependences of the coefficients on temperature $T(t)$ are also possible. Below is an algorithm for finding D_*, g_*, s_*, b_*, k, and k_* at $T(t) = (\bar{T}) = \text{const}$. This fundamental problem is an inverse problem of mathematical physics. If temperature variations of D_*, g_*, s_*, b_*, k, and k_* are known, one can also find the parameters in the dependences $D_*(T)$, …, $k_*(T)$ (or D_{*0}, E_{D_*}, …, b_{*0}, E_{b_*}, … in the Arrhenius case). Note that, although formally, s_* does not appear in model (1)–(12) at $\mu s_* p_* \approx 0$, it is specified by other parameters (see (14)).

IDENTIFICATION ALGORITHM

From physical considerations, it is clear the parameters to be evaluated are not independent of each other. The rate constants k and k_* for transfer through the interface must be closely related to the coefficients g, b, s, g_*, b_*, and s_*, which govern the dynamics of surface processes. With associated relationships, the dimension of the evaluation problem will be reduced.

First, let us place a double-layer sample (other than a partition as above) into a vacuum chamber and heat it to enhance hydrogen absorption. For example, the nickel substrate can be heated by passing a current through it. If the hydrogen pressure $\bar{p}$ and temperature $\bar{T}$ are constant, steady-state equilibrium concentrations $\bar{c}$ and $\bar{c}_*$ will set in the layers after a time. From (3) and (4) (all the derivatives are zero), we obtain $\bar{c} = \gamma\sqrt{\bar{p}}$, $\gamma = g\sqrt{\mu s}/\sqrt{b}$. Since g, b, and s are as yet consid-

ered to be known, the coefficient of equilibrium solubility γ is also known. Hence, we know $\bar{c}$. Now sharply cool the sample (the current is off). The room-temperature rates of hydrogen adsorption/desorption are very small. Pump off the gas from the chamber. In this case, the adsorbed hydrogen is nearly totally left in the sample. Degasify the sample by heating it to a high temperature on evacuation. Knowing the total amount of the adsorbed hydrogen, the concentration $\bar{c}$, and the sample geometry, one can easily calculate $\bar{c}_*$. From (12), $k\bar{c} = k_*\bar{c}_*$; hence, $\lambda \equiv k/k_* = \bar{c}_*/\bar{c}$ is a known number at a temperature $\bar{T}$. Within the adopted transfer model,

$$\bar{c}_* = \gamma_*\sqrt{\bar{p}}, \quad \gamma_* = g_*\sqrt{\mu s_*}/\sqrt{b_*},$$
$$\lambda = k/k_* = \gamma_*/\gamma = g_*\sqrt{\mu s_* b}/(g\sqrt{\mu s b_*}). \tag{14}$$

Remark 1. The coefficients of equilibrium solubility γ and γ_* for each of the materials are readily derived from experiments under conditions when the equilibrium concentrations are proportional to the square root of the gaseous hydrogen pressure. Therefore, they are thought of as given. For the subsequent discussion, the fact that the ratio $\lambda = k/k_*$ is known and that it is related (within our model) to the surface parameters g, g_*, b, b_*, s, and s_* through (14) will suffice. Thus, the posed multiparameter identification problem is, in essence, reduced to the four-dimensional subproblem, namely, finding D_*, g_*, b_*, and k_* for fixed temperatures $\bar{T}$.

Make the experiment more complicated: turn back to the above method of permeability. The sample is a degassed double-layer partition in a vacuum chamber. Basically, complete degassing is not imperative (see the remark below). On the input side, the pressure is sharply raised and then kept constant ($\bar{p}$ = const). The temperature $\bar{T}$ is fixed. On the output side, the system is evacuated and measurements are made according to (13).

First, we are interested in information that can be gained from the steady-state regime of permeability. Steady-state conditions are set in a time t_*: $J(t) = \bar{J}$ = const, $t \geq t_*$. The time derivatives in model (1)–(12) vanish. From (3) and (4), $c_0(t) = \bar{c}_0$ = const at $t \geq t_*$ and

$$\bar{c}_0 = gb^{-1/2}(\mu s\bar{p} - \bar{J})^{1/2}. \tag{15}$$

In fact, from (9) (at $\dot{q}_* = 0$ and $\mu s_* p_* = 0$) and (13), we have $\bar{J} = -D_* c_{*x}$, $t \geq t_*$. The diffusion and desorption fluxes equal each other in magnitude. Since $c_t = c_{*t} = 0$ in (1) and (6), the distribution of the concentrations over the thickness is linear; i.e., the gradients of c_x and c_{*x} are constant. From (11), $Dc_x = -\bar{J}$, $t \geq t_*$. Substituting Dc_x into (4) in view of $\dot{q} = 0$ and (3) yields (15). Note that $\bar{c}_0 < \bar{c}$ because of the subtrahend $\bar{J}$.

The physical meaning of (15) ($\bar{J} = \mu s\bar{p} - bg^{-2}\bar{c}_0^2$) is the following. As soon as the input concentration reaches the saturation value $\bar{c}_0$, corresponding to $\bar{p}$, dynamic equilibrium sets in the system: the penetrating flux is equal to a difference between the flux incident on the surface, $\mu s\bar{p}$, and the desorption flux backward to the chamber. This qualitative reasoning was verified in numerical experiments; hence, the model is physically adequate.

Remark 2. Let D for the first layer be known but the surface parameters g, b, and s not. In this case, $\bar{c}_0$ cannot be calculated from (15). However, by increasing l, l_*, and $\bar{p}$ and appropriately selecting the substrate, the condition $\mu s\bar{p} \gg \bar{J}$ can be met. The incident flux far exceeds the permeability of the sample. Then, from (15), $\bar{c}_0 \approx gb^{-1/2}(\mu s\bar{p})^{1/2}$. This value coincides with the equilibrium concentration $\bar{c} = \gamma\sqrt{p}$, where γ can be obtained experimentally. Then, $\bar{c} = \gamma\sqrt{\bar{p}}$ should be used instead of $\bar{c}_0$ in all of the formulas. If s is also known, then $\bar{c}_0 = [(\mu s\bar{p} - \bar{J})/(\mu s)]^{1/2}\gamma$.

Now it is easy to derive analytic expressions for the steady-state concentrations at the edges of the layers:

$$(\bar{c}_l - \bar{c}_0)/l = c_x = -D^{-1}\bar{J} \longrightarrow \bar{c}_l = \bar{c}_0 - lD^{-1}\bar{J},$$
$$\bar{J} = b_*\bar{q}_*^2 = b_* g_*^{-2}\bar{c}_{*l_*} \longrightarrow \bar{c}_{*l_*} = g_* b_*^{-1/2}\bar{J}^{1/2},$$
$$(\bar{c}_{*l_*} - \bar{c}_{*0})/l_* = c_{*x}$$
$$= -D_*^{-1}\bar{J} \longrightarrow \bar{c}_{*_0} = \bar{c}_{*_{l_*}} + l_* D_*^{-1}\bar{J}.$$

At $t \geq t_*$, (12) has the form $k\bar{c}_l - k_*\bar{c}_{*0} = \bar{J}$. Substituting the found values of $\bar{c}_l$ and $\bar{c}_{+0}$, multiplying the equation by l_*, and designating

$$x_1 = l_*^2/D_*, \quad x_2 = g_* l_*, \quad x_3 = b_*^{-1/2}, \quad x_4 = l_*/k_*,$$

we come to

$$(x_1 + x_4)\bar{J} + x_2 x_3 \bar{J}^{1/2} = l_*\lambda(\bar{c}_0 - lD^{-1}\bar{J}). \tag{16}$$

This equation allows us to uniquely determine $\Sigma = x_1 + x_4$ and $\Pi = x_2 x_3$ from $\bar{p}_1$ and $\bar{p}_2$ and corresponding values of $\bar{J}_1$ and $\bar{J}_2$. The unique determination of x_1, x_2, x_3, and x_4 needs at least two equations more. This stage is the most complicated, since it involves transient analysis.

Let us perform auxiliary transformations. By virtue of (1) and (6) and also the formula for integration by parts, the equality

$$
\begin{aligned}
0 &= \int_0^{t_*}\int_0^{l}\psi(t,x)(c_t - Dc_{xx})\,dx\,dt \\
&+ \sigma\int_0^{t_*}\int_0^{l_*}\psi_*(t,x)(c_{*t} - D_*c_{*xx})\,dx\,dt \\
&= \int_0^{l}\{\psi(t_*,x)c(t_*,x) - \psi(0,x)c(0,x)\}\,dx \\
&- \int_0^{t_*}\{\psi(t,l)Dc_x(t,l) - \psi(t,0)Dc_x(t,0)\}\,dt \\
&+ \int_0^{t_*}\{D\psi_x(t,l)c(t,l) = D\psi_x(t,0)c(t,0)\}\,dt \\
&+ \sigma\int_0^{l_*}\{\psi_*(t_*,x)c_*(t_*,x) - \psi_*(0,x)c_*(0,x)\}\,dx \\
&- \sigma\int_0^{t_*}\{\psi_*(t,l_*)D_*c_{*x}(t,l_*) - \psi_*(t,0)D_*c_{*x}(t,0)\}\,dt \\
&+ \sigma\int_0^{t_*}\{D_*\psi_{*x}(t,l_*)c_*(t,l_*) - D_*\psi_{*x}(t,0)c_*(t,0)\}\,dt
\end{aligned}
\tag{17}
$$

is valid for smooth functions $\psi(t, x)$ and $\psi_*(t, x)$. Here, we omit two double integrals; however, they go to zero if the functions $\psi(t, x)$ and $\psi_*(t, x)$ obey the conjugate equations

$$
\frac{\partial\psi}{\partial t} = -D\frac{\partial^2\psi}{\partial x^2}, \quad \frac{\partial\psi_*}{\partial t} = -D_*\frac{\partial^2\psi_*}{\partial x^2}. \tag{18}
$$

The terms associated with surface processes, i.e., those involved in (13), are left. The further strategy consists in expressing all the terms through the model parameters to obtain an algebraic equation of type $f(x_1, \ldots, x_4) = 0$.

The membrane is predehydrogenated, and the terms with $c(0, x)$ and $c_*(0, x)$ in (17) are zero. The steady-state concentrations $c(t_*, x)$ and $c_*(t_*, x)$ are easy to calculate:

$$
c_*(t_*, x) = \bar{c}_{*0} - xD_*^{-1}\bar{J}, \quad k\bar{c}_l - k_*\bar{c}_{*0} = \bar{J},
$$

$$
\bar{c}_l = \bar{c}_0 - lD^{-1}\bar{J},
$$

$$
\begin{aligned}
\bar{c}_0 &= gb^{-1/2}(\mu s\bar{p} - \bar{J})^{1/2} \Rightarrow c_*(t_*, x) \\
&= \lambda\bar{c}_0 - (\lambda lD^{-1} + 1/k_* + xD_*^{-1})\bar{J}, \\
c(t_*, x) &= \bar{c}_0 - xD^{-1}\bar{J}.
\end{aligned}
\tag{19}
$$

Experimental data for the fluxes at the interfaces ($x = l$ and $x = 0$ for the first and the second layers, respectively) are unknown. To exclude the related terms, we add to (18) matching conditions similar to (11) and (12):

$$
\sigma = k_*/k = 1/\lambda, \quad D\frac{\partial\psi}{\partial x}(t, l) = D_*\frac{\partial\psi_*}{\partial x}(t, 0), \tag{20}
$$

$$
k\psi(t, l) - k_*\psi_*(t, 0) = -D\frac{\partial\psi}{\partial x}(t, l). \tag{21}
$$

Eventually, (17) takes the form

$$
\begin{aligned}
0 &= \int_0^{l}\psi(t_*, x)c(t_*, x)\,dx + \int_0^{t_*}\psi(t, 0)Dc_x(t, 0)\,dt \\
&- \int_0^{t_*}D\psi_x(t, 0)c(t, 0)\,dt + \lambda^{-1}\int_0^{l_*}\psi_*(t_*, x)c_*(t_*, x)\,dx \\
&- \lambda^{-1}\int_0^{t_*}\psi_*(t, l_*)D_*c_{*x}(t, l_*)\,dt \\
&+ \lambda^{-1}\int_0^{t_*}D_*\psi_{*x}(t, l_*)c_*(t, l_*)\,dt.
\end{aligned}
\tag{22}
$$

Here, all the terms are calculable if the functions ψ and ψ_* satisfy (18), (20), and (21). It is essential that (18) is not subjected to initial and boundary conditions. There are an infinitely large number of appropriate functions ψ and ψ_*, and it is convenient to separate the variables: $\psi = \beta(t)r(x)$ and $\psi_* = \beta_*(t)r_*(x)$. We will find specific forms of (22), trying to obtain the simplest equations of type $f(x_1, \ldots, x_4) = 0$.

Variant 1. Let ψ = const. Since (22) is homogeneous with respect to ψ and ψ_*, we put $\psi = 1$. Then, by virtue of matching condition (21), $\psi_* = \lambda$. Calculate the integrals in (22):

$$
I_1 = \int_0^{l}c(t_*, x)\,dx = \int_0^{l}(\bar{c}_0 - xD^{-1}\bar{J})\,dx = \bar{c}_0 l - D^{-1}\bar{J}l^2/2,
$$

$$I_2 = \int_0^{t_*} Dc_x(t, 0)dt = \int_0^{t_*} (\dot{q} - \mu s\bar{p} + bq^2)dt \approx g^{-1}\bar{c}_0 - \bar{J}t_*,$$

$$I_4 = \int_0^{l_*} c_*(t_*, x)dx = \lambda\bar{c}_0 l_* - (\lambda l_* l D^{-1} + l_*/k_*)\bar{J} - D_*^{-1} l_*^2 \bar{J}/2,$$

$$I_5 = -\int_0^{t_*} D_* c_{*x}(t, l_*)dl = \int_0^{t_*} (\dot{q}_* + J)dt = b_*^{-1/2}\bar{J}^{1/2} + S.$$

Comments. In calculating the integrals including the fluxes Dc_x and $D_* c_{*x}$, we, hereafter, use dynamic equations (4) and (9) and expression (13) for the desorption flux $J(t)$. In I_5, $q_*(0) = 0$ ($\varphi_*(x) \equiv 0$), $\bar{J} = b_* q_*^2(t_*) \Rightarrow$ $q_*(t_*) = b_*^{-1/2}\bar{J}^{1/2}$. Designate the integral of $J(t)$ as S ($t \in [0, t_*]$); $I_3 = I_6 = 0$.

Particular attention should be given to approximately calculating the integral I_2, more precisely, the integral of $bq^2(t) = bg^{-2}c_0^2(t)$ (the rest of the terms pose no difficulties: $q(t_*) = g^{-1}c_0(t_*) = g^{-1}\bar{c}_0$, $\mu s\bar{p} = \text{const}$). At the input, only the pressure $\bar{p}$ is known, i.e., only the term in the right of differential equation (4). Therefore, both the concentration $c_0(t) = c(t, 0)$ and the flux $Dc_x(t, 0)$ remain unclear. One could experimentally determine the input flux from the hydrogen flux rate. Then, numerically integrating (4) with zero input data, we would obtain $c_0(t)$ [$q(t) = g^{-1}c_0(t)$]. However, the high input pressure $\bar{p}$ is a serious handicap to this. The concentration $c_0(t)$ [$q(t)$] is also problematic to measure. The way out is to measure $J(t)$ on evacuation. Therefore, we will proceed as follows: by virtue of (4), the flux $Dc_x(t, 0)$ is replaced by $\dot{q} - \mu s\bar{p} + bg^{-2}c_0^2$, and the integrals where the concentration $c_0(t)$ appears are calculated approximately. This is not a mathematical drawback. To identify a "black box" correctly, one should know both output and input data. Input measurements would significantly improve the correctness of the identification problem.

To take the $c_0(t)$-containing integrals, we should bear in mind that the rates of the surface processes on the input and output surfaces of a double-layer membrane markedly differ when a pressure drop is very large (7 to 9 orders of magnitude). At the output, the surface is hydrogen-depleted due to evacuation and its accumulation is a rate-limiting process [see dynamic equation (9)]. At the input ($\bar{p} \gg p_*$), the surface is rapidly saturated to $\bar{q}$, corresponding to $\bar{p}$, with slow diffusate backflow into the chamber. The transition time is negligible in comparison with the time t_* taken to attain the steady-state level $\bar{J}$. In experiments, a concentration jump can be simulated with a fairly good accuracy by increasing $\bar{p}$ and especially l and l_*, as well as by properly selecting the substrate. Thus, when calculating the integrals with $c_0(t)$ within a long time interval $[0, t_*]$, one can put $c_0(t) \approx \bar{c}_0$ [see (15)]. This qualitative reasoning has been confirmed by numerical simulation. Eventually, in terms of the variables $x_1 = l_*^2/D_*$, $x_2 = g_* l_*$, $x_3 = b_*^{-1/2}$, and $x_4 = l_*/k_*$, equation (22) at $\psi = 1$ and $\psi_* = \lambda$ takes the form

$$f_1 = -x_4\bar{J} - x_1\bar{J}/2 + x_3\bar{J}^{1/2} + A + S = 0, \quad (23)$$
$$A = \bar{c}_0 l - D^{-1}l^2\bar{J}/2 + g^{-1}\bar{c}_0 - \bar{J}t_* + \lambda\bar{c}_0 l_* - \lambda l_* l D^{-1}\bar{J}.$$

Excluding $x_4 = \Sigma - x_1$, we obtain the linear equation with respect to x_1 and x_3.

Variant 2. Let $\psi = x/l$, where l is a normalizing factor. Then, for linear $\psi_* = \alpha x + \beta$ in (20) and (21), we arrive at

$$\psi_* = DD_*^{-1}x/l + (kl + D)/(k_* l).$$

In the integral I_5, we replace the flux $-D_* c_{*x}(t, l_*)$ by $\dot{q}_* + J$. In addition, $I_2 = 0$, $I_3 \approx -\bar{c}_0 Dt_*/l$, $q_*(t_*) = x_3\bar{J}^{1/2}$, and the expression

$$c_*(t, l_*) = g_* q_*(t) = g_* b_*^{-1/2} J^{1/2}(t) = x_2 x_3 J^{1/2}(t)/l_* = \Pi J^{1/2}/l_*$$

is substituted into I_6.

Eventually, after excluding $x_4 = \Sigma - x_1$, equation (22) is written in the form

$$f_2 = a_1 x_1^2 + a_2 x_1 + a_3 x_3 + a_4 = 0, \quad (24)$$

where the coefficients a_i are given by

$$a_1 = D\bar{J}/(3\lambda l_* l), \quad a_2 = D\bar{J}\Sigma/(\lambda l_* l) - \bar{c}_0 D/(2l) + \bar{J},$$

$$a_3 = (D\Sigma/(\lambda l_* l) + 1)\bar{J}^{1/2},$$

$$a_4 = \bar{c}_0 l/2 - D^{-1}\bar{J}l^2/3 - \bar{c}_0 Dt_*/l - D\bar{J}\Sigma^2/(\lambda l_* l) + \Sigma(\bar{c}_0 D/l - 2\bar{J}) + \lambda\bar{c}_0 l_* - \lambda D^{-1} l_* l\bar{J} + (D\Sigma/(\lambda l_* l) + 1)S + D\Pi S_{1/2}/(\lambda l_* l),$$

and

$$S = \int_0^{t_*} J\,dt, \quad S_{1/2} = \int_0^{t_*} J^{1/2}\,dt.$$

Variant 3. For $\psi = (x - l)/l$, we have

$$\psi_* = DD_*^{-1}x/l + D/(k_*l),$$

$$I_2 \approx -g^{-1}\bar{c}_0 + \bar{J}t_*, \quad I_3 \approx -D\bar{c}_0 t_*/l.$$

As compared with variant 2, in an equation $f_3 = 0$ [like (24)], the coefficient a_1 remains unchanged, $\bar{J}/2$ replaces $\bar{J}$ in a_2, a_3 loses the unity, and

$$a_4 = -\bar{c}_0 l/2 + D^{-1}l^2\bar{J}/6 - D\bar{c}_0 t_*/l - g^{-1}\bar{c}_0 + \bar{J}t_*$$
$$+ \Sigma(D\bar{c}_0/l - \bar{J}) - D\bar{J}\Sigma^2/(\lambda l_* l) + D\Sigma S/(\lambda l_* l)$$
$$+ D\Pi S_{1/2}/(\lambda l_* l).$$

Variant 4. For more complex representations like $\psi = \beta(t)\sin(\omega x)$, $\beta(t)\cos(\omega x)$, or $\beta(t)\exp(\omega x)$, associated analytical expressions are very cumbersome. Any linear combination of the above pairs ψ and ψ_** (for example, $f_2 - f_3 = f_1$) would be appropriate.

Remark 3. The physical meaning of selecting various ψ's and ψ_*'s ("trial functions") is as follows. In variant 1, (22) does not contain terms with the boundary concentrations $c_0(t)$, and $c_{*l_*}(t)$. Variant 2 does not involve the flux $Dc_x(t, 0)$, because $\psi(t, 0) = 0$, and in the integrals, the steady-state concentrations $c(t_*, x)$ and $c_*(t_*, x)$ are assigned different weights across the membrane. In other words, one can choose parameters that have a decisive effect on deriving the equations $f = 0$.

Remark 4. There are many equations to determine $x_1, \ldots, x_4$. Equation (24) is however quadratic with respect to x_1. From physical considerations, we are interested in positive solutions. Their existence follows from the construction of the equations, but their uniqueness is open to question. At large x_3's (small b_*'s), the roots will have the different signs as $a_1 < 0$ and $a_3 > 0$. We take a positive x_1. The parameter b_* should be small, since it stands before the concentration squared. As it increases, hydrogen ceases to accumulate on the surface. Within a physically reasonable range of the parameters, the selection of the root x_1 poses no problems. Subsequently, however, we can do without equation (24).

Two values, $\bar{J}_1$ and $\bar{J}_2$, that correspond to pressures $\bar{p}_1$ and $\bar{p}_2$, respectively, are needed for identification. In addition, because of experimental errors, it is desirable that the number of the equations $f(x_1, \ldots, x_4) = 0$ exceed the least theoretical number. To perform two independent experiments (to degas the sample again, etc.) seems unreasonable. Therefore, we will modify the method of permeability in the following way.

The first stage of the experiment remains the same. Let the initial gas pressure be $\bar{p}_1$. After the steady-state value $\bar{J}_1$ is established at a time instant t_{*1}, we sharply raise the pressure to $\bar{p}_2 > \bar{p}_1$ and measure the output desorption flux density $J(t)$, $t = t_{*1} + t_{*2}$, until a new steady-state value $\bar{J}_2$ at a time instant $t \in [0, t_{*1} + t_{*2}]$ is attained.

If, at the second stage, the time reference point is transferred to t_{*1}, we will come to equations of the same form as (23) and (24). One correction only is needed: the system "starts" not from $\varphi = \varphi_* = 0$, but from values equal to the steady-state concentration distributions for the pressure $\bar{p}_1$:

$$\varphi(x) = \bar{c}_{01} - xD^{-1}\bar{J}_1, \quad \bar{c}_{01} = gb^{-1/2}(\mu s\bar{p}_1 - \bar{J}_1)^{1/2}, \tag{25}$$
$$\varphi_*(x) = c_*(t_{*1}, x) = \lambda\bar{c}_{01} - (\lambda l D^{-1} + 1/k_* + xD_*^{-1})\bar{J}_1.$$

For the second stage, we have, instead of (23),

$$f_4 = f_1^{(2)} - I_1^{(1)} - I_4^{(4)} - g^{-1}\bar{c}_{01} - x_3\bar{J}_1^{1/2}.$$

The superscript (i) means that $\bar{c}_0$ and $\bar{J}$ are replaced by $\bar{c}_{0i}$ and $\bar{J}_i$. The two last terms are due to the fact that $q(0) = g^{-1}\bar{c}_{01}$ in I_2 and $q_*(0) = x_3\bar{J}_1^{1/2}$ in I_5. After rearrangements and the replacement $x_4 = \Sigma - x_1$, we obtain

$$f_4 = x_1(\bar{J}_2 - \bar{J}_1)/2 + x_3(\bar{J}_2^{1/2} - \bar{J}_1^{1/2}) + S^{(2)} + B = 0,$$
$$B = l(\bar{c}_{02} - \bar{c}_{01}) - D^{-1}l^2(\bar{J}_2 - \bar{J}_1)/2 + g^{-1}(\bar{c}_{02} - \bar{c}_{01})$$
$$+ \lambda l_*(\bar{c}_{02} - \bar{c}_{01}) - \lambda l_* l D^{-1}(\bar{J}_2 - \bar{J}_1) - \Sigma(\bar{J}_2 - \bar{J}_1) \tag{26}$$
$$- \bar{J}_2 t_{*2} + S^{(2)}.$$

By $S^{(2)}$, we designate the result of the (numerical) integration of $J(t)$ in the interval $[0, t_{*2}]$ ($[t_{*1}, t_{*1} + t_{*2}]$). Similarly, for variant 2, we can obtain

$$f_5 = f_2^{(2)} - I_1^{(1)} - I_4^{(1)} - a_3^{(1)}x_3\bar{J}_1^{1/2} = 0, \tag{27}$$

where I_i are the integrals in (22) (ψ and ψ_* for variant 2):

$$I_1^{(1)} = \bar{c}_{01}l/2 - D^{-1}\bar{J}_1 l^2/3,$$

$$I_4^{(1)} = -x_1 D\bar{J}_1/(3\lambda l_* l) + x_1(\bar{c}_{01} D/(2l) - \bar{J}_1)$$
$$- x_4^2 D\bar{J}_1/(\lambda l_* l) + x_4(\bar{c}_{01} D/l - 2\bar{J}_1)$$
$$- x_1 x_4 D\bar{J}_1/(\lambda l_* l) + \lambda\bar{c}_{01} l_* - \lambda D^{-1} l_* l\bar{J}_1,$$

$$x_4 = \Sigma - x_1.$$

On rearrangements, equation (27) takes the form (24). In a_4, the term $-\bar{c}_0 Dt_*/l$ should be replaced by $-\bar{c}_{02} Dt_*/l$ [integral I_3 in (22)]. In all of the other expressions for a_i, the parameters $\bar{c}_{02} - \bar{c}_{01}$, $\bar{J}_2 - \bar{J}_1$, and $\bar{J}_2^{1/2} - \bar{J}_1^{1/2}$ should be substituted for $\bar{c}$, $\bar{J}$, and $\bar{J}^{1/2}$. S, and $S_{1/2}$ are the integrals of $J(t)$ and $J^{1/2}(t)$ in the time interval of $[0, t_{*2}]$ ($[t_{*1}, t_{*1} + t_{*2}]$).

In the brief form, the identification algorithm looks as follows:

(1) Let D, $gb^{-1/2}$, γ, and γ_* be known ($\sqrt{\mu s} = \gamma/(gb^{-1/2})$). Experimental conditions: $t = 0 \Rightarrow \varphi = \varphi_* = 0$, $p = \bar{p}_1$, $T = \bar{T}$; $t = t_{*1} \Rightarrow J = \bar{J}_1$, $p = \bar{p}_2 > \bar{p}_1$, $t_{*1} \longrightarrow 0$, φ and φ_* are given by (25); $t = t_{*2}$ ($t = t_{*1} + t_{*2}$) $\Rightarrow$ $J = \bar{J}_2$.

(2) From equations (16) for $\bar{c}_{01}$, $\bar{J}_1$, and $\bar{c}_{02}$, $\bar{J}_{02}$, we find

$$\Sigma = x_1 + x_4 = l_*^2/D_* + l_*/k_*,$$
$$\Pi = x_2 x_3 = g_* l_* b_*^{-1/2}.$$

The equations are linear with respect to Σ and Π. The concentrations $\bar{c}_{0i}$ are determined from (15) or, more roughly, as $\bar{c}_{0i} \approx \gamma\sqrt{\bar{p}_i}$ (then there is no need to know $gb^{-1/2}$ and s).

(3) x_1 and x_3 are determined from linear equations (23) ($f_1^{(1)} = 0$) and (26). Equations (24) and (27) are suitable for checking or when the least-squares method is applied (in the case of great experimental errors). Four integrals of $J(t)$, $J^{1,2}(t)$ in the intervals $[0, t_{*1}]$ and $[0, t_{*2}]$ ($[t_{*1}, t_{*1} + t_{*2}]$) must be numerically taken in advance.

(4) Find $D_* = x_1^{-1} l_*^2$, $b_* = x_3^{-1/2}$, $k_* = x_4^{-1} l_* = (\Sigma - x_1)^{-1} l_*$, $g_* = x_2/l_* = \Pi/(x_3 l_*)$, $k = \lambda k_*$. Finally, from (14), $s_* = b_* \lambda^2\gamma^2/(g_*^2 \mu)$.

(5) Knowing D_*, g_*, b_*, s_*, k, and k_* at different $\bar{T}$'s, we obtain all the twelve parameters D_{*0}, E_{D_*}, …, k_{*0}, E_{k_*}.

A great body of experimental data must be collected to minimize an experimental error (hence, a large number of experiments). However, a large set of bulk and surface parameters related to hydrogen permeability can eventually be determined.

SIMPLIFICATIONS AND CONCLUDING REMARKS

It was assumed that the hydrogen permeability of the first-layer material had carefully been examined. In general, we may think that both layers are to be studied. Then, with equations (16) and (23)–(27) for different $\bar{p}_i$'s, the solution to the starting inverse problem, involving the differential equations, can be reduced to analysis of a set of algebraic equations. This analysis can be carried out numerically. It is the author's opinion, however, that the unique determination of the ten parameters at T = const by the method of permeability is unrealistic. It is appropriate to characterize the substrate material in advance.

Consider briefly the case of a single-layer metal membrane. This problem can be considered as a preliminary stage. Expressions (1)–(5) are supplemented by (8) and (9), where the subscript * is omitted (except for $q_* p_*$); $c_l(0) = \varphi(l)$. The steady-state distribution of the concentration is given by

$$c(t_*, x) = (l - x)D^{-1}\bar{J} + gb^{-1/2}\bar{J}^{1/2}.$$

Putting $x = 0$, we obtain, by virtue of (15), the equation

$$gb^{-1/2}(\mu s\bar{p} - \bar{J})^{1/2} = gb^{-1/2}\bar{J}^{1/2} + lD^{-1}\bar{J}. \qquad (28)$$

From two pairs $\bar{p}_i$, $\bar{J}_i$, one can find s and the product $Dgb^{-1/2}$. Similarly to (23) and (26), we obtain from (17) ($\sigma = 0$, $\psi = 1$, $c_0(t) \approx \bar{c}_0$, $t \geq \varepsilon \ll t_*$)

$$f_1 = x_1(X\xi_1 - \bar{J}_1/2) + x_3(\xi_1 + \bar{J}_1^{1/2}) + S^{(1)} - \bar{J}_1 t_{*1} = 0,$$
$$x_1 = l^2/D, \quad x_3 = b^{-1/2}, \quad \xi_i = (\mu s\bar{p}_i - \bar{J}_i)^{1/2},$$
$$X = Dgb^{-1/2}/l = x_1^{-1} x_2 x_3,$$
$$f_4 = x_1(X(\xi_2 - \xi_1) - (\bar{J}_2 - \bar{J}_1)/2)$$
$$+ x_3(\xi_2 + \bar{J}_2^{1/2} - \xi_1 - \bar{J}_1^{1/2}) + S^{(2)} - \bar{J}_2 t_{*2} = 0.$$

For $\psi = x/l$ [instead of $\bar{c}_0$ from (15)], one can also use the right of (28) to obtain

$$f_2 = x_1(\bar{J}_1/6 + X\bar{J}_1^{1/2}/2) + x_3\bar{J}_1^{1/2} + A_1 = 0,$$

$$f_5 = x_1((\bar{J}_2 - \bar{J}_1)/6 + X(\bar{J}_2^{1/2} - \bar{J}_1^{1/2})/2) + x_3(\bar{J}_2^{1/2} - \bar{J}_1^{1/2}) + A_2 = 0,$$

$$A_i = S^{(i)} + XS_{1/2}^{(i)} - \bar{J}_i t_{*i} - X\bar{J}_i^{1/2} t_{*i}.$$

These equations are linear with respect to x_1 and x_3. Their number exceeds that of the variables. If experimental errors are large, it is appropriate to apply the least-squares method. Knowing x_1 and x_3, we find x_2 from X. If $\mu s \bar{p} \gg \bar{J}$ and $\bar{c}_0 \approx \gamma\sqrt{\bar{p}}$ ($\gamma = g\sqrt{\mu s}/\sqrt{b}$), the parameters X, $D\gamma = lX\sqrt{\mu s}$, and, hence, s are derived from two steady-state values of $\gamma\sqrt{\bar{p}}$ in the left of (28). From x_1 and x_3, one obtains x_2 and γ. If γ is known, the parameters D, $gb^{-1/2}$, and s are found from (28). Having determined x_3 from $f_i = 0$, we calculate g. Thus, all the parameters D, g, b, and s are determined uniquely by the method of permeability.

Let the solubility coefficient γ be known and γ_* not. Then λ [see (14)] is considered as an additional variable. From $(16)_{1,2}$, we find $\tilde{\Sigma} = \Sigma/\lambda$ and $\tilde{\Pi} = \Pi/\lambda$. Equations (23) and (26) are linear with respect to x_1, x_3, and λ. Having expressed x_i through λ, we obtain equation (24) for λ ($\Sigma = \tilde{\Sigma}\lambda$, $\Pi = \tilde{\Pi}\lambda$). In S and $S_{1/2}$, time instants t_{*i} should be as short as possible (obeying the condition $J \approx \tilde{J}$, $t \geq t_*$), so that information provided by transients will not be shadowed by steady-state processes upon integration.

There is no need to faithfully copy the experiments for different $\bar{T}$'s, for example, degasify the sample again. At $T = \bar{T}_0$, we apply the admission pressure $\bar{p}_0$ and wait until gases, other than hydrogen, leave the membrane. Once the steady-state value $\bar{J}_0$ is established, we sharply raise the pressure twice: to $\bar{p}_1 > \bar{p}_0$, waiting for the steady-state value $\bar{J}_1$, and then to $\bar{p}_2 > \bar{p}_1$, waiting for $\bar{J}_2$. Theoretically, one pressure rise is sufficient. Equations (26) and (27) are then employed for identification. After the membrane is heated to a new temperature $T = \bar{T}_1$ and the steady-state conditions are set, the pressure is raised again (before the heating, it could be decreased), the parameters at $T = \bar{T}_1$ are found, etc. Here, however, we have to choose the root of the quadratic equation for x_1. If the pressure $\bar{p}$ is raised twice at each step, two linear equations like (26) will suffice to determine x_1 and x_3.

Let us reverse the positions of the layers. The pressure $\bar{p}$ is now applied on the side of the material under test. If, when taking the integrals from 0 and $\tilde{t}_*$, one *a priori* assumes for the material under test that $c_{*0}(t) \approx \bar{c}_{*0}$, $t \geq \varepsilon \ll \tilde{t}_*$, the parameters D_*, g_*, b_*, s_*, and k_* in all of the equations $f = 0$ should formally be replaced by the associated asterisked quantities. For example, the equation similar to (23) will now be linear with respect to D_*^{-1}, g_*^{-1}, and k_*^{-1}. However, the application of the "impact" $\bar{p}$ to the substrate and taking measurements on the side of a material being tested seems to be more reasonable and correct.

Consider the case when the hydrogen is free to evolve from the second layer into the chamber. Instead of (8)–(10), the flux balance model is used:

$$\mu s_*(T) p_*(t) - b_*(T) c_*^2(t, l_*) - D_*(T)\frac{\partial c_*}{\partial x}(t, l_*) = 0.$$

The hydrogen desorbs from the volume immediately without accumulating on the surface. As before, $J(T) = b_* c_*^2(t, l_*)$ is to be measured. D_*, b_*, s_*, k, and k_* are the desired parameters. Formally, this situation corresponds to $g_* = 1$ and $\dot{q}_* = 0$ in (8) and (9). Upon evacuation, we put $\mu s_* p_* \approx 0$. The identification algorithm is greatly simplified. From (16), we find $\Sigma = x_1 + x_4$ and $\Pi = l_* x_3 = l_* b_*^{-1/2}$. The terms containing x_3 in (23)–(27) will be absent (they appeared after the integration of $\dot{q}_*$ between 0 and t_*). The value of D_* ($x_1 = l_*^2/D_*$) can be found from one of equations (23)–(27). Then, $k_* = (\Sigma - x_1)^{-1} l_*$, $k = \lambda k_*$, and $s_* = b_* \lambda^2 \gamma^2/\mu$.

Let $\gamma_* = \sqrt{\mu s_*}/\sqrt{b_*}$ [$\bar{c}$ in (15) or $\bar{c}_0 = \gamma\sqrt{\bar{p}}$] be unknown ($\gamma$, D, and g are known). From $(16)_{1,2}$, we find $\tilde{\Sigma} = (x_1 + x_4)/\lambda$ and $\tilde{\Pi} = l_* x_3/\lambda$ ($g_* - 1$). Represent in (23) x_4 as $\tilde{\Sigma}\lambda - x_1$ (the term with x_3 is absent). Similarly, in (26) without x_3, we substitute $\Sigma = \tilde{\Sigma}\lambda$. Eventually, we arrive at two linear equations with respect to x_1 and λ. Nonlinear equations (24) and (27) are also applicable. From $\tilde{\Sigma}$ and $\tilde{\Pi}$, we find x_4 and x_3 and then $k = \lambda k_*$, $\gamma_* = \lambda\gamma$, and $s_* = \gamma_*^2 b_*/\mu$.

The identification algorithm will be computationally stable if the terms with x_1, x_2, x_3, and x_4 in equations (16) and (23)–(27) are comparable in order. This depends on the choice of the materials, l, and l_*. In particular, the orders of l^2/D and l_*^2/D_* must not be too far different from each other; otherwise, the set of the equation will be ill-conditioned. In our computational experiments, the reference values were the following: $\bar{p} = 0.1$ torr, $l = 0.02$ cm, $l_* = 0.0002$ cm, $D = 10^{-6}$ cm^2/s,

$D_* = 10^{-9}$ cm^2/s, $g = 10^2$, $g_* = 10^3$ cm^{-1}, $b = 10^{-16}$, $b_* = 10^{-18}$ cm^2/s, $s = 10^{-4}$, $s_* = 10^{-2}$, $k = 10^{-7}$, $k_* = 10^{-6}$ cm/s, and $\mu = 1.46 \times 10^{21}$ mol/cm^2 s Torr. Because of the smallness of b and b_* (the coefficients before the concentrations squared), it is useful to use the variable $\tilde{x}_3 = x_3 \times 10^{-6}$ instead of x_3.

REFERENCES

1. *Hydrogen in Metals*, Ed. by G. Alefeld and J. Voekl (Springer-Verlag, New York, 1978; Mir, Moscow, 1981).
2. P. V. Gel'd and L. P. Mokhracheva, *Hydrogen and Physical Properties of Metals and Alloys* (Nauka, Moscow, 1985).
3. *Interaction of Hydrogen with Metals*, Ed. by A. P. Zakharov (Nauka, Moscow, 1987).
4. I. E. Gabis, A. A. Kurdyumov, and A. V. Samsonov, Pis'ma Zh. Tekh. Fiz. **21** (5), 1 (1995) [Tech. Phys. Lett. **21**, 165 (1995)].
5. O. I. Kon'kov, I. N. Kapitonov, I. N. Trapeznikov, and E. I. Terukov, Pis'ma Zh. Tekh. Fiz. **23** (1), 3 (1997) [Tech. Phys. Lett. **23**, 9 (1997)].
6. I. E. Gabis, Fiz. Tekh. Poluprovodn. (St. Petersburg) **31** (2), 145 (1997).
7. A. V. Samsonov, A. A. Koren'kov, I. E. Gabis, and A. A. Kurdyumov, Zh. Tekh. Fiz. **68** (1), 128 (1998) [Tech. Phys. **43**, 114 (1998)].
8. I. E. Gabis, A. A. Kurdyumov, and N. A. Tikhonov, Vestn. St. Peterb. Univ., Ser. 4: Fiz., Khim., No. 2, 77 (1993).
9. O. M. Alifanov, E. A. Artyukhin, and S. V. Rumyantsev, *Extreme Methods for Solving Ill-Posed Problems* (Nauka, Moscow, 1988).
10. Yu. V. Zaĭka, Zh. Vychisl. Mat. Mat. Fiz. **36** (12), 108 (1996).
11. G. I. Marchuk, *Conjugate Equations and Complex Systems Analysis* (TRANS) (Nauka, Moscow, 1992).

Translated by V. Isaakyan

Technical Physics, Vol. 45, No. 5, 2000, pp. 563–565. Translated from Zhurnal Tekhnicheskoĭ Fiziki, Vol. 70, No. 5, 2000, pp. 40–42.

SOLIDS

The Effect of Space Charge and Crystallite Size on the Formation of Properties of Ferropiezoceramic Materials

A. Ya. Dantsiger, V. Z. Borodin, L. A. Reznitchenko, S. I. Dudkina, V. A. Servuli, S. V. Gavrilyatchenko, L. A. Shilkina, and V. A. Borodina

Research Institute of Physics, Rostov State University, Rostov-on-Don, 344090 Russia

Received January 28, 1999

Abstract—The effect is treated of the space charge field and of the crystallite size on the properties of ferroceramics of different compositions. The established qualitative correlation between the structure and electrophysical parameters, the crystallite size, and the space charge field may be useful in designing ferropiezoceramic materials for different applications and devices involving such materials. *© 2000 MAIK "Nauka/Interperiodica".*

INTRODUCTION

The properties of ferroelectrics and, in particular, ferropiezoceramic materials are largely defined by the formation of space charges in such materials. In view of this, the study of the correlation between the fields of space charges and microstructures and other parameters of ferropiezoceramic materials is an important problem associated with the development of materials for different applications. We investigated ferropiezoceramic solid solutions of systems involving lead zirconate-titanate and alkali metal niobates. Two methods were used for measuring the space charge field E_{sp}, namely, (1) the oscillographic method of determining the internal field and (2) the method of polarization reversal by pulsed fields of variable amplitude.

EXPERIMENTAL METHODS AND RESULTS

The effect of the space charge field on the singularities of a hysteresis loop obtained by the former of the above-identified methods was treated in [1, 2] for some models of space charge formation. In newly prepared ferroceramic samples or in those regenerated by electrothermal treatment, the hysteresis loop $P(E)$ has a standard symmetric form, and the current loop $I(E)$ exhibits two symmetrically arranged current maxima for ascending and descending branches of the hysteresis loop. By the position of each of these maxima, one can estimate the coercive field E_c if the field amplitude $E_m > 3E_c$. In aged, extremely polarized samples, asymmetric loops of $P(E)$ and $I(E)$ are observed as a result of formation of the space charge field. The current maxima correspond to the fields $E_{k1} = E_c - E_i$ and $E_{k2} = -E_c - E_i$, where E_i is the internal field which is further treated as the space charge field E_{sp}. Hence it follows that

$$E_{sp} = -(E_{k1} + E_{k2})/2, \quad E_c = (E_{k1} - E_{k2})/2. \qquad (1)$$

The variation of the space charge field when the external field is switched on prevents one from correctly estimating its magnitude under normal conditions of observation of dielectric hysteresis. We used the method of short-term ($7–10 \times 10^{-2}$ s) time-relay switching on of a measuring field of preassigned amplitude to measure E_{sp}.

The other method is described in sufficient detail in [3] in application to studies into ferropiezoceramics. It was also used in [4]. According to this method, the curves of polarization reversal by a series of variable-amplitude pulses are used to determine the critical fields E_{k1} and E_{k2} recorded by the amplitude of pulses corresponding to zero piezoactivity ($Kp = 0$). The space charge field and coercive field are calculated by formulas (1). The shape, duration, and manner of variation of repolarizing pulses are selected from the condition of minimum degree of regeneration, i.e., the least destruction of the internal field by measuring pulses. The dependence of intensity of space charge field E_{sp} for one and the same composition prepared under different conditions (case A) was investigated using the method 2, and that for different compositions of solid solutions with varying concentration of the components (case B), by the methods 1 and 2. In both cases (A and B), the space charge field proves to depend inversely on the crystallite size $\bar{d}$ (Figs. 1 and 2 illustrate the cases A and B, respectively). It follows from Fig. 1 (according to the data of Rogach *et al.* [4]) that the space charge field in one of the compositions of solid solutions of the $PbTiO_3$–$PbZrO_3$–$PbNb_{2/3}Mn_{1/3}O_3$–$PbNb_{2/3}Zn_{1/3}O_3$ system decreases with increasing mean size of the crystallites, which may be attributed to the decrease of the surface layer of the space charge.

1063-7842/00/4505-0563$20.00 © 2000 MAIK "Nauka/Interperiodica"

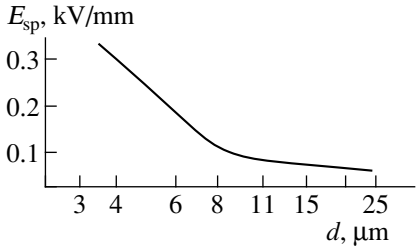

Fig. 1. The space charge field as a function of the crystallite size for one composition of the $PbTiO_3$–$PbZrO_3$–$PbNb_{2/3}Mn_{1/3}O_3$–$PbNb_{2/3}Zn_{1/3}O_3$ system, prepared under different conditions [4].

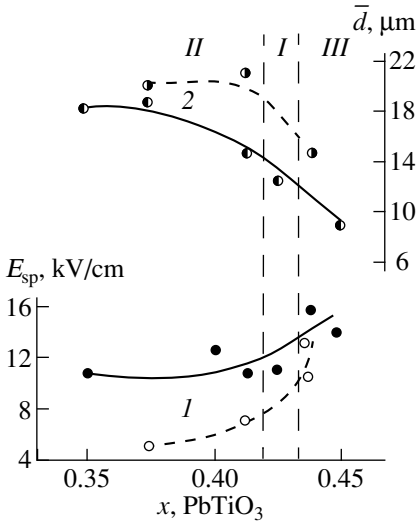

Fig. 2. The dependence of (*1*) the space charge field and (*2*) the crystallite size on the $PbTiO_3$ content in one of the rays of the $PbTiO_3$–$PbZrO_3$–$PbNb_{2/3}Mn_{1/3}O_3$–$PbW_{1/2}Mg_{1/2}O_3$ system: *I*, morphotropic region; *II*, rombohedral phase; *III*, tetragonal phase.

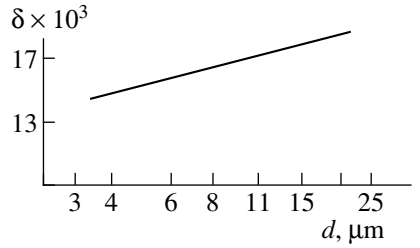

Fig. 3. The uniform deformation parameter δ as a function of the crystallite size for one composition of the $PbTiO_3$–$PbZrO_3$–$PbNb_{2/3}Mn_{1/3}O_3$–$PbNb_{2/3}Zn_{1/3}O_3$ system, prepared under different conditions [4].

Figure 2 gives two parameters E_{sp} (*1*) and $\bar{d}$ (*2*) as functions of the $PbTiO_3$ content in one of the rays of the $PbTiO_3$–$PbZrO_3$–$PbNb_{2/3}Mn_{1/3}O_3$–$PbW_{1/2}Mg_{1/2}O_3$ system. The results of measurements by the method 1 are indicated by the solid line, and those by the method 2, by the broken line. A considerable difference is observed between the values of space charge field intensity measured by the first and second methods in the case of rombohedral (*II*) compositions, and their convergence for a tetragonal (*III*) composition. The data of Fig. 2 indicate that an increase of the $PbTiO_3$ concentration has opposite effects on the variation of the space charge field and on that of the mean crystallite size. A qualitative agreement is observed with the behavior of the dependence of the space charge field on the mean crystallite size in the case A.

Also determined is the correlation between the crystallite size $\bar{d}$ and the uniform parameter δ of spontaneous deformation of crystal cell [5]. This correlation proves to be different for the cases A and B being treated. In the former case, these parameters ($\bar{d}$ and δ) depend directly on one another, and in the latter case, inversely. This is demonstrated in Fig. 3 (case A) and Fig. 4 (case B). The direct dependence of the quantity δ on $\bar{d}$ in the case A may be attributed to the fact that, as the crystallite size decreases, internal stresses arise in one and the same composition, which suppress spontaneous deformation. The concentration dependences of δ and $\bar{d}$ given in Fig. 4 for the binary $(1 - x)NaNbO_3$–$xPbTiO_3$ system were analyzed in detail in [6]. We will only note here the opposite behavior of their variation with increasing x. The above-mentioned inverse correlation between the quantities being treated in the case B is attributed to the increase, with an increase of spontaneous deformation (upon variation of the composition), of internal stresses impeding the crystallite growth during sintering. It would seem that the size of crystallites forming at high temperatures during the sintering of ferroceramic cannot be affected by the degree of spontaneous deformation arising at a much lower temperature of ferroelectric phase transition. However, it must be taken into account that this transition occurs twice: during the heating of synthesized powder and during the cooling of sintered ceramic. Even during heating, spontaneous deformation occurs in the ferroelectric case, which later disappears, but develops internal stresses the memory of which persists at high temperatures as well, i.e., during the crystallite formation. Therefore, it appears that in the case A the crystallite size $\bar{d}$ is primary, which defines the uniform deformation parameter δ, and in the case B spontaneous deformation is primary, which defines the mean crystal size.

We will briefly dwell on the correlation between the above-described parameters E_{sp}, δ, and $\bar{d}$ and other parameters of ferropiezoceramic in the simpler case A, when spontaneous deformation increases with the mean crystallite size (Fig. 3). At the beginning, the variation of another structure parameter η (Fig. 5) representing the degree of domain reorientations in the process of polarization is the same [7], because the increase of the crystallite size and, consequently, the decrease of the space charge field facilitate the rear-

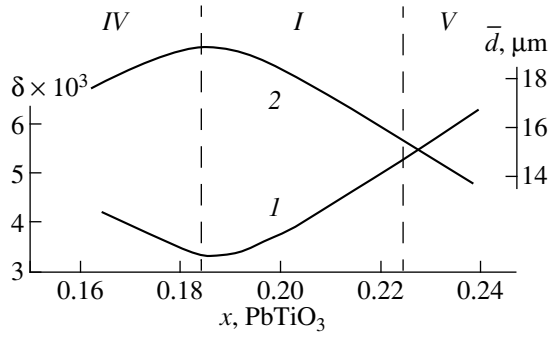

Fig. 4. The dependence of (*1*) the uniform deformation parameter δ and (*2*) the crystallite size $\bar{d}$ on the $PbTiO_3$ content in the $(1-x)NaNbO_3$–$xPbTiO_3$ system (*I*, morphotropic region; *IV* and *V*, monoclinic and pseudotetragonal phases, respectively) [6].

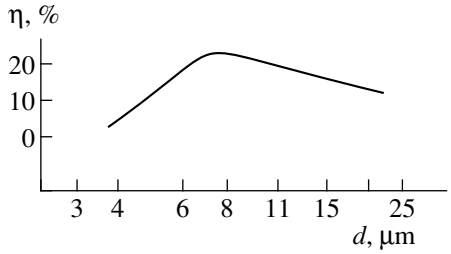

Fig. 5. The degree η of domain reorientations in the process of polarization as a function of the crystallite size for one composition of the $PbTiO_3$–$PbZrO_3$–$PbNb_{2/3}Mn_{1/3}O_3$–$PbNb_{2/3}Zn_{1/3}O_3$ system [4].

rangement of the domain structure as a result of external effects. However, the degree of domain reorientations increases only up to a certain level of increasing $\bar{d}$ and decreasing E_{sp}, after which it starts decreasing to form a maximum. This decrease of η may be attributed to a deceleration of the drop of the space charge field and of the effect made in this case on η by increasing spontaneous deformation (Figs. 1, 3, 5). Three generalized parameters E_{sp}, η, and δ being treated help explain the dependence of other electrophysical characteristics on the crystallite size. The dielectric permittivity $\varepsilon_{33}^T/\varepsilon_0$ decreases with increasing $\bar{d}$ and, consequently, δ, as a result of the existing inverse correlation between $\varepsilon_{33}^T/\varepsilon_0$ and δ. As to the remanent reorientation polarization P_r and the dependent piezoelectric parameters g_{ij}, K_{ij}, and d_{ij}, they are affected mostly by the value of η and pass through a maximum when the crystallite size corresponds to the maximum value of η. This crystallite size defines the piezoelectric parameters which are optimal for numerous applications.

CONCLUSIONS

The effect of the space charge field and of the crystallite size on the properties of ferropiezoceramic solid solutions is investigated for two cases, namely, case A for one and the same composition prepared under different conditions, and case B for different compositions of solid solutions with varying concentration of the components. It is demonstrated that in the case A, the crystallite size which defines spontaneous deformation is primary, and in the case B, spontaneous deformation which defines the mean crystallite size is primary.

The correlation is found between the structure and electrophysical parameters, the space charge field, and the crystallite size, which may be useful in designing ferropiezoceramic materials for different applications and devices involving such materials.

REFERENCES

1. A. L. Khodakov and V. Z. Borodin, Izv. Vyssh. Uchebn. Zaved. Élektromekh., No. 11, 1280 (1962).
2. K. Okazaki, *Ceramic Dielectric Technology* (Énergiya, Moscow, 1976).
3. K. Okazaki and K. Nagata, J. Am. Ceram. Soc. **56**, 82 (1973).
4. T. V. Rogach, S. V. Gavrilyachenko, L. D. Grineva, *et al*., Diélektr. Poluprovodn. **20**, 43 (1981).
5. E. G. Fesenko, V. S. Filip'ev, and M. F. Kupriyanov, Fiz. Tverd. Tela (Leningrad) **11** (2), 466 (1969) [Sov. Phys. Solid State **11**, 366 (1969)].
6. L. A. Reznichenko, A. Ya. Dantsiger, O. N. Razumovskaya, *et al*., in *Proceedings of International Conference on Fundamental Problems of Piezoelectronics "P'ezoteknika-95."* (Kniga, Rostov-on-Don, 1995), Vol. 2, pp. 13–32.
7. E. G. Fesenko, A. Ya. Dantsiger, and O. N. Razumovskaya, *New Piezoceramic Materials* (Rostov. Univ., Rostov-on-Don, 1983), p. 156.

Translated by Henri A. Bronstein

Technical Physics, Vol. 45, No. 5, 2000, pp. 566–570. Translated from Zhurnal Tekhnicheskoĭ Fiziki, Vol. 70, No. 5, 2000, pp. 43–47.

SOLIDS

Dynamics of Fluxons in Josephson Junctions under the Noise Current Action

F. Kh. Abdullaev, M. R. Jumaev, and É. N. Tsoĭ

Physicotechnical Institute, Academy of Sciences of Uzbekistan, Mavlyanova ul. 2B, Tashkent, 700084 Uzbekistan

Received February 25, 1999

Abstract—The motion of magnetic flux quanta (fluxons) in long Josephson junctions (LJJ) under action of direct and random currents is under investigation. The velocity distribution function of fluxons is calculated which, even in the absence of the direct current component, is non-Gaussian. As a consequence, the current–voltage characteristic of a noise junction differs from that for a regular one. The dependence of the voltage difference on the current for junctions, both with and without the noisy current component, is shown to be nonmonotonic. There is a good agreement between the calculation data and the numerical simulation results. *© 2000 MAIK "Nauka/Interperiodica".*

In recent years, the dynamics of the magnetic flux quanta (fluxons) in long Josephson junctions (LJJ) has been actively studied (for example, [1–3]). This is explained by both the possibility of verifying predictions of nonlinear waves theory and the prospects for developing novel electronic devices. In a recent study [4], in addition, it was shown that there was a Josephson coupling between layers of a crystal in high temperature superconductors. Therefore, the results of LJJ investigations may be useful in analyzing the properties of new superconductors as well.

In this paper, the influence of a random current on fluxon parameters is under investigation. This problem is closely related to that of the behavior of fluxons placed in a thermostat. A number of studies [5–7] was devoted to consideration of this issue. In particular, it has been shown that the average kinetic energy of a fluxon is equal to $\frac{1}{2}k_BT$ and the single phonon mode energy corresponds to k_BT, where k_B is the Boltzmann constant and T is the temperature of a system. In experiments, the effect of fluctuations may be observed by the radiation spectrum at the end of a Josephson junction. For an ideal junction, the radiation frequency is determined by the ratio $u/(2L)$, where u is the fluxon velocity, and L is the length of a junction. The occurrence of noises leads to a random addition to the velocity and, as a result, to the spectrum line broadening. The spectral characteristics were calculated in [5, 6]. Note that in the studies mentioned above, the case of small fluxon velocities was mainly considered. It was revealed in the experiments [8] that the resonance-line broadening of the order of several tens of kilohertz at a frequency of 10 GHz agreed with the calculation results. An investigation of the fluctuation effect on the dynamics of the bound states of fluxons in multilayered LJJ was performed in [9]. The distribution function for fluxon-pair parameters was found.

We calculated the distribution function (DF) for arbitrary velocities ($|u| < 1$) which was, in general, non-Gaussian. This fact is significant, since its neglecting leads to misinterpretation and disagreement of the theoretical results and (numerical) experiments by an order of magnitude and more (see, e.g., [10]). On the basis of the DF, we calculated the current–voltage characteristic (CVC) of a junction. The given dependency is compared with the CVC of a noise-free junction. The dependence of the voltage difference on the current is shown to have a nonmonotonic character. In the case of small noise intensities, the position of the maximum is independent of parameters of the random current component. A comparison of these dependencies with the results of the numerical investigations provides satisfactory agreement. The numerical calculation also shows that, when the fluxon velocity approaches the Swihart velocity, new excitations (breathers, fluxon–antifluxon pairs) are generated, resulting in a significantly modified dynamics of a system [1, chapter 15].

The dynamics of fluxons in LJJs, in most experimental cases, is well described by the sine-Gordon (SG) equation [1],

$$\varphi_{tt} - \varphi_{xx} + \sin\varphi = -\alpha\varphi_t + \beta\varphi_{xxt} - \gamma(t), \qquad (1)$$

where φ is the phase difference of the wave functions of superconducting layers, α and β are the dissipation coefficients, and γ is the bias current density.

The spatial variable x is directed along the junction and normalized to the Josephson penetration depth λ_j. Time t is measured in units of ω_p^{-1} [1], where ω_p is the plasma frequency of the junction. The current is normalized to the value of the critical current in the junc-

1063-7842/00/4505-0566$20.00

tion. In what follows, the parameters α, β, and γ are regarded to be small.

In an unperturbed system ($\alpha = \beta = \gamma = 0$), a fluxon is described by the kink solution of the SG equation,

$$\varphi = 4\arctan[\exp((x - ut)/\sqrt{1 - u^2})], \qquad (2)$$

where u is the fluxon velocity.

To analyze the fluxon motion under the action of dissipation and bias currents, we use the adiabatic perturbation theory for the SG equation [11]. Then the velocity obeys an equation of the form

$$\frac{du}{dt} = -\alpha u(1 - u^2) - \frac{\beta}{3}u + \frac{\pi\gamma(t)}{4}(1 - u^2)^{3/2}. \qquad (3)$$

Since the perturbation associated with a random force does not vanish at infinity in (1), it is necessary to perform renormalization in order to satisfy this condition [12]. Physically, this fact means that the noise influences a fluxon via induced oscillations of the homogeneous state. Here, a change of fluxon parameters, due to emission of linear waves, is neglected as well. As will be shown below, however, for small noise intensities, the approach used in the paper is in good agreement with the numerical calculation results. The bias current will be assumed to consist of the direct and random current components,

$$\gamma(t) = \gamma_0 + f(t). \qquad (4)$$

The random function $f(t)$ is assumed to be the delta-correlated Gaussian noise with the following characteristics:

$$\langle f(t)\rangle = 0, \quad \langle f(t)f(t')\rangle = 2\sigma_\gamma^2\delta(t - t'). \qquad (5)$$

Note that a random force is involved in equation (3) multiplicatively, but transformation to momentum variables ($u = p/\sqrt{1 + p^2}$) makes it possible to derive an equation with the additive noise,

$$\frac{dp}{dt} = -\alpha p - \beta p(1 + p^2)/3 + \pi\gamma(t)/4, \qquad (6)$$

which describes the Langevin model at $\beta = 0$.

By using stochastic equation (6), it is easy to obtain the Fokker–Planck equation for the DF. Applying well-known methods for solving this equation (e.g., [13]), we find the DF fluxons in momentum:

$$F(p) = C\exp\left\{\frac{1}{\sigma^2}\left[\frac{\pi\gamma_0}{4}p - \frac{\alpha}{2}p^2 - \frac{\beta}{12}(2p^2 + p^4)\right]\right\}, \qquad (7)$$

where $\sigma^2 = (\pi/4)^2\sigma_\gamma^2$, and the constant C is determined from the normalization condition:

$$\int_{-\infty}^{\infty} F(p)dp = 1.$$

It is seen that the allowance for the dissipation β caused by the quasi-particle current in superconducting electrodes leads to the situation when both the momentum and velocity DFs become non-Gaussian. It follows that the average and the most probable values of the fluxon momentum do not coincide, and statistical moments of the second or higher order are not zero.

Let us now analyze various interesting physical situations. For simplicity, we suggest the parameter $\beta = 0$. Then the momentum DF takes the form ($-\infty < p < \infty$)

$$F(p) = \sqrt{a/\pi}\exp[-a(p - b)^2], \qquad (8)$$

where the parameters a and b are expressed by the formulas $a = \alpha/(2\sigma^2)$ and $b = \pi\gamma_0/(4\alpha)$, respectively.

The quantities $a^{-1/2}$ and b can be considered as the characteristic momentum values associated with the random and direct current components, correspondingly.

By using equation (8), one can determine the average fluxon velocity of $\langle u\rangle = \langle p/\sqrt{1 + p^2}\rangle$. Let us write the asymptotic dependencies for small noise intensities, i.e., at $a \gg 1$, and for $\sqrt{a}\,b \ll 1$ corresponding to an intense noise or small direct current values,

$$\langle u\rangle = \frac{b}{\sqrt{1 + b^2}}\left[1 - \frac{3}{4a(1 + b^2)^2}\right] \quad \text{at} \quad a \gg 1, \qquad (9)$$

$$\langle u\rangle = \sqrt{\frac{a\exp(a)}{\pi}}b\exp(-ab^2)[4K_1(a/2) + a(K_1(a/2) - K_2(a/2))] \quad \text{at} \quad \sqrt{a}b \ll 1, \qquad (10)$$

where $K_1(\mu)$ and $K_2(\mu)$ denote the modified Hankel functions.

Normalized voltage U across a Josephson junction is proportional to the average fluxon velocity $U \equiv \langle\varphi_t\rangle = 2\pi\langle u\rangle/L$, where the brackets $\langle\ldots\rangle$ denote the average over time and coordinate, and L is the junction length. Since the characteristic time of the system is $\omega_p \sim 10^{11}$ s^{-1}, the voltage determined in an experiment corresponds to the value averaged over a large time interval. Therefore, equations (9) and (10) can be considered as the voltage–current characteristics of the junction. For small noise intensities, which is the case in our consideration, the CVCs of the noise and noise-free junctions do not differ qualitatively. In both cases, a monotonic voltage rise takes place as the current γ_0 increases. However, as is seen from (9), there is an interesting feature at $a \gg 1$. It is known that the fluxon velocity (normalized voltage) in LJJ with the noise-free direct current is defined by the relationship $u_d = b/(1 + b^2)^{1/2}$. Consider the velocity difference $\Delta u = u_d - \langle u\rangle$. Then from (9), we derive that the dependence Δu on current γ_0 has a maximum, the position of which is independent

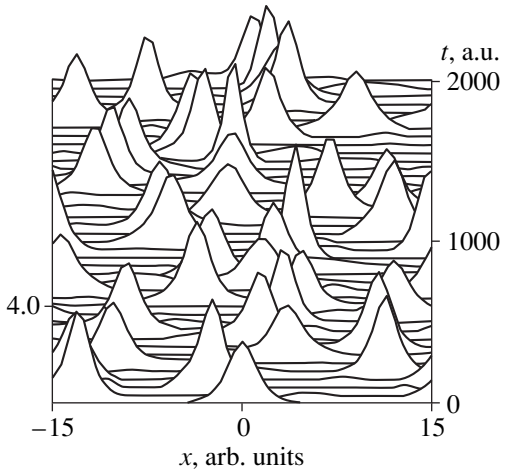

Fig. 1. The dependence $\varphi_x(x, t)$ for $\sigma_x = 0.1$, $\gamma_0 = \gamma_m = 0.0318$.

of the parameters of the random current and defined by the condition $|b_m| = 1/2$ or $|\gamma_m| = 2\alpha/\pi$. At this value, the maximal difference is $\Delta u(\gamma_m) = 12\sqrt{5}/(125a)$. We emphasize that this distinction of CVC is not obvious. Indeed, it follows from (8) that the average momentum and fluxon momentum in a regular system are equal $\langle p \rangle = p_d = b$. Because of the nonlinear dependence of $u(p)$, however, the DF for u is no longer Gaussian, resulting in a modified CVC.

To verify the results obtained, we performed the numerical simulation of stochastic equations (1) and (6). A conventional method of transformation of the uniform distribution was used for the generation of white noise. For equation (1), we employed a 3-layer and 5-point scheme with the spatial $\Delta x = 0.05$ and temporal $\Delta t = 0.02$ steps. For integrating equation (6), we used the Runge–Kutta method of the 7th order. The calculation was performed for two values of the variance $\sigma_\gamma = 0.05$ and 0.1, and the parameters α and β were equal to 0.05 and 0, respectively. The reduced current γ varied within the range from 0 to 0.5. Fig. 1 shows the evolution of a fluxon under the noise action. The amplitude of radiated linear waves is seen to be small as compared with the fluxon amplitude. It is also important that there is a single fluxon in the system at each instant of time. Thus, the adiabatic approach used in the paper is correct in the given range of the parameters. In Fig. 2, the DF derived from the simulation (6) is compared with the analytical function that is found from (8) and the relationship $F(u) = F(p)|dp/du|$. As is seen, the DF for u, which is constructed over 1000 realizations, has a pronounced asymmetric character. Fig. 3 shows the dependence of the voltage difference on the direct current. When numerically calculating equation (6), we measured the instantaneous velocity which was averaged over 1000 realizations. When integrating the equation SG (1), we determined the mean velocity in the interval $T = 1000$, which was then averaged over 20 realizations. Note that noticeable fluctuations of the voltage difference for each realization were observed. From this fact, it follows that the measurement time must be long enough for obtaining such a dependence in an actual experiment. Fig. 3 also presents analytically calculated and numerically simulated CVCs. We see that the numerical results for (1) and (6) are, as a whole, in qualitative agreement. They are in agreement with the calculated dependencies (9) and (10) as well. It is seen that the positions of maxima in the function $\Delta u(\gamma)$ is approximately the same and independent of the

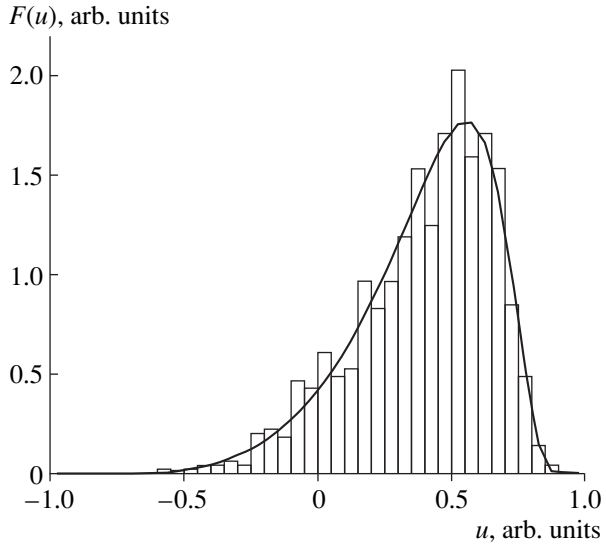

Fig. 2. The velocity distribution function. The parameters are the same as in Fig. 1; the curve and the histogram are the theoretical (8) and numerical calculations, respectively.

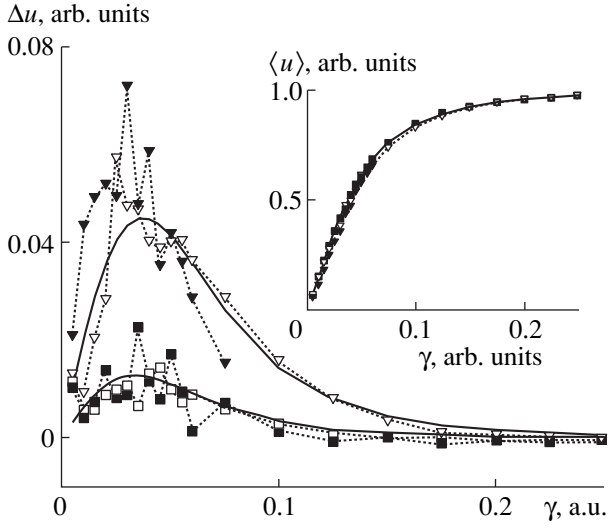

Fig. 3. The dependence Δu on γ. The analytically and numerically calculated CVCs are shown in the insert. Solid lines are the theory and the filled and hollow signs are the numerical calculations obtained from (1) and (6), respectively; σ_γ: (□) 0.1 and (▽) 0.05.

noise intensity. At a small direct current, the dominant role in fluxon dynamics is played by the random current component, which explains noticeable fluctuations in the given range. Note that at higher noises (e.g., $\sigma_\gamma > 0.1$ for $\alpha = 0.05$), other nonlinear modes are excited in the system and the adiabatic approach becomes invalid. In numerical calculations, the emergence of new modes was detected by both a change in the $\varphi(x, t)$ profile and a sharp increase in the voltage across a junction.

Now, consider the case when the direct current is absent, $\gamma_0 = 0$. In this case, the average fluxon velocity and, consequently, the voltage are zero. In the experiments, however, it is quite possible to measure the absolute voltage value or the squared voltage. In this case, the dynamics is completely determined by the random current and the noise characteristics, in particular σ_γ, can be found immediately. The velocity distribution function has the form ($\gamma_0 = 0$),

$$\Phi(u) = \sqrt{a/\pi}(1-u^2)^{-3/2}\exp[-au^2/(1-u^2)]. \quad (11)$$

Using DF (11), we obtain the following expression for the mean square velocity of a fluxon:

$$\langle u^2\rangle = 1 - \sqrt{\pi a}\exp(a)\mathrm{erfc}(\sqrt{a}) \equiv 1 - \sqrt{\pi a}\langle |u|\rangle, \quad (12)$$

where erfc(x) is the additional error function.

We see that in the limit of strong fluctuations, formula (12) gives finite values of $\langle u^2\rangle$, whereas the classical consideration leads to an infinite rise of the mean square velocity. In Fig. 4, the analytical and numerical dependencies of $\langle |u|\rangle$ on σ_γ are presented, which were calculated by using expressions (12) and (6), respectively. The comparison of these dependencies shows their good agreement. This curve can be considered as the noisy CVC, which enables one to determine the parameters of the random current. The curve corresponds to the dependence with the use of the Gaussian distribution function $\Phi_{cl}(u) = \sqrt{a/\pi}\exp[-au^2]$, which is valid only at small velocities. In Fig. 5, the DF obtained numerically is compared with the dependencie (11) and $\Phi_{cl}(u)$. We see that the DF is non-Gaussian, which is similar to the case of $\gamma \neq 0$. This is especially noticeable at large velocities. Note that $\Phi(u)$ corresponding to a strong noise in the interval $0 < a < 3/2$ has two maxima positioned symmetrically relative to the origin of coordinates, whereas at $a > 3/2$, there is a single maximum at $u = 0$. The quantity $a = 3/2$ can be considered as the threshold value separating strong and small fluctuations.

Thus, in the present paper, we have found the momentum fluxon distribution function. On its basis, the CVC of the noisy junction is calculated. Nonmonotonic character of the dependence of the voltage difference on direct current is shown. The possibility of determining the noise signal parameters by measuring the absolute value or the square of voltage is demonstrated. The results of this study can also be used in the case of multimode laser excitation rather than a random perturbation.

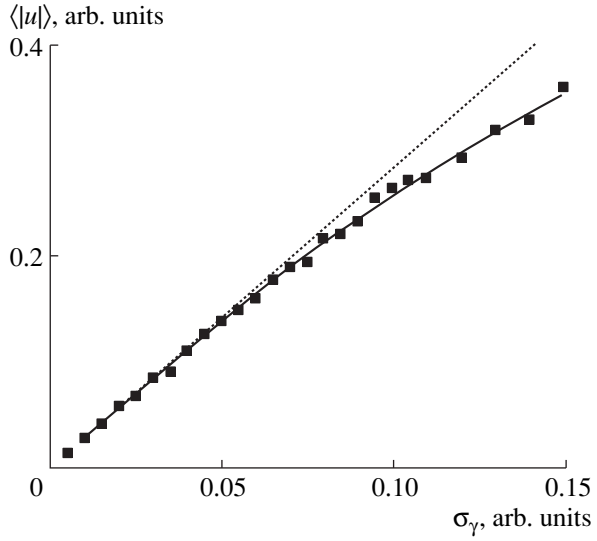

Fig. 4. The dependence of the absolute fluxon velocity on σ_γ: (■) the numerical calculation using equation (6); the solid line is the analytical calculation using equation (12); and the dotted line is the absolute velocity $\langle |u_{cl}|\rangle$ obtained from the Gaussian DF.

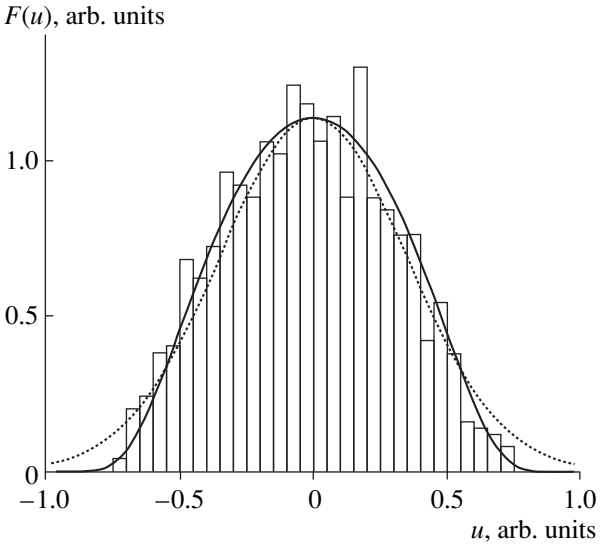

Fig. 5. The velocity distribution function $\Phi(u)$ for $\sigma_x = 0.1$ and $\gamma_0 = 0$. The solid line is the theory (11), the dotted line is $\Phi_{cl}(u)$, and the histogram is the numerical calculation using (6).

ACKNOWLEDGMENTS

The authors acknowledge the U.S. Civilian Research and Development Foundation (grant no. ZM1-342) and the Foundation for Basic Research GKNT (grant no. 21/98) for their partial support of these investigations. We are grateful to the coworkers of the Labora-

tory of Solid-State and Semiconductor Theory of the Physicotechnical Institute (Academy of Sciences of Uzbekistan) for useful discussions.

REFERENCES

1. K. K. Likharev, *Introduction to the Dynamics of Josephson Contacts* (Nauka, Moscow, 1985).
2. N. F. Pedersen and A. V. Ustinov, Supercond. Sci. Technol. **8**, 389 (1995).
3. R. D. Parmentier, in *Proceedings of the Workshop "Nonlinear Physics: Theory and Experiment,"* Ed. by E. Alfinito, M. Boiti, L. Martina, and F. Pempinelli (World Scientific, Singapore, 1996), p. 582.
4. R. Kleiner and P. Müller, Phys. Rev. B **49**, 1327 (1994).
5. D. J. Kaup, Phys. Rev. B **27**, 6787 (1983).
6. M. Salerno, E. Joergensen, and M. R. Samuelsen, Phys. Rev. B **30**, 2635 (1984); M. Salerno, M. R. Samuelsen, and H. Svensmark, Phys. Rev. B **38**, 593 (1988).
7. F. G. Bass, V. V. Konotop, and Yu. A. Sinitsin, Zh. Éksp. Teor. Fiz. **38**, 541 (1985) [Sov. Phys. JETP **61**, 318 (1985)].
8. E. Joergensen, V. P. Koshelets, R. Monaco, *et al.*, Phys. Rev. Lett. **49**, 1093 (1982).
9. F. Kh. Abdullaev, D. N. Navotny, and B. A. Umarov, Phys. Lett. A **244**, 155 (1998).
10. F. If, P. L. Christiansen, R. D. Parmentier, O. Skovgaard, *et al*., Phys. Rev. B **32**, 1512 (1985).
11. V. I. Karpman and E. M. Maslov, Zh. Éksp. Teor. Fiz. **73**, 537 (1977) [Sov. Phys. JETP **46**, 281 (1977)]; D. W. McLaughlin and A. C. Scott, Phys. Rev. A **18**, 1652 (1978).
12. O. H. Olsen and M. R. Samuelsen, Phys. Rev. Lett. **48**, 1569 (1982).
13. N. G. van Kampen, *Stochastic Prosesses in Physics and Chemistry* (North-Holland, Amsterdam, 1992; Mir, Moscow, 1994).

Translated by Yu. Vishnyakov

Technical Physics, Vol. 45, No. 5, 2000, pp. 571–573. Translated from Zhurnal Tekhnicheskoĭ Fiziki, Vol. 70, No. 5, 2000, pp. 48–50.

SOLIDS

Differential Conductivity at the Transverse Runaway of Hot Electrons

Z. S. Kachlishvili, N. K. Metreveli, and F. G. Chumburidze

Dzhavakhishvili State University of Tbilisi, pr. Chavchavadze 3, Tbilisi, 380028 Georgia

Received February 19, 1999

Abstract—Differential conductivity under the transverse runaway of hot electrons is investigated. Quasi-elastic scattering and electronic-temperature approximations are considered for equilibrium and heated phonon subsystem. In both approximations, the differential conductivity is shown to tend to infinity, keeping the sign. Phonon heating retards transverse runaway. © *2000 MAIK "Nauka/Interperiodica".*

1. In the case of runaway hot electrons, the problem arises of how to keep such a state stationary. The behavior of differential conductivity may unambiguously tackle the question. However, as far as we know, the general relation between the transverse runaway of hot electrons and differential conductivity has not been found. We believe that there is no such a parameter that fully characterizes the differential conductivity, on the one hand, and the behavior of runaway hot electrons on the other. We mean the following. For example, according to [1], different runaway modes in the quasi-elastic scattering approximation are defined by the asymptotic behavior of the heating function (the function determining the degree of electron heating), but the differential conductivity does not depend on this function. If the runaway is related to the overheating mechanism of scattering [2], the differential conductivity depends on the electronic temperature, but the latter cannot be uniquely determined under runaway. It is known only that, under the runaway, the electronic temperature (corresponding to the distribution function) becomes too large and cannot provide the finiteness of some macroparameters of the system (for example, average energy). However, the "too large" increase of the electronic temperature is "sensed" by various macroparameters in quite a different way due to different energy dependences of values to be averaged.

The effect of transverse runaway (TR) of hot electrons seems to be the exception in this sense. In fact, by definition, TR is an effect taking place under open-circuit conditions (open Hall contacts) for a certain combination of momentum and energy scattering mechanisms. It is significant that TR is observed only at a specific threshold value of an applied electric (or magnetic) field when the inner (heating) field, or electron temperature, tends to infinity [3–5]. This allows us to investigate the differential conductivity at TR of hot electrons and, thus, gain an idea of the nonlinearity of the current–voltage characteristic (CVC), i.e., to find necessary conditions for the CVC to be S- or N-shaped. It will be shown below that the differential conductivity in this case depends on the inner field, or electronic temperature. In this paper, we report the results of such an investigation. The influence of phonon heating on the differential conductivity is also discussed.

2. Consider a rectangular piece of a semiconductor. Let electric field E_x and current j_x be parallel to the x-axis and magnetic field H, to the z-axis. Under the open-circuit conditions, the Hall field is determined from the equality $j_y = 0$. Then, using the energy equation to exclude dZ_0/dE_x from the expression for differential conductivity σ_d, one comes to the well known expression [6]

$$\sigma_d = \sigma \frac{\dfrac{d\ln(P\sigma)}{dZ_0}}{\dfrac{d\ln\left(\dfrac{P}{\sigma}\right)}{dZ_0}}. \qquad (1)$$

In this case, σ is given by

$$\sigma = \sigma_0 \frac{\mu_1}{\mu_0}\left(1 + \frac{\mu_2^2}{\mu_1^2}\right). \qquad (2)$$

Here, μ_1 and μ_2 are the transverse and longitudinal mobilities, $Z_0 \equiv E$ is the inner field in the quasi-elastic scattering approximation, $Z_0 \equiv \Theta \equiv T_e/T$ (T_e and T are the electronic and lattice temperatures, respectively) is that in the electronic temperature approximation, and

$$\frac{\mu_1}{\mu_0} = \frac{\Gamma(3/2)}{\Gamma((t+5)/2)}\frac{I_1}{I_0}, \quad \frac{\mu_2}{\mu_0} = \frac{\Gamma(3/2)}{\Gamma(t+5/2)}\sqrt{\eta}\frac{I_2}{I_0}, \qquad (3)$$

where

$$I_1 = \int_0^\infty \left(-\frac{\partial f_0}{\partial x}\right)\frac{x^{\frac{t+3}{2}}}{1+\eta x^t}dx, \qquad (4)$$

1063-7842/00/4505-0571$20.00 © 2000 MAIK "Nauka/Interperiodica"

$$I_2 = \int_0^\infty \left(-\frac{\partial f_0}{\partial x}\right)\frac{x^{\frac{2t+3}{2}}}{1+\eta x^t}dx, \quad (5)$$

$$I_0 = \int_0^\infty x^{1/2} f_0 dx; \quad (6)$$

σ_0, and μ_0 are the conductivity and mobility in a weak electric field, $\Gamma(t)$ is the gamma-function, and f_0 is a nonequilibrium distribution function.

We assume that the energy dependences of the free paths for momentum, l, and energy, $\tilde{l}$, can be expressed as

$$l = l_0 x^{\frac{1+t}{2}}, \quad \tilde{l} = \tilde{l}_0 x^{\frac{1+s}{2}}. \quad (7)$$

The values of t and s for all known scattering mechanisms are presented in [7]; also,

$$\eta \equiv \left(\frac{H}{H_0}\right)^2, \quad H_0 \equiv \frac{(2mc^2 k_0 T)^{1/2}}{e l_0}.$$

Here, e and m are the charge and effective mass of an electron and k_0T is the thermal energy. In formula (1), P is the power transported by hot electrons to the lattice [6]:

$$P \equiv P_0(T)\frac{\frac{2}{3}\langle x\rangle - 1}{\langle \tau_e\rangle}, \quad (8)$$

where $P_0(T) \equiv nk_0T$, n is the free-electron concentration, $x \equiv \varepsilon/(k_0T)$ is the dimensionless energy, τ_e is the energy relaxation time, and the symbol $\langle\ldots\rangle$ means averaging over the nonequilibrium distribution function.

3. Consider the quasi-elastic hot-electron scattering approximation. Since analytical expressions can be derived only for strong and weak fields under strong heating, the corresponding nonequilibrium distribution functions can be written in the compact form

$$f_0(x) = N\exp\left(-\frac{\eta^\zeta x^\xi}{\alpha\,\xi}\right), \quad \xi \neq 0, \quad (9)$$

where N is a normalizing factor,

$$\xi = \xi_1 \equiv 1 - \frac{t+s}{2}$$

and $\zeta = 0$ in the weak magnetic field $\eta(\langle x\rangle)^t \ll 1$,

$$\xi = \xi_2 \equiv 1 + \frac{t-s}{2}$$

and $\zeta = 1$ in the strong magnetic field $\eta(\langle x\rangle)^t \gg 1$, and

$$\alpha = \left(\frac{E}{E_0}\right)^2, \quad E_0 = \frac{\sqrt{3}k_0T}{e(l_0\tilde{l}_0)^{1/2}}.$$

A similar consideration of the weak and strong magnetic fields in (4) and (5) results in the expressions for I_1 and I_2:

$$I_i = \frac{1}{\eta^\zeta}\int_0^\infty \left(-\frac{\partial f_0}{\partial x}\right)x^{\beta i}dx; \quad i = 1, 2. \quad (10)$$

At $i = 1$, $\beta_1 \equiv (t+3)/2$ and $\zeta = 0$ in the weak magnetic field and $\beta_1 \equiv (3-t)/2$ and $\zeta = 1$ in the strong magnetic field.

At $i = 2$, $\beta_2 \equiv (2t+3)/2$ and $\zeta = 0$ in the weak magnetic field and $\beta_2 \equiv 3/2$ and $\zeta = 1$ in the strong magnetic field.

The calculation of μ_1 and μ_2 in view of (9) and (10) and also $\langle x\rangle$ and $\langle\tau_e\rangle$ gives for conductivity (2) and transmitted power (8)

$$\frac{\sigma}{\sigma_0} = a_0\eta^{\frac{3-2\beta_1-2\xi}{2\xi}\zeta}\alpha^{\frac{2\beta_1-3}{2\xi}} \times\left[1+\frac{\Gamma^2\left(\frac{\beta_2}{\xi}+1\right)}{\Gamma^2\left(\frac{\beta_1}{\xi}+1\right)}(\xi\alpha)^{\frac{2(\beta_2-\beta_1)}{\xi}}\eta^{\frac{\xi+2\zeta(\beta_1-\beta_2)}{\xi}}\right], \quad (11)$$

$$a_0 \equiv \frac{\Gamma\left(\frac{3}{2}\right)\Gamma\left(\frac{\beta_1}{\xi}+1\right)\xi^{\frac{2\beta_1+2\xi-3}{2\xi}}}{\Gamma\left(\frac{t+5}{2}\right)\Gamma\left(\frac{3}{2\xi}\right)},$$

$$\frac{P}{P_0} = \frac{\frac{2}{3}\left(\frac{\alpha\xi}{\eta^\zeta}\right)^{\frac{1}{\xi}}\Gamma\left(\frac{5}{2\xi}\right)-\Gamma\left(\frac{3}{2\xi}\right)}{\tau_0\left(\frac{\alpha\xi}{\eta^\zeta}\right)^{\frac{s}{2\xi}}\Gamma\left(\frac{s+3}{2\xi}\right)}. \quad (12)$$

Taking into account (11) and (12), one obtains the explicit dependence of σ_d on E. It is too cumbersome and is omitted.

At TR, the inner field was noted to tend to infinity. Hence, proceeding to the limit $E \longrightarrow \infty$ and taking into account that always $\beta_2 - \beta_1 = t/2$ and $t > 0$ [3–5], we have for differential conductivity

$$\frac{\sigma_d}{\sigma} = \frac{1+t+\frac{1}{2}(2\beta_1-3-s)}{1-t-\frac{1}{2}(2\beta_1-3+s)}. \quad (13)$$

In the weak magnetic field, $2\beta_1 = t+3$ and

$$\frac{\sigma_d}{\sigma} = \frac{2+3t-s}{2-3t-s}. \quad (14)$$

As follows from this expression, $\sigma_d = \infty$ at $3t + s = 2$, which corresponds to TR in the weak magnetic field [4]. The numerator is other than zero, for $t > 0$ under TR [3, 4].

In the strong magnetic field, $2\beta_1 = 3 - t$ and

$$\frac{\sigma_d}{\sigma} = \frac{2 + t - s}{2 - t - s}. \quad (15)$$

Here, $\sigma_d = \infty$ at $t + s = 2$ and the numerator is also nonzero. As is known [3, 4], this is the second possible combination of scattering mechanisms for which TR in a strong electric field is observed.

4. Consider now the electronic-temperature approximation. In this case, the nonequilibrium distribution function can be changed to

$$f_0 = Ne^{-\frac{x}{\Theta}}. \quad (16)$$

Calculating I_i, $\langle x \rangle$, and $\langle \tau_e \rangle$ with (16), we have for the conductivity and transmitted power

$$\frac{\sigma_d}{\sigma} = \frac{\Gamma(\beta_1 + 1)}{\Gamma\left(\frac{t+5}{2}\right)} \frac{\Theta^{\left(\beta_1 - \frac{3}{2}\right)}}{\eta^{\zeta}} \left[1 + \eta \frac{\Gamma^2(\beta_2 + 1)}{\Gamma^2(\beta_1 + 1)} \Theta^{2(\beta_2 - \beta_1)}\right] \quad (17)$$

and

$$P(\Theta) = P'\Theta^{\gamma}(\Theta - 1), \quad (18)$$

where $\gamma = -(s/2)$ and $P' = P_0(T)$ in the presence of equilibrium phonons and $\gamma = \alpha$ and $P' = P_{fl}(T)$ under phonon heating.

It should be noted that the nonequilibrium distribution functions for hot electrons and phonons are derived by solving a set of Boltzmann kinetic equations for electrons and phonons. However [8], this problem is greatly simplified if distribution functions for electron and phonon subsystems are approximated by the Maxwell and Planck functions, respectively, with the same effective temperature equal to the electronic temperature Θ. In this case, we arrive at a single equation for Θ instead of a set of energy equations. Thus, heated electrons and long-wavelength phonons have the same temperature. The latter, in turn, transfer the energy taken from the electrons either to short-wavelength phonons acting as a thermal "tank" or to the crystal boundaries. In the first case, $P' = P_{ff}$ and $\alpha = 2$, while in the second case, $P' = P_{fl}$ and $\alpha = 3/2$. In view of (17) and (18), one has for differential conductivity under TR conditions ($\Theta \longrightarrow \infty$)

$$\frac{\sigma_d}{\sigma} = \frac{\gamma - \beta_1 + 2\beta_2 - \frac{1}{2}}{\gamma + \beta_1 - 2\beta_2 + \frac{5}{2}}. \quad (19)$$

(1) In the case of equilibrium phonons, $\gamma = -(s/2)$. Knowing the values of β_1 and β_2 in the weak and strong magnetic fields, it is easy to check that we come to expressions (14) and (15), respectively, for differential conductivity.

(2) Under phonon heating, $\gamma = \alpha$. In the presence of the thermal tank $\alpha = 2$; hence,

$$\frac{\sigma_d}{\sigma} = \frac{2 + t}{2 - t}, \quad (20)$$

and in the weak magnetic field, and

$$\frac{\sigma_d}{\sigma} = \frac{6 + t}{6 - t} \quad (21)$$

in the strong magnetic field.

If the energy is transferred to the crystal boundaries, $\alpha = 3/2$. Then,

$$\frac{\sigma_d}{\sigma} = \frac{5 + 3t}{5 - 3t}, \quad (22)$$

in the weak magnetic field, and

$$\frac{\sigma_d}{\sigma} = \frac{5 + t}{5 - t} \quad (23)$$

in the strong magnetic field.

Expressions (20)–(23) imply that the differential conductivity does not pass through infinity under phonon heating, since appropriate scattering mechanisms do not exist.

Thus, for the equilibrium phonon subsystem, the differential conductivity of runaway hot electrons passes through infinity in both approximations, suggesting that an *S*-shaped CVC may occur. Under phonon heating, the differential conductivity also passes through infinity, but actual scattering mechanisms behind this effect are absent.

REFERENCES

1. I. B. Levinson, Fiz. Tekh. Poluprovodn. (Leningrad) **6**, 2113 (1964) [Sov. Phys.–Solid State **6**, 1665 (1964)].
2. F. G. Bass, Zh. Éksp. Teor. Fiz. **48**, 275 (1965) [Sov. Phys.–JETP **21**, 181 (1965)].
3. Z. S. Kachlishvili, Zh. Éksp. Teor. Fiz. **78**, 1955 (1980) [Sov. Phys.–JETP **51**, 982 (1980)].
4. Z. S. Kachlishvili and F. G. Chumburidze, Zh. Éksp. Teor. Fiz. **87**, 1834 (1984) [Sov. Phys.–JETP **60**, 1055 (1984)].
5. Z. S. Kachlishvili, Zh. Éksp. Teor. Fiz. **113**, 688 (1998) [JETP **86**, 380 (1998)].
6. V. L. Bonch-Bruevich and S. G. Kalashnikov, *Physics of Semiconductors* (Nauka, Moscow, 1990).
7. Z. S. Kachlishvili, Phys. Status Solidi A **33**, 15 (1976).
8. T. M. Gasymov and L. É. Gurevich, Fiz. Tverd. Tela (Leningrad) **9**, 106 (1967) [Sov. Phys.–Solid State **9**, 78 (1967)].

Translated by S. Egorov

Technical Physics, Vol. 45, No. 5, 2000, pp. 574–583. Translated from Zhurnal Tekhnicheskoĭ Fiziki, Vol. 70, No. 5, 2000, pp. 51–60.

SOLIDS

Electron and Phonon Mechanisms of Friction in Crystalline Solids in Atomically Close Contact at Low Temperatures

V. L. Popov

Institute of Strength Physics and Material Science, Siberian Branch of the Russian Academy of Sciences, Tomsk, 634021 Russia

Universität Paderborn, Fachbereich Physik, AG Theoretische Physik, Paderborn, D-33098 Germany

Received September 28, 1998; in final form March 18, 1999

Abstract—Recent experimental and theoretical studies have shown that an atomically close contact between two crystalline solids can be free from friction of rest in the event that their lattice constants are incommensurate and the interaction at their interface does not exceed a certain threshold value. In this case, the sole mechanisms of friction are the phonon emission and the excitation of conduction electrons. Theoretical estimations of both phonon and electron contributions to the frictional force have been carried out (the latter contribution has been considered both in the normal and superconducting states of metal). © *2000 MAIK "Nauka/Interperiodica".*

INTRODUCTION

New possibilities for experimental study of friction at an atomic level (first of all, using atomic force microscopy and quartz-crystal microbalances [1]), as well as the increased computer speeds that made possible large-scale simulations with the use of molecular dynamics methods, have led to rapid progress in the understanding of basic processes of friction [1, 2]. As a result of recent experimental [1–3] and theoretical [4, 5] studies, a remarkable conclusion has been made that the "atomically close" contact between two crystalline solids can be free from friction of rest if the lattice constants of the contacting solids are incommensurate. An additional condition is that there are no so-called "elastic instabilities" at the contact of the two solids [6–8]. Under these conditions, interaction of the solids is characterized by a viscous force, typical of macroscopic systems with lubrication. The reason for the absence of the friction of rest is that surface atoms of the contacting incommensurate lattices are necessarily found in various (high and low) energy positions relative to each other. The relative motion of the solids results, therefore, only in a changing pattern of atoms in low- and high-energy positions without causing changes in the macroscopic energy of the solids. For this reason, even an infinitesimal force can cause the relative motion of the solids. These arguments fail if the contacting bodies form a multistable system (that is, in general, if several equilibrium states of the system correspond to the specified set of boundary conditions). In this case, atoms cannot proceed in a continuous quasi-static manner adiabatically, but, from time to time, experience transitions into new equilibrium positions. In these transitions, some finite energy is dissipated per unit displacement, which is the physical cause of finite quasi-static frictional force. The picture outlined above corresponds to the widely used intuitive concept of broken bonds between atoms as a cause of the friction of rest. The breaking of bonds and formation of new bonds is essentially a manifestation of the system metastability. As long as the contact remains monostable, there is no static frictional force between contacting bodies with incommensurate lattice constants [6, 7]. The argumentation based upon broken bonds is inapplicable in that case. The picture to be considered is rather a continuous (adiabatic) movement of atoms of one solid in the potential field created by atoms of the other solid.

At weak enough interaction of surfaces, the condition of contact monostability is always fulfilled, and the friction of rest is zero. This situation is typical of, for example, solid layers of inert gases adsorbed on gold and silver surfaces [4]. But the absence of the static friction was also confirmed experimentally for a tungsten–silicon contact [3]. The latter example is in the category of metal–covalent crystal tribologic contacts and shows that zero friction of rest between crystalline materials with incommensurate lattices can occur in the systems of practical importance.

Below, the contact with zero friction of rest is assumed. This, however, does not imply that the frictional force is completely lacking. Interaction of the surface atoms results, in general, in a generation of phonons, and excitation of the electronic subsystem manifested in a viscous frictional force, which is proportional to the relative velocity of the bodies.

The above picture is based on the classic concepts about the origin of excitations in a crystal. Previously, it has been shown [9, 10] that the quantum-mechanical nature of the elementary excitations in a crystal makes the phonon generation impossible if the velocity of motion is much less than a minimum velocity of sound

1063-7842/00/4505-0574$20.00 © 2000 MAIK "Nauka/Interperiodica"

in the solid. For this reason, similar to the situation with superfluid helium, a solid is found to consist of the "superslippery" and "normal" components. The latter is composed of the gas of elementary excitations: electrons and phonons. As noted in [9, 10], the fundamental difference between a solid and a superfluid liquid is the occurrence of a finite interaction between superslippery and normal components in the former due to umklapp processes as well as to electron and phonon scattering by lattice inhomogeneities. However, because of the impossibility of phonon generation, friction is only possible due to interaction of bodies via their normal components.

In this paper, theoretical estimations of both the phonon and electron contributions to the frictional force (the latter both in the normal and superconducting state of the metal) have been carried out. The proposed model gives a natural explanation of the abrupt change of the friction strain between an atomically flat metallic surface and a dielectric layer adsorbed on it, which was observed experimentally at the metal–superconductor transition state [11].

1. PHONON EXCITATION AT LOW TEMPERATURES

First of all, we explain the physical reasons for the impossibility of phonon generation in the relative motion of two solids. We will be using L.D. Landau's arguments for superfluidity [12]. First, we consider the friction process at absolute zero temperature when both solids are in their ground, unexcited state. Consider the motion of body 2 relative to body 1 with a constant velocity v. The occurrence of friction would have been manifested as dissipation of the kinetic energy of the body and gradual slowing down of its motion. Such a process in a quantum system can proceed either by generation of elementary excitations in the body or by direct transfer of energy and momentum to the body as a whole (as in the case of Mösbauer effect). Observation of the direct momentum transfer to the body as a whole would have meant the existence of a finite quasi-static frictional force. Since we suppose that such a force is absent at the contact considered, the only remaining way for the transfer of energy and momentum from one body to the other will be the generation of elementary excitations.

The appearance of a single elementary excitation with momentum p and energy $\varepsilon(p)$ (measured in moving body two-axes system) will change the energy of body 2 by an amount

$$\delta E = \varepsilon + pv \tag{1}$$

(in a frame of reference at rest, that is the one associated with body 1). The expression (1) is a simple consequence of Galilean transformation for energy. The change of energy (1) should be negative, since the energy of the moving body is decreasing $\varepsilon + pv < 0$. At a given absolute value of p, the left side of this inequality has a minimum when p and v are antiparallel. Thus, the condition $\varepsilon - pv < 0$ should always be fulfilled or

$$v > \frac{\varepsilon}{p}. \tag{2}$$

The only type of low-energy elementary lattice excitations with low momentum p in crystalline dielectrics are acoustic phonons with a linear dispersion law

$$\varepsilon = cp, \tag{3}$$

where c is the velocity of sound and ε is the phonon energy. Since the ratio $\varepsilon/p = c$ is nonzero, at velocities less then c, the excitations in the layer cannot emerge. This means that the layer cannot slow down. In other words, the superslipperiness should set in (by analogy with the superfluidity).

Landau's argumentation above shows that the exterior friction at zero absolute temperature should be zero in all cases where the friction of rest is absent and the spectrum of low energy excitations with small wave vectors contains only acoustical phonon branches. Whereas in a Bose liquid such a shape of the phonon spectrum is a nontrivial fact stemming from the quantum mechanical indistinguishability of particles of the liquid and from the particular permutation symmetry of Bose particles for such a solid shape of the spectrum at temperatures lower than the melting point is trivial.

2. NORMAL AND SUPERSLIPPERY COMPONENTS OF A SOLID

Let us consider now the same bodies at a finite temperature. As before, the motion of one body relative to the other cannot result in the generation of new phonons if the condition $v < c$ is fulfilled. Already available phonons are the cause of the observed macroscopic friction. At a finite temperature, the medium contains elementary excitations or a "gas of quasi-particles" and its motion is accompanied by the transfer of energy and momentum, so that an effective mass can be attributed to this gas. For a linear phonon spectrum, the mass density of the phonon gas associated with a particular acoustic phonon branch can be determined as [12, p. 116]

$$\rho_n = \frac{2\pi^2 (kT)^4}{45\hbar^3 c^5}, \tag{4}$$

where c is the velocity of sound corresponding to a particular branch of the phonon spectrum; k is Boltzmann constant, $\hbar$ is Planck's constant, and T is the absolute temperature of the body.

As one body moves along the other, nothing stands in the way of the interaction or momentum exchange between quasi-particles and the contacting body. As a result, the motion of the gas of elementary excitation will be slowed down. It means that, same as in the theory of superfluidity, at a finite temperature, the part of the crystalline body characterized by density (4) will

behave as a normal viscous liquid which is entrained at the boundary by the motion of the second body. The rest of the body mass will behave as an ideal elastic body without viscosity and friction of rest at the contact surface.

There is also a fundamental difference between the motion of the superfluid helium and the above-mentioned slipperiness at absolute zero temperature related to the possibility in a crystalline solid of the umklapp processes accompanying phonon–phonon collisions, which result in a quasi-momentum change by the reciprocal lattice vector. Due to umklapp processes, interaction of the phonon gas with the crystal lattice as a whole occurs [13], and a finite friction between superslippery and normal components arises. At low temperatures (much lower than Debye temperature), when only phonons with small quasi-momenta are excited, the probability of the umklapp processes and the frictional force between superslippery and normal components decrease exponentially.

It should be noted that in the classic limit $\hbar \longrightarrow 0$, the normal component density (4) would have become infinite. The absurdity of this result shows that, in reality, the characteristic temperature, at which the density of the normal component is of the same order of magnitude as the total density of the medium, becomes zero and the solid behaves in a classic manner at any nonzero temperature. In real solids, the characteristic temperature of the transition from quantum-mechanical to classic behavior is around room temperature or higher (see Section 7). This circumstance implies, in particular, that at low temperatures, the classic methods, including the classic molecular dynamics, are inapplicable for analysis of friction processes involving phonon excitation.

Below, we conduct an assessment of the frictional force resulting both from the interaction of the phonon gases of two bodies and from the interaction of their electronic subsystems.

3. INTERACTION OF THE PHONON SUBSYSTEMS

With the provision that the phonon free path l_N for the normal scattering processes (with quasi-momentum conservation) is small compared with the free path l_U for the processes violating the quasi-momentum conservation law (processes of umklapp and scattering by lattice inhomogeneities), it is possible to write a system of hydrodynamic equations for the phonon gas in a dielectric, which, in the case of a steady-state flow, have the form [13],

$$\eta_1 \Delta V_1 - \frac{\rho_1 V_1}{\tau_{U,1}} = 0, \quad \eta_2 \Delta V_2 - \frac{\rho_2 V_2}{\tau_{U,2}} = 0, \qquad (5)$$

where η is a dynamic viscosity of the phonon gas; V is its hydrodynamic velocity; ρ is a mass density associated with the motion of the phonon gas; τ_U is a phonon mean free time for processes violating the quasi-momentum conservation law; and the indices 1 and 2 refer to quantities associated with the first and the second body, respectively.

At low temperatures, the mass density associated with the phonon gas is defined by the expressions

$$\rho_1 = \frac{2\pi^2 (kT)^4}{45\hbar^3}\left(\frac{1}{(c_{\parallel,1})^5} + \frac{2}{(c_{\perp,1})^5}\right),$$
$$\rho_2 = \frac{2\pi^2 (kT)^4}{45\hbar^3}\left(\frac{1}{(c_{\parallel,2})^5} + \frac{2}{(c_{\perp,2})^5}\right), \qquad (6)$$

which are the direct generalization of (4); here $c_\parallel$ and $c_\perp$ are the velocities of longitudinal and transverse sound waves in the solid.[1]

Despite the fact that direct momentum transfer between the bordering atoms (by phonons emission) turns out to be impossible, no obstacles exist for the interaction of the gases of elementary excitations of the two bodies. Their interaction at the boundary decelerates surface layers of the phonon gas in the moving body and entrains the phonon gas in the body (Fig. 1).

Let the x-axis be in the direction of the relative motion of the bodies, and the y-axis a norm to the friction surface. For definiteness, assume that the domain occupied by body 2 corresponds to positive values of the y coordinate and body 2 moves relative to body 1 along the positive direction of the x-axis.

In the described geometry, the velocity of the phonon gas inside each body has only the x-component. The equation of hydrodynamics of the phonon gas for the first body can be written in this geometry as follows:

$$\eta_1 \frac{\partial^2 V_1}{\partial y^2} - \frac{\rho_1 V_1}{\tau_{U,1}} = 0, \qquad (7)$$

where V_1 is the x-component of the velocity and τ_U is a phonon mean free time for the processes violating the quasi-momentum conservation law.

A similar equation can be written for the phonon gas in the second body by simply replacing index 1 by 2 for each quantity in the equation (7). The solutions of the equations, which tend to zero and to $V^{(0)}$ inside the first and the second body, respectively, have the form (at $y \longrightarrow \pm\infty$)

$$V_1(y) = V_1(0)\exp(y/l_1) \qquad (8)$$

in the first body and

$$V_2(y) = V^{(0)} - (V^{(0)} - V_2(0))\exp(-y/l_2) \qquad (9)$$

[1] Since many of the calculations in this paper represent rough estimates, calculations at this point are limited to the case of an isotropic solid. Taking into account the specific shape of the phonon spectrum would have been unwarranted regarding the accuracy of the present calculations.

in for the second body, where,

$$l_1 = \sqrt{\frac{\eta_1 \tau_{U,1}}{\rho_1}}, \quad l_2 = \sqrt{\frac{\eta_2 \tau_{U,2}}{\rho_2}}. \tag{10}$$

Suppose that the phonon gases in the first and the second body have equal velocities at the friction boundary,

$$V_2(0) = V_1(0). \tag{11}$$

This is a usual boundary condition at the boundary between two viscous gases or liquids. For the phonon gas in a solid, this condition is in no way self-evident, since the phonon gas in a solid can interact with its boundary. At the same time, in our special case of atomically flat surfaces and low temperatures (and, accordingly, longer wavelengths), the interaction of phonons with unperturbed surfaces of solids can be neglected. The interaction proceeds only as a result of the long-wavelength distortions of the contact surface by the phonons available in both bodies, and this means direct interaction of the phonon gases in disregard, so to speak, of the interface. Similar reasoning leads to a requirement that the σ_{xy} component of the viscous strains at the boundary be continuous,

$$\eta_1 \frac{\partial V_1(0)}{\partial y} = \eta_2 \frac{\partial V_2(0)}{\partial y}. \tag{12}$$

From (11) and (12), we find

$$V_1(0) = V_2(0) = V^{(0)} \frac{\eta_2 l_1}{\eta_2 l_1 + \eta_1 l_2}. \tag{13}$$

Equations (8) and (9) show that friction in the surface layers of both the contacting conductors creates velocity gradients of the phonon gases. Due to viscosity, these gradients cause mechanic energy losses, and their power per unit area of the surface can be written as

$$\begin{aligned} w &= \int_{-\infty}^{\infty} \sigma_{xy} \frac{\partial V}{\partial y} dy = \int_{-\infty}^{0} \eta_1 \left(\frac{\partial V_1}{\partial y}\right)^2 dy + \int_{0}^{\infty} \eta_2 \left(\frac{\partial V_2}{\partial y}\right)^2 dy \\ &= \frac{\eta_1 V_1(0)^2}{2 l_1} + \frac{\eta_2 V_2(0)^2}{2 l_2} = \frac{\eta_1 \eta_2 V^{(0)^2}}{2(\eta_2 l_1 + \eta_1 l_2)}. \end{aligned} \tag{14}$$

For macroscopically detectable friction strain σ, the corresponding expression is

$$\sigma = \frac{w}{V^{(0)}} = \frac{\eta_1 \eta_2 V^{(0)}}{2(\eta_2 l_1 + \eta_1 l_2)}. \tag{15}$$

Using a simple gas-dynamics estimation for the viscosity [13],

$$\eta = \rho c l_N, \tag{16}$$

where c is an average velocity of sound; l_N is the phonon free path for the normal processes, it is easy to show, using (10), that

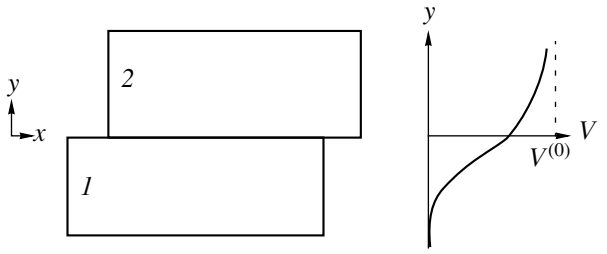

Fig. 1. Dependence of the velocity of phonon gas on the coordinate in the direction normal to the surface of friction of contacting bodies. The phonon density deep inside the body at rest has a zero velocity, while in the body in motion, its velocity is equal to the velocity V_0 of its macroscopic movement. In the interfacial region, the velocity gradually increases from zero to V_0 due to interaction of the normal components of the bodies.

$$l_1 = \sqrt{l_{N,1} l_{U,1}}, \quad l_2 = \sqrt{l_{N,2} l_{U,2}}. \tag{17}$$

Using these relations, expression (15) can be rewritten in the form

$$\sigma = \frac{1}{2} \frac{\rho_1 \rho_2 c_1 c_2 (l_{N,1} l_{N,2})^{1/2} V^{(0)}}{\rho_2 c_2 (l_{N,2} l_{U,1})^{1/2} + \rho_1 c_1 (l_{N,1} l_{U,2})^{1/2}}. \tag{18}$$

In the case of two bodies with phonon gases having identical properties, this expression can be substantially simplified,

$$\sigma = \frac{1}{4} \rho V^{(0)} c \left(\frac{l_N}{l_U}\right)^{1/2}. \tag{19}$$

If the properties of the phonon systems of two bodies are essentially different (for definiteness we assume that $\rho_2 c_2 (l_{N,2}, l_{U,1})^{1/2} \ll \rho_1 c_1 (l_{N,1} l_{U,2})^{1/2}$), then the friction is determined solely by the properties of the phonon system of the body with minimal value of the specified parameter (in our case of the second body),

$$\sigma = \frac{1}{2} \rho_2 V^{(0)} c_2 \left(\frac{l_{N,2}}{l_{U,2}}\right)^{1/2}. \tag{20}$$

For estimation of the friction strain and its dependence on the material parameters in expression (6) for the phonon gas density, we ignore the term that contains $c_\parallel$ (introducing an error of 1–2% for the majority of real solids) and substitute the obtained value of ρ into (19),

$$\sigma = V^{(0)} \frac{\pi^2 (kT)^4}{45 \hbar^3 (c_\perp^{(1)})^4} \left(\frac{l_N}{l_U}\right)^{1/2}. \tag{21}$$

It is seen that in the considered approximation, the friction depends almost exclusively on the transverse sound wave velocity and on the ratio of the phonon free paths for the normal scattering processes and the pro-

cesses violating the quasi-momentum conservation law.

4. INTERACTION OF THE ELECTRONIC SUBSYSTEMS

Let us analyze now the role of electronic excitations in friction. The spectrum of electronic excitations does not obey the Landau condition for superfluidity. The electron gas represents, therefore, the normal component of a solid. In the case of the electronic subsystem, all the equations above remain valid if the following substitutions are made,

$$\rho \longrightarrow nm_e, \quad c \longrightarrow v_F \tag{22}$$

and l_N and l_U are assumed to denote the electron free paths for the normal processes (with conservation of quasi-momentum) and for the umklapp processes, respectively. Here, n is the carrier density, m_e is the carrier effective mass at the Fermi surface, and v_F is the velocity of electrons at the Fermi surface. The equation of the electron gas hydrodynamics for a steady-state flow in the described geometry is as follows:

$$\eta\frac{\partial^2 V}{\partial y^2} - \frac{\rho V}{\tau_U} = 0, \tag{23}$$

where $V = V(y)$ is the x component of the hydrodynamic velocity of the electron gas, η is the viscosity of the electron gas, ρ is its mass density, and τ_U is the characteristic mean free time for the processes violating the quasi-momentum conservation law.

Using coefficients of equation (23), the characteristic length can be written as

$$l = (\eta\tau_U/\rho)^{1/2}. \tag{24}$$

Note that equation (24) is applicable in the case that the mean free path l_N is much less than the size of the body. Since we assume that $l_U \gg l_N$, then $l \approx (l_U l_N)^{1/2} \gg l_N$ (see (17)). Therefore, equation (1) is applicable at less distances than the characteristic length l as well.

Interaction of the massive bodies. Suppose that the thickness of the contacting bodies is much larger than the characteristic length (24), so that their dimension in the transverse direction can be assumed infinitely large. For the friction strain in that case, we can write without making additional calculations (by analogy with (18)),

$$\sigma = \frac{1}{2}\frac{m_{e,1}n_1 m_{e,2}n_2 v_{F,1}v_{F,2}(l_{N,1}l_{N,2})^{1/2}V^{(0)}}{m_{e,2}n_2 v_{F,2}(l_{N,2}l_{U,2})^{1/2} + m_{e,1}n_1 v_{F,1}(l_{N,1}l_{U,2})^{1/2}}. \tag{25}$$

In the case of two metals with the electron gases having identical properties, the equation for the frictional force is again essentially simplified:

$$\sigma = \frac{m_e V^{(0)} V_F n}{4}\left(\frac{l_N}{l_U}\right)^{\frac{1}{2}}. \tag{26}$$

A comparison of (21) and (26) shows that, at low temperatures, the electron contribution to the friction is dominating. It becomes equal to the phonon contribution if

$$m_e n v_F \approx \rho c \cong \frac{\pi^2 (kT)^4}{45\hbar^3 (c_\perp)^4}. \tag{27}$$

This occurs at a temperature

$$T_\times \approx \frac{c_\perp}{k}\left(\frac{45 m_e n v_F \hbar^3}{\pi^2}\right)^{1/4}. \tag{28}$$

For estimation, using the relation between the carrier density and the Fermi velocity in an ideal Fermi gas expression,

$$n = \frac{m_e^3 v_F^3}{3\pi^2\hbar^3}, \tag{29}$$

we find

$$kT_\times \approx 0.6 m_e c_\perp v_F. \tag{30}$$

Despite intensive theoretical studies of the phonon [14, 15] and electron [16, 17] contributions to the viscous frictional force described above, their magnitudes and relationships are still the subject of discussions. Apparently, the most direct way to isolate the electronic contribution would have been the measurement of the frictional force in the region of the superconducting transition. Measurements of the frictional force between a lead layer and the layer of solid N_2 adsorbed on it gave unexpected results, which could not be interpreted in the framework of existing theoretical models [11]. Namely, these measurements have revealed the occurrence of a sudden change of the frictional force at the superconducting transition [11]. In addition, the fraction of the electrons forming the superconducting condensate gradually increased from zero up to temperatures below T_c. The remaining normal electrons continued to be excited by the adsorbed layer. So, a gradual decrease in the friction strain at temperatures below T_c could be expected. Below, it will be shown that the model proposed above gives a simple explanation of the sudden change of the friction strain at the superconducting transition.

5. CONTRIBUTION OF THE REVERSE CURRENT TO THE ENERGY DISSIPATION AT FRICTION. THE SUDDEN CHANGE OF THE FRICTIONAL FORCE AT THE METAL–SUPERCONDUCTOR TRANSITION

In accordance with the conditions of the experiment carried out in [11], consider a metal sample in the form of a parallelepiped of thickness d with one of the surfaces coated with a monolayer of adsorbed crystalline dielectric. The concept of phonon gas is inapplicable to a monoatomic layer because of its small thickness. In this case, it can be considered that electrons in the metallic sample are excited directly by the motion of the layer (rather than the phonon gas in it). Therefore, for analysis of hydrodynamics of the electron gas in the metallic sample, equation (23) can be applied with the boundary condition $V(0) = V^{(0)}$, where $V^{(0)}$ is the velocity of the adsorbed layer.

Equation (23) does not take into account, however, one important circumstance. The described entrainment of the electron gas and related surface current will create an electric field (in a metal in normal state) and a bulk current flowing in opposite directions. In the presence of an electric field, equation (23) should be changed in the following way,

$$\eta\frac{\partial^2 V}{\partial y^2} - \frac{\rho V}{\tau_U} + enE = 0, \tag{31}$$

where e is the elementary charge, n is the electron density and E is the electric field. The latter, in turn, is determined from the condition of total zero current in the sample. The reverse current will result in an additional energy dissipation and increase in the friction strain.

Let us consider, separately, the limiting cases of thick ($d \gg l$) and thin ($d \ll l$) metallic layers.

(1) $d \gg l$.

The solution of equation (31), with a boundary deep inside the sample (at $y \longrightarrow \infty$) and satisfying the condition of zero total current in the sample,

$$\int_0^d V(y)dy = 0, \tag{32}$$

has the form

$$V(y) = -V^{(0)}\frac{l/d}{1-l/d} + V^{(0)}\frac{1}{1-l/d}\exp(-y/l). \tag{33}$$

As only the mechanism of friction by momentum transfer to the crystalline solid via the electron gas is considered, the friction strain can be determined as a viscous strain in the electron gas at $y = 0$,

$$|\sigma_n| = \eta\left|\frac{\partial V}{\partial y}\right|_{y=0} = \eta\frac{V^{(0)}}{l}(1-l/d)^{-1}. \tag{34}$$

It is seen that the correction for the reverse current is of the order of l/d and can be neglected in massive samples (at $d \gg l$).

(2) $d \ll l$.

The influence of the electric field turns out to be essential for thin layers. This is just the case corresponding to the experimental conditions in [11] where lead electrodes of thickness 1500 Å evaporated onto quartz crystal were used.

(a) *Metal in normal state*. The solution of equation (31) with the boundary conditions $V(0) = V^{(0)}$, $V(d) = 0$, which satisfies condition (32), has the form

$$V(y) = V^{(0)}(1 - 4y/d + 3(y/d)^2). \tag{35}$$

For the friction strain, we obtain

$$|\sigma_n| = \eta\left|\frac{\partial V}{\partial y}\right|_{y=0} = \eta\frac{4V^{(0)}}{d}. \tag{36}$$

(b) *Metal in superconducting state.* In this case, the reverse current is produced by the flow of superconducting electrons at $E \equiv 0$. Accordingly, the flow of electron gas in the sample is given by equation (23) with the same boundary conditions as above. Its solution has the form

$$V(y) = V^{(0)}(1 - y/d). \tag{37}$$

For the friction strain, we have

$$|\sigma_s| = \eta\left|\frac{\partial V}{\partial y}\right|_{y=0} = \eta\frac{V^{(0)}}{d}. \tag{38}$$

A comparison of equations (36) and (38) shows that, at the superconducting transition, the friction strain, which is caused by the conduction electrons, changes abruptly; in thin samples ($d \ll l$), the friction strain, at the transition of the metal to the superconducting state, drops by a factor of four.

In the general case of a metallic layer of arbitrary thickness, the solution of equation (31), with additional condition (32) for the metal in the normal state and with equation (23) for the metal in the superconducting state, results in the following expressions for the friction stress:

in the superconducting state,

$$|\sigma_s| = \frac{\eta V^{(0)}}{l}\frac{e^{d/l} + e^{-d/l}}{e^{d/l} - e^{-d/l}} \tag{39}$$

and the normal state,

$$|\sigma_n| = \frac{\eta V^{(0)}}{l}\frac{(1 + d/l)e^{-d/l} - (1 - d/l)e^{d/l}}{4 - 2(e^{d/l} + e^{-d/l}) + (d/l)(e^{d/l} - e^{-d/l})}. \tag{40}$$

Curves of σ_s, σ_n, and σ_n/σ_s as functions of the layer thickness measured in units of l are presented in Fig. 2. The experimentally observed ratio $\sigma_n/\sigma_s \approx 2$ [11] is achieved at $d/l \approx 2.2$. Hence, the characteristic length of

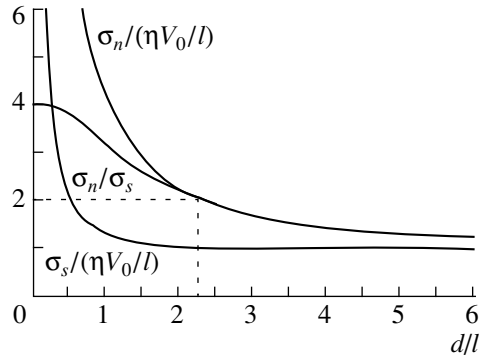

Fig. 2. Friction strain in the normal σ_n and the superconducting σ_s phases and their ratio as a function of the layer thickness d.

the electron gas disturbance in lead at the temperature of superconducting transition is estimated as $l \approx 650$ Å. Consideration of the phonon contribution to the friction does not change this result, since, according to (30), the phonon contribution to the friction at the temperature of superconducting transition of lead (7.2 K) is much less than the electronic one (see also estimates in the next section).

Thus, we have shown that the physical reason for the abrupt change of friction at the superconducting transition is that the energy dissipation results from both the current, due to entrainment of electrons at the friction surface, and the reverse current maintaining the sample electroneitrality. At the transition to superconducting state, the latter contribution turns zero, since the reverse current is carried by superconducting electrons without dissipation. Correspondence of this result with the experiment is an indirect confirmation of the proposed theory.

6. ACOUSTIC EMISSION IN THE CASE OF COMPARABLE LATTICE CONSTANTS

In the case where the periods (lattice constants) of contacting bodies are comparable, the interaction energy of the surfaces depends on their relative positions at the contact plane. The potential energy of interaction per unit area is a periodic function of coordinates (x, z). Assume that the vectors of Bravais lattice at the contact plane are directed along x and z axes and the corresponding periods are a_x and a_z. Surface density of the potential energy can be represented as a Fourier series,

$$U(x, z) = \sum_{n, m} U_{n, m} \exp\left[i\left(\frac{2\pi}{a_x}\right)nx + i\left(\frac{2\pi}{a_z}\right)mz \right]. \quad (41)$$

Accordingly, for nonzero components of the mechanic strain at the boundary, we obtain

$$\sigma_{yx} = \frac{\partial U(x, z)}{\partial x} = \sum_{n, m} iU_{n, m}\left(\frac{2\pi}{a_x}\right)n \times \exp\left[i\left(\frac{2\pi}{a_x}\right)nx + i\left(\frac{2\pi}{a_z}\right)mz \right], \quad (42)$$

$$\sigma_{zx} = \frac{\partial U(x, z)}{\partial z} = \sum_{n, m} iU_{n, m}\left(\frac{2\pi}{a_z}\right)m \times \exp\left[i\left(\frac{2\pi}{a_x}\right)nx + i\left(\frac{2\pi}{a_z}\right)mz \right]. \quad (43)$$

For motion in the contact plane with high enough velocity $v = (v_x, v_z)$ (the criterion of "enough" is given below), it can be considered within zeroth-order perturbation theory that the strains (42) and (43) are periodic functions of time,

$$\sigma_{yx}(t) = \sum_{n, m} iU_{n, m}\left(\frac{2\pi}{a_x}\right)n e^{\omega(n, m, v_x, v_z)t}, \quad (44)$$

$$\sigma_{zx}(t) = \sum_{n, m} iU_{n, m}\left(\frac{2\pi}{a_z}\right)m e^{\omega(n, m, v_x, v_z)t}, \quad (45)$$

where

$$\omega(n, m, v_x, v_z) = \left\{ \left(\frac{2\pi}{a_x}\right)n v_x + \left(\frac{2\pi}{a_z}\right)m v_z \right\}. \quad (46)$$

The strains (44) and (45) will result in excitation of elastic vibrations inside the contacting bodies and corresponding energy losses. Determine, now, the flux of energy from the surface induced by the periodic strains (44) and (45). At velocities $v \ll c$, the frequency of strains (44) and (45) is low and calculations can be carried out in the approximation of an elastic solid, which, for simplicity, would be considered isotropic. Strains (44) and (45) excite only transverse vibrations. The equation of motion of the latter vibrations can be written as

$$\rho\ddot{u} = \mu\Delta u, \quad (47)$$

where ρ is the density of the medium, μ is the shear modulus.

The boundary condition for equation (47) has the form

$$2\mu\left(\frac{\partial u_i}{\partial x_k} + \frac{\partial u_k}{\partial x_i}\right)_{y = 0} = \sigma_{ik}|_{y = 0}, \quad (48)$$

where $\sigma_{ik}|_{y = 0}$ is defined by equations (44), (45)

The solution of equation (47) will be sought in the form.

$$u(y, t) = \sum_{n, m} u_{n, m} \exp[i\omega(n, m, v_x, v_z)(t - y/c_\perp)]. \quad (49)$$

To determine Fourier coefficients in this expansion, the boundary conditions (48) will be used. The obtained result is,

$$u_{x; n, m} = -\frac{4\pi c_\perp}{\mu a_x \omega(n, m, v_x, v_z)} nU_{n, m}, \quad (50)$$

$$u_{z;\,n,\,m} = -\frac{4\pi c_\perp}{\mu a_z \omega(n, m, v_x, v_z)} m U_{n,\,m}. \quad (51)$$

The density of the energy wave E, which is double the density of kinetic energy, can be defined as

$$E = \rho \dot{u}^2 = \rho \sum_{n,\,m} [|u_{x;\,n,\,m}|^2 + |u_{z;\,n,\,m}|^2] \omega(n, m, v_x, v_z)^2 = \frac{16\pi^2}{\mu} \sum_{n,\,m} \left[\frac{n^2}{a_x^2} + \frac{m^2}{a_z^2}\right] |U_{n,\,m}|^2. \quad (52)$$

For the energy flux, we have

$$j = E c_\perp = \frac{16\pi^2}{\sqrt{\mu\rho}} \sum_{n,\,m} \left[\frac{n^2}{a_x^2} + \frac{m^2}{a_z^2}\right] |U_{n,\,m}|^2. \quad (53)$$

The total energy flux entering both contacting bodies is obtained by inserting in equation (53) indices 1 and 2 for the first and second body, respectively, and then taking their sum,

$$j_{\text{tot}} = j_1 + j_2 = 16\pi^2 \left[\frac{1}{\sqrt{\mu_1\rho_1}} + \frac{1}{\sqrt{\mu_2\rho_2}}\right] \times \sum_{n,\,m} \left[\frac{n^2}{a_x^2} + \frac{m^2}{a_z^2}\right] |U_{n,\,m}|^2. \quad (54)$$

Note that the energy losses in the considered approximation are dependent neither on the value, nor on the direction of the relative motion velocity of the two bodies. It means that the friction strength is decreased in inverse proportion to the absolute value of the relative velocity,

$$\sigma_{\text{fr}} = \frac{j_{\text{tot}}}{v}. \quad (55)$$

The condition for validity of the above calculations is that the variable component of the surface velocity δv should be much less than the average velocity v of the relative movement:

$$\delta v \ll v, \quad (56)$$

where

$$\delta v^2 = \frac{E}{\rho} = \frac{16\pi^2}{\mu\rho} \sum_{n,\,m} \left[\frac{n^2}{a_x^2} + \frac{m^2}{a_z^2}\right] |U_{n,\,m}|^2. \quad (57)$$

In the simplest case of harmonic interaction potential with equal periods a in both directions in the sliding plane, we can limit all Fourier expansions by terms with $n = m = 1$. The coefficients $U_{1,1}$ in this case, without any loss of generality, can be assumed real. Amplitude of the potential variations is $2U_{1,1}$. The strain of the friction of rest can be found as the amplitude value of strains (42), (53),

$$\sigma_{\text{stat}} = \frac{4\pi}{a} U_{1,1}. \quad (58)$$

The dynamic friction strain (55) becomes

$$\sigma = \frac{2\sigma_{\text{stat}}^2}{v} [(\mu_1\rho_1)^{-1} + (\mu_2\rho_2)\Pi^{-1}], \quad (59)$$

and the condition (56) is written as

$$\sigma_{\text{stat}} \sqrt{\frac{2}{\mu\rho}} \ll v. \quad (60)$$

It is easy to see that it can be written also in the form

$$\sigma \ll \sigma_{\text{stat}}. \quad (61)$$

Thus, after overcoming the static limit of strain, the friction decreases as the relative velocity of the bodies is further increased. At higher velocities, contributions (21) and (26), which are linear in velocity, come into play, and arises from interaction of the electron and phonon subsystems, respectively, of the two bodies, so that after achievement of the minimal value, the strain will increase again. The value and position of the minimum are dependent on the temperature and the properties of both static and dynamic contribution to the frictional force (including properties of electron and phonon subsystems of the solids).

7. NUMERICAL ESTIMATIONS

As the temperature rises, an increasingly greater part of the medium becomes normal and at some temperature T^*, the superslipperiness should completely disappear. Let us estimate the characteristic temperature T^* values for some materials. In Table 1, the longitudinal $c_\parallel$ and transverse $c_\perp$ sound wave velocities in the crystalline materials are presented as well as their density ρ and the critical temperature T^*, at which the total density of the normal component (6) related to all three acoustical phonon branches becomes equal to the total density of the medium.

We see that at room temperature, all listed materials except Al_2O_3, Sn, and Pb should be in the state of superslipperiness if, of course, equation (4) is still valid up to the temperatures given. In reality, expression (4) is inapplicable at such high temperatures, if for no other reason than the fact that the linear dispersion assumed in the calculations occurs only at phonon momentum values much lower than the Debye's value, and, therefore, expression (4) can be used only at temperatures much lower than the Debye temperature. For this reason, the given values of the characteristic temperature T^*, calculated from (6), are only rough estimates. Their purpose is to illustrate the fact that the elastic solids, even at fairly high temperatures, are essentially quantum mechanical objects (with regard to excitation of

Table 1. Parameters of the materials and the estimated values of characteristic temperature for some crystalline materials

Crystal	$c_{\parallel}$, m/s	c_{-}, m/s	ρ, kg/m^3	T^*, K
Diamond	18000	12000	3510	2342
Si	8000	3900	2550	540
Ge	4900	2500	5350	372
SiO_2	6400	2700	2650	344
Al_2O_3	3500	1400	3900	200
ZrO_2–Y_2O_3(8%)	8500	2300	5490	340
Al	6260	3080	2700	406
Fe	5850	3230	7880	562
Cu	4700	2260	8930	372
Ni	5630	2960	8900	521
Sn	3320	1670	7290	242
Pb	3600	1590	11350	255
W	5200	2000	19300	390

Table 2. Estimated values of the normalized friction strain $\sigma/V^{(0)}$, kPa s/m, at 300 and 80 K

Material	300 K	80 K
Diamond	0.9	0.004
Si	80	0.4
Ge	450	2
SiO_2	300	1.5
Al_2O_3	5000	20
Al	20	1
Fe	150	1
Cu	700	3
Ni	200	1
Sn	2000	10
Pb	100	0.5
W	25	0.1

Note: The values given represent the friction strain measured in Pa units at a relative movement velocity $V^{(0)} = 1$ m/s.

their internal motion). A more important reason to consider temperatures listed in Table 1, as indicative of a gradual transition from the quantum mechanical to classic behavior rather than of a phase transition, is that in a solid, as already mentioned, at any temperature, there exists, in contrast to a superfluid liquid, the interaction between the normal and the superslippery components, which strengthens with temperature, so that at the temperature T^*, no qualitative changes of the properties of a solid take place at all.

Let us estimate the temperature at which the phonon and electron contribution to the frictional force become equal. Substituting $m_e = 9.1 \times 10^{-31}$ kg, $k = 1.38 \times 10^{-23}$ J/K and the values of v_F and $c_\perp$ typical of good metals—$v_F = 10^6$ m/s and $c_\perp \approx 3 \times 10^3$ m/s—gives $T_\times \approx 120$ K. This estimate shows that in good metals, the phonon contribution dominates at room temperature and the electronic contribution at low temperatures. For metals with a small density of conduction electrons, these temperatures are lower.

In crystals of dielectrics, strain (21), which is due to interaction of the phonon systems, is the only contribution to the frictional force. This contribution drops steeply as the temperature is decreased. The character of the decrease depends on the density of defects in the crystal. In "dirty" materials, the free path for scattering by impurities should be used as l_U. l_N depends on the temperature as T^5, while l_U as T^4 [13, Secs. 69, 70]. The dependence of the frictional force on temperature is, therefore, proportional to $T^{4,5}$.

In pure materials, the only mechanism of the momentum exchange between the phonon gas and the lattice is the umklapp processes. Their probability decreases exponentially ($\propto e^{-\Theta/T}$, where Θ is Debye temperature) with decreasing temperature. Accordingly, the dependence of the frictional force (order-of-magnitude estimate) on temperature is given by the expression $T^4 e^{-\Theta/2T}$. At room temperature, the equation (21) is, strictly speaking, inapplicable, but can be used for order-of-magnitude estimations. The estimated values of the normalized friction strain ($\sigma/V^{(0)}$) at 300 and 80 K for some crystalline solids are presented in Table 2.

CONCLUSIONS

In this paper, two different effects are considered. The first consists in the absence of the static frictional force at the contact of two crystalline solids in the case that the interaction force between them does not exceed some critical value and the periods of their lattices are incommensurate. In the system with zero static frictional force, there is only viscouslike dynamic friction related to the excitation of phonons and conduction electrons. In dielectric crystals, the phonon contribution to the frictional force is the only one.

The second effect consists in the disappearance of the phonon contribution as the absolute zero temperature is approached. At finite temperatures, the frictional force is a finite quantity, but rapidly decreases with decreasing temperature. In ideal (defect-free) crystals, this decrease has an exponential character, which makes possible the slip effect with anomalously low friction in the case of two crystals with incommensurate lattice constants, one of which is a dielectric. Both the effect of zero static friction (superlubricity) and the described above effect of zero dynamic friction (superslipperiness) can be of great practical importance for tribologic systems such as micromechanical devices, further miniaturization of which is hampered by the occurrence of the frictional forces.

ACKNOWLEDGMENTS

The author is grateful to the Alexander von Humboldt Foundation for the financial support of this work.

REFERENCES

1. J. Krim, Sci. Am. **275** (4), 74 (1996).
2. *Physics of Sliding Friction*, Ed. by B. N. J. Persson and E. Tossatti (Kluwer Academic, Dordrecht, 1996), *Proceedings of NATO Adriatico Research Conference on the Physics of Sliding Friction, 1996.*
3. M. Hirano *et al*., Phys. Rev. Lett. **78**, 1448 (1997).
4. M. O. Robbins and J. Krim, MRS Bull. **23** (6), 23 (1998).
5. E. D. Smith, M. O. Robbins, and M. Cieplak, Phys. Rev. B **54**, 8252 (1996).
6. T. Gyalog, M. Bammerlin, R. Lüthi, *et al.*, Europhys. Lett. **31**, 269 (1995).
7. T. Gyalog and H. Thomas, Europhys. Lett. **37**, 195 (1997).
8. A. P. Sutton and R. W. Balluffi, *Interfaces in Crystalline Materials* (Clarendon, Oxford, 1995).
9. V. L. Popov, Zh. Tekh. Fiz. **21** (20), 60 (1995) [Tech. Phys. Lett. **21**, 843 (1995)].
10. V. L. Popov, Tribol. Schmierungstech., No. 5, 28 (1999).
11. A. Dayo, W. Alnasrellah, and J. Krim, Phys. Rev. Lett. **80**, 1690 (1998).
12. L. D. Landau and E. M. Lifshitz, *Statistical Physics* (Nauka, Moscow, 1978; Pergamon, Oxford, 1980), Part 2.
13. L. D. Landau and E. M. Lifshits, *Physical Kinetics* (Nauka, Moscow, 1979).
14. M. Cieplak, E. D. Smith, and M. O. Robbins, Science **256**, 1209 (1994).
15. M. S. Tomassone *et al*., Phys. Rev. Lett. **79**, 4798 (1997).
16. B. N. J. Persson, Phys. Rev. B **44**, 3277 (1991).
17. J. B. Sokoloff, Phys. Rev. B **52**, 5318 (1995).

Translated by M. Lebedev

Technical Physics, Vol. 45, No. 5, 2000, pp. 584–590. Translated from Zhurnal Tekhnicheskoĭ Fiziki, Vol. 70, No. 5, 2000, pp. 61–67.

OPTICS, QUANTUM ELECTRONICS

Transformation of the Spectral Density of Intensity Fluctuations of the Pulsed Radiation from a Quasi-Single-Mode Heterolaser in an Optical Fiber

Yu. A. Morozov

Institute of Radio Engineering and Electronics, Saratov Branch, Russian Academy of Sciences, Saratov, 410019 Russia

Received April 15, 1999

Abstract—The spectral density of intensity fluctuations of quasi-single-mode heterolaser radiation under pseudorandom pulsed modulation of the pumping current has been studied for the first time by numerical methods. In the limit of the second-order dispersion theory, the effect of the chromatic dispersion of an optical fiber on the noise characteristics of laser radiation (spectral density of fluctuations and signal-to-noise ratio in the operating range of the photodetector) was investigated. The effect of the laser parameters and modulation on the transformation of the intensity fluctuations in a fiber-optic communication line was studied. © *2000 MAIK "Nauka/Interperiodica".*

INTRODUCTION

The semiconductor heterolaser (HL) is presently considered as practically the only source of optical radiation in digital systems of data transmission through a fiber-optic communication line. As a consequence, since the early 1980s and up to the present time, intensive studies focused both on making more sophisticated HLs [1–5] and studying the processes of radiation and signal propagation through an optical fiber [6–10], were carried out. In particular, it has been found that the chromatic dispersion, which results in temporal displacement of the spectral components of the pulse and, therefore, in the destruction of autocorrelation of the fluctuations in radiation modes of an HL, is the cause of the mode-partition-noise as well as of the noise due to intrapulse frequency modulation (chirp). Among the physical factors to be dealt with in the improvement of communication line characteristics, these noise sources are the foremost [11]. The applied character of the considered phenomena was manifested in a one-sided approach to the study of fluctuations of the HL radiation in the pulsed regime and in their transformation in a dispersive delay line, namely, nearly all investigations dealt with temporal characteristics; that is, only the dependence on time of the statistic moments of radiation intensity in HL modes was studied [6–11].

Analysis in the frequency domain can supplement and elucidate known results and make the physical picture of the transformations of intensity fluctuations of the entire HL radiation easier to visualize.

This paper presents, for the first time, numerical calculations of the spectral density of fluctuations of HL radiation intensity at the output of a dispersive transmission line with modulation of the injection current by a quasi-random pulse sequence. Measurements of the noise power integrated over a specified photodetector frequency range and its dependence on the conditions of transmission through optical fiber for individual modes, as well as for the whole HL radiation, have been done, for example, in [6, 10]. The results of our simulations are consistent with the basic conclusions drawn from the experiments. Earlier, studies of the intensity noise at the output of an HL operated under regular pulsed modulation of the pumping current were carried out by numerical methods [12, 13].

BASIC EQUATIONS

To describe the radiation dynamics of a quasi-single-mode heterolaser, taking into account the effect of spontaneous density fluctuations of carriers and photons, the following system of stochastic rate equations is routinely used:

$$\begin{aligned}\dot{\nu} &= C(T) - (S_0 + S_1)[1 - \varepsilon(S_0 + S_1)] + \chi_1,\\ \dot{S}_0 &= \eta\{[\nu - \varepsilon(S_0 + S_1)]S_0 + \beta N_{\text{th}}\} + \chi_2,\\ \dot{S}_1 &= \eta\{[(\nu - \Delta) - \varepsilon(S_0 + S_1)]S_1 + \beta N_{\text{th}}\} + \chi_3,\end{aligned} \qquad (1)$$

where $\nu = (n - n_{\text{th}})g\tau_{p0}$ is the normalized deviation of carriers density n from the threshold density n_{th}; $S_{0,1} = s_{0,1}g\tau_n$ is a dimensionless photon density in the main (with "0" subscript) and side (with "1" subscript) modes; g is a constant, which determines the linear part of the gain of the active medium and τ_n and τ_{p0} are the lifetimes of the carriers and photons in the main mode, respectively.

1063-7842/00/4505-0584$20.00

The excess of the instantaneous value of the pumping current $j(T)$ over the threshold value jth is determined by the quantity $C(T) = (j(T) - j_{th})g\tau_n\tau_{p0}/ed$, where e is the elementary charge, and d is a thickness of the laser active layer. The fraction of the spontaneous radiation in both laser modes is assumed constant and equal to β; $N_{th} = n_{th}g\tau_{p0}$; $\eta = \tau_n/\tau_{p0}$. The effect of the random process of carrier generation–recombination ϕ_n and of spontaneous photon emission $\phi_{s0,1}$ is taken into account by the introduction of δ-correlated sources $\chi_1 = g\tau_n\tau_{p0}\phi_n$ and $\chi_{2,3} = g\tau_n^2\phi_{s0,1}$. The partition into the main and side modes is due to different photon lifetimes attributed to these modes and determined by a parameter $\Delta = (\tau_{p0} - \tau_{p1})/\tau_{p1} \ll 1$. Differentiation in (1) is carried out with respect to the dimensionless time $T = t/\tau_n$. Numerical analysis shows that under modulation of the injection current of an HL by a regular sequence of short pulses over an ultrahigh frequency range, when the radiation pulse is too short for relaxational oscillations to arise, the effect of optical gain saturation on the dynamics and fluctuations can be ignored [12–14]. In the case of current modulation by a pseudorandom sequence of pulses in the non-return-to-zero (NRZ) format and realization of several binary units in succession, the current pulse duration can prove sufficient for the relaxational oscillations to develop and the effect of gain saturation will be significant. In the present paper, this effect is accounted for by the introduction of a normalized gain saturation coefficient $\varepsilon = \varepsilon_0/g\tau_n$. The condition of carrier density stabilization at the threshold level, $\nu \ll 1$, was used in derivation of (1).

The pumping current $j(T)$ was taken in the form of a pseudorandom succession of pulses superimposed on a constant current component j_0, i.e.,

$$j(t) = j_0 + \sum_{k=0}^{\infty} a_k j_\sim(T - kT_m).$$

Here, $\{a_k\}_0^\infty$ is the pseudorandom succession of binary zeros and units appearing with equal probability; $T_m = (BR)^{-1}$ with $(BR)^{-1}$ the bit-rate; the current pulse shape $j_\sim(T)$ is defined as follows:

$$j_\sim(T) = \begin{cases} 0, & T < 0, \\ j_m \tanh pT, & 0 \le T \le T_m, \\ j_m[1 - \tanh p(T - T_m)], & T > T_m, \end{cases}$$

where the parameter p characterizes the build-up (decay) rate of a pulse and j_m its amplitude.

According to Dub's theorem [15], a multidimensional random process with coordinates (ν, S_0, S_1) related by equations (1) can be approximated as a Markovian one. Using an approach described in [12–14], the following system of ordinary differential equations for the statistical moments of the distribution of quantities ν, S_0, S_1 can be obtained instead of stochastic equations (1):

$$\begin{aligned}
\dot y_1 &= C(T) - y_2 - y_3 + E_1, \\
\dot y_2 &= \eta(Y_1 y_2 + 1.5\beta N_{th} + Y_7), \\
\dot y_3 &= \eta[(Y_1 - \Delta)y_3 + 1.5\beta N_{th} + Y_8], \\
\dot y_4 &= D_{11} - 2(y_7 + y_8) + E_4, \\
\dot y_5 &= D_{22} + 2\eta(Y_1 y_5 + Y_7 y_2), \\
\dot y_6 &= D_{33} + 2\eta[(Y_1 - \Delta)y_6 + Y_8 y_3], \\
\dot y_7 &= D_{12} - (y_5 + y_9) + \eta(Y_1 y_7 + Y_4 y_2) + E_7, \\
\dot y_8 &= D_{13} - (y_6 + y_9) + \eta[(Y_1 - \Delta)y_8 + Y_4 y_3] + E_8, \\
\dot y_9 &= D_{23} + \eta[Y_8 y_2 + Y_7 y_3 + (2Y_1 - \Delta)y_9].
\end{aligned} \tag{2}$$

Here, $y_1 = \langle\nu\rangle$, $y_2 = \langle S_0\rangle$, and $y_3 = \langle S_1\rangle$ are the first-order moments; $y_4 = \langle\nu^2\rangle - \langle\nu\rangle^2 = \sigma_\nu^2$, $y_5 = \sigma_{s0}^2$, and $y_6 = \sigma_{s1}^2$ are the variances; $y_7 = \langle\nu S_0\rangle - \langle\nu\rangle\langle S_0\rangle$, $y_8 = \langle\nu S_1\rangle - \langle\nu\rangle\langle S_1\rangle$, $y_9 = \langle S_0 S_1\rangle - \langle S_0\rangle\langle S_1\rangle$ are the covariances of carrier and photon densities; and, in addition,

$$\begin{aligned}
E_1 &= \varepsilon[(y_2 + y_3)^2 + y_5 + y_6 + 2y_9], \\
E_4 &= 4\varepsilon(y_2 + y_3)(y_7 + y_8), \\
E_7 &= 2\varepsilon(y_2 + y_3)(y_5 + y_9), \\
E_8 &= 2\varepsilon(y_2 + y_3)(y_6 + y_9), \\
Y_1 &= y_1 - \varepsilon(y_2 + y_3), \quad Y_4 = y_4 - \varepsilon(y_7 + y_8), \\
Y_7 &= y_7 - \varepsilon(y_5 + y_9), \quad Y_8 = y_8 - \varepsilon(y_6 + y_9).
\end{aligned}$$

The mean values of the diffusion coefficients D_{ij} were determined as in [8],

$$\begin{aligned}
D_{11} &= \gamma(2N_{th} + C) + 2\beta(y_2 + y_3)N_{th}/\eta, \\
D_{22} &= 2\beta\eta y_2 N_{th}, \quad D_{33} = 2\beta\eta y_3 N_{th}, \\
D_{12} &= -2\beta y_2 N_{th}, \quad D_{13} = -2\beta y_3 N_{th}, \quad D_{23} = 0,
\end{aligned}$$

where $\gamma = g\tau_{p0}/V \ll 1$ and V is the volume of the laser active region.

The system (2) can be used to describe the dynamic behavior of HL taking into account spontaneous fluctuations of carriers and photons, and requires up to two orders of magnitude less time for solving, compared with the initial system (1).

The energy spectrum of the radiation intensity of a quasi-single mode HL in the pulsed regime can be presented as in earlier works [12, 13] as the sum of a continuous component $F^n(\omega)$ and a discrete component $F^d(\omega)$

$$F(\omega) = F^n(\omega) + F^d(\omega).$$

It can be shown that the discrete component exists only at zero frequency if modulation of the pumping current by the pseudorandom succession of pulses in NRZ format is used, and in the instance of the basic mode it can be presented as follows:

$$F^d(0) = \lim_{T\to\infty}\frac{8\pi}{T^2}\delta(0)\int_0^T dU\int_0^{T-U} y_2(U)y_2(U+\tau)d\tau. \quad (3)$$

According to Wiener–Khinchin theorem, in nonstationary processes, the continuous component of the energy spectrum $F^n(\omega)$ can be defined by the correlation function $Z(T, \tau)$ of the photon density at moments of time shifted by τ

$$F^n(\omega) = \lim_{T\to\infty}\frac{4}{T}\int_0^T dU\int_0^{T-U} Z(U,\tau)\cos\omega\tau d\tau. \quad (4)$$

Thus, to calculate the spectral density of the intensity fluctuations in the main and the side modes, as well as of the total radiation, the following correlation functions will be needed: $Z_{00}(T, \tau) = \langle S_0(T)S_0(T+\tau)\rangle - y_2(T)y_2(T+\tau) = \langle S_0S_{0\tau}\rangle - y_2y_{2\tau}$; $Z_{11}(T, \tau) = \langle S_1S_{1\tau}\rangle - y_3y_{3\tau}$; $Z_{ss}(T, \tau) = \langle (S_0+S_1)(S_{0\tau}+S_{1\tau})\rangle - (y_2+y_3)(y_{2\tau}+y_{3\tau})$.

The system of ordinary differential equations to determine the correlation function $Z_{00}(T, \tau)$ of the photon density in the main mode derived as in [12, 13] has the form

$$\begin{aligned}\dot Z_{00}(T,\tau) &= \eta(Y_{1\tau}Z_{00} + y_{2\tau}Z_{02} + E_{02}),\\ \dot Z_{01}(T,\tau) &= \eta[(Y_{1\tau}-\Delta)Z_{01} + y_{3\tau}Z_{02} + E_{01}],\\ \dot Z_{02}(T,\tau) &= -[(Z_{00}+Z_{01}+2(E_{00}+E_{01})],\end{aligned} \quad (5)$$

where $Z_{01} = \langle S_0S_{1\tau}\rangle - y_2y_{3\tau}$, $Z_{02} = \langle S_0\nu_\tau\rangle - y_2y_{1\tau}$ are the cross-correlation functions; $E_{00} = -\varepsilon y_{2\tau}(Z_{00}+Z_{01})$; and $E_{01} = -\varepsilon y_{3\tau}(Z_{00}+Z_{01})$. The initial conditions for solving system (5) are determined by first solving the system of equations (2)

$$Z_{00}(T,0) = y_5(T),\quad Z_{01}(T,0) = y_9(T),$$
$$Z_{02}(T,0) = y_7(T).$$

The correlation function for the photon density in the side mode $Z_{11}(T, \tau)$ can be obtained by solving the following system of equations:

$$\begin{aligned}\dot Z_{10}(T,\tau) &= \eta(Y_{1\tau}Z_{10} + y_{2\tau}Z_{12} + E_{10}),\\ \dot Z_{11}(T,\tau) &= \eta[(Y_{1\tau}-\Delta)Z_{11} + y_{3\tau}Z_{12} + E_{11}],\\ \dot Z_{12}(T,\tau) &= -[Z_{10}+Z_{11}+2(E_{10}+E_{11})]\end{aligned} \quad (6)$$

with the initial conditions

$$Z_{10}(T,0) = y_9(T);\quad Z_{11}(T,0) = y_6(T);$$
$$Z_{12}(T,0) = y_8(T).$$

In (6), the designations $Z_{10} = \langle S_1S_{0\tau}\rangle - y_3y_{2\tau}$, $Z_{12} = \langle S_1\nu_\tau\rangle - y_3y_{1\tau}$, $E_{10} = -\varepsilon y_{2\tau}(Z_{10}+Z_{11})$, $E_{11} = -\varepsilon y_{3\tau}(Z_{10}+Z_{11})$ are introduced. The correlation function $Z_{ss}(T, \tau)$ of the total intensity of laser radiation can be expressed in terms of the known quantities

$$Z_{ss} = Z_{00} + Z_{11} + Z_{01} + Z_{10}. \quad (7)$$

SPECTRAL DENSITY OF THE INTENSITY FLUCTUATIONS OF RADIATION PASSED THROUGH A SINGLE-MODE OPTICAL FIBER

Since the frequency interval between HL modes is typically 100–300 GHz, i.e., much wider than the intensity fluctuation spectrum of a separate mode (~10 GHz) [12, 13], it can be assumed that all spectral components of a mode are delayed by time τ_d relative to another mode. That is, in this model for each mode taken separately, the first-order dispersion theory is valid, while the second-order theory should be applied to the total radiation [16]. In this paper, only lasers with a not-too-high side-mode suppression ratio (*SMSR*) of the order of 5–15 dB are considered. In that case, the mode partition noise dominates over the noise caused by chirp, and the latter can be ignored. In the framework of the suppositions made, the correlation functions $Z_{00}(T, \tau)$ and $Z_{11}(T, \tau)$ and, consequently, the intensity spectra of the separate modes do not change as a result of their passage through a fiber-optic line. Transformation of the spectral density of intensity fluctuations of the total radiation in their passage through the optical fiber is related to the variation of the cross-correlation functions $Z_{01}(T, \tau)$ and $Z_{10}(T, \tau)$. For the sake of definiteness, the side mode is assumed to be delayed relative to the main one. Then, according to (4) and (7), the continuous component of the total radiation spectrum $F^n_{ss}(\omega)$ at the fiber output can be written in the form

$$\begin{aligned}F^n_{ss}(\omega) = F^n_{00}(\omega) + F^n_{11}(\omega) + (F^n_{01}(\omega) + F^n_{10}(\omega))\cos\omega\tau_d\\ + (\Phi^n_{10}(\omega) - \Phi^n_{01}(\omega))\sin\omega\tau_d,\end{aligned} \quad (8)$$

where

$$F^n_{01}(\omega) = \lim_{T\to\infty}\frac{4}{T}\int_0^T dU\int_0^{T-U} Z_{01}(U,\tau)\cos\omega\tau d\tau,$$

$$F^n_{10}(\omega) = \lim_{T\to\infty}\frac{4}{T}\int_0^T dU\int_0^{T-U} Z_{10}(U,\tau)\cos\omega\tau d\tau$$

determine the even part of the mutual energy spectrum, and

$$\Phi^n_{01}(\omega) = \lim_{T\to\infty}\frac{4}{T}\int_0^T dU\int_0^{T-U} Z_{01}(U,\tau)\sin\omega\tau d\tau,$$

$$\Phi_{10}^{n}(\omega) = \lim_{T\to\infty}\frac{4}{T}\int_0^T dU \int_0^{T-U} Z_{10}(U,\tau)\sin\omega\tau\, d\tau$$

determine its odd part; $F_{00}^{n}(\omega)$ and $F_{11}^{n}(\omega)$ are the spectra of the main and the side modes, respectively.

At $\tau_d = 0$, that is, at the output of the laser

$$F_{ss}^{n}(\omega) = F_{00}^{n}(\omega) + F_{11}^{n}(\omega) + F_{01}^{n}(\omega) + F_{10}^{n}(\omega),$$

and, as shown in [6, 10, 12, 13], at comparable levels of intensity fluctuations in the modes, these fluctuations cancel out in the total radiation $F_{ss}^{n}(\omega) \le F_{00}^{n}(\omega) + F_{11}^{n}(\omega)$. The canceling is most pronounced at frequencies that are low compared with the frequency of relaxational oscillations; in this range, the random intensity fluctuations in the laser modes are essentially of opposite phases. As the relaxation frequency is approached, the phase shift between fluctuations in the modes becomes increasingly different from π, while the spectral density of the total radiation intensity noise rises and attains its maximum value at that frequency.

From (8), it can be seen that the influence of delay between the modes on the spectral density of the intensity fluctuations shows up at frequencies such that the phase $\omega\tau_d$ is of the order of unity and can be neglected at $\omega \approx 0$. In other words, mutual suppression of the intensity fluctuations of the total laser radiation on account of anticorrelation of the fluctuations in the modes is disrupted due to chromatic dispersion only for spectral components of high enough frequencies. It should be noted that in the actual experiments [6, 10], the pseudorandom succession of the radiation pulses emerging from a single-mode optical fiber is processed in a photodetector and then a low-pass filter (LPF), which has a cutoff frequency at a level of 3 dB numerically equal to $BR/2$. That is, not the total power of the intensity fluctuations is of importance, but only its portion found within the LPF pass-band. Therefore, as regards the laser noise, the parameter of prime importance for operation of communication systems is the signal-to-noise ratio (*SNR*), which is defined as the ratio of the discrete component power to the total noise power in the LPF band, that is

$$SNR_s = \frac{2\pi i_s^d(0)}{\int_0^\infty F_{ss}^{n}(\omega)|G(\omega)|^2 d\omega},$$

where $G(\omega)$ is the LPF frequency response and $i_s^d(0)$ is the power of a discrete component of the total laser radiation.

Taking the LPF cutoff frequency as the maximum frequency in the intensity spectrum, an evaluation of the relative delay $\tau_d^r = \tau_d/T_m = \tau_d BR$ can be obtained for which the influence of the dispersion is high,

$$2\pi f_0\tau_d = \pi r_d^r \approx 1,$$

that is, $\tau_d^r \approx 1/\pi$. Results of experiments and calculations based on other approaches [6] give approximately the same result ($\tau_d^r \approx 0.3$–0.5).

As a measure for the relative level of the spectral density of intensity fluctuations, the following expression can again be used [12, 13]:

$$RIN_s(\omega) = 10\log\frac{i_s^n(\omega)}{i_s^d(0)},$$

where $i_d^n(\omega)$ is the noise power in a 1-Hz frequency band near the angular frequency ω.

RESULTS OF NUMERICAL CALCULATIONS

All calculations in this paper were performed for the following values of the laser parameters: $\tau_n = 2\times10^{-9}$ s, $\tau_{p0} = 10^{-12}$ s, $g = 10^{-6}$ cm^3/s, $d = 2\times10^{-5}$ cm, $V = 0.45\times10^{-10}$ cm^3, $n_{th} = 2\times10^{18}$ cm^{-3}, $\beta = 10^{-4}$, and $\varepsilon_0 = 2\times10^{-17}$ cm^3. The direct bias current j_0 and the time of pulse buildup to the value $0.9j_m$–$0.1(BR)^{-1}$ were always assumed equal to j_{th} and $0.1(BR)^{-1}$, respectively. It was also assumed that the frequency characteristic of the LPF has the following form [6]:

$$G(F) = \left\{1 - \frac{2}{5}F^2 + j\left(F - \frac{1}{15}F^3\right)\right\}^{-1},$$

where $F = f/(0.57f_0)$, and the limiting frequency is $f_0 = BR/2$.

Fig. 1 shows a part of a pseudorandom succession (*1*) of the radiation pulses of HL under modulation of the pumping current (*0*) in NRZ format at the rate of 2.5 Gbit/s ($\langle s_s\rangle = (y_2 + y_3)/h\tau_n$). Maximum deviation of the current from the threshold value, owing to the modulation, was $j_m = 0.5j_{th}$. For comparison, curve *2* in this figure shows the results of a calculation neglecting the coefficient of the optical gain saturation (i.e. at $\varepsilon = 0$). From these plots, it follows that the role of the gain saturation is most pronounced in the transmission of several binary units in succession, and it should be taken into account in simulations of the dynamics of an HL emitting a pseudorandom pulse succession.

It is known that the main factor which determines the suppression of the average level of radiation in the side mode compared with the main mode, is the difference between the photon lifetimes (total optical losses) in these modes. This difference, which is mainly caused by selectivity of the laser resonator, is represented in this paper by a parameter Δ. Because of its effect on the

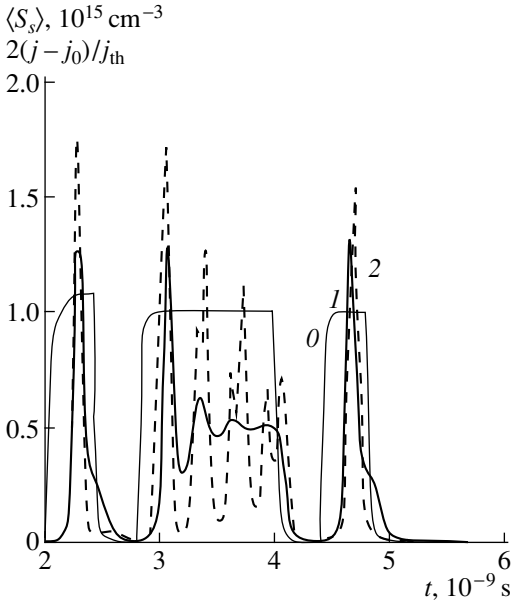

Fig. 1. Variation with time of the injection current (*0*), and of the average photon density, taking into account (curve *1*) and neglecting (curve *2*) the coefficient of gain saturation ε.

side mode intensity, the parameter Δ is very important in forming the spectral density of intensity fluctuations of the total radiation at the output of an optical fiber (Fig. 2). As already mentioned, from the viewpoint of HL applications in pulsed-modulation communication systems, the intensity noise characteristics in the LPF band, that is, in the range of ~0–f_0, are of major importance. To make this clearly seen, the f_0 frequency position is shown by a dashed line. Also of interest is the fact that the relative level of the noise spectral density of noise at the output of lasers with different values of the parameter Δ is practically the same (curves *1*), but differs radically in the radiation exiting the fiber (curves *2*). At the moderate side-mode suppression ratio of *SMSR* = 5.0 dB, corresponding to the laser and modulation parameters given in Fig. 2a, the relative delay of modes results in a drastic increase of the spectral density of noise of the total radiation intensity in the LPF band and, therefore, in lower signal-to-noise ratio (SNR_s = 28 dB at the laser output, and 15.8 dB at the output of a fiber with a relative delay of modes τ_d^r = 0.5). As Δ is increased, and, thus, both the average power and the power of fluctuations in the side mode are reduced compared with the corresponding characteristics of the main mode, the effect of dispersion on the fluctuations of the total radiation intensity becomes less. Thus, in Fig. 2b, the curves for τ_d^r = 0 and τ_d^r = 0.5 nearly coincide. The signal-to-noise ratios are also approximately the same: $SNR_s(\tau_d^r = 0)$ = 26.7 dB and

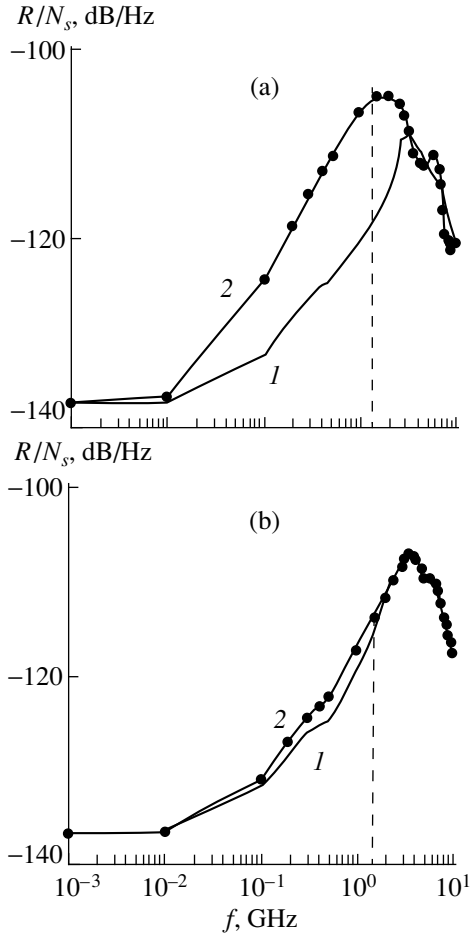

Fig. 2. Effect of the parameter Δ on the frequency dependence of the relative spectral density of intensity fluctuations at the outputs of the laser (*1*), and the optical fiber with τ_d^r = 0.5 (*2*) under current modulation with an amplitude $j_m = 0.5j_{th}$ at *BR* = 2.5 Gbit/s. Δ = (a) 0.01, (b) 0.03.

$SNR_s(\tau_d^r = 0.5)$ = 25.8 dB. The side-mode suppression ratio for Fig. 2b is equal to 13.9 dB.

Fig. 3 illustrates the effect of the current modulation amplitude on the noise characteristics of laser radiation and their transformation in the optical fiber. Here, the variation with frequency of the spectral density of intensity fluctuations at the output of the laser, in which the current is modulated with amplitudes $j_m = 0.5j_{th}$ and $j_m = 1.5j_{th}$, is shown by dashed lines *1* and *2*, respectively. An increase in the amplitude j_m results in a reduction in the RIN_s level and a shift of the relaxation peak of the relative spectral density of fluctuations to higher frequencies. Because of higher frequencies of the relaxation oscillations, the intensity fluctuations in the laser modes are found in better anticorrelation at higher current modulations; i.e. they maintain an approximate phase opposition in the LPF band. Therefore, the signal-to-noise ratio rises (SNR_s values for curves *1* and *2* are 27.5 and 37.9 dB, respectively). An extra phase shift

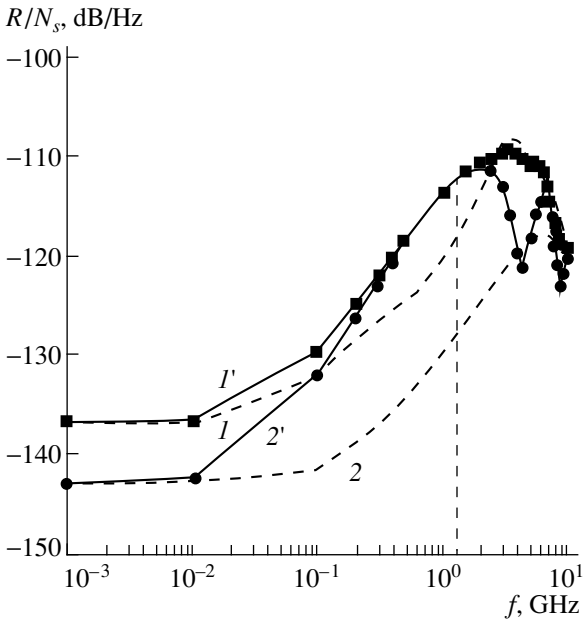

Fig. 3. Effect of the modulation amplitude j_m of the injection current on the relative spectral density of the intensity fluctuations at the outputs of the laser (*1*, *2*), and the optical fiber with $\tau_d^r = 0.5$ (*1*', *2*') at a bit rate $BR = 2.5$ Gbit/s and $\Delta = 0.02$.

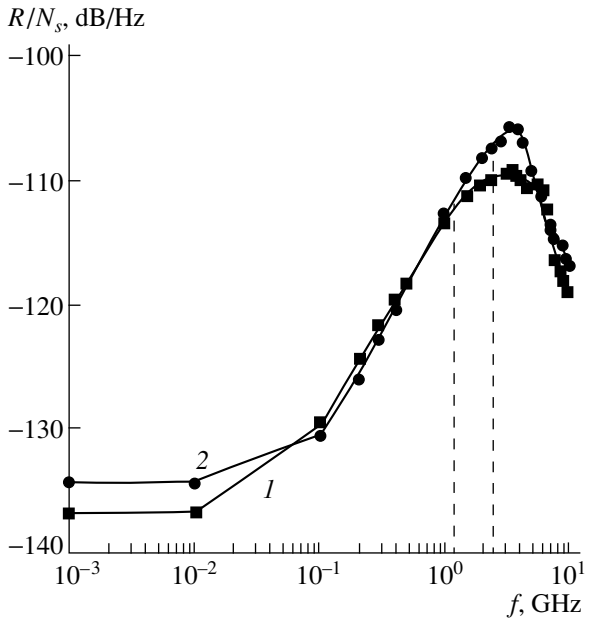

Fig. 4. Effect of the bit rate *BR* on the transformation of RIN_S in an optical fiber for a laser with $\Delta = 0.02$ under pumping current modulation with an amplitude $j_m = 0.5j_{th}$. *BR*, Gbit/s: (*1*) 2.5; (*2*) 5.

between the spectral components of the intensity fluctuations in the modes caused by chromatic dispersion is manifested as an increase in the noise of the total radiation intensity. To a greater extent, this applies to the laser radiation with larger modulation amplitude. The result is that the noise characteristics of the laser radiation at the output of an optical fiber are essentially independent of the modulation amplitude (SNR_s values for parameters of curves *1*' and *2*' are 23.0 and 23.4 dB, respectively).

The effect of the bit rate *BR* on frequency dependence of the spectral density of intensity fluctuations of the radiation at the output of an optical fiber with the relative delay of modes $\tau_d^r = 0.5$ is shown in Fig. 4. Current modulation at a higher rate results in deterioration of the noise characteristics: $SNR_s(BR = 2.5$ Gbit/s) = 23.0 dB and $SNR_s(BR = 5$ Gbit/s) = 15.5 dB. This is mainly associated with the broadening of the LPF band required for the transmission of a higher rate communication (the f_0 frequency values for different bit rates *BR* are shown by the dashed lines in Fig. 4).

CONCLUSIONS

Numerical simulations of the dynamics and calculation of the spectral density of the intensity fluctuations were performed for the quasi-single-mode HL under modulation of the pumping current by a pseudorandom succession of pulses in NRZ format. In a first approximation of the dispersion theory for each mode and in second-order approximation for the total radiation calculations of the transformation of the spectral density of intensity, fluctuations of HL in an optical fiber were carried out. The effect of the laser parameters and modulation on the noise, because of the mode partition due to chromatic dispersion, was studied. The results are as follows.

The relative spectral density of intensity fluctuations at the laser output is practically unaffected by the parameter Δ, which determines the side-mode suppression ratio. However, the relative delay of modes in the optical fiber results in a considerable increase in the noise power of the total radiation in the LPF band of the detector for lasers with $\Delta \le 0.03$ ($G_d \approx 4$–5 cm^{-1}).

An increase in the modulation amplitude of the current pulses does not result in a significant improvement of the noise characteristics of the radiation at the output of the fiber-optic delay line. In this case, the signal-to-noise ratio is considerably higher.

With an increasing bit rate (*BR*), deterioration of the signal-to-noise ratio is observed. However, this occurs mainly because of the need to have a wider detector bandwidth.

REFERENCES

1. J. E. Bowers, Solid-State Electron. **30** (1), 1 (1987).
2. K. Uomi, T. Mishima, and N. Chinone, Appl. Phys. Lett. **51** (2), 78 (1987).
3. R. Nagarajan, M. Ishikawa, T. Fukushima, *et al.*, IEEE J. Quantum Electron. **28**, 1990 (1992).

4. Y. Matsui, H. Murai, S. Arahira, *et al.*, IEEE Photonics Technol. Lett. **9** (1), 25 (1997).
5. D. Marcuse, IEEE J. Quantum Electron. **26** (2), 262 (1990).
6. C. Olsen, K. Stubkjaer, and H. Olesen, J. Lightwave Technol. **LT-7** (4), 657 (1989).
7. S. Miller, IEEE J. Quantum Electron. **QE-25** (8), 1771 (1989).
8. J. Cartledge, IEEE J. Quantum Electron. **QE-26** (12), 2046 (1990).
9. M. Shikada, S. Fujita, N. Henmi, *et al.*, J. Lightwave Technol. **LT-5**, 1488 (1987).
10. B. Hakki, F. Bosch, and S. Lumish, J. Lightwave Technol. **LT-7**, 804 (1989).
11. T. Shen and G. Agrawal, J. Lightwave Technol. **LT-5**, 653 (1987).
12. Yu. A. Morozov and I. V. Krasnikova, Zh. Tekh. Fiz. **66** (6), 131 (1996) [Tech. Phys. **41**, 593 (1996)].
13. Yu. A. Morozov, Zh. Tekh. Fiz. **67** (4), 78 (1997) [Tech. Phys. **42**, 394 (1997)].
14. Yu. A. Morozov, IEEE J. Quantum Electron. **QE-34**, 1209 (1998).
15. D. L. Dub, *Probability Processes* (Moscow, 1956).
16. M. B. Vinogradova, O. V. Rudenko, and A. P. Sukhorukov, *Theory of Waves* (Nauka, Moscow, 1979).

Translated by M. Lebedev

Technical Physics, Vol. 45, No. 5, 2000, pp. 591–596. Translated from Zhurnal Tekhnicheskoĭ Fiziki, Vol. 70, No. 5, 2000, pp. 68–73.

Computation of the Tracking Force Acting on a Relativistic Electron Beam Propagating in a Conducting Waveguide under the Ohmic and Ion-Focused Regimes

E. K. Kolesnikov and A. S. Manuĭlov

St. Petersburg State University, Universitetskaya nab., St. Petersburg, 199164 Russia
Smirnov Institute of Mathematics and Mechanics, St. Petersburg, 198904 Russia

Received August 12, 1999

Abstract—The force of interaction between a relativistic electron beam deflected by resistive hose instability and the eddy current induced in a tubular plasma channel of finite conductivity is computed. Dependences of the force on channel ohmic conductivity and current rise time in a beam pulse are studied. For a beam propagating through a perfectly conducting waveguide under the ion-focused regime, the interaction of the beam with the ion-channel electrostatic image on the waveguide wall is studied for the case when the beam and the channel are deflected from the waveguide axis as a result of ion hose instability. The dependence of the force on both deflection amplitudes is ascertained for the nonlinear phase of instability. It is demonstrated that the force under study may become comparable to the beam–channel interaction force if the deflections are large. © *2000 MAIK "Nauka/Interperiodica".*

Novel applications of relativistic electron beams call for further investigation into their transport in gas–plasma media [1–4]. Of special interest in this field is a stability analysis of the transport over an ohmic plasma channel. The stabilizing action of the channel on beam propagation was addressed in [6–14]. In particular, the authors of [8–12] concentrated on the channels where the major portion of a plasma return current is outside the beam. This situation inhibits resistive hose instability (RHI) in the presence of lateral beam deflections. Recall that RHI is the most dangerous instability upon beam transporting.

RHI can be suppressed by using a perfectly conducting waveguide to propagate the beam, as demonstrated in [2]. Alternatively, the effect can be achieved with a laser-induced tubular plasma channel of finite conductivity, as follows from experiments [7] and theoretical studies [8, 11, 12].

This paper presents a numerical analysis of the tracking force experienced by a relativistic electron beam from the preformed plasma channel. We obtained dependences of the force on the distance between a deflected beam and the channel wall, as well as on current rise time of a beam pulse and conductivity of the channel. The case of a perfectly conducting waveguide was considered as well. We computed the tracking force from the electrostatic image of a deflected ion channel under the ion-focused regime (IFR). As is known, the IFR may occur in gas–plasma media at low pressures ($P \le 1$ torr) if the plasma-channel density per unit length, N_p, is less than the beam density, N_b [15–19]. When the beam enters a preformed plasma channel, background electrons are expelled by the electric field of the beam head and the remaining ions focus the beam, preventing its transverse dispersion.

It has been demonstrated theoretically and experimentally that transport of a relativistic electron beam over a plasma channel under the IFR may be accompanied by various types of instability, ion hose instability (IHI) being the most dangerous [15–21]. With lateral deflections of the beam, the ion channel lags behind the center-of-mass axis of the beam, due to inertia. This excites oscillations in the beam, which may lead to its breakup.

Here we employed the rigid-beam model, where the traverse of beam current density is assumed to be immune to beam deflection [1, 2]. For a perfectly conducting waveguide, we studied the dependence of the tracking force on the deflection of the ion-channel axis, D, and on the deflection of the center-of-mass axis of the beam, Y. Also, we compare the tracking force with the beam–channel interaction force F_{ch}.

First, let us look at the case of an ohmic plasma channel. Consider an axially symmetric paraxial monoenergetic beam propagating in a plasma with uniform scalar conductivity σ_c. The propagation medium is contained in a tubular plasma channel of finite conductivity σ_W ($\sigma_W > \sigma_c$). The thickness and inner radius of the channel are denoted as S and R_W, respectively. Assume σ_c to be so large that $4\pi\sigma_c R_b/c \gg 1$, where R_b is the beam radius and c is the velocity of light. The space charge of the beam is thus fully neutralized. Furthermore, assume that the channel is thin, $S \ll R_W$, and

1063-7842/00/4505-0591$20.00

that the skin effect is weak:

$$S \ll \Psi = \frac{c}{(2\pi\sigma_W\omega)^{1/2}}, \quad (1)$$

where Ψ is the thickness of the skin layer for an alternating electromagnetic field of frequency ω.

The analysis is carried out in cylindrical coordinates (r, ϑ, z) with the z-axis aligned with the axis of the beam–channel system. Note once again that we use the rigid-beam model, which agrees well with more rigorous ones at low frequencies [3].

Instead of t, we will use the shifted time $\tau = t - z/v_z$, where v_z is the longitudinal component of the beam-electron velocity, thus switching from independent variables (t, z) to (z, τ). According to [1], the linear phase of RHI dynamics is described by

$$\frac{\partial^2 Y}{\partial z^2} = \frac{c\pi}{I_b^2}\left(\frac{I_b}{I_A}\right)\int_0^\infty dr r\left[J_{b1}\frac{\partial A_{z0}}{\partial r} + \frac{J_{b0}}{r}\frac{\partial}{\partial r}(rA_{z1})\right], \quad (2)$$

where Y is the amplitude of hose oscillation; I_b and I_A are the net beam current and limiting Alfven current, respectively; J_{b0} and J_{b1} are the equilibrium and perturbed portions of beam current density, respectively; and A_{z0} and A_{z1} are the equilibrium and perturbed portions of the z-component of the vector field potential, respectively.

Since the beam is assumed to be quasi-stationary, A_{z0} can be found from

$$\frac{1}{r}\frac{\partial}{\partial r}\left(r\frac{\partial A_{z0}}{\partial r}\right) = -\frac{4\pi}{c}J_{z0}, \quad (3)$$

where J_{z0} is the equilibrium value of the z-component of net current density in the beam–plasma system.

Note that the terms of the sum under the integral in (2) represent the effect of magnetic field on the respective portions of beam current density: the first term refers to the stabilizing action of an equilibrium magnetic field on J_{b1}, whereas the second one refers to the destabilizing action of the magnetic field of channel eddy current (resulting from beam deflection) on J_{b0}.

In the context of the rigid-beam model [1], we have for the perturbed component

$$J_{b1} = -Y\frac{\partial J_{b0}}{\partial r}. \quad (4)$$

If the perturbation of σ_c is negligible, then A_{z1} meets the equation

$$\frac{\partial}{\partial r}\frac{1}{r}\left(\frac{\partial}{\partial r}rA_{z1}\right) - \frac{4\pi\sigma_p}{c^2}\frac{\partial A_{z1}}{\partial \tau} = -\frac{4\pi}{c}J_{z1}, \quad (5)$$

where

$$\sigma_p(r) = \begin{cases}\sigma_c, & r < R_W,\\ \sigma_W, & R_W \le r \le R_W + S,\end{cases} \quad (6)$$

and J_{z1} is the perturbed value of the z-component of net current density in the plasma–beam system.

The boundary conditions for A_{z0} and A_{z1} are, respectively,

$$\left.\frac{\partial A_{z0}}{\partial r}\right|_{r=0} = 0, \quad \left.\frac{1}{r}\frac{\partial}{\partial r}\left(r\frac{\partial A_{z0}}{\partial r}\right)\right|_{r=\infty} = 0 \quad (7)$$

and

$$A_{z1}|_{r=0} = 0, \quad \left.\frac{1}{r}\frac{\partial}{\partial r}(rA_{z1})\right|_{r=\infty} = 0. \quad (8)$$

In view of (3)–(5) and (7)–(8), equation (2) is recast to

$$\frac{\partial^2 Y}{\partial z^2} = 2\left(\frac{I_b}{I_A}\right)\frac{\pi}{I_b}\int_0^\infty dr I_b(r)\left[Y\frac{\partial J_{z0}}{\partial r} + J_{z1}\right], \quad (9)$$

where $I_b(r)$ is the beam current through a cylinder of radius r.

Since the beam is paraxial and its charge is fully neutralized, the charge conservation law implies:

$$\frac{\partial J_{z0}}{\partial \tau} + \frac{J_{z0}}{\tau_m} = \frac{J_{b0}}{\tau_m}, \quad (10)$$

and

$$\frac{\partial J_z}{\partial \tau} + \frac{J_{z1}}{\tau_m} = -\frac{Y}{\tau_m}\frac{\partial J_{b0}}{\partial r}, \quad (11)$$

where,

$$\tau_m(\tau) = \frac{2\pi\sigma_c(\tau)R_b^2(\tau)}{c^2}\ln\frac{R_W}{R_b} \quad (12)$$

is the skin time.

For the sake of simplicity, assume that J_{b0} is independent of τ. It then follows from (9)–(11) that

$$\frac{\partial^2 Y}{\partial z^2} = F_W + F_h, \quad (13)$$

where,

$$F_W = 2\pi\frac{I_W}{I_b}\left(\frac{I_b}{I_A}\right) \quad (14)$$

and

$$F_h = -k_s^2 Y(1 - f_m) + k_s^2\int_{-\infty}^{\tau} d\xi \exp G(\tau, \xi)\frac{Y(z, \xi)}{\tau_m(\xi)} \quad (15)$$

are, respectively, the force acting on the beam from the channel eddy current and the force from the equilibrium and dipole eddy currents in the plasma ($r < R_W$). In (14) and (15),

$$I_W = \int_{R_W}^{R_W + S} dr J_{z1}(r, \tau) \tag{16}$$

is the channel eddy current per unit length, f_m is the magnetic neutralization fraction,

$$k_s^2 = 4\pi^2\left(\frac{}{I_A}\right)\int_0^\infty dr r\left(\frac{J_{b0}(r)}{I_b}\right)^2 \tag{17}$$

is the hose wavenumber, and

$$G(\tau, \xi) = \int_\tau^\xi \frac{d\mu}{\tau_m(\mu)}. \tag{18}$$

Owing to $S \ll R_W$, we can regard I_W as a surface eddy current. With (1), we then have

$$\left.\frac{\partial A_{z1}}{\partial r}\right|_{R_W^-} - \left.\frac{\partial A_{z1}}{\partial r}\right|_{R_W^+} = \frac{4\pi}{c} I_W, \tag{19}$$

and

$$I_W = -\frac{1}{c}\frac{\partial A_{z1}}{\partial \tau}\sigma_W S|_{R_W}. \tag{20}$$

Solving the Ampere equation for A_z and A_{z1} under corresponding boundary conditions with the help of (10), (11), (16), (19), and (20), we arrive at the following equation for I_W:

$$\frac{\partial I_W}{\partial \tau} + \frac{I_W}{\tau_W} = -\frac{1}{\pi R_W^2 \tau_m}\int_{-\infty}^{\tau} d\xi \exp[G(\tau, \xi)]\frac{\partial [Y(z, \xi) I_b(\xi)]}{\partial \xi}, \tag{21}$$

where $\tau_W = 2\pi S R_W/c^2$ is the skin time for channel eddy currents.

Let us concentrate on the tracking force F_W. Due to (14) and (21),

$$F_W = -\frac{k_W^2}{I_b}\int_{-\infty}^{\tau} d\xi \exp\left(\frac{\xi - \tau}{\tau_W}\right)\frac{1}{\tau_m(\xi)} \times \int_{-\infty}^{\xi} d\eta \exp[G(\xi, \eta)]\frac{\partial [Y(z, \eta) I_b(\eta)]}{\partial \eta}, \tag{22}$$

where $k_W^2 = 2I_b/(I_A R_W^2)$.

Consider the case where the current in a beam pulse rises as

$$I_b(\tau) = I_{b0}\tanh\left(\frac{\tau}{\tau_r}\right). \tag{23}$$

where τ_r is the characteristic current rise time.

For simplicity, we assume that $Y(z, \tau)$ is independent of τ. Then, from (22) and (23),

$$F_W = -\left(\frac{2R_b}{R_W^2}\right)\left(\frac{I_{b0}}{I_A}\right)\frac{Y_1}{\xi_m \Omega}\exp\left(-\frac{\xi}{\xi_W}\right) \times \int_{-\infty}^{\xi} d\lambda[\exp(\Omega\xi) - \exp(\Omega\lambda)] \times \exp\left(\frac{\lambda}{\xi_m} + \frac{2\lambda}{\xi_r}\right)\frac{4}{\xi_r\left[\exp\left(\frac{2\lambda}{\xi_r}\right) + 1\right]^2}, \tag{24}$$

where $\Omega = (\xi_m - \xi_W)/(\xi_m \xi_W)$, $Y_1 = Y/R_b$,

$$\xi_m = \frac{2\pi\sigma_c R_b}{c}\ln\left(\frac{R_W}{R_b}\right), \quad \xi_W = \frac{2\pi\sigma_W S R_W}{c R_b}. \tag{25}$$

Here, ξ_m and ξ_W are the dimensionless skin lengths for the plasma and waveguide, respectively.

Figure 1 depicts the dependence of $F_{W1} = -F_W/F_0$ ($F_0 = 10^{-3}$ [1/cm]) on $\sigma_1 = \sigma_W/\sigma_0$ ($\sigma_0 = 10^{12}$ 1/s) for $S = 0.05$, $R_W/R_b = 1.5$, $R_b = 1$ cm, $I_{b0} = 10$ kA, $\gamma = 10$ ($E = 5$ MeV), $Y_1 = 0.5$, $\xi_1 = \xi/R_b = 50$, $\xi_{r1} = \xi_r/R_b = 15$, $\sigma_{c1} = \sigma_c/\sigma_0 = 1$. Notice that F_{W1} is very sensitive to channel conductivity.

Figure 2 displays the dependence of $\Re = |R_W/F_{sh}|$ on $\sigma_1 = \sigma_W/\sigma_0$ at $f_m = 0.5$, the other parameters being the

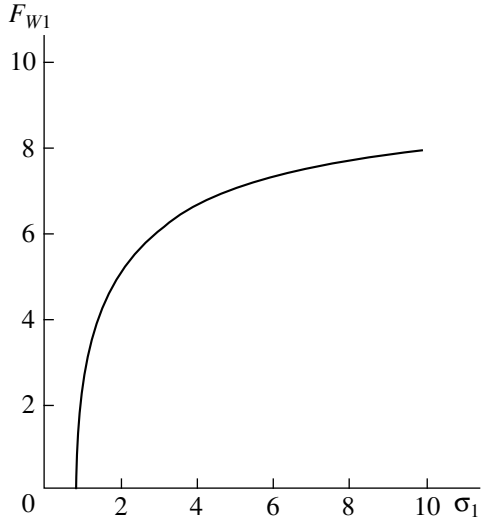

Fig. 1. Tracking force F_{W1} vs. normalized waveguide conductivity.

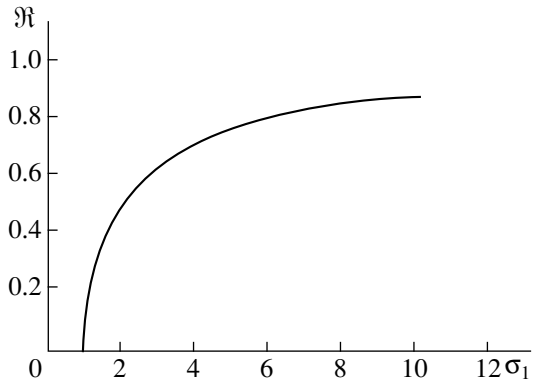

Fig. 2. Ratio of the tracking force F_W to the force F_{sh} vs. normalized waveguide conductivity.

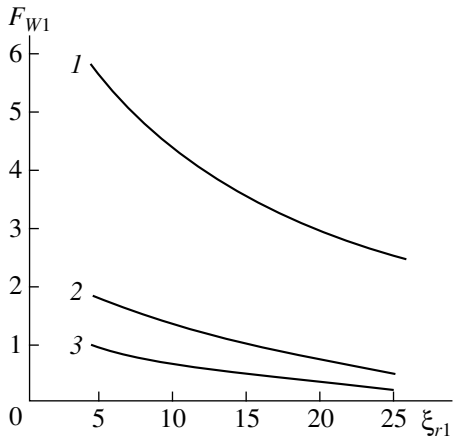

Fig. 3. Tracking force F_{W1} vs. beam-current rise time at η = (*1*) 2, (*2*) 3, and (*3*) 4.

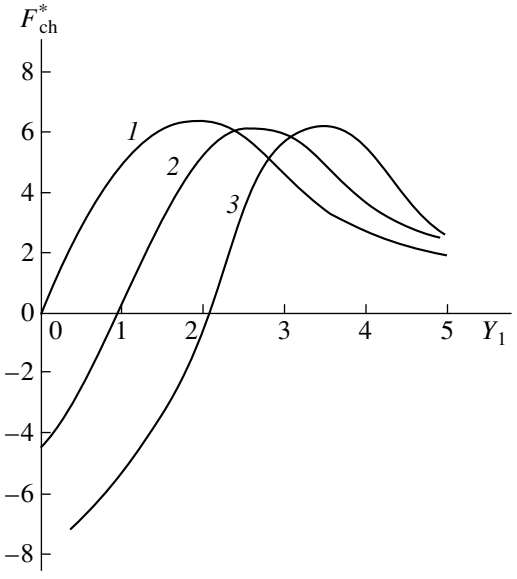

Fig. 4. Normalized force of interaction between the ion plasma channel and the beam vs. the normalized displacement Y_1 of the beam axis at D_1 = (*1*) 0.5, (*2*) 1, and (*3*) 2.

same as in Fig. 1. Here, $F_{sh} = f_m k_s^2 Y$ is the tracking force experienced by the perturbed portion of the beam from the unperturbed component of the magnetic field in the plasma–beam system. Notice that F_{W1} becomes comparable to F_{sh} at the given Y_1 if $\sigma_1 \geq 2$.

Figure 3 shows the dependence of F_{W1} on the current rise time of the beam pulse, $\xi_{r1} = \xi_r/R_b$, for different values of $\eta = R_W/R_b$ at $\sigma_1 = 10^2$, $I_{b0} = 10$ kA, $\gamma = 10$, $R_b = 0.5$ cm, $S = 0.1$, $\xi_1 = 20$, and $\sigma_{c1} = 1$. It is seen that F_{W1} is very sensitive to η and the characteristic current rise time of the beam pulse ξ_r.

Now, let us proceed to the case of a perfectly conducting waveguide with a relativistic electron beam propagating under the IFR. Recall that we are dealing with the rigid-beam model (the radial beam profile is assumed to remain undistorted). We will study the tracking force as a function of D and Y and compare it with F_{ch}.

The IFR means that the pressure in a background gas–plasma medium is low so as to suppress additional ionization of the background plasma by the electrons that leave the beam region of the preformed plasma channel under the action of the transverse component of the beam-head electric field. The ionization is negligible if

$$\lambda_1 \gg R_b, \tag{26}$$

where λ_1 is the characteristic buildup length of avalanche ionization and R_b is the characteristic beam radius [15, 23, 24].

As demonstrated in [23, 24], constraint (26) is satisfied if

$$\frac{E}{P_g} \gg 1 \left[\frac{\text{keV}}{\text{cm torr}}\right], \tag{27}$$

where E is the transverse component of the beam-head electric field and P_g is the pressure of the background gas.

For nitrogen, we have [24]

$$\frac{E}{P_g} > 30 \left[\frac{\text{keV}}{\text{cm torr}}\right]. \tag{28}$$

The above condition is met if

$$P_g < P_{g1} = \frac{1}{R_b}\left(\frac{I_b}{10}\right), \tag{29}$$

where I_b is the net beam current, kA; R_b is the beam radius, cm; and P_{g1} is the critical pressure of the background gas, torr.

If $I_b = 10$ kA and $R_b = 1$ cm, then IFR condition (4) becomes

$$P_g < 1 \text{ [torr]}. \tag{30}$$

Consider an axially symmetric paraxial monoenergetic beam propagating in a low-density gas contained in a preformed plasma channel. Assume that the system is confined to a grounded cylindrical perfectly conducting waveguide of radius R_W. Initially, the waveguide is coaxial with the beam–channel system. Take a cylindrical coordinate system (r, θ, z) with the z-axis aligned with the waveguide axis. The background gas pressure is supposed to be such that (26) and (27) are met. Also, assume that

$$f_n = \frac{N_i}{N_b} \le 1, \tag{31}$$

where f_n is the charge neutralization fraction (due to plasma ions) and N_i and N_b are the concentrations of channel ions and beam electrons per unit length, respectively.

Let the beam be ultrarelativistic so that the Lorentz factor γ is much larger than unity, $\gamma \gg 1$. In the context of the rigid-beam model, the radial concentration profiles for beam electrons and channel ions are Gaussian with characteristic radii R_b and R_i, respectively.

In a perfectly conducting and grounded waveguide, a displaced ion channel induces a charge on its wall as IHI develops, which is equivalent to the creation of the electrostatic image at the distance R_W^2/D from the waveguide axis. According to [15–21, 25], neglecting the mixing of phase trajectories for beam electrons allows us to write

$$\frac{\partial^2 Y}{\partial z^2} = F_{\rm ch} + F_{\rm tr}, \tag{32}$$

where

$$F_{\rm ch} = -2R_b^2 k_{se}^2 \Omega(R_b, R_i, Y, D), \tag{33}$$

$$F_{\rm tr} = -2R_b^2 k_{se}^2 \Omega(R_b, R_i, L, Y), \tag{34}$$

$$\Omega(\xi, \mu, A, B) \equiv \frac{1}{(A-B)}\left[1 - \exp\left(-\frac{|A-B|^2}{\xi^2 + \mu^2}\right)\right]. \tag{35}$$

Equation (32) describes the dynamics of IHI. In (35), ξ, μ, A, and B are the arguments of the function Ω. In (33) and (34), $L = R_W^2/D$ is the distance from the waveguide axis to the image of the displaced ion channel, Y and D are, respectively, the displacement of the center-of-mass axis of the beam and that of the channel axis, $k_{se}^2 = (I_b f_n)/(I_A R_b^2)$ is the squared betatron wavenumber of beam electrons; I_b and I_A are, respectively, the beam current and the limiting Alfven current; and f_n is the charge neutralization fraction. In the right-hand side of (32), $F_{\rm ch}$ is the force of interaction between the beam and the ion channel when their centers of mass are displaced from the waveguide axis and $F_{\rm tr}$ is the tracking force due to the interaction of the beam and the electrostatic image of the ion channel. The latter force always plays a stabilizing role.

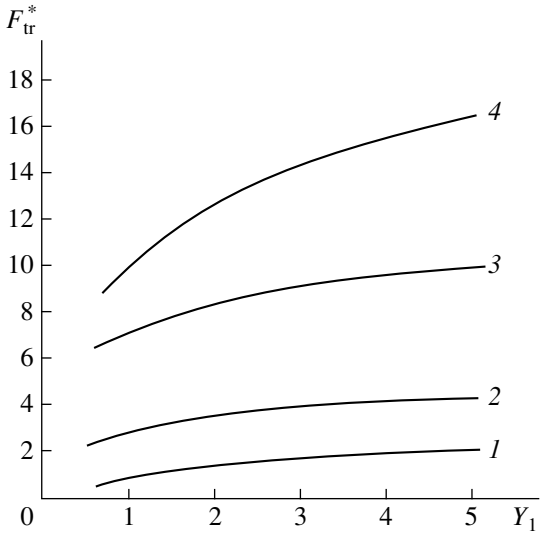

Fig. 5. Normalized tracking force $F_{\rm tr}^*$ vs. Y_1 at D_1 = (*1*) 0.5, (*2*) 1, (*3*) 2, and (*4*) 3.

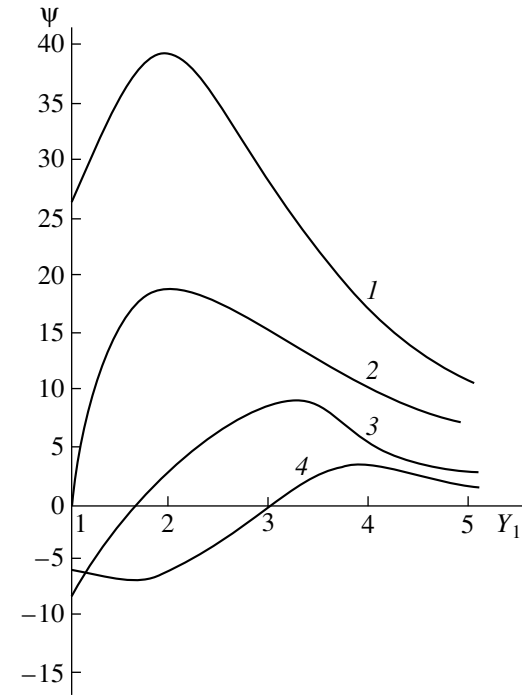

Fig. 6. Force ratio $\Psi = F_{\rm ch}/F_{\rm tr}$ vs. Y_1 for D_1 values the same as in Fig. 5.

Note that formulas (33)–(35) are valid for arbitrary displacements of the beam and the channel. Thus, they also apply to the nonlinear phase of IHI, when $Y_1 = Y/R_b \ge 1$ and $D_1 = D/R_b \ge 1$. Furthermore, we can neglect the images of the charge and current of the beam itself, since the beam is ultrarelativistic.

Figure 4 depicts the dependence of $F_{ch}^* = -F_{ch}/F_0$ ($F_0 = 10^{-2}$ cm^{-1}) on $Y_1 = Y/R_b$ at different values of $D_1 = D/R_b$. The other parameters are $\eta = R_W/R_b = 6$, $f_n = 0.5$, $R_b = 0.5$ cm, $I_b = 10$ kA, $\gamma = 10$ ($E = 5$ MeV), and $R_{11} = R_1 R_b = 0.5$. Note that Fig. 1 is drawn at $Y_1 \leq 5$, since $\eta = 6$.

Figure 5 displays the dependence of the tracking force $F_{tr}^* = -F_{tr}/F_1$ ($F_1 = 10^{-3}$ cm^{-1}) on $Y_1 = Y/R_b$ and $D_1 = D/R_b$ for the nonlinear phase of IHI (when $Y_1 \geq 1$). The value of F_{tr}^* rises to become comparable to F_{ch}^* as D_1 increases.

Figure 6 presents the dependence of $\Psi = F_{ch}/F_{tr}$ on Y_1 and D_1 for the nonlinear phase of IHI ($Y_1 \geq 1$). The two forces are comparable to each other for large deflections ($D_1 \geq 3$). Figures 5 and 6 are obtained with parameter values similar to those for Fig. 4.

REFERENCES

1. E. P. Lee, Phys. Fluids **21**, 1327 (1978).
2. H. S. Uhm and M. Lampe, Phys. Fluids **23** (8), 1574 (1980).
3. W. M. Sharp, M. Lampe, and H. S. Uhm, Phys. Fluids **25**, 1456 (1982).
4. E. R. Nadezhdin and G. A. Sorokin, Fiz. Plazmy **9**, 988 (1983) [Sov. J. Plasma Phys. **9**, 576 (1983)].
5. E. R. Nadezhdin and G. A. Sorokin, Fiz. Plazmy **14**, 619 (1988) [Sov. J. Plasma Phys. **14**, 365 (1988)].
6. E. K. Kolesnikov and A. S. Manuĭlov, Zh. Tekh. Fiz. **60** (3), 40 (1990) [Sov. Phys.–Tech. Phys. **35**, 298 (1990)].
7. D. P. Murphy, M. Raleigh, R. E. Pechacek, *et al.*, in *Proc. 5th Int. Conf. on High Power Particle Beams, San Francisco, 1983*, pp. 389–392.
8. R. F. Fernsler, S. P. Slinker, and R. F. Hubbard, Phys. Fluids B **3**, 2696 (1991).
9. D. P. Murphy, R. E. Pechasek, D. P. Taggart, *et al.*, Phys. Fluids B **4**, 3407 (1992).
10. D. R. Welch and B. B. Godfrey, Phys. Rev. Lett. **65**, 3128 (1990).
11. E. K. Kolesnikov and A. S. Manuĭlov, Zh. Tekh. Fiz. **61** (12), 43 (1991) [Sov. Phys.–Tech. Phys. **36**, 1351 (1991)].
12. E. K. Kolesnikov and A. S. Manuĭlov, Zh. Tekh. Fiz. **67** (6), 69 (1997) [Tech. Phys. **42**, 648 (1997)].
13. E. K. Kolesnikov and A. S. Manuĭlov, Zh. Tekh. Fiz. **67** (12), 78 (1997) [Tech. Phys. **42**, 1442 (1997)].
14. R. E. Fernsler, R. F. Hubbard, and M. Lampe, J. Appl. Phys. **75**, 3278 (1994).
15. H. L. Buchanan, Phys. Fluids **30**, 221 (1987).
16. R. A. Bosch and R. M. Gilgenbach, Phys. Fluids **31**, 634 (1988).
17. R. F. Lucey, R. M. Gilgenbach, J. D. Miller, *et al.*, Phys. Fluids B **1**, 430 (1989).
18. V. B. Vladyko and Yu. V. Rudyak, Fiz. Plazmy **17**, 623 (1991) [Sov. J. Plasma Phys. **17**, 366 (1991)].
19. S. E. Rosinskiĭ and V. G. Rukhlin, Zh. Tekh. Fiz. **42** (3), 511 (1972) [Sov. Phys.–Tech. Phys. **17**, 405 (1972)].
20. E. K. Kolesnikov and A. S. Manuĭlov, Radiotekh. Élektron. (Moscow) **37**, 694 (1992).
21. E. K. Kolesnikov and A. G. Zelenskiĭ, Zh. Tekh. Fiz. **65** (5), 188 (1995) [Tech. Phys. **40**, 510 (1995)].
22. E. K. Kolesnikov and A. D. Savkin, Pis'ma Zh. Tekh. Fiz. **20** (1), 54 (1994) [Tech. Phys. Lett. **20**, 26 (1994)].
23. R. J. Briggs and S. S. Yu, Livermore Lab. Report UCID-19399 (1982), p. 47.
24. A. W. Ali, Laser Part. Beams **6**, Part 1, 105 (1988).
25. R. F. Fernsler, R. F. Hubbard, and S. P. Slinker, Phys. Fluids B **4**, 4153 (1992).

Translated by A. A. Sharshakov

Technical Physics, Vol. 45, No. 5, 2000, pp. 597–604. Translated from Zhurnal Tekhnicheskoĭ Fiziki, Vol. 70, No. 5, 2000, pp. 74–81.

ELECTRON AND ION BEAMS, ACCELERATORS

Forming a Beam of Ions Extracted from Glow-Discharge Plasma

N. V. Gavrilov[1] and D. R. Emlin[2]

[1] *Institute of General Physics, Russian Academy of Sciences, Moscow, 117942 Russia*

[2] *Institute of Electrophysics, Ural Division, Russian Academy of Sciences, Komsomol'skaya ul. 34, Yekaterinburg, 620049 Russia*

Received December 10, 1998

Abstract—In plasma-emitting structures based on glow-discharge, the potential difference between the ion-emitting plasma and the screening electrode of an ion-optic system depends on particular features of the electrode system of glow discharge and can vary in a range 0–1 kV. Results are presented of an experimental study and computer simulation of the formation of ion beams with ion energy 0–1 keV and current density 1–10 mA/cm^2 in ion sources based on such structures. © *2000 MAIK "Nauka/Interperiodica".*

INTRODUCTION

Basic requirements for ion beams of large cross section used for modifying surfaces of materials are high current density j and its uniform distribution $j(r)$ over the beam cross section. These parameters of beams formed by multiaperture electrostatic ion-optics systems depend not only on the density and spatial uniformity of the emitting plasma, but also on the beam angular divergence and drift region length. Considerable angular divergence, besides reducing the average current density, transforms a uniform beam into one with a gaussian profile [1]. Therefore, the divergence angle of the flows formed in elementary cells of ion optics should be a minimum. On the other hand, these flows should still have some angular spread so that their overlap could make $j(r)$ distribution uniform over a specified cross section. Thus, one of the main problems in forming wide uniform beams with the use of multiaperture electrostatic ion optics is the provision of an optimum angular beam divergence, which would eliminate both small-scale undulations of $j(r)$, revealing the discrete structure of the optics when the divergence angle is too small, and the large-scale nonuniformity of $j(r)$ arising from beam current redistribution at large divergence angles. The main problem in systems with low-energy beams is to reduce the divergence angle, whereas in high-energy beams with rather low purveyance, both of these nonuniformity types may occur when the beam parameters are varied in wide limits.

Alongside such characteristics of the beam and the ion optics as the normalized beam purveyance per hole (NPH) [2], the ratio of the accelerating gap length to the optics hole radius [3], and the ratio R of the potential difference determining the ultimate ion energy to the total voltage across the accelerating gap [4], plasma-emission structures using glow discharge have a distinctive feature: beam forming is significantly affected by the potential difference $\Delta\phi$ between the plasma and the screening electrode of the optics, which may vary in wide limits. The ion-emitting plasma can be produced either in anode or in cathode cavities, depending on the type of glow-discharge electrode system used [5]. Because the optics forming a wide beam have a large-area screening electrode in contact with the plasma, the potential of this electrode has a considerable effect on the discharge characteristics and cannot be chosen arbitrarily. In the discharge with a hollow cathode, high potential of the elements of the electrode system in contact with plasma is the cause of higher rates of loss of fast electrons making it necessary to raise of the arc voltage and gas pressure [6]. In plasma-emission structures of this type [7, 8], between the plasma generated in the cathode cavity and the screening electrode held under cathode potential, there exists a space-charge layer; the drop of potential over this layer $\Delta\phi$ amounts to hundreds of volts, depending on the arc voltage, and its thickness can vary from fractions of a millimeter to a few millimeters.

In structures where ions are swept out from the plasma in the anode cavity of the glow-discharge electrode system through holes in the screening electrode held at a floating potential, there also forms a near-electrode layer with considerable potential drop across it. Because of the presence in the glow-discharge plasma of primary electrons emitted by the cathode and having an average energy which depends on the extent of their energy relaxation and can be much higher than the thermal energy, the floating potential of the screening electrode proves to be considerably lower (by 100–200 V) than the plasma potential.

The presence of a layer with large potential drop and of considerable thickness influences the shape of the emitting surface and conditions of ion extraction from plasma and of beam forming.

1063-7842/00/4505-0597$20.00 © 2000 MAIK "Nauka/Interperiodica"

This work presents the results of an experimental study and computer simulation of the formation of argon ion beams with ion energy 0–50 keV and current density 1–10 mA/cm^2 in systems with plasma ion emitter based on glow discharge.

EXPERIMENTAL RESULTS

The formation of argon ion beams was studied experimentally in two energy ranges, 1–3 and 30–50 keV. Three-electrode accelerating–decelerating ion-optics systems were used with holes of the same diameter d in all electrodes equal to 3 mm in low-energy optics and 10 mm in high-energy optics. The ratio R of the voltage U_n, determining the ultimate ion energy at the exit of the forming system to the overall accelerating voltage U_t for the high-energy optics, was determined from the reflection condition for the reverse electron flow and was close to unity. In forming low-energy beams, R was varied in the range 0.25–1 in order to find out conditions for obtaining the minimum beam divergence angle ω for a specified ultimate energy of ions and emission current density. Dimensions of the optics elementary cell, the accelerating voltage, and the ion emission current density were chosen in such a way as to ensure the possibility, in both energy ranges, of varying the value of normalized purveyance per hole in some interval around the values $1–3 \times 10^{-9}$ A/V$^{3/2}$. The maximum value of NPH is given by the formula [2]

$$(I/U_t^{3/2})(l_c d)^2 = \pi\varepsilon_0/9(2q/M)^{1/2}, \qquad (1)$$

and for argon it is 6.79×10^{-9} A/V$^{3/2}$. Here, I is the beam current; q, M are the charge and mass of an ion, respectively; $l_c = (l^2 + d^2/4)^{1/2}$ is the effective length of the accelerating gap; and l, d are the length of the accelerating gap and diameter of the optics apertures. According to [2], in forming argon ion beams with minimum divergence angles, NPH values smaller by a factor of 2–3 than the limiting value should be used. However, one has to bear in mind that the presence of a layer where the ions acquire the initial energy, which is a significant fraction of the total energy of ions in the accelerating gap, makes the use of expression (1) for estimating NPH incorrect. Under these conditions, the value of R is defined as the ratio of the supply voltage determining the ultimate ion energy to the output voltage of the source connected between the glow-discharge anode and the accelerating electrode, which gives an estimate of the ion deceleration rate, but is at variance with the definition of U_t in [2] as the total voltage across the accelerating gap.

Different electrode systems of glow discharge were used with generation of the ion emitting plasma both in the cathode and anode cavities. The ion-optics screening electrode potential was measured relative to the discharge system anode and was equal to 500–700 V for an electrode connected to the cathode and 150–180 V for an isolated electrode. Discharge regimes were used with the plasma potential close to the anode potential. According to results of mass-spectrometric study of plasma composition in the anode cavity of a glow-discharge [5, 7, 8], the content of doubly charged argon ions did not exceed 10% and the content of metal ions in plasma could reach a few percent. A moveable probe was used in the experiments for measuring radial current density profiles in the wide beam and the beam formed by the optics elementary cell, as well as the beam current and currents in the circuits of the ion-optics electrodes. The measurement results were used for estimating the efficiency of ion extraction from the plasma, losses of the current of accelerated ions, and the beam angular divergence.

(a) *Formation of low-energy beams*. For this experiment, a glow-discharge electrode system with hollow anode and hollow cathode under applied magnetic field was designed, which was capable of producing an emitting plasma of higher homogeneity. Ions were extracted from plasma generated inside the anode cavity of the discharge system, and the screening electrode potential could therefore be varied from the floating to the cathode potential without significantly changing the discharge characteristics. An additional factor in reducing the differences between conditions for discharge and the plasma density generated in the two regimes was the use of multiaperture optics. The large total area of the apertures made the accelerating field an effective means of controlling the discharge conditions. The nonuniformity of the radial distribution of the emitting plasma density did not exceed 5% in a circle 80 mm in diameter, which corresponded to the optics diameter. An ion emission current density of $j_e \sim 1$ mA/cm^2 was achieved with a discharge current of 0.7 A and arc voltage of 670 V. The gas flow leaked into the discharge system was kept constant at 10 cm^3 × atm/min; the pressure in the vacuum chamber was 10^{-2} Pa. The diameter of the optics apertures was 3 mm, the accelerating gap length was variable in the range 2–4 mm, the decelerating gap of 2 mm was kept constant, and the electrode thickness was 1.2 mm. The total area of the optics holes was 25 cm^2. The source operated in a self-compensation regime of the beam space charge.

Plots illustrating the effect of R on forming conditions for an ion beam of energy $eU_n = 1$ keV with optics having an accelerating gap length of $l = 4$ mm with the screening electrode at the cathode and floating potentials are shown in Figs. 1 and 2, respectively. The maximum beam current, close to the current of ion emission from plasma, is achieved at minimum R values. In the system with the screening electrode at the cathode potential (Fig. 1), an increase in R leads to a drastic drop in the beam current, but the ion emission current from plasma measured in the voltage source circuit U_n changed insignificantly. With the screening electrode at the floating potential (Fig. 2), the beam current decreases continuously with increasing R and its value differs insignificantly from the ion emission current.

Beam profile measurements were carried out with the use of a translating Faraday cylinder at a negative potential of –100 V encased in a grounded housing. The entrance hole had a diameter of 1.5 mm. The overall beam divergence angle was estimated by the measured beam profile data at $2\omega = 1/2(l_{0.9} - l_{0.1})/L$, where $l_{0.1}$, $l_{0.9}$ are beam width values at the 0.1 and 0.9 levels of the current amplitude, respectively, and L is the length of the beam drift region. The factor 1/2 takes into account the fact that the beam, spreading because of angular divergence, results in both broadening of the beam profile at the bottom and narrowing of the plateau at the profile top [1]. The minimum angle $\omega \sim 5°$ in the system with floating potential was observed for $R \sim 0.5$. The value of R at the cathode potential was around 0.4, but the beam current was about half as great on account of ion loss at the optics electrodes. Reduction of the accelerating gap length to 2 mm improved the beam formation in the system with a cathode layer at small R, but caused higher loss of beam current in the system with floating potential at large R values.

(b) *Formation of high-energy beams*. Beam formation in the optics elementary cell was studied in an ion source based on discharge with a hollow cathode in a magnetic field [7], in which single-aperture optics with holes 10 mm in diameter were substituted for multiaperture optics and the accelerating gap length was variable within 10–15 mm. The optics electrodes had a thickness of 1.5 mm. The emitting plasma was produced in the cathode cavity and the optics screening electrode also had the cathode potential. The pulsed arc voltage at a current of 5–15 A was 400–500 V. The emission current density of argon ions varied in the range 3–10 mA/cm^2. The ion beam profile was measured at a distance of 300 mm from the optics using a probe in the form of a tungsten wire 0.5 mm in diameter, which was translated along a slit of 2-mm width. In Fig. 3, beam profiles obtained at an ion emission current density of 10 mA/cm^2 and different values of the accelerating voltage are presented. In Fig. 4, plots of the total divergence angle as a function of accelerating voltage are given for different values of the emission current density. The divergence angle was estimated from the ratio of the beam profile full width at half height to the beam drift region length. As seen in Fig. 4, the minimum angle of divergence is close to 0.02 rad and the NPH values, corresponding to the minima of curves *1* and *2*, are 1.5×10^{-9} and 2×10^{-9} A/V$^{3/2}$, respectively. With decreasing current density and increasing layer width, the normalized purveyance becomes lower.

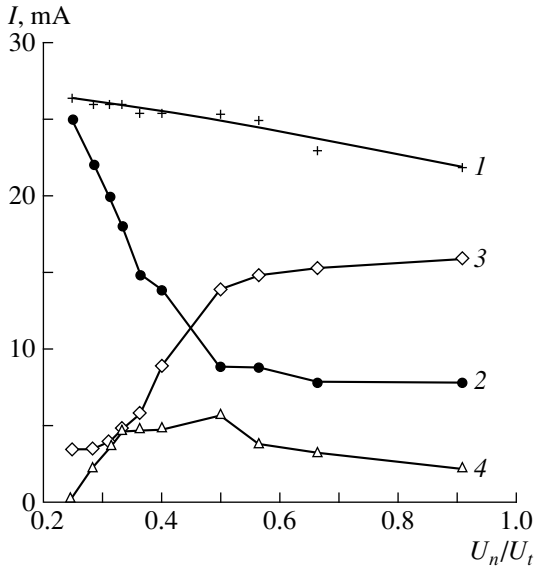

Fig. 1. Variations with the voltage ratio R of the (*1*) current of argon ions at the entrance to the optics, (*2*) ion beam current, (*3*) current flowing to the accelerating electrode, and (*4*) current flowing to the decelerating electrode. The screening electrode is at the cathode potential.

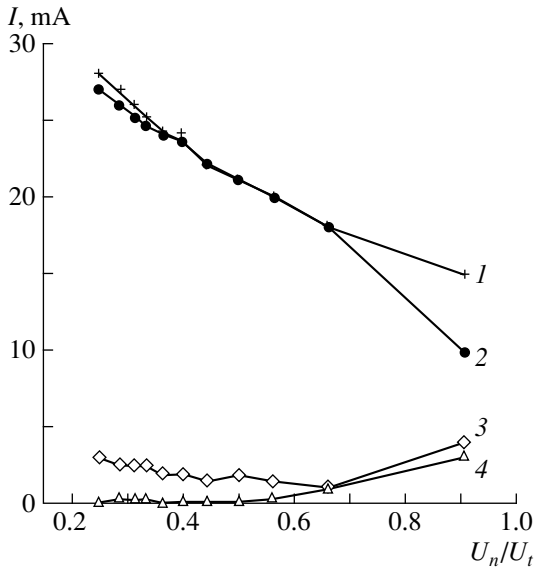

Fig. 2. Same as in Fig. 1, with the screening electrode at floating potential ($\Delta\varphi$ = 160 V).

Simulation Results

The BEAM-CAD program developed by Yu. A. Kovalenko (All-Russia Electrotechnical Institute, Moscow) was used in simulations of the conditions of ion beam formation with single-aperture three-electrode accelerating–decelerating optics in two ion energy ranges, 0.5–3 and 20–50 keV. The ion emitter was an argon plasma with a density of singly charged ions $n \sim 3 \times 10^{10}$–3×10^{11} cm^{-3} and an electron temperature of 5–10 eV. The calculations were performed with a view to elucidating the effect of the layer on the ion extraction and initial beam forming processes; therefore, for the sake of simplicity, the influence of the beam plasma was neglected. The presence in the glow-discharge plasma of fast electrons was also not taken

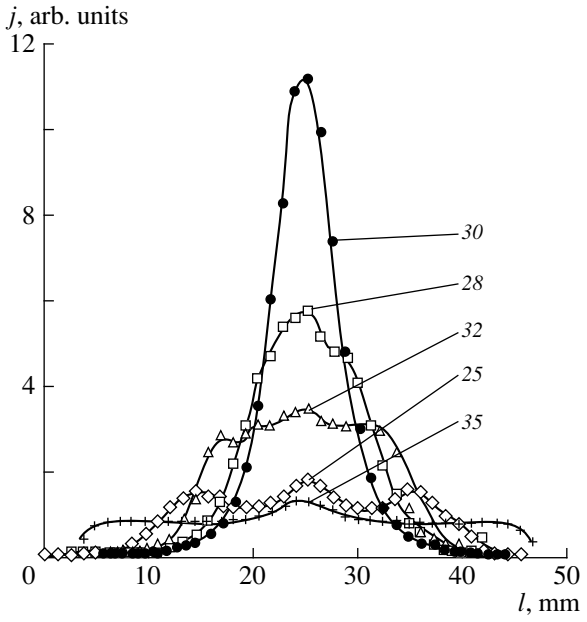

Fig. 3. Density profiles of the beams formed at different voltages across the accelerating gap (in kV, indicated by numbers at the curves). The discharge current is 15 A, and voltage is 500 V.

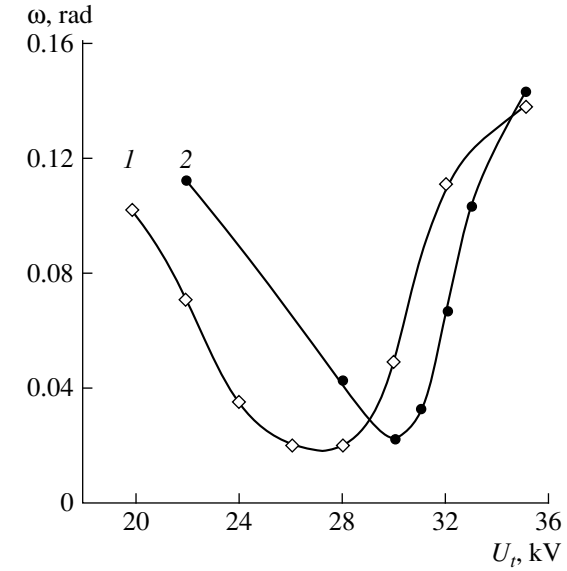

Fig. 4. Dependence of the full beam divergence angle on the accelerating voltage at different current density values j_e, mA/cm^2: (*1*) 6.7, (*2*) 10; $l = d = 10$ mm.

into account in the model. Therefore, estimates of the floating potentials and ion emission current densities were approximate. Because of the adopted approximations and assumptions, the derived relationships are for the most part qualitative. The program uses the usual calculation algorithm, which specifies the geometry and potential distribution of the optics electrodes, as well as the initial position of the plasma surface and its ion-emitting properties. Then the solution of the Laplace equation for specified boundaries is obtained and the ion trajectories calculated. The next step is the calculation of the ion space-charge density and solution of the Poisson equation. After a number of iterations, the plasma boundary is displaced in such a way as to have a zero electric field strength at the plasma surface. Calculations are continued until a self-consistent solution is obtained. Beam formation conditions for minimum loss at the optics electrodes are determined; and a half-angle ω of the beam divergence and distribution of the current density $j(r)$ in a given cross section is calculated, as well as the relationship between the current of ions lost to the screening electrode and the beam current. The screening electrode potential was taken as $\Delta\phi = 0.150$ and 500 V, which corresponded to the floating and cathode potentials at the screening electrode.

Figure 5 shows calculation results of the optics dimensions and R values required for obtaining minimum angular divergence of a beam of 1 keV argon ions at the ion emission current density from the plasma equal to 2 mA/cm^2 in the absence of the layer ($\Delta\phi = 0$). The calculation was carried out for three optical system designs with identical hole diameters $d = 4$ mm and decelerating gap lengths $l_d = 2$ mm. The length l of the accelerating gap and the voltage U_t for the three designs were different and chosen such as to have NPH equal to one-half of its maximum value. It follows from the obtained results that at $R > 0.3$ and $\Delta\phi = 0$, values of ω are minimum for the system with the largest gap length l. Considerably lower values of ω at small R for curves *2* and *3* are explained by the focusing action of the electrostatic lens in the aperture of the decelerating electrode. The change of sign of ω is due to the fact that the divergence angle is determined at a distance of 5 mm from the optics, whereas at considerable distances from the optics and low R, the beam is highly divergent. For small l (curve *1*), no focusing is obtained; at $R < 0.3$, the current flowing to the decelerating electrode was much higher.

The calculation results for the beam-forming system with ultimate ion energy 1 keV and the screening electrode at the cathode potential ($\Delta\phi = 500$ V) are shown in Fig. 6. In the calculation, the ion emission current density is 1 mA/cm^2. The diameter of the holes is 3 mm, the decelerating gap length is 2 mm, and the accelerating gap length is varied in an interval of 2–4 mm. As R is reduced, the beam divergence angle decreases; both the beam current I_b and the current I_c of ions extracted from plasma through a hole in the screening electrode increase. The ratio of the currents also rises, owing to lower losses at the accelerating and decelerating electrodes of the optics. Losses also decrease with diminishing accelerating gap length. The relatively small beam divergence angle at the optics exit at $R > 0.5$ is due to the loss to the decelerating electrode of peripheral ions having trajectories at large angles to the axis. A beam without losses at around $R = 0.5$ is formed only

at a minimum gap length of l = 2 mm. At R < 0.5, the beam convergence at the optics exit rises sharply.

Results obtained for the screening electrode at a floating potential ($\Delta\phi$ = 150 V) are given in Fig. 7. At R = 0.5–0.8 the beam passes the optics without losses for all values of the accelerating gap length (l = 2–4 mm). At small gap lengths, the beam diverges abruptly as R is reduced. Considerable field nonuniformity in the screening electrode hole increases aberrations, with the beam crossover failing to form. The deviation angle is highest for peripheral ion trajectories. The ion current at the system entrance and the beam current rise with a reduction of the gap length and an increase in the total accelerating voltage.

Estimates of the ionic layer thickness by the three-halves power law gave a value of ~1.5 mm for the screening electrode at a floating potential and ~3.5 mm at the cathode potential. Because of considerable layer thickness, the plasma meniscus near the optics aperture at low field strengths in the accelerating gap is concave, making the ion beam extracted from the plasma divergent. This reduces the average current density in the beam compared with the saturation density of ion current from the plasma. The initial convergence of the ion beam in the accelerating gap is created by the radial field component in the screening electrode hole. To increase the beam current and convergence in the accelerating gap, a higher accelerating voltage or smaller gap length had to be adopted in the calculations.

Some simulation results for the high-voltage optics at U_t = 30–50 kV and j = 1–30 mA/cm^2 are presented in Fig. 8. The divergence angle ω and the average beam current density j as a function of plasma density n have been calculated for the optics with aperture diameter d = 10 mm, accelerating gap length l = 15 mm, electrode thickness 1.5 mm, and decelerating gap length 5 mm. The $\omega(n)$ functions (curves *1*, *2*) are nonmonotonic, and the beam divergence angle in the minima of the curves is about 0.02 rad. From the $j(n)$ plots (curves *3*, *4*), it follows that the efficiency of ion extraction from the plasma is largely dependent on the accelerating voltage U_t and the density n and is variable in very wide limits. But using the left branches of $\omega(n)$ functions (curves *1, 2*), an optimum combination of U_t and n values can be obtained yielding beam current density values close to the emission current density (dashed curve); and at the beam divergence angles ω > 0.05 rad, the wide beam will be uniform over its cross section 0.2–0.3 m away.

At low plasma density, the average beam current density turns out to be higher than the ion emission current density as a result of the formation of a convex plasma interface focusing ions coming from the surface, which is larger by severalfold than the hole area. It is the higher plasma density that causes the shift of the plasma boundary towards the accelerating gap and the change in its curvature and shape. The drop of the current in the beam is due to redistribution of ions emitted by plasma at the periphery of aperture; there are no beam current losses to the accelerating and decelerating electrodes. The decrease in the beam angular divergence $\omega(n)$ with increasing n is also due to the escape to the screening electrode of the peripheral ions which make the largest contribution to the beam divergence. With a further increase in n, the emitting plasma surface becomes less curved and ω rises.

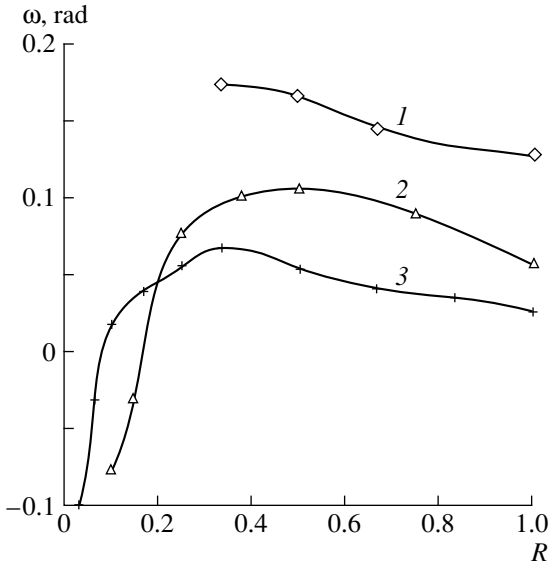

Fig. 5. Dependence of the beam divergence angle on voltage ratio R. *1*—U_t = 1.5 kV, l = 3.75 mm; *2*—U_t = 2 kV, l = 4.75 mm; *3*—U_t = 3 kV, l = 6.5 mm; j_e = 2 mA/cm^2.

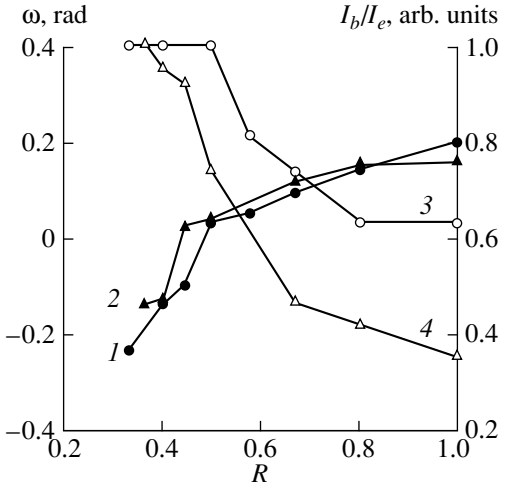

Fig. 6. Plots of the divergence angle (*1*, *2*) and voltage ratio at the optics entrance and exit (*3*, *4*) on R. Ultimate energy of argon ions 1 keV; l = 2 (*1*, *3*) and 4 mm (*2*, *4*).

Thus, results of the experiments and calculations indicate that for reducing the divergence and increasing the intensity of the low-energy ion beams in systems with the cathode layer, the intensity of the accelerating electric field should be raised. In systems forming high-

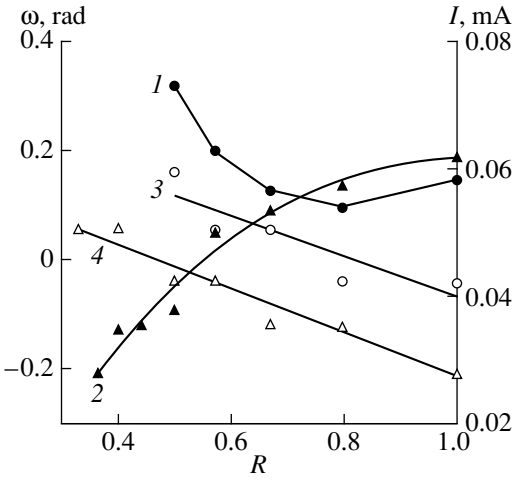

Fig. 7. Plots of the divergence angle (*1*, *2*) and the current at the optics entrance (*3*, *4*) versus voltage ratio R at $\Delta\varphi = 150$ V, $j_e = 1$ mA/cm^2; ultimate energy of argon ions 1 keV; $l = 2$ (*1*, *3*) and 4 mm (*2*, *4*).

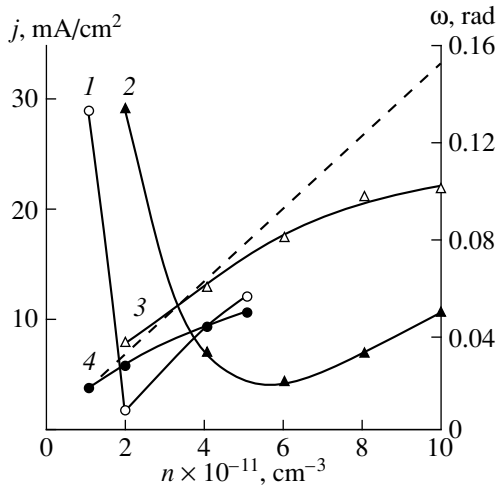

Fig. 8. Plots of the beam divergence angle (*1*, *2*) and the beam current (*3*, *4*) versus plasma density at the accelerating voltages 30 (*1*, *4*) and 50 kV (*2*, *3*). Dashed line is the saturation current due to plasma ions.

energy beams, the presence of a space-charge layer with a voltage drop of a few hundred volts is not an obstacle to producing beams with low angular divergence, but can substantially interfere with the efficiency of ion extraction out of the glow-discharge plasma.

DISCUSSION

Whereas the plasma boundary position in the central part of the optics hole is determined by the potential difference between the plasma and the accelerating electrode and by the saturation current density due to plasma ions, nearer the hole periphery the plasma boundary position is influenced by the space-charge layer between the screening electrode and plasma. At significant layer thicknesses, the emitting plasma surface becomes convex, which affects the current of ions extracted from the plasma as well as the initial beam convergence.

Analysis of a simple ion optics model, not taking into account the effect of the ionic layer, is given in [3]. The model is based on an assumption that the resultant beam divergence angle depends on two effects: convergence of the beam of ions emitted by the spherical plasma surface and propagating in the field of a spherical diode and the divergence produced by the field of electrostatic lens in the hole of the accelerating electrode. The analysis has shown that the minimum beam divergence can be achieved by the right choice of the operating purveyance of the beam. The expression derived in [3] for the half-angle subtended by the beam has the form

$$\omega = 0.29d/2l(1 - 2.14P/P_0), \qquad (2)$$

where P is the beam operating purveyance determined by values of the current and accelerating voltage and P_0 is the maximum purveyance of a planar diode determined by its geometry and dimensions. The ratio of these quantities determines the value of NPH. Our calculations also confirm the conclusion that for obtaining minimum beam divergence in two-electrode systems, NPH values close to one-half of its maximum values should be used. In three-electrode accelerating–decelerating systems with prescribed ultimate ion energy, the reduction of the beam divergence can be achieved by increasing the l/d ratio and the total voltage across the accelerating gap, i.e., using small but finite values of R. This result corresponds to that obtained earlier in [4]. Thus, our calculation model gives an adequate description of the processes involved in beam formation.

The effect of arc voltage, (i.e., the potential difference between the screening electrode at cathode potential and plasma at a potential close to that of the anode) on the angular divergence of the beam of ions extracted from the low-voltage discharge with thermionic cathode was studied in [4]. As the arc voltage was increased from 32 to 50 V, the beam divergence angle decreased by 2–3 degrees, and the NPH value corresponding to the best beam focusing also decreased. The influence of the arc voltage depended on the ultimate beam energy and became less at higher arc voltages. In the emission systems of this study, the arc voltage and the floating potential of the screening electrode are considerably higher than those of [4]; the ionic layer thickness is larger as well. Under such conditions, the curvature of the emitting plasma surface is negligible and the primary ion focusing is done by the electrostatic lens in the hole of the screening electrode. Ions exiting towards the lens have a considerable axial velocity component determined by the voltage drop across the ionic layer. The focal length for a diaphragm with a circular hole is

determined by the screening electrode potential relative to the plasma and by the difference of the values of the electric field in the layer E_d and the field E_t in the accelerating gap [9]:

$$f = 4\Delta\phi/(E_t - E_d). \quad (3)$$

With increasing voltage drop across the layer, in order to keep the initial beam convergence, it is necessary in accordance with (3) to increase the field strength in the accelerating gap. To define the conditions for forming a beam with minimum angular divergence, one has, by analogy with [10], to consider the entire system of an electrostatic lens containing focusing diaphragms with holes in the screening and decelerating electrodes and a scattering diaphragm in the accelerating electrode. Qualitative estimates made in a paraxial approximation and neglecting the space charge have shown that raising the total voltage across the accelerating gap or reducing the decelerating gap length improves the beam focusing at the optics exit, in agreement with the calculations and experimental results. Instead of calculating the beam focal length from the plasma curvature radius as in [10], expression (3) was used for this purpose.

The layer between the plasma and the screening electrode seriously affects the efficiency of ion extraction from the plasma. When the layer thickness is considerable, the form of the plasma boundary is such that the flow of ions from the plasma becomes divergent; therefore, even in the absence of current leaks to the optics electrodes, there can be realized an extraction regime for which the beam currents differ by as much as several-fold. In this case, the conditions for maximum beam current do not coincide with those for forming a beam having minimum angular divergence. The maximum current is obtained in a divergent beam, whose diameter in the hole of the decelerating electrode is close the hole diameter. The thickness of the screening electrode has about the same effect on the ion extraction conditions and beam forming as the ionic layer thickness.

It is to be noted that the results of the study of the details of forming the low-energy beam in systems with the cathode layer obtained for a prescribed current density are valid in a fairly wide range of j values, because a variation of the ion current density influences the cathode layer thickness and the accelerating gap length required for minimum beam divergence in about the same way, whereas a variation of the accelerating voltage changes the role of the ionic layer. The reason is that forming a beam with low angular divergence requires that some optimal NPH value be established and maintained within a narrow range. Raising U_t while keeping the density j constant requires larger accelerating gap lengths l and, consequently, hole diameters d; the relative thickness of the ionic layer will thus be reduced and its effect limited to processes at the periphery of the plasma meniscus.

The calculations have shown that the most advantageous conditions for ion extraction from plasma and formation of high-energy beams of energy in the range of tens of kiloelectronvolts and current density of a few mA/cm^2 in systems with a cathode layer are obtained with ion optics having large aperture diameters (8–10 mm) and relatively thin screening electrodes (1–1.5 mm). These optics create a fairly efficient sagging of the accelerating field into the hole, so that the emitting plasma surface is found not inside the channel of the hole, but beyond the screening electrode; and even in the presence of the ionic layer, this surface can have the convex shape needed for highly efficient ion extraction from plasma and optimal angular beam divergence.

CONCLUSIONS

In plasma-emitting structures based on glow discharge, the positive space-charge layer arising between the ion-emitting plasma and the screening electrode of the electrostatic ion-optic system exerts significant influence on the position and shape of the emitting plasma surface in the elementary cell of the ion optics.

The importance of this layer depends on the relation between the layer thickness and the diameter of the optics apertures. For comparable dimensions of the layer and apertures, the beam divergence is at a minimum if the ion-emitting plasma surface is only slightly curved. In this case, the initial convergence of the ion beam will be created by the focusing of the ions accelerated in the ionic layer by the field of the diaphragm with a hole. Considerable axial component of the ion velocity at the lens entrance degrades the beam focusing, which then has to be improved by increasing the electric field strength in the accelerating gap. Therefore, maximum attainable beam densities in such systems are typically lower, being limited by the vacuum breakdown voltage in the accelerating gap.

The layer parameters influence not only the beam angular divergence, but also the efficiency of ion extraction from the plasma. Divergence of the flow of plasma-emitted ions at the entrance to the forming system increases the current lost to the screening electrode and the beam current. The influence of the layer is greater for low ion energies; therefore, plasma-emitting structures based on glow discharge in which plasma is generated in the cathode cavity cannot be efficient in generating low-energy ($eU \sim 1$ keV) beams having small divergence and high beam current density.

At higher ion energies, the relative layer thickness is reduced because of the need to increase the accelerating gap length and the size of the apertures in order to maintain conditions for small beam divergence. The use of optics with large-diameter apertures (10 mm) and relatively small screening electrode thickness (1–2 mm) for forming ion beams of energy around tens of kiloelectronvolts and current densities of 1–10 mA/cm^2

ensures both high efficiency of ion extraction and optimum angular beam divergence for beam uniformity.

ACKNOWLEDGMENTS

The authors are grateful to Yu. A. Kovalenko (All-Russia Electrotechnical Institute, Moscow) for making available the calculation program BEAM-CAD, as well as to V.V.Bersenev and S.P.Nilulin for their participation in the experiments.

The study was performed in the framework of NIS-IPP and USIC-IPP programs (contract no. 0248U0016-35 with the Los Alamos National Laboratory, and contract no. 857153 with the Brookhaven National Laboratory).

REFERENCES

1. S. I. Molokovskiĭ and A. D. Sushkov, *Intense Electron and Ion Beams* (Énergoatomizdat, Moscow, 1991).
2. G. Aston, H. R. Kaufman, and P. J. Wilbur, AIAA J. **16** (5), 516 (1978).
3. J. R. Coupland, T. S. Green, D. R. Hammond, and A. C. Riviere, Rev. Sci. Instrum. **44**, 1258 (1973).
4. G. Aston and H. R. Kaufman, AIAA Pap. **78-669**, 1 (1978).
5. N. V. Gavrilov, G. A. Mesyats, G. V. Radkovskii, and V. V. Bersenev, Surf. Coat. Technol. **96** (1), 81 (1997).
6. A. S. Metel', Zh. Tekh. Fiz. **54** (2), 241 (1984) [Sov. Phys. Tech. Phys. **29**, 141 (1984)].
7. N. V. Gavrilov, G. A. Mesyats, S. P. Nikulin, *et al.*, J. Vac. Sci. Technol. A **14**, 1050 (1996).
8. N. V. Gavrilov, S. P. Nikulin, and G. V. Radkovskiĭ, Prib. Tekh. Éksp., No. 1, 93 (1996).
9. V. M. Kel'man and S. Ya. Yavor, *Electron Optics* (Nauka, Leningrad, 1968).
10. T. S. Green, J. Phys. D **9**, 1165 (1976).

Translated by B. Kalinin

Technical Physics, Vol. 45, No. 5, 2000, pp. 605–612. Translated from Zhurnal Tekhnicheskoĭ Fiziki, Vol. 70, No. 5, 2000, pp. 82–91.

EXPERIMENTAL INSTRUMENTS AND TECHNIQUES

Dynamic Characteristics of Solids in Microvolumes: Modern Principles, Techniques, and Results of Investigation

Yu. I. Golovin, A. I. Tyurin, V. I. Ivolgin, and V. V. Korenkov

Derzhavin State University, Tambov, 392000 Russia

Received June 9, 1997; in final form, March 9, 1999

Abstract—Several radically new independent *in situ* techniques for characterizing physicomechanical properties of materials in microvolumes are described. In particular, mechanisms behind the formation of an indent and the surrounding deformation zone were studied at a microlevel. With ionic crystals, it was demonstrated that indentation, followed by the formation of the deformation zone, passes the following stages: purely elastic deformation stage, the stage of monoatomic displacement of a material from under the indenter; and a number of final stages where dislocation plasticity is essential. Kinetic, dissipative, and activation parameters of indentation were determined, and basic mass transfer micromechanisms for each of the stages were elucidated.

1. INTRODUCTION

Over the last two or three decades, a variety of modern techniques whereby solid surface and thin surface layers are investigated have been developed. Yet the microhardness method remains the most used, the easiest, and the most rapid [1–8]. However, the true meaning of the notion of "microhardness" is still vague, since an applied load-to-indent area ratio, the usual measure of the microhardness H, is an effective value. It cannot be uniquely related to a single physical process where firmly established physical objects (point defects, dislocations, etc.) and micromechanisms are involved. Neither can it be associated with particular fundamental properties of solids, since it depends on many parameters and external effects.

The major reason for this is the specific stressed state under the indenter: the strain is strongly localized (within the region comparable to the indent size), the maximum stresses far (several hundred times) exceed the yield stress even under quasi-static indentation, and the structure and interatomic distances are highly distorted. Under such conditions, the material behavior greatly differs from that under moderate uniaxial compression or stretching. For example, the amorphization of initially crystalline surface layers under the indenter has been observed [8–11]. Also, such conditions induce exotic elementary mass-transfer and plasticity mechanisms (including interstitial and crowd mechanisms), as directly evidenced by various independent techniques [10–12]. The theoretical characterization of these mechanisms has been given in [13].

Another difficulty in studying the dynamic characteristics of thin surface layers and small volumes (~1 μm^3) is that strain rates $d\varepsilon/dt$ upon indentation are usually very high. Moreover, indentation is accompanied by many short-term processes. If, for example, an indent, a contact spot, or a surface peak has a size $R \sim 1$ μm and the lateral (over the surface) or vertical (indentation) rate v is about 1 mm/s (which is much below ultimate values), the local value of $(d\varepsilon/dt) \sim v/R$ may attain 10^3 s^{-1}.

Thus, it is unjustified to think that the response of a material under such severe conditions (a combination of high stresses, high strains, and high strain rate) will even vaguely resemble its behavior under quasi-static uniaxial compression or stretching. Such a situation occurs, in particular, during microhardness measurements and, in general, at a momentary contact between solids (the collision of particles with each other or with vehicles, including space vehicles; microabrasive wear due to dry friction between rough surfaces, of which a read (write) head–magnetic carrier friction pair is an example; abrasive grinding; etc.). Hence, an experiment where, on one hand, a material would be subjected to such conditions and, on the other hand, it would be possible to record its time-dependent response (spectrum of defects; their mobility, interaction, and effect on macroproperties; etc.) seems to be of great practical value.

In this work, we describe several approaches to studying dynamic properties of a solid material in microvolumes under controllable pulse indentation and report tentative results obtained with them.

1. INVESTIGATION TECHNIQUES

We used several techniques to study a set of physicomechanical properties and time-dependent parameters of materials.

(1) Standard indentation. A hard indenter penetrates into the material, and the size of an indent and the surrounding deformation zone is measured after the

1063-7842/00/4505-0605$20.00 © 2000 MAIK "Nauka/Interperiodica"

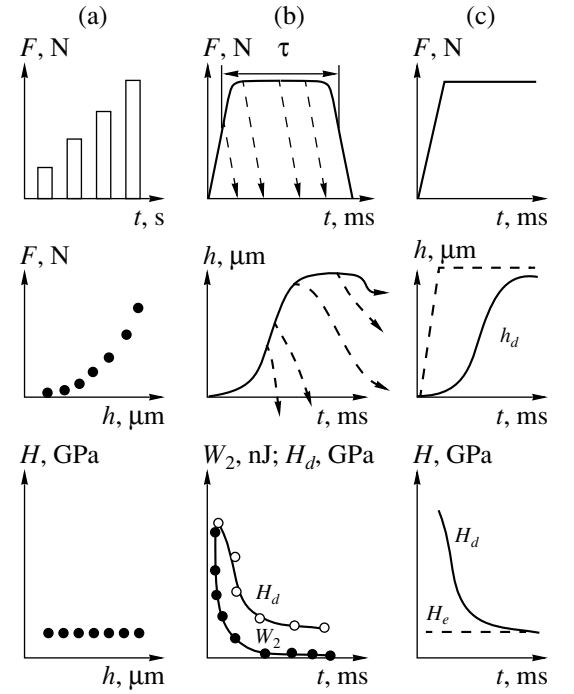

Fig. 1. Techniques and parameters to be determined. (a) Conventional microindentation by a discretely varied load, (b) dynamic microindentation with continuous recording of the indentation depth and indenter velocity in the case of sharp loading, and (c) nanoindentation by a load pulse of controllable width τ. W_2, rebound energy of the indenter after unloading; *F*, indentation force; *h*, indent depth; *t*, time; and *H*, hardness. The subscripts *e* and *d* refer to equilibrium and dynamic values, respectively.

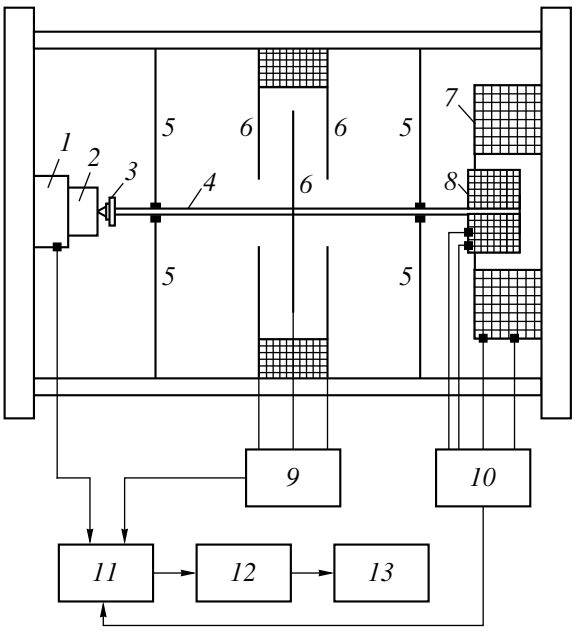

Fig. 2. Experimental setup. *1*, piezosensor; *2*, specimen; *3*, indenter; *4*, rod; *5*, suspension; *6*, capacitive displacement sensor; *7*, fixed coil; *8*, mobile coil; *9*, signal processing unit of capacitive sensor; *10*, current pulse generator; *11*, ADC with signal switch; *12*, computer; and *13*, printer.

indenter is lifted up (Fig. 1a). The deformation zone was delineated by selective chemical etching. The sizes of the indent and deformation zone were measured with the optical part of a ПМТ-3 microhardness meter or with an optical microscope. In our work, standard indentation was applied for calibration.

(2) Indentation by a momentary pulse load (Fig. 1b). In general, the load duration may vary within six orders of magnitude (from 1 ms to 10^3 s). The indent plus deformation zone size was measured after load removal. Short pulse loading makes it possible to examine elementary processes taking place at each stage of indentation, thereby visualizing the formation of an indent and the surrounding zone.

(3) Dynamic indentation. It is known that dynamic properties of a system are best and most easily understood by analyzing its response to a step disturbance. In our experiments, a constant step test load was applied to the indenter, and the kinetics of its insertion was continuously recorded with an appropriate time resolution (Fig. 1c). We thus were able to *in situ* trace the strain rate as a function of instantaneous contact stresses, separate process stages, and analyze them by thermal activation methods to judge underlying micromechanisms in the near-indent region.

(4) Direct measurements of time-dependent dissipative properties of a material during contact. Here, we measure the energy imparted to a rod with an indenter by a drive and the energy of rod rebound after a load pulse is over. Their difference, measured as a function of contact duration (Fig. 1b), is the energy dissipated during the formation of an indent and surrounding zone.

When combined, these techniques greatly extend our investigative capabilities and provide an opportunity to study a wide spectrum of dynamic properties.

2. EXPERIMENTAL

The test setup (Fig. 2) consists of a horizontal rod suspended on wires that provide translatory motion without friction. The net stiffness of such a suspension is 1 N/m. A standard indenter (a Vickers diamond pyramid) is attached at one end of the rod. A capacitive displacement sensor is located in the middle part of the rod. Its movable electrode touches the rod, while its stationary electrodes are rigidly fixed on the body of the setup.

Loading was accomplished with an electrodynamic drive, i.e., two interacting current coils. The movable coil was fixed at the other end of the rod, and the stationary one was mounted on the body. Momentum was generated by passing current through both coils. Varying the amplitude, duration, and shape of current pulses, we could vary those of the pulse loads applied to the indenter.

The setup allows indentation with the zero and nonzero velocity of the indenter. In the former case, the

specimen is gently brought into contact with the indenter by means of a microscrew and then is pulse-loaded.

The touch instant and the penetration depth $h(t)$ vs. time were recorded with the capacitive displacement sensor. Also, the touch instant and the indentation load F can be determined with a piezosensor situated immediately under the specimen. The sensitivity of the force-measuring path is $\sim 2 \times 10^3$ N.

Signals from both sensors were applied to an analog-to-digital converter and then processed using a special computer program. This provides synchronous recording of sensor signals (with an accuracy of 25 μs).

The displacement sensitivity of the path was 20 nm, and the time resolution was 50 μs.

The setup and the adopted measuring method made it possible to trace micro- and nanoindentation at loads from several millinewtons to 2N within an indentation time range of 0.1 ms–1000 s. Rapid application of the load to the indenter was provided by a sharp rise in the coil current (the pulse leading edge duration is 100 μs).

Calibration experiments showed that, in the absence of the specimen, the indenter executed uniformly accelerated motion (Figs. 3a, 3b). This means that a constant force does act in the indenter–rod system; hence, an experimental time dependence of the penetration depth $h(t)$ (Figs. 4, 5a) reflects the dynamics of physical processes in the deformation zone and can be used to determine failure micromechanisms under the indenter.

In a number of experiments, a rising $h(t)$ curve exhibited damped oscillations of a signal from the displacement sensor (Fig. 4d). The oscillations were found to appear only when hard materials (MgO, Si at room temperature, LiF at $T \le 200$ K, and NaCl and KCl at $T \le 100$ K) were subjected to short-rise-time ($\tau_f \le 2$ ms) load pulses. The room-temperature indentation of KCl, NaCl, LiF, Pb, and Al did not cause the oscillations. As follows from preliminary analysis, they arise in the rod–deformation zone system and are not related to self-oscillations of parts of the setup. A dynamic model of an oscillating system in Fig. 6 includes the mass m of the movable parts of a loader, the stiffness of a suspension C_1, the stiffness of a rod C_2, the stiffness of a specimen in the contact region C, and damping properties of these elastic parts (damping coefficients D_1, D_2, and D). The most complex and, at the same time, most important parameter here is $C = kE_r A^{1/2}$ [3, 5], where k is a proportionality factor which depends on the indenter shape; $E_r = [(1 - \nu^2)E^{-1} + (1 - \nu_i)E_i^{-1}]^{-1}$ is the reduced Young's modulus; E and ν are Young's modulus and Poisson's ratio of the specimen, respectively; E_i and ν_i are the same parameters of the indenter; $A = 13.2h^2$ is the Vickers indent area projected onto the specimen surface; and $k = 1.15$ [3]. The angular frequency ω of natural damped oscillations is related to these parameters through the obvious relationship $\omega = \{[(C^{-1} + C_2^{-1})^{-1} + C_1]m^{-1} - D^2\}^{1/2}$. In our setup, the conditions $C_2 \gg C$, $C_1 \ll C$, and $D_1 \ll D$, $D_2 \ll D$ are satisfied (namely, $C_2 = 50$ MN/m, $C_1 = 1$ kN/m, $D_1 < 1$ s^{-1}, $D_2 < 0.1$ s^{-1}, and $D \ge 30$ s^{-1}; the measured values of C were between 3 and 5 MN/m). Therefore, to a first approximation, indentation conditions and an oscillation mode were defined only by the material properties in the contact zone, i.e., by C and D. Since C grows in proportion to h, the condition $Cm^{-1} \ge D^2$ is set starting from some critical value h_c, after which the aperiodic regime is changed to the oscillatory regime. In the crystals studied (KCl, NaCl, LiF, and MgO), the latter was observed at $h_c = 3$–14 μm for a load of several newtons.

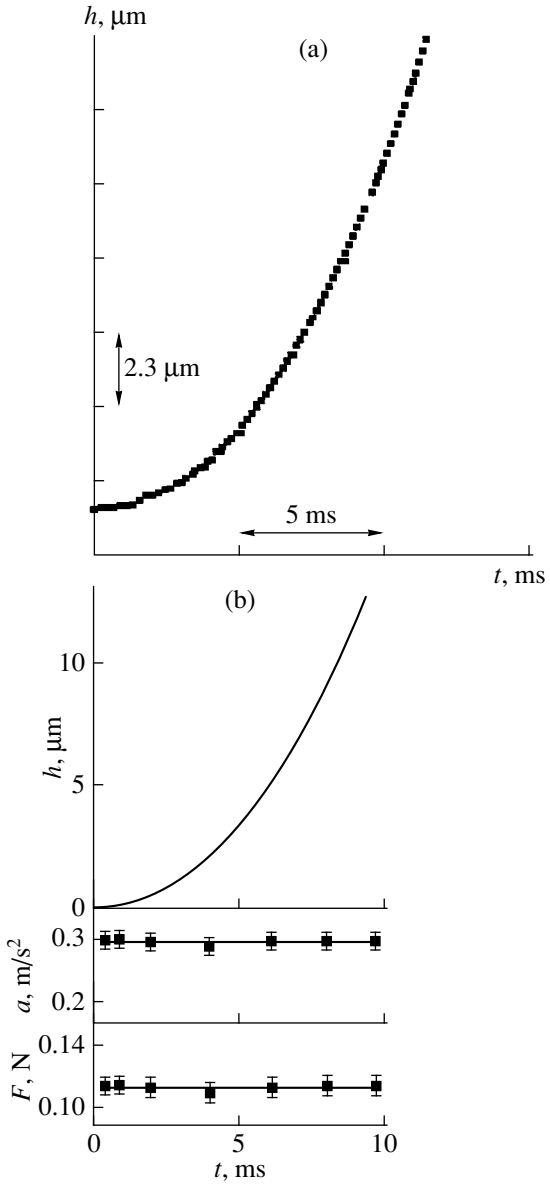

Fig. 3. (a) Displacement of the rod with the indenter in time and (b) associated dependences $h(t)$, $a(t) = 2h/t^2$, and $F(t)$ in the absence of the specimen. Force pulse is 0.11 N, $T = 293$ K.

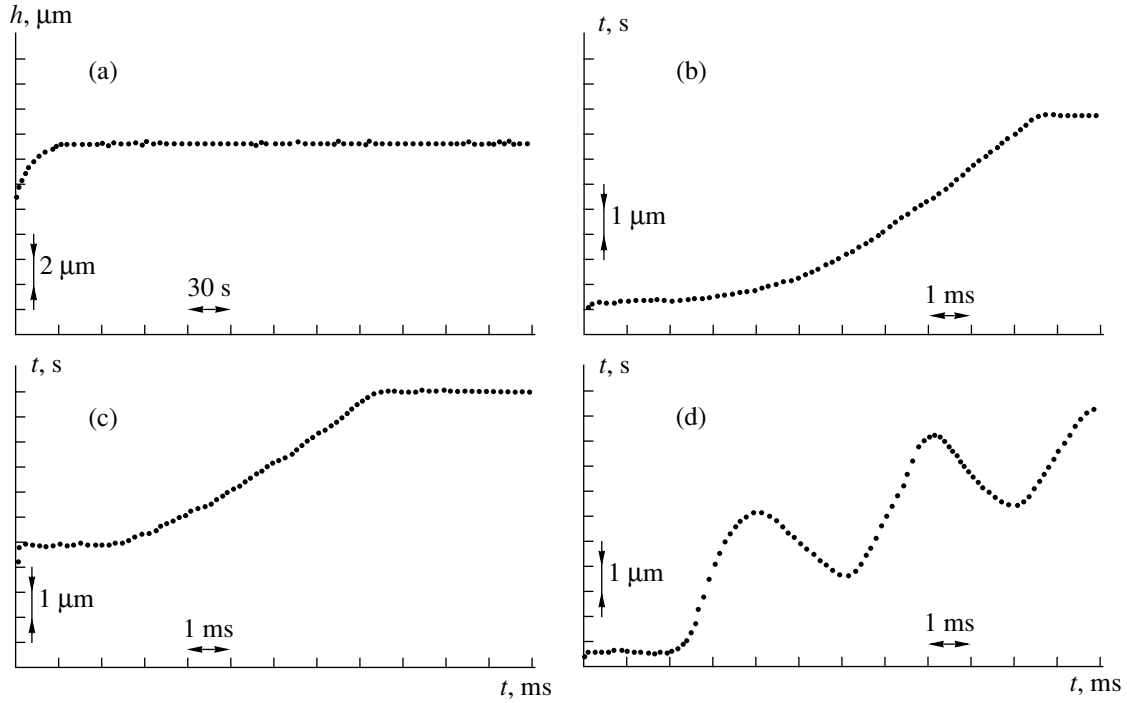

Fig. 4. Indentation kinetics at the early stages for ionic crystals. (a, b, d) LiF; (c) KCl : Ba (C = 10 mol %). T = (a, b) 293 and (c, d) 77 K.

The eigenfrequency of oscillations of the suspended rod is $\omega_p \ll \omega$, and the eigenfrequency of oscillations of individual rod parts is $\omega_i \gg \omega$; hence, the latter does not influence the measurement results.

When the material under the indenter does not fail, the Young's moduli E_s derived from the eigenfrequency values coincide with reference values E_c with an accuracy of better than 10%. For example, in the absence of damage around the indent, we obtained E_s = 50 GPa, E_c = 49 GPa for NaCl and E_s = 125 GPa, E_c = 114 GPa for LiF. On the other hand, in the case of MgO crystals, for which indentation is accompanied by extensive failure, E_s = 41 GPa and E_c = 286 GPa. The coincidence of the calculated and reference data for the LiF and NaCl crystals is not accidental, despite the fact that E_s is an effective parameter (since it reflects the properties of a material in the highly and nonuniformly deformed region near the contact). If indentation causes cracking, $E_c < E_s$, which seems to be quite natural, since the compliance of the crystal lattice is augmented by that due to crack nucleation and crack opening displacement.

Thus, the amplitude, frequency, and damping decrement of the oscillations bear information on the mechanical properties of the material in the contact region. If the specimen is made from a material not prone to brittle fracture, the parameters of natural oscillations in the indenter–specimen system can be used for estimating Young's modulus in volumes from 1 to 10^3 μm^3. In the case of brittle materials, this technique is appropriate for detecting crack nucleation in the puncture zone (by a loss of Young's modulus).

Our setup and the described techniques allowed us to measure a set of time-variable material parameters (dynamic microhardness, deformation zone size, dissipated energy, effective modulus of elasticity, etc.).

3. RESULTS

Experiments were carried out with ionic crystals of a different composition at T = 77–300 K. Data for no less than ten indents obtained under identical experimental conditions were processed. Despite the fact that the mechanical properties of the crystals being tested greatly differed (by more than one order of magnitude for Young's modulus and by almost two orders of magnitude for the hardness), the indentation kinetics were qualitatively similar (Fig. 4).

Within the first 10 or 15 ms of motion, the penetration depth of the indenter h attained 70–90% of its final value. The stationary (or close-to-stationary) values of h are established within tens or hundreds of seconds, depending of the crystal type, temperature, and load.

By continuously recording the penetration depth vs. time, we could determine the instantaneous velocity of the indenter $v(t) = dh/dt$, the force exerted on the material by the moving indenter $F(t) = F_0(t) - m(d^2h/dt^2)$, the indent-area-averaged contact stresses under the indenter $\sigma(t) = F(t)/S(t)$, and the dynamic hardness $H_d(t) = k_2F(t)/h^2(t)$. Here, $F_0(t)$ is the force applied to

the rod on the side of the drive, m is the mass of the rod with the indenter, $S(t) = k_1h^2(t)$ is the current indent area projected onto the material surface, and k_1 and k_2 are coefficients taking into account the indenter geometry (for a Vickers indenter, $k_1 = 24.5$ and $k_2 = 0.03784$). Typical dynamic curves $v(t)$, $F(t)$, and $H_d(t)$ for NaCl crystals are shown in Figs. 5 and 9.

Plotted in the semilogarithmic coordinates, the kinetic curves $\ln(dh/dt) = f(t)$ (Fig. 7) exhibit several straight portions which can be associated with stages of indent formation. This means that indentation on ionic crystals should be thought of as proceeding in as many as five stages rather than in two (fast and slow), as is usually believed. The near-linear fall of the velocity logarithm at each of the stages (starting from the second) indicates the exponential character of relaxation. The exponents at the different stages diverge by four and the preexponentials by five orders of magnitude. Under constant applied loads (Figs. 3b, 5b) and constant contact stresses (starting from 10–15 ms), such behavior of $dh/dt = f(t)$ is obviously an indication of mass transfer mechanism changeover in the contact zone.

The first stage of $h(t)$ growth implies that the indenter moves with a positive acceleration. At the second stage (starting from 5 ± 2 ms, Fig. 7a), the acceleration is negative but always less than 0.3 m/s^2 in magnitude. From the third stage on, the curves $h(t)$ and $H_d(t)$ saturate within several milliseconds (Figs. 5b, 9).

Figure 8 shows the evolution of the deformation zone on the LiF and KCl surfaces. The size of the zone was determined by the technique described in Section 1.2. The indentation process was interrupted at each of the loading stages; then the load was removed, the specimen was chemically etched, and the deformation zone was measured with an optical microscope. The length of the rays of a dislocation rosette was taken for a measure of the zone size. It is seen from Fig. 8 that the time dependences of the indent diagonal $d = f(t)$ and those of the ray length $l = f(t)$ have fast and slow phases. During the former (lasting from 2 to 10 ± 2 ms, depending on the crystal type, applied load, and temperature), both parameters attain 70–80% of their steady-state values. The ultimate (steady-state) values are established in the following several seconds or several tens of seconds.

The dynamics of indent and rosette formation (Fig. 8) indicates that the times of fast rise in d and l under pulse loading (indentation) correlate with the durations of the fast stages in indent formation that were obtained from the analysis of continuous indentation.

Data for the energy $W_p = W_1 - W_2$ absorbed (dissipated) by the NaCl crystals upon indentation are given in Fig. 9. Here, W_1 is the energy supplied by the drive and W_2 is the kinetic rebound energy of the rod–indenter system. We measured the value W_1 as the sum

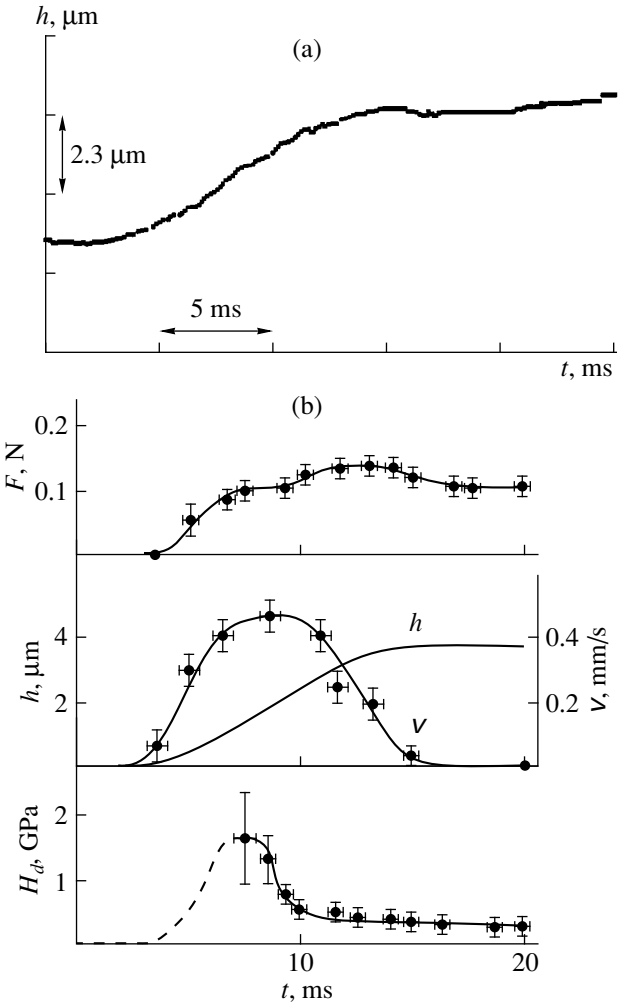

Fig. 5. (a) Kinetics of the active stage of indentation for the (001) face of NaCl and (b) dependences $h(t)$, $v(t)$, $F(t)$, and $\sigma(t)$). $T = 293$ K, indentation force is 0.11 N.

of W_k and W_f (where $W_k = m(v_1)^2/2$ is the kinetic energy supplied to the rod–indenter system by the drive when the indenter does not touch the specimen, v_1 is the rod velocity at the touch instant, and $W_f = Fh$ is the drive energy that causes the indenter to penetrate into the specimen to a depth h). $W_2 = m(v_2)^2/2$, where v_2 is the velocity of the rod–indenter system at the instant of contact breaking. As is seen, for $\tau \geq 50$ ms, W_2 drops 30- to 40-fold, approaching zero (Fig. 9).

4. DISCUSSION

Knowing the indentation dynamics, one can gain a better insight into the sequence and nature of processes under the indenter. For example, the indenter force (Figs. 3, 5) remains practically constant throughput the indentation process (variations are within 10–20%). However, the values of $h(t)$, and hence the area of an indent $S(t)$ early in its formation, are very small. This

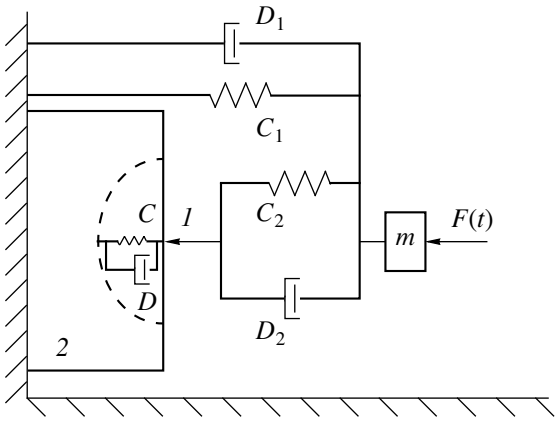

Fig. 6. Model of an oscillating system. *1*, indenter; *2*, specimen; *m*, mass of the movable parts of a loader.

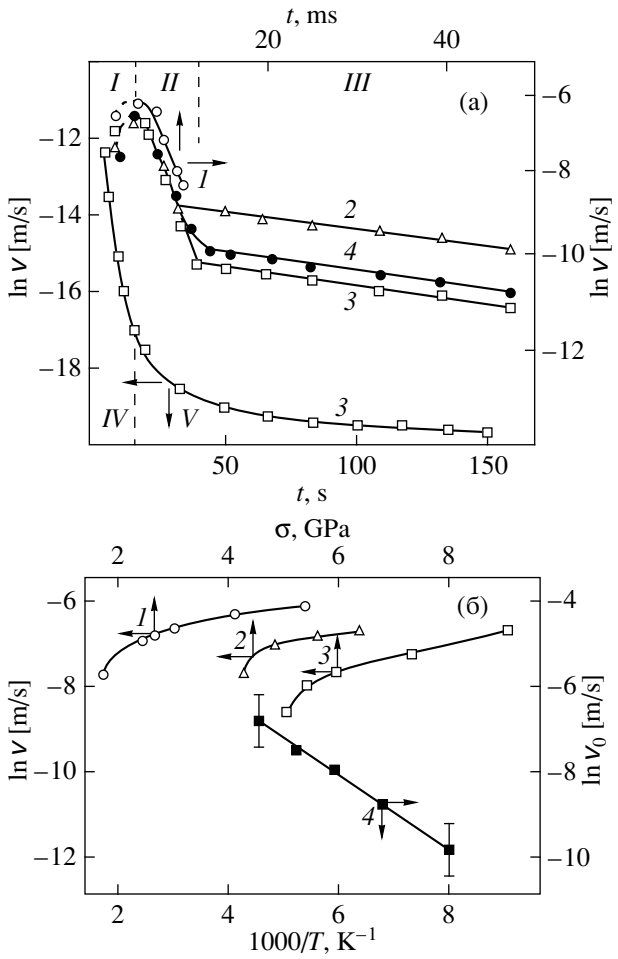

Fig. 7. (a) ln v vs. indentation time at T = (*1*) 293, (*2*) 196, and (*3*) 77 K. Roman numerals mean indentation stages; (b) (*1*)–(*3*) ln $v = f(\sigma)$ and (*4*) ln $v_0 = f(1/T)$ for the same crystals at T = (*1*) 293, (*2*) 196, and (*3*) 126 K.

means that the dynamic hardness H_d may be comparable to the theoretically estimated value. For example, within the first milliseconds, the peak value of $H_{d\,\max}$ for the NaCl crystals was ~1.6 ± 0.8 GPa. In the following 8–10 ms, $H_d(t)$ drops to values close to the steady-state microhardness of the material.

At the second and following stages of indentation, σ and dh/dt drop and h slightly varies; therefore, these stages can be treated in terms of conventional approaches. A force dependence of the indentation rate plotted in the semilogarithmic coordinates $\ln(dh/dt) = f(\sigma)$ has nearly linear portions (Fig. 7b). By extrapolation to $\sigma_0 = 0$, one can then find the initial indentation rate dh_0/dt at various temperatures. The dependence $\ln(dh_0/dt) = f(1/T)$ also has almost linear portions (Fig. 7b). This allows us to argue that the flow is of thermally activated character, at least within some ranges of σ and T, and to determine the activation parameters. At the second stage of loading, the activation volumes γ obtained from the slopes of the $\ln(dh/dt) = f(\sigma)$ dependences are very small for all of the ionic crystals: $\gamma \approx 10^{-30}$ m^3 (Fig. 10). The energies of activation are about 0.1 eV. Clearly, such low values of U and γ are due to the high values of σ at this stage, where elastic strains alone may be as high as several percent.

The fact that activation volumes account for only several tenths of that occupied by a cation in the lattice under normal pressure is direct evidence that deformation is due to the movement of individual atoms [10–13]. In experiments where the diffusion rate was studied as a function of omnidirectional pressure, the values of γ have also been estimated at 0.6–0.7 of the cation volume in the lattice [14]. Reliable independent data for the activation parameters of the formation and motion of interstitials and vacancies under high pressure (~0.1–1 Mbar) are lacking; therefore, it is impossible to decide with certainty between interstitial and vacancy mechanisms, although interstitial (crowd) mechanisms become more plausible as the pressure grows.

As the indenter penetrates farther (from the third stage on), $H_d(t)$ approaches the static microhardness value ($t \geq$ 10–12 ms), U grows to 0.2–0.3 eV, and γ increases to 10^{-28} m^3 (Fig. 10). Thus, γ becomes equal to ~$10b^3$ by order of magnitude, where b is the Burgers vector of glide dislocations. This is consistent with data in [15, 16] and implies that dislocation flow is dominant under the indenter late in indentation. Since instabilities of external stresses and the effect of internal ones were ignored in the calculations, the error in determining γ in the above experiments is relatively high, ~50%. Yet, even such a large error is indicative of the prevailing effect of structure defects responsible for mass transfer at each of the stages, since taking into account the above and other factors cannot change the order of γ. Note that γ's for monoatomic and dislocation mechanisms differ by two or three orders of magnitude [13].

The deformation zone evolution observed in the experiments shows (Fig. 8) that its size l is specified solely by the indent size d. The correlation between d and l is explained, in our opinion, either by the small

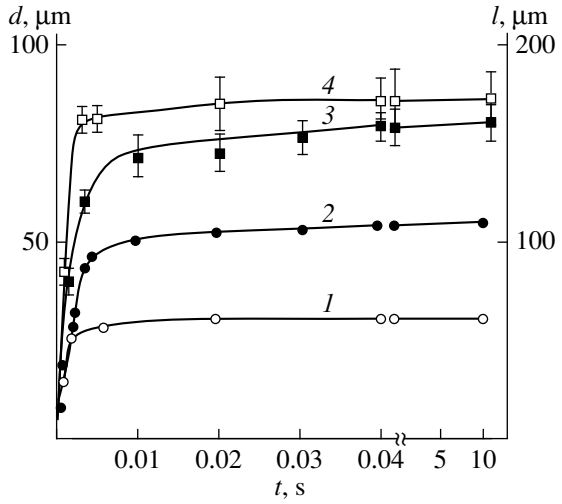

Fig. 8. Indent diagonal d and the length of rays of the dislocation rosette l vs. indentation time. (*1*) d and (*2*) l for KCl; (*3*) d and (*4*) l for LiF.

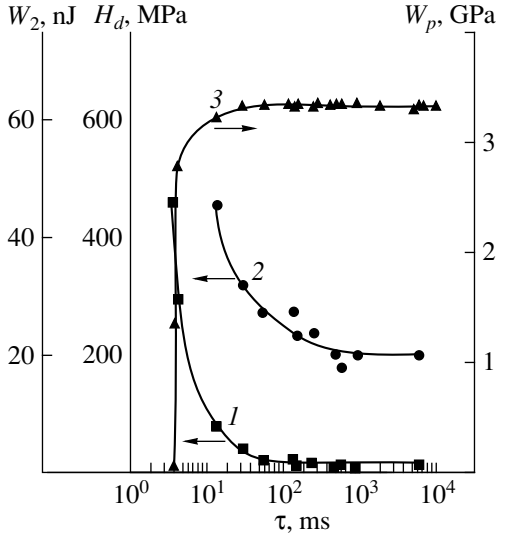

Fig. 9. Kinetic dependences of the (*1*) rebound energy W_2, (*2*) dynamic hardness H_d, and (*3*) time-dependent part of the absorbed energy normalized by the indent volume W_p upon dynamic indentation for NaCl crystals.

relaxation time (≤1 ms) of the dislocation structure or by its rearrangement during unloading and subsequent chemical etching. The former reason appears to be less probable. Chemical etching is a sluggish process and gives no chance to answer the question as to whether the dislocation rosette forms during indentation and keeping the indenter in the material or material relaxation during unloading and subsequent etching are largely responsible for its formation. From general considerations, it is clear that the shorter the loading time, the more probable stress relaxation is during unloading and etching.

That the dislocation structure may reconfigure also follows from a change in the photoelasticity rosette picture [17] and in the electric dipole moment [18–22]; both effects were observed in ionic crystals upon indentation and unloading.

Thus, the results obtained suggest a correlation between the size of an indent and the length of the rays of a relaxed dislocation rosette for the wide range of indentation times (from 1 ms to 30 s).

The interruption of loading early in indentation allows us to find dependences of the dynamic microhardness H_d and the rebound energy of the indenter W_2 on indentation time τ. For example, for pure NaCl crystals subjected to a rectangular force pulse $F = 0.2$ N of width τ from 4 ms to 10 s at room temperature, the dependence $W_2 = f(\tau)$ turned out to be even stronger than $H_d = f(\tau)$ in Fig. 9. From this figure, it also follows that, at $\tau \geq 1$ s, H_d equals ~200 MPa, which is common for NaCl; at shorter τ's, it steeply rises (to ~450 MPa for $\tau = 10$ ms). At $\tau = 4$ ms, W_2 is 45 nJ (Fig. 8); and at $\tau \geq 10^2$ ms, W_2 becomes comparable to mechanical fluctuations of the rod with the indenter (~1 nJ). Thus, the time-dependent part of the reduced absorbed energy $W_p(\tau) = (W_1 - W_2)/V$ (V is the indent volume) varies several tens of times in the interval from several milliseconds to several tens of milliseconds (Fig. 9). This suggests that H_d, W_2, and W_p are independent characteristics of a material and describe its time-variable elastoplastic and dissipative properties in the contact zone with a volume of ~1 μm^3. The sharp increase in

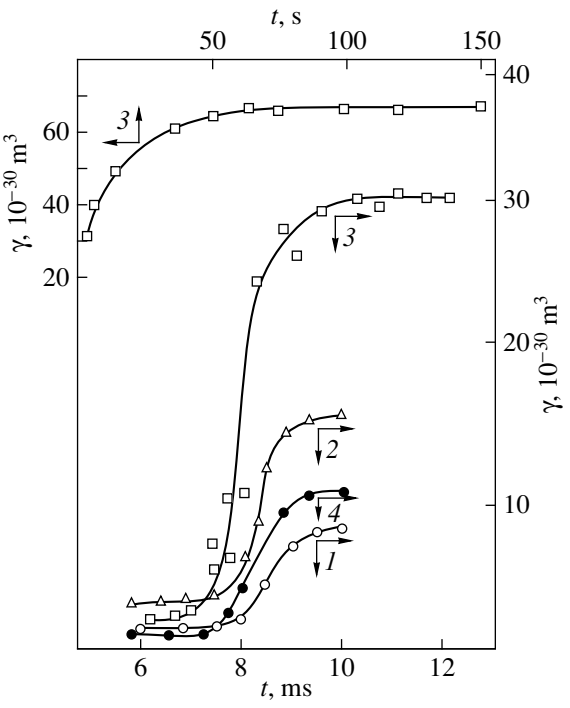

Fig. 10. Room-temperature variation of the activation volume γ: (*1*) KCl : Ba, (*2*) NaCl, (*3*) LiF, and (*4*) MgO.

the dissipation energy between 10 and 20 ms, as demonstrated by the $W_p(\tau)$ dependence, confirms the conclusion based on thermal activation analysis that the leading mass transfer mechanism changes at this stage of indentation. The characteristic times of change of H_d and W_p are obviously defined by the dynamics of plastic flow in the contact zone due to a momentarily applied constant force. Also, they bear information on the origination and dynamics of structure defects, which are elementary "carriers" of this flow, under high local stresses and at high strain rates. In fact, even at $\tau = 10$ ms, the mean values of contact stresses $\sigma \approx H_d$ exceed the yield stress of the same NaCl crystals under quasi-static uniaxial compression almost 1000-fold (or more when $H_d = H_{max} = 1.6$ GPa). In spite of the not too high absolute value of the indenter velocity dh/dt (its maximum < 1 mm/s), the strain rate $(d\varepsilon/dt) \approx (dh/dt)/h$ for $h < 1$ μm reaches $\sim 10^3$ s^{-1}, which is typical of the collision of macrobodies moving with high velocities.

CONCLUSION

(1) We proposed a number of radically new independent techniques for determining dynamic physicomechanic properties of materials in micro- and submicrovolumes and elucidating the mechanisms of formation of an indent and the surrounding deformation zone. The first one makes it possible to study the indentation kinetics when the indenter is first brought close to the surface (without contact) and then sharply loaded by a constant force. This technique and the associated setup enable us to *in situ* investigate the evolution of the deformed material under such conditions (with a time resolution of 50 μs) and gain information on the dynamic microhardness H_d and mass transfer micromechanisms at all stages of local loading. The second technique (the indenter is subjected to a force pulse of controllable duration) gives a good idea of intermediate states of the structure under the indenter and the specific energy absorbed at one or another indentation stage.

(2) Indentation with a hard indenter was found to be a multistage process in all of the crystals studied. Its basic, including activation, parameters were determined; and prevailing mass transfer mechanisms for each of the stages were revealed. It was shown that an indent is formed in several steps: purely elastic deformation of the material, monoatomic displacement of the material from under the indenter, and final steps where dislocation plasticity plays a decisive role.

(3) It was found that the dynamic microhardness of ionic crystals approaches its static value at indentation times $\tau \geq 1$ s and that the energy is absorbed most intensely at the dislocation stages of indent formation.

ACKNOWLEDGMENTS

This work was supported by the Russian Foundation for Basic Research (grant no. 98-02-16549).

REFERENCES

1. V. K. Grigorovich, *Hardness and Microhardness of Metals* (Nauka, Moscow, 1976).
2. S. I. Bulychev and V. P. Alekhin, *Materials Testing by Continuous Indentation* (Mashinostroenie, Moscow, 1990).
3. G. C. Pharr, W. C. Oliver, and F. R. Brotzen, J. Mater. Res. **7** (3), 613 (1992).
4. S. V. Hainsworth and T. F. Page, J. Mater. Sci. **29** (21), 5529 (1994).
5. Y. Murakami, K. Tanaka, M. Itokazu, and A. Shimamoto, Philos. Mag. A **69**, 1131 (1994).
6. B. Ya. Farber, V. I. Orlov, and A. H. Heuer, Phys. Status Solidi A **166**, 115 (1998).
7. B. Ya. Farber, V. I. Orlov, V. I. Nikitenko, and A. H. Heuer, Philos. Mag. A **78**, 671 (1998).
8. A. Kailer, Y. G. Gogotsi, and K. G. Nickel, J. Appl. Phys. **81** (7), 3057 (1997).
9. T. F. Page, W. C. Oliver, and C. J. Hargue, J. Mater. Res. **7**, 450 (1992).
10. M. Sh. Akchurin, V. G. Galstyan, and V. R. Regel, Scanning **14**, 194 (1992).
11. M. Sh. Akchurin and V. R. Regel, Chem. Rev. (Washington, D.C.) **23**, 59 (1998).
12. M. Sh. Akchurin, V. G. Galstyan, V. R. Regel, and V. N. Rozhanskiĭ, Poverkhnost, No. 3, 119 (1983).
13. V. L. Indenbom, Pis'ma Zh. Éksp. Teor. Fiz. **12**, 526 (1970) [JETP Lett. **12**, 369 (1970)].
14. V. I. Zaĭtsev, E. I. Lyafer, and V. V. Tokiĭ, Fiz. Tverd. Tela (Leningrad) **17**, 1866 (1975) [Sov. Phys. Solid State **17**, 1227 (1975)].
15. Yu. S. Boyarskaya, D. Z. Grabko, and M. S. Kats, *Physics of Microindentation* (Shtiintsa, Kishinev, 1986).
16. S. I. Bulychev, V. P. Alekhin, and M. Kh. Shorshorov, Fiz. Khim. Obrab. Mater., No. 5, 69 (1979).
17. Yu. I. Golovin, A. A. Shibkov, A. I. Tyurin, *et al.*, Fiz. Tverd. Tela (Leningrad) **30** (11), 3491 (1988) [Sov. Phys. Solid State **30**, 2005 (1988)].
18. Yu. S. Boyarskaya, Yu. I. Golovin, M. S. Kats, *et al.*, Latv. Fiz. Tekh. Zh., No. 5, 41 (1991).
19. Yu. I. Golovin and A. I. Tyurin, Pis'ma Zh. Éksp. Teor. Fiz. **60** (10), 722 (1994) [JETP Lett. **60**, 742 (1994)].
20. Yu. I. Golovin and A. I. Tyurin, Izv. Akad. Nauk, Ser. Fiz. **59**, 49 (1995).
21. Yu. I. Golovin and A. I. Tyurin, Kristallografiya **40** (5), 884 (1995) [Crystallogr. Rep. **40**, 818 (1995)].
22. Yu. I. Golovin and A.I. Tyurin, Fiz. Tverd. Tela (St. Petersburg) **38** (6), 1812 (1996) [Phys. Solid State **38**, 1000 (1996)].

Translated by V. Isaakyan

Technical Physics, Vol. 45, No. 5, 2000, pp. 613–617. Translated from Zhurnal Tekhnicheskoĭ Fiziki, Vol. 70, No. 5, 2000, pp. 92–96.

EXPERIMENTAL INSTRUMENTS AND TECHNIQUES

X-ray Diffractometry Diagnosis of Laser Diffusion of Aluminum into Silicon

V. A. Bushuev and A. P. Petrakov

Moscow State University, Vorob'evy gory, Moscow, 119899 Russia

Received January 14, 1999

Abstract—High-resolution X-ray diffractometry was used to study alterations of the structure of single-crystal silicon taking place in the process of nonequilibrium solid-state diffusion of aluminum atoms occurring under heating of the near-surface layer by radiation of a CO_2 laser with pulse durations 1, 2, and 3 s. Crystal lattice deformation profiles, diffusion lengths, and densities of dislocation loops have been determined. *© 2000 MAIK "Nauka/Interperiodica".*

INTRODUCTION

Diffusion of impurity atoms in semiconductor crystals involves a range of problems in solid-state physics. Diffusion processes take place at almost all technological stages in the production of semiconductor materials, beginning with purification of the starting material all the way up to the creation of *pn* junctions. At present, along with widely used isothermal diffusion [1], much attention is being paid to nonequilibrium solid-state diffusion taking place under pulsed laser heating of a crystal surface coated with impurity [2–5].

pn junctions can be formed [3] by way of laser diffusion of aluminum into silicon. In [4], electrical characteristics of *p*-type near-surface layers in silicon doped with aluminum have been determined. Secondary-ion mass spectrometry was used to derive impurity distribution profiles [5]. But much less attention was paid to the crystalline structure of these layers, although it determines most of the electrical and physical properties of semiconductor materials in the near-surface region.

Analysis of X-ray scattering patterns is an effective method of investigating alterations of a crystalline structure in near-surface layers caused by the introduction of impurity by both isothermal diffusion [6–8] and ion implantation [9–12]. In [13], using X-ray diffractometry data, deformation and amorphization profiles in thin silicon layers were monitored in the course of laser diffusion of boron.

In this work, double- and triple-crystal X-ray diffractometry studies have been carried out of the changes in the crystalline structure of thin near-surface layers of single-crystal silicon formed as a result of nonequilibrium solid-state laser-induced diffusion of aluminum for different CO_2 laser pulse durations.

EXPERIMENTAL TECHNIQUE

On the surface of a single-crystal silicon wafer, coinciding with the (111) face, a layer of amorphous aluminum of thickness 0.1 μm was deposited by thermal sputtering. The process was performed in a vacuum in a VUP-4 apparatus. The wafer thickness was 500 μm.

The samples prepared in this way were irradiated with a CO_2 laser ($\lambda = 10.6$ μm). The laser radiation was incident on the sample side, opposite the side sputtered with aluminum at right angles. The irradiation power density was 350 W/cm^2. One group of crystals was irradiated for a time $\tau = 1$ s, the other for 2 s, and the third for 3 s. After irradiation, the remaining aluminum was removed with alkali (KOH) solution.

The near-surface layer of the starting crystals and crystals with an aluminum coating subjected to laser diffusion were investigated using an automatic X-ray diffractometer based on a DRON-UM1 apparatus with double- and triple-crystal diffraction schemes in dispersionless geometries $(n, -n)$ and $(n, -n, n)$, respectively. Cu$K_{\alpha 1}$ radiation was used. Highly perfect silicon crystals with a single symmetric (111) reflection were used as monochromator and analyzer. Double-crystal rocking curves (RC) and curves of triple-crystal X-ray diffractometry (TC-XRD) were measured.

EXPERIMENTAL RESULTS AND DISCUSSION

Silicon is practically transparent to CO_2 laser radiation; therefore, diffusion of impurity into the near-surface region of the silicon wafers can be carried out by irradiation from the substrate side. The laser radiation is absorbed in a skin layer of the aluminum film, whose thickness does not exceed 10 nm. Absorption of the laser radiation raises the temperature in the vicinity of the film/substrate interface, enhancing the diffusion of aluminum into the silicon wafer. It is worth noting that

1063-7842/00/4505-0613$20.00

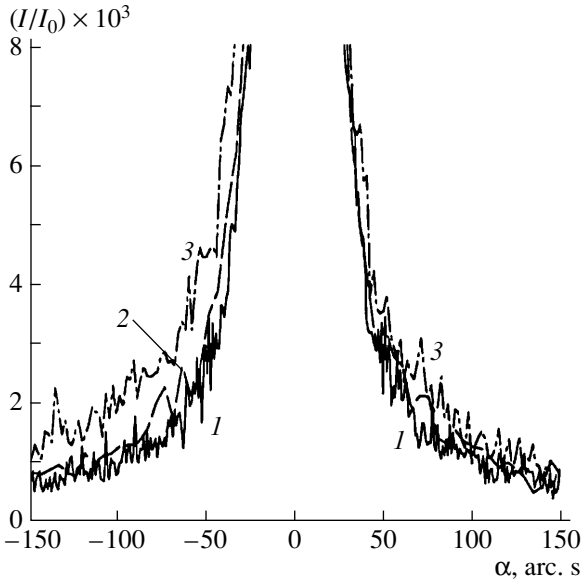

Fig. 1. Dependence of the diffraction in Si(111) reflection of Cu$K_{\alpha 1}$-radiation on the laser diffusion time of aluminum τ, s: (*1*) 1, (*2*) 2, and (*3*) 3.

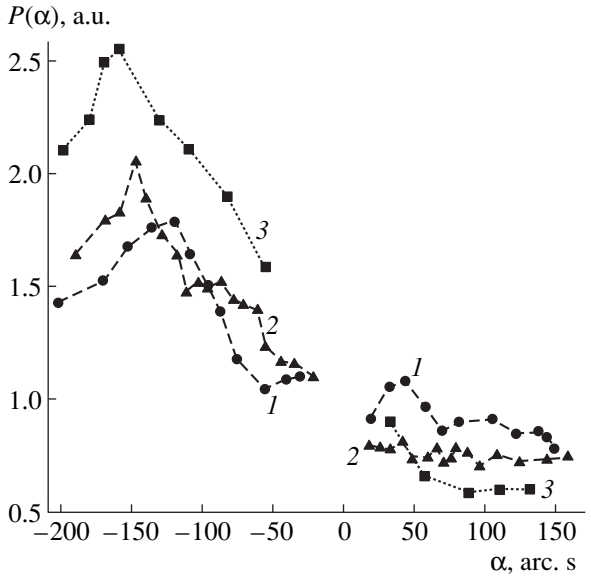

Fig. 2. Reduced intensity functions of the main peaks in the triple-crystal X-ray diffractometry of crystals studied. (*1–3*) same as in Fig. 1.

an aluminum film serving as a source of diffusing impurity at the same time inhibits its evaporation.

It is known that mechanical strains arise in crystals in the process of nonequilibrium solid-state diffusion; but their magnitude is minimal, since the laser irradiation lasts only seconds [2].

Shown in Fig. 1 are rocking curves for the (111) reflection measured as a function of the sample rotation angle $\alpha = \Theta - \Theta_B$ in a double-crystal diffractometer and normalized to the incident X-ray intensity I_0, where Θ_B is the Bragg angle. Rocking curves of crystals irradiated with 1-s pulses closely followed corresponding curves for the initial substrates. Raising the irradiation time to 2 s caused a slight asymmetric intensity enhancement of the rocking curves in the region of negative angles α. At the irradiation time of 3 s, the intensity of the curves in the region of negative angles α increased still further, and some enhancement of the rocking curves in the region of $\alpha > 0$ was observed (Fig. 1, curve *3*). Note that the values of full width at half maximum $\Delta\alpha_B$ of the rocking curves were 9.6, 9.95, and 11.1 arc-seconds at $\tau = 1$, 2, and 3 s, respectively, which is only slightly higher than the value of $\Delta\alpha_B = 9.4$ arc-seconds calculated for an ideal crystal taking into account convolution from the monochromator and both polarization states.

Figure 2 shows the normalized intensity functions [14] $P(\alpha) = AI_{MP}\alpha^2$, where I_{MP} is the intensity of the main peak in TC-XRD curves measured at various fixed sample position angles α in the scanning mode of the analyzer. The main peak intensity is highest for the analyzer angle $\Delta\Theta = 2\alpha$. The normalization factor A is obtained from the condition that $P(\alpha) = 1$ for the starting substrates in the investigated range of α. In distinction from double-crystal rocking curves, the main peak intensity $I_{MP}(2\alpha)$ is determined exclusively by coherent scattering from an "average" crystal lattice. No contribution to the reflection intensity comes from diffuse scattering by defects of the structure.

All $P(\alpha)$ functions display peaks in the range of negative angles, which tend to shift to higher (absolute) values of α as the laser irradiation time is increased. Longer irradiation times also cause a noticeable intensity increase in these peaks. In the range of $\alpha > 0$, a weak peak is observed, but only for $\tau = 1$ s. As the irradiation time is increased, this peak disappears.

The change in the rocking curve shapes in the process of laser diffusion can be caused by both lattice deformation and diffuse scattering by generated defects. The peaks in the normalized intensity functions appearing at negative angles indicate the presence of a near-surface crystal layer with a positive lattice deformation. This is explained by the fact that diffusing aluminum atoms occupy positions at the lattice sites; and because they have a larger covalent radius of $r_{Al} = 0.126$ nm than that of silicon, $r_{Si} = 0.117$ nm, the crystal lattice expands. Average magnitudes of the deformation estimated from the relation $\Delta d/d = -\alpha_0 \cot\Theta_B$, where α_0 is an angular position of the peak of function $P(\alpha)$, amount to 2.3×10^{-3}, 2.8×10^{-3}, and 3.0×10^{-3} for irradiation times $\tau = 1$, 2, and 3 s, respectively.

The weak feature in the $P(\alpha)$ function in the range of angles $\alpha > 0$ at $\tau = 1$ s is evidence of a thin crystalline layer having negative deformation $\Delta d/d \approx -0.8 \times 10^{-3}$. The slight compressive deformation is apparently caused by replacement of silicon atoms with oxygen,

which is present in small concentrations in the starting crystals and has a radius $r_O = 0.066$ nm $< r_{Si}$. At longer irradiation times τ, the dominant role is played by aluminum, because of its higher concentration.

It is quite reasonable to suppose that the deformation profile $\Delta d(z)/d$ has a shape similar to the impurity concentration profile observed after thermal diffusion [7]

$$\Delta d(z)/d = \varepsilon_0 \exp[-(z/L)^m], \quad (1)$$

where $\varepsilon_0 = \Delta d(0)/d$ is the deformation at the surface, L is the diffusion length, and m is a factor varying in the range from $m = 1$ to $m = 2$.

For the case of isothermal diffusion from a thin surface layer, $m = 2$ [7].

Figure 3 shows positive deformation profiles $\Delta d(z)/d$, which were first sketched from the shapes and magnitudes of measured rocking curves and then corrected for angular intensity dependence of the main peaks. Calculation of the coherent scattering component was performed using the Takagi–Topen equation [15] with the deformation profile in the form of (1). The best fit of theoretical and experimental curves is obtained for $m = 1.7 \pm 0.1$. The diffusion length L is equal to 28, 32, and 48 nm for $\tau = 1$, 2, and 3 s, respectively. It is seen in Fig. 3 that the magnitude of deformation and the thickness of a deformed layer increase with irradiation time.

For the (111) reflection, the deformation is related to the concentration of impurity C atoms by $\Delta d(z)/d = 1.44\beta C$ [6], where $\beta = (r_{Al} - r_{Si})/Nr_{Si} = 1.54 \times 10^{-24}$ cm^3 is the deformation factor and $N = 5.0 \times 10^{22}$ cm^{-3} is the density of silicon atoms. Now, the concentration of aluminum atoms near the surface can be easily obtained: $C = 1.1 \times 10^{21}$, 1.4×10^{21}, and 1.5×10^{21} cm^{-3} at $\tau = 1$, 2, and 3 s, respectively. It is nearly two orders of magnitude higher than the equilibrium solubility limit of aluminum at the temperature to which the silicon wafer is heated by laser radiation [1]. The high level of aluminum concentration develops because of the nonequilibrium character of diffusion occurring at pulsed laser irradiation as observed in laser diffusion of other impurities [3. 13].

In the case considered, the temperature increase can be estimated from the relationship

$$\Delta T \approx 2(W/\chi)(\alpha\tau)^{1/2}, \quad (2)$$

where W is the radiation power density, $a \approx 0.5$ cm^2/s is the thermal diffusivity, $\chi \approx 0.8$ W/(cm K) is the thermal conductivity, and τ is the irradiation time [3].

The irradiation was carried out at room temperature; therefore, the near-surface layer should have been heated to temperatures 640, 900, and 1100 °C for laser irradiation times $\tau = 1$, 2, and 3 s, respectively. Larger deformations for longer laser pulses seen in Fig. 3 are related to the increase with temperature of the solubility of aluminum in silicon.

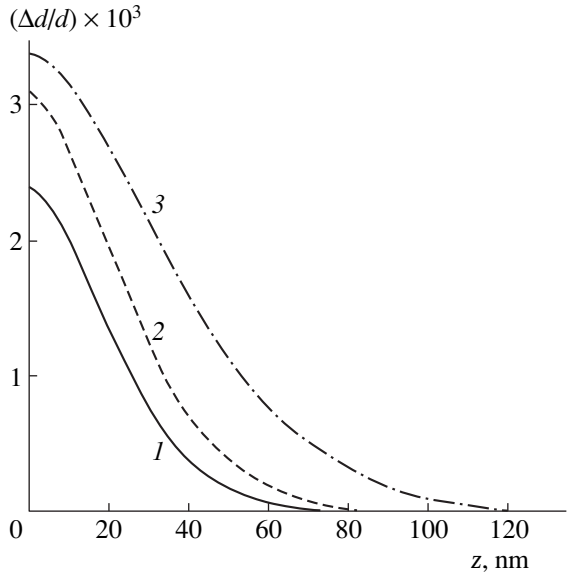

Fig. 3. Deformation profiles in silicon crystals subjected to laser diffusion of aluminum. (*1–3*) same as in Fig. 1.

The difference in impurity concentration is not the only distinction between laser and isothermal diffusion. One more distinction is the extremely high coefficient of solid-state laser diffusion D. Its value can be estimated from the formula $L \approx (D\tau)^{1/2}$. Using the above values of the diffusion length L, we get $D \approx (7 \pm 1) \times 10^{-12}$ cm^2/s. Let us compare this value with diffusion coefficients given by an Arrhenius equation, which is valid for isothermal diffusion [16],

$$D_T = D_0 \exp(-Q/kT), \quad (3)$$

where $D_0 \approx 8$ cm^2/s is a coefficient, which is almost independent of temperature, and $Q = 3.47$ eV is the diffusion activation energy of an impurity atom [1].

The calculations by (3) showed that for $\tau = 1$ s, the laser diffusion coefficient is seven orders of magnitude higher than the coefficient of isothermal diffusion ($D_T \approx 6 \times 10^{-19}$ cm^2/s); and for $\tau = 3$ s, the value of D is nearly six times as large ($D_T \approx 1.2 \times 10^{-12}$ cm^2/s) as in the case of isothermal diffusion. Such a great difference between the laser and isothermal diffusion parameters has been corroborated in other studies [3].

Triple-crystal diffractometry curves of irradiated crystals differ from the curves of starting crystals not only in intensities of the main peaks, but also in the emergence of broad diffuse peaks in the interval of crystal-analyzer angles $\Delta\Theta \approx 2\alpha\sin^2\Theta_B$. These peaks in the TC-XRD curves are due to diffuse X-ray scattering by defects induced in the structure by laser diffusion. The intensity of diffuse scattering I_D for negative sample rotation angles α is higher than for positive angles, indicating the presence of vacancy defects [17], which could form as a result of condensation of excess vacancies on heterogeneous nucleation centers.

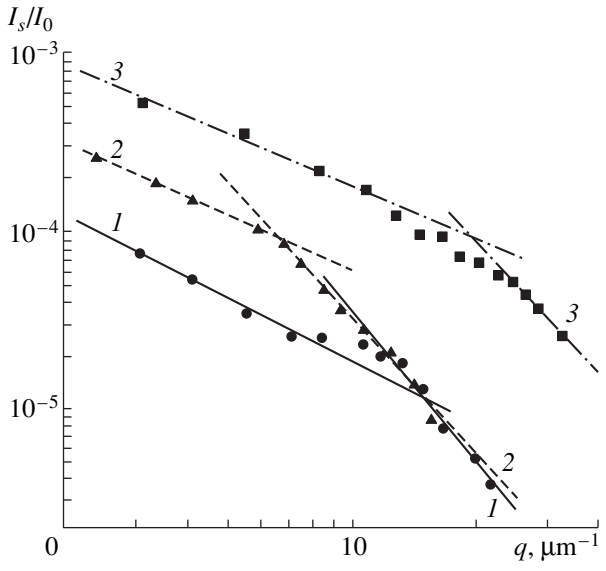

Fig. 4. Intensity of the symmetrical part of diffuse X-ray scattering as a function of the separation q between the reciprocal (111) lattice site and the Ewald's sphere. (*1–3*) same as in Fig. 1.

Figure 4 is a log–log plot of the symmetrical part of the intensity of diffuse peaks integrated over the exit angle $\Delta\Theta$ as a function of the separation q between the reciprocal (111) lattice site and the Ewald's sphere $I_S(q) = [I_D(q) + I_D(-q)]/2$, where $q = \alpha h \cos\Theta_B$, $h = (4\pi/\lambda)\sin\Theta_B$ is the reciprocal lattice vector and λ is the X-radiation wavelength.

It is seen from Fig. 4 that the diffuse scattering intensity increases with increasing irradiation time. In addition, the experimental points are amenable to approximation with sections of straight lines having different slopes relative to the q axis in the regions of small and large q values. This implies that the diffuse scattering intensity decay obeys a power law $I_D \sim 1/q^n$. Measured exponents n are equal to 1.2, 1.04, and 1.01 in the range of small q; and $n \approx 2.9$, 2.6, and 2.5 in the range of large q for curves *1–3*, respectively.

Slopes of the straight lines in Fig. 4 are indicative of defects of the dislocation-loop type for which the absolute value of the slope angle tangent is $n = 1$ in the Xuang region ($q < 1/R$) and $n = 3$ in the Stocks–Willson region ($q > 1/R$), where R is the average radius of a defect [17].

The radii of dislocation loops can be estimated from the relation $R \approx [q_0(\pi hb)^{1/2}]^{-1}$ [17], where q_0 are the coordinates of the intersection points of the sections of straight lines of different slopes and b is the modulus of the Burgers vector (in this particular case, $b = (1/2)\langle 110\rangle = 0.384$ nm). Finally, we get that $R \approx 14$, 30, and 11 nm for samples irradiated for 1, 2, and 3 s, respectively.

The increase in diffuse scattering intensity with irradiation time indicates the growing number of defects in the near-surface layer. To take account of the diffuse scattering, which reduces the intensity of the main peaks in TC-XRD curves, the static Debye–Waller factor $f = \exp(-w)$ was introduced in the rocking curve calculations. The amorphization profile $w(z)$ was assumed in the form of (1). Also taken into account was the fact that the diffuse scattering intensities in Fig. 4 are proportional to the product wL. From these calculations, average values of w have been derived: $w \approx 0.7 \pm 0.02$, 0.16 ± 0.03, and 0.29 ± 0.05 for irradiation times $\tau = 1$, 2, and 3 s, respectively. For dislocation loops, $w \approx (1/2)c_l R^3 (hb)^{3/2}$ [18]; hence, their concentration q_l equals approximately 2.5×10^{15}, 5×10^{14}, and 2×10^{16} cm^{-3} for $\tau = 1$, 2, and 3 s, respectively.

Formation of the defects can be accounted for by both the temperature gradient and introduction of impurities. In [11, 13, 19], it has been shown that the temperature gradient produced by a millisecond exposure to laser radiation causes generation of dislocations in silicon. Therefore, in our case, the formation of dislocation loops depends significantly on the nonequilibrium diffusion of impurities. This is also confirmed by the generation of dislocation loops during thermal processing of silicon crystals doped by ion implantation [20].

CONCLUSIONS

The following conclusions can be made from the performed investigations. Irradiation of single-crystal silicon with a CO_2 laser for 1–3 s on the substrate side induces nonequilibrium solid-state diffusion of aluminum from the surface layer to a depth of 50–100 nm. The aluminum concentration achieved in this way is much higher than in isothermal diffusion. The laser diffusion produces in the near-surface layer of silicon crystal a positive deformation of the lattice $\varepsilon_0 \sim 2.4$–3.4×10^{-3} and generates dislocation loops of diameter $R \sim 10$–30 nm of density from 5×10^{14} cm^{-3} for irradiation time $\tau = 2$ s to 2×10^{16} cm^{-3} for $\tau = 3$ s.

REFERENCES

1. *Atomic Diffusion in Semiconductors*, Ed. by D. Shaw (Plenum, London, 1973; Mir, Moscow, 1975).
2. S. G. Kiyak, Izv. Akad. Nauk SSSR, Ser. Fiz. **53** (3), 417 (1989).
3. V. I. Fistul' and A. M. Pavlov, Fiz. Tekh. Poluprovodn. (Leningrad) **17**, 854 (1983) [Sov. Phys. Semicond. **17**, 535 (1983)].
4. V. I. Fistul', A. M. Pavlov, A. P. Ageev, and A. Sh. Aronov, Fiz. Tekh. Poluprovodn. (Leningrad) **20**, 2140 (1986) [Sov. Phys. Semicond. **20**, 1339 (1986)].
5. S. L. Antonov, A. A. Manenkov, G. N. Mikhaĭlov, *et al.*, Poverkhnost, No. 5, 151 (1991).
6. A. Fukuhara and Y. Takano, Acta Crystalllogr. Sect. A **33** (1), 137 (1977).
7. V. Holy and J. Kubena, Czech. J. Phys., Sect. B **29**, 1161 (1979).

8. A. Iida, Phys. Status Solidi A **54**, 701 (1979).
9. R. N. Kyutt, P. V. Petrashen, and L. M. Sorokin, Phys. Status Solidi A **60** (2), 381 (1980).
10. V. S. Speriosu, J. Appl. Phys. **52**, 6094 (1981).
11. V. A. Bushuev and A. P. Petrakov, Fiz. Tverd. Tela (St. Petersburg) **35**, 355 (1993) [Phys. Solid State **35**, 181 (1993)].
12. V. A. Bushuev and A. P. Petrakov, Kristallografiya **40**, 1043 (1995) [Crystallogr. Rep. **40**, 968 (1995)].
13. A. P. Petrakov and E. A. Golubev, Fiz. Tverd. Tela (St. Petersburg) **40**, 156 (1998) [Phys. Solid State **40**, 140 (1998)].
14. A. M. Afanas'ev, P. A. Aleksandrov, and R. M. Imamov, *X-ray Diffractometry of Submicron Layers* (Nauka, Moscow, 1982).
15. Z. G. Pinsker, *X-ray Crystal Optics* (Nauka, Moscow, 1982).
16. V. S. Eremeev, *Diffusion and Stress* (Énergoatomizdat, Moscow, 1984).
17. P. H. Dederichs, Phys. Rev. B **4**, 1041 (1971).
18. P. H. Dederichs, Phys. Rev. B **1**, 1306 (1970).
19. V. A. Bushuev and A. P. Petrakov, Poverkhnost, No. 9, 64 (1992).
20. J. W. Mayer, L. Eriksson, and J. A. Davies, *Ion Implantation in Semiconductors: Silicon and Germanium* (Academic, New York, 1970; Mir, Moscow, 1973).

Translated by B. Kalinin

Technical Physics, Vol. 45, No. 5, 2000, pp. 618–622. Translated from Zhurnal Tekhnicheskoĭ Fiziki, Vol. 70, No. 5, 2000, pp. 97–101.

A Computerized Complex for Recording and Processing of Reflected High-Energy Electron Diffraction Patterns

V. N. Petrov, V. N. Demidov, N. P. Korneeva, N. K. Polyakov, and G. É. Tsyrlin

Institute of Analytical Instrument Making, Russian Academy of Sciences, Rizhskiĭ pr. 26, St. Petersburg, 198103 Russia

Received February 10, 1999

Abstract—An efficient and high-speed complex for visualization, reading, and processing of reflected high-energy electron diffraction patterns is described. The block diagrams and technical data of the complex, as well as its interface with devices controlling molecular-beam epitaxy of semiconductor structures, are presented. Dedicated software for processing high-energy electron diffraction patterns, including in real time, is suggested. The complex was used for studying heteroepitaxial growth and the formation of InAs nanostructures on the GaAs and Si surfaces. *© 2000 MAIK "Nauka/Interperiodica".*

INTRODUCTION

Reflected high-energy electron diffraction (RHEED) is an efficient *in situ* method for examining solid surface morphology and is widely used in fabricating semiconductor structures, particularly by molecular-beam epitaxy (MBE). RHEED information is visualized on a fluorescent screen as a result of the diffraction of 5- to 25-keV electrons impinging on a solid surface under grazing angles [1].

Analysis of static diffraction patterns allows one to gain insight into the crystal structure of surface layers and quantitatively characterize the surface (misorientation, density of monatomic steps, and distribution of two-dimensional nuclei) [2]. Variations of the intensities of RHEED reflections and their shapes, as well as nonsynchronous changes in the intensities of different reflections during MBE, provide valuable information on fundamental surface processes. Moreover, with such data, one can accurately estimate the growth rate. Generally, the time of growth of a monolayer correlates with the period in the oscillating time dependence of the intensity of a certain reflection [3].

The complete utilization of the potentialities of the RHEED method necessitates recording and quantitative analysis of the entire diffraction pattern or its part. The intensity measurement time should be much less than the time of growth of a monolayer.

In this paper, we describe a modified computerized complex for real-time RHEED pattern optical recording, measurement, and analysis. An earlier version was reported elsewhere [4].

HARDWARE OF THE COMPLEX

The block diagram of the complex is presented in Fig. 1. It includes a video camera (VC), a TV monitor, and a video tape recorder (VTR), all incorporated into IBM PCs with standard monitors; a video input; and a record/playback VTR synchronizer. The complex is controlled by dedicated software.

A Chiper CRT-8260 camera with a conventional TV signal at the output was used. It was fixed on the flange of the MBE growth module in such a way as to keep direct light from entering the objective lens and to display a desired area of the RHEED pattern on the fluorescent screen of a DЭ1202 fast-electron diffractometer, which is used in EP-type MBE equipment.

RHEED patterns observed on the fluorescent screen are recorded by the video camera. A video signal from the camera enters the VTR; and then concurrently, in the "stop" or "record" mode of the VTR, comes to the videoinput and TV monitor. The latter provides a continuous observation of RHEED patterns during experiments. In the "playback" mode of the VTR, the prerecorded signal is automatically applied to the video input and TV monitor.

The video input is intended for the conversion of an analog video signal to the digital form (256 intensity levels, 512×512 pixels) and for storing a TV frame in a RAM with a refresh rate of 50 Hz. Also, it provides software-controlled entry of stored data into a com-

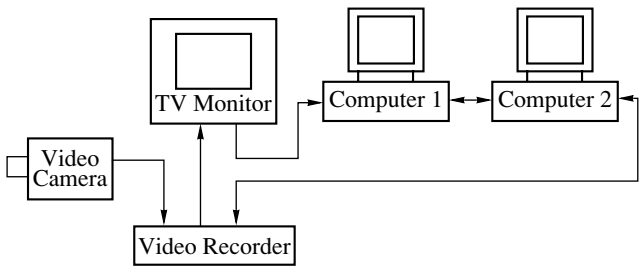

Fig. 1. Block diagram of the complex for computer processing of RHEED patterns.

1063-7842/00/4505-0618$20.00 © 2000 MAIK "Nauka/Interperiodica"

puter. The video input card is inserted into a free ISA slot of computer 1 (any IBM-compatible computer like a IBM PC AT 386SX or a higher version with a monitor resolution no less than 800 × 600 pixels). The block diagram of the video input is presented in Fig. 2.

The record/playback synchronizer creates marks on the sound track of the tape upon recording. In addition, upon processing recorded data, it synchronously emulates the growth program used upon recording in order to correlate RHEED patterns being processed with growth conditions (the position of shutters and opening/closing time). The synchronizer card is inserted into a free ISA slot of computer 2, which controls the shutters of molecular sources. The block diagram of the synchronizer is shown in Fig. 3. It consists of two independent channels for mark writing on and reading out of the tape. The write channel is intended for creating marks on instructions from the shutter control program and consists of an address selector (AS) and a controlled generator (CntrdG). The read channel comprises a comparator (Cm) and an interrupt query generator (IQ). This channel reads out recorded marks.

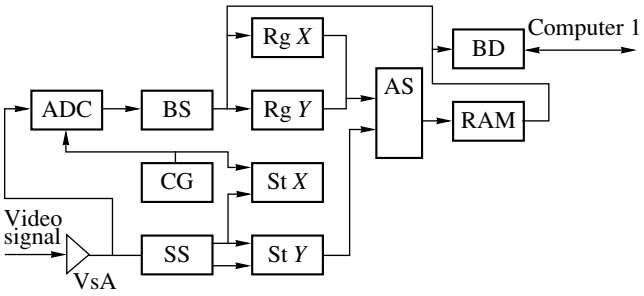

Fig. 2. Block diagram of the video input: VsA, video signal amplifier; ADC, analog-to-digital converter; CG, clock generator; BS, buffer storage; Rg*X* and Rg*Y*, BS address registers; St*X* and St*Y*, binary counters for BS addressing; BD, bus drivers; RAM, random-access memory; AS, address switch; SS, sync pulse selector.

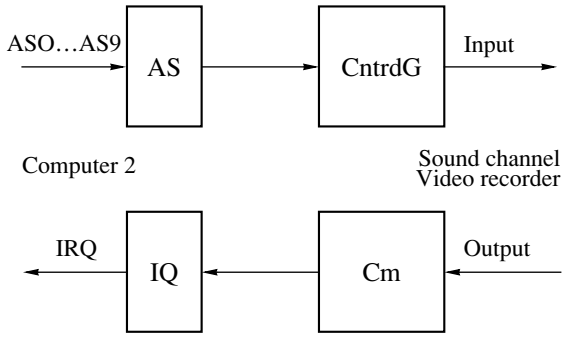

Fig. 3. Block diagram of the synchronizer: AS, address selector; CntrdG, controlled generator; IQ, interrupt query generator; Cm, comparator.

SOFTWARE

The program package allowed the control of the complex hardware, as well as the real-time collection and processing of data for the reflection intensities. The programs were written in the C language for the MS DOS operating system (version 5.0 or higher).

The programs make it possible to read the reflection intensities as the video intensities from the video input. The data are refreshed at a rate of 50 Hz. A readout static RHEED pattern (an image from the video camera or VTR 512 × 512 pixels, 256 levels of signal intensity) can be displayed on the PC monitor and filed on the hard disk in the Windows Bitmap format. The file can be further processed by conventional packages for processing and printing graphic images.

One can receive information both on the whole frame (512 × 512 pixels) and on its separate segments. The programs for reading and processing data on the reflection intensity are available in two versions: one-window and linear. In the former case, an area (window) that contains the most informative reflections is selected. In the latter case, windows along a certain line are selected. The number of windows (to 16) is preset. In both cases, the window size (to 50 × 50 pixels) and the time of observation are specified. During this time, the signal intensities from areas of interest are read out and averaged and the time dependence of the intensity is also displayed. In the linear (multiwindow) version, measurements taken in a preset reference window are displayed.

After the program is fully executed or interrupted by an operator, the information is saved. A user can then display the time dependence for any of the windows; measure, with the help of special markers, time intervals and growth rates; and display the intensity distribution along a diffraction reflection. Data obtained in the linear regime may also be used for the analysis of diffraction profiles by comparing the RHEED intensities between two arbitrary points within any field of the diffraction pattern at a given time instant. The information on signal intensity variations in all the windows can be saved for further processing. It is recorded on a disk in the text file format compatible with conventional plotters. Subsequent analysis can be performed with secondary processing programs, also available in the two versions. A negative image obtained in the linear mode of the secondary processing program is presented in Fig. 4. The basic principles and algorithms for constructing the programs were detailed earlier [4].

The growth control program loaded into computer 2 automatically executes the given sequence of instructions (written as a text file with a specialized language). It also sends labeling instructions that mark the start of the growth program to the record/playback synchronizer. If the computers are directly connected, the growth control and RHEED processing programs can be started simultaneously. All the programs are trans-

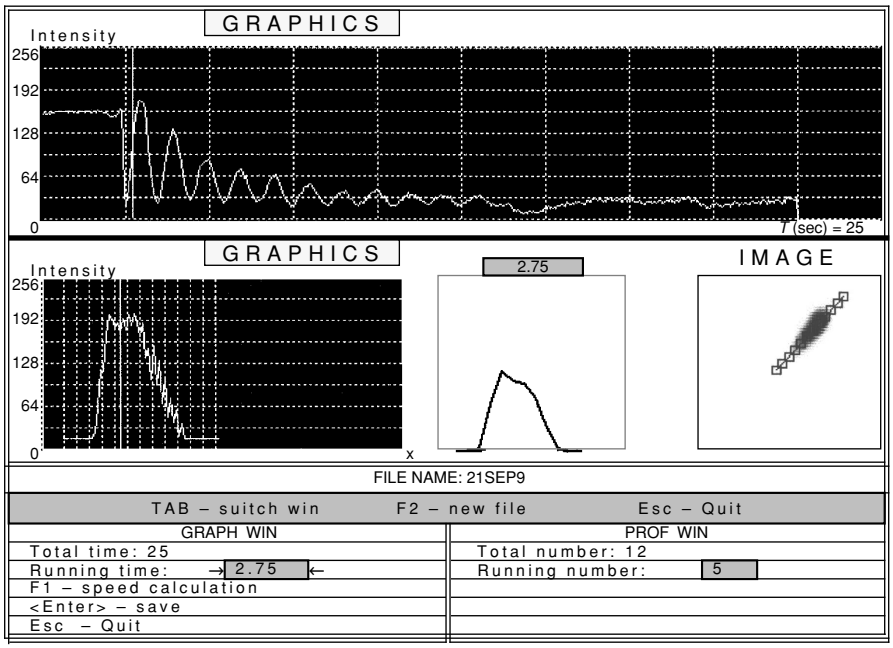

Fig. 4. Negative image on the PC monitor obtained in the linear mode of the secondary-processing program.

lated into English and have a user-friendly menu with the necessary explanations. Both keyboard and mouse controls are available.

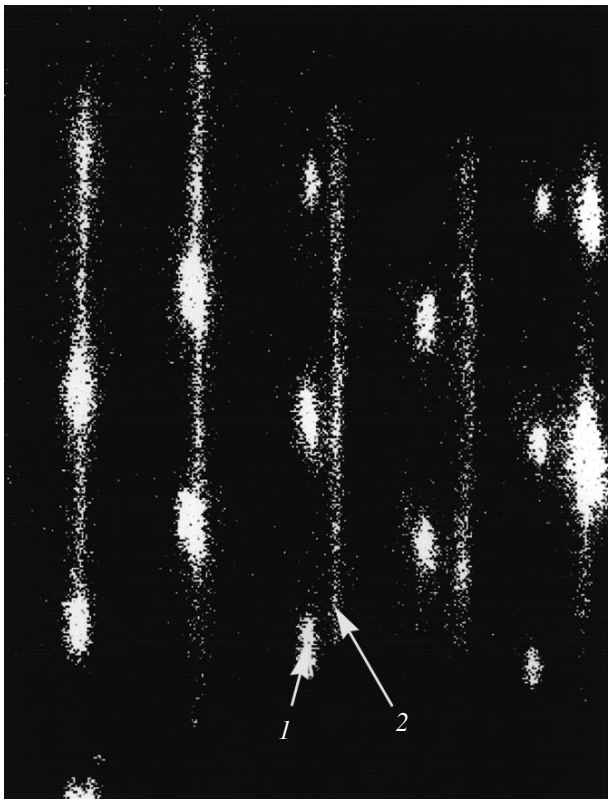

Fig. 5. RHEED pattern in the [011] direction after the deposition if two InAs monolayers on the Si surface at 380°C.

EXPERIMENTAL RESULTS

The application of silicon in light-emitting electronic devices has not yet become common, although dislocation-free large-diameter silicon wafers are cheap. Silicon is an indirect-gap material, where radiative recombination without participation of an extra particle is impossible. However, it has been supposed [5] that, by analogy with III–V compounds, the creation of narrow-gap semiconductor (for example, InAs) quantum dots in the silicon matrix is appropriate for fabricating good light-emitting devices. The fundamental possibility of forming InAs quantum-size structures directly on the silicon surface by MBE has been experimentally confirmed in [6]. Using our complex, we have found [7] that both The Volmer–Weber (purely island) and Stransky–Krastanov mixed growth mechanisms may take place in this heteroepitaxial system. The latter is characterized by the simultaneous formation of a wetting layer and three-dimensional islands. The RHEED pattern taken at angles of incidence and reflection of 1° and 1.5°, respectively, in the direction [011] from two InAs monolayers is shown in Fig. 5. They were deposited at a rate of 0.1 monolayer/s for an As_4-to-In flux rate ratio of 10 and a substrate temperature of 380°C. The pattern indicates that the Volmer–Weber mechanism occurs under such conditions. It is seen that diffraction lines from the Si substrate and spots, typical of three-dimensional growth and corresponding to InAs dots, superpose. The growth time dependences of the diffraction intensity for points *1* (InAs) and *2* (Si) in Fig. 5 are shown in Fig. 6. They were obtained with the RHEED processing program in the linear regime. As follows from the intensity varia-

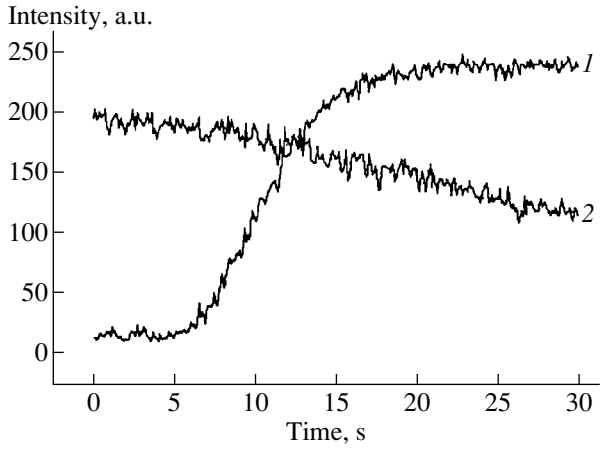

Fig. 6. Time dependences of the diffraction intensity during epitaxial growth by the Volmer–Weber mechanism: (*1*) InAs and (*2*) Si.

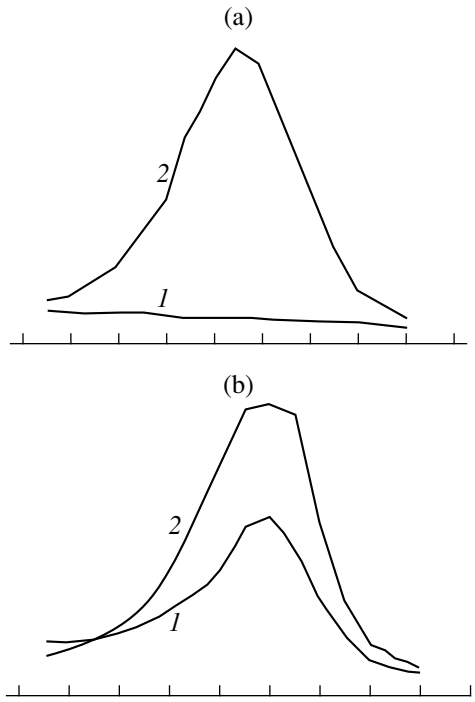

Fig. 7. Intensity profiles of the (01) reflection during SMSE after the deposition of (*1*) 1.3 and (*2*) two InAs monolayers on (a) the starting GaAs surface and (b) InAs quantum dots covered by 20 GaAs monolayers.

tion at point *1*, the transition from two-dimensional to three-dimensional growth (the appearance of the spots) takes place at an InAs thickness of about 0.7 monolayer.

Recently, a technique for creating multilayer epitaxial structures with quantum dots has been offered [8]. It has been shown that, with increasing number of layers, the lateral sizes of the dots increase and their density decreases. The use of so-called "stacked" quantum dots as the active area of semiconductor lasers has substantially improved their performance [9]. We studied changes in the RHEED patterns during self-organization of quantum dots in InAs/GaAs multilayered structures obtained by submonolayer migration-stimulated epitaxy (SMSE) [10]. The profiles of the (01) reflection intensity for (*1*) 1.3 and (*2*) two monolayers of InAs SMSE-growth on the starting GaAs surface are shown in Fig. 7a. Figure 7b gives the same profiles when the InAs dots are covered by 20 GaAs monolayers. The presented results obviously indicate that, at the second and subsequent stages of InAs/GaAs growth by SMSE, the transition from two-dimensional to three-dimensional growth (breakdown of the pseudomorphic layer) is already observed at 1.0–1.1 monolayers. At the first stage, three-dimensional islands form after the evaporation of 1.7 monolayers [11]. This effect can be associated with stress buildup caused by three-dimensional islands present in the underlying layers and contributing to the stress state of a multilayer structure.

CONCLUSION

The described complex is a help in observing and analyzing RHEED patterns during MBE. It was used for the sophisticated treatment of the formation kinetics of quantum dots in InAs/GaAs and InAs/Si systems. Its application has allowed us to discover a periodic split of diffraction profiles during GaAs (100) growth [4], a shift in time dependences of the diffraction intensity at different points [11], and the appearance of reflections making an angle of 45° with the basic ones [12].

The complex can be integrated into a closed-loop MBE control system to provide reproducible growth of quantum-size structures. The thickness of the layers can be program-controlled to within fractions of a monolayer in any MBE equipment equipped with tools for RHEED analysis.

The complex can be used for processing optical images with minor hardware and software modifications.

ACKNOWLEDGMENTS

The authors thank Yu.B. Samsonenko for his participation in the growth experiments and V.G. Dubrovskiĭ for valuable discussions.

This work was supported in part by the Russian Foundation for Basic Research (project no. 98-02-18317) and scientific programs "Physics of Solid-State Nanostructures" (project no. 98-2029) and "Promising Technologies and Devices for Micro- and Nanoelectronics" (project no. 02.04.5.1.40.É.46).

REFERENCES

1. M. A. Herman and H. Sitter, *Molecular Beam Epitaxy. Fundamentals and Current Status* (Springer, Berlin, 1989).

2. A. P. Senichkin, A. S. Bugaev, and R. A. Molchnovsky, in *Proc. Int. Symp. "Nanostructures: Physics and Technology," St. Petersburg, 1993*, pp. 102–103.
3. J. N. Neave, B. A. Joyce, P. J. Dobson, *et al.*, Appl. Phys. A **31**, 1 (1983).
4. G. M. Gur'yanov, V. N. Demidov, N. P. Korneeva, *et al.*, Zh. Tekh. Fiz. **67** (8), 111 (1997) [Tech. Phys. **42**, 956 (1997)].
5. N. N. Ledentsov, in *Proceedings of 23rd International Conference on Physics of Semiconductors, 1996*, Ed. by M. Scheffler and R. Zimmermann (World Scientific, Singapore, 1996), Vol. 1, pp. 19–21.
6. G. É. Tsyrlin, V. N. Petrov, V. G. Dubrovskiĭ, *et al.*, Pis'ma Zh. Tekh. Fiz. **24** (8), 10 (1998) [Tech. Phys. Lett. **24**, 290 (1998)].
7. G. É. Tsyrlin, N. K. Polyakov, V. N. Petrov, *et al.*, in *Proceedings of Conference "Nanophotonics-99," Nizhni Novgorod, 1999*, pp. 165–167.
8. J. Tersoff, C. Teichert, and M. G. Lagally, Phys. Rev. Lett. **76**, 1675 (1996).
9. A. E. Zhukov, A. Yu. Egorov, A. R. Kovsh, *et al.*, Fiz. Tekh. Poluprovodn. (St. Petersburg) **31** (4), 483 (1997) [Semiconductors **31**, 411 (1997)].
10. G. É. Tsyrlin, A. O. Golubok, S. Ya. Tipisev, *et al.*, Fiz. Tekh. Poluprovodn. (St. Petersburg) **29** (9), 1997 (1995) [Semiconductors **29**, 884 (1995)].
11. G. E. Cirlin, N. P. Korneeva, Y. N. Demidov, *et al.*, in *Physics Conference "Compound Semiconductors 1996," 1997*, No. 155, p. 821.
12. G. É. Tsyrlin, N. P. Korneeva, V. N. Demidov, *et al.*, Fiz. Tekh. Poluprovodn. (St. Petersburg) **31** (10), 1230 (1997) [Semiconductors **31**, 1057 (1997)].

Translated by V. Voitenko

Technical Physics, Vol. 45, No. 5, 2000, pp. 623–626. Translated from Zhurnal Tekhnicheskoĭ Fiziki, Vol. 70, No. 5, 2000, pp. 102–105.

EXPERIMENTAL INSTRUMENTS AND TECHNIQUES

Superconducting Cluster in $YBa_2Cu_3O_{7-x}$ Ceramic

D. R. Dzhuraev and B. Yu. Sokolov

Tashkent State University, Universitetskaya ul. 95, Vuzgorodok, Tashkent, 700095 Uzbekistan

Received January 28, 1999

Abstract—The method of point laser heating of a sample is used to perform experimental investigations of the electrical conductivity of $YBa_2Cu_3O_{7-x}$ ceramic in the vicinity of its critical state. It is found that, in the vicinity of transition to the superconducting state, the electrical conductivity of the ceramic exhibits a clusterlike behavior substantially nonuniform over the sample cross section. The topology of a superconducting cluster is investigated, as well as its spatial localization in the sample. A model of the formation of a superconducting cluster in a ceramic superconductor is suggested. © *2000 MAIK "Nauka/Interperiodica".*

In a model representation, high-temperature superconducting (HTSC) ceramics in the subcritical temperature region are often treated as a plurality of superconducting granules, i.e., crystallites interconnected by Josephson contacts ("weak couplings") [1]. Such a model is used to advantage to describe the electrical conductivity of an HTSC ceramic in the vicinity of its critical state. In so doing, it is assumed that, in the immediate vicinity of superconducting transition, all of the macrocurrent J flowing in the ceramic is concentrated in an infinite cluster (IC) which incorporates superconducting regions combined by a random network of weak couplings. This random network is some cellular structure characterized by a correlation radius L, with the topology and properties of this cellular structure defining the current-carrying capacity of the HTSC ceramic.

The conductivity of the weak coupling network is usually studied with the aid of computer simulation. However, depending on the selected model and calculation algorithm, the obtained results often differ appreciably and sometimes contradict one another (see, for example, [2, 3]). Therefore, in order to verify and specify the existing model concepts, experimental investigations of superconducting IC in $YBa_2Cu_3O_{7-x}$ ceramics were performed, the results of which are given below.

MEASURING PROCEDURE AND SAMPLES

The IC investigations involved the use of the so-called procedure of laser testing for spatial nonuniformity of the electrical conductivity of a superconductor [4, 5], which essentially consists in the following. A current $J < J_c$ is passed through a sample at a temperature $T < T_c$ (T_c and J_c denote the critical temperature and critical current of the sample, respectively); the sample is simultaneously affected by the focused radiation of a laser serving the function of a source of concentrated heat. Under conditions of fairly local heating of the sample, a disintegration of the IC occurs; i.e., some region of the sample at the point of heating changes to a resistive state (a part of the weak couplings changes to a normal state; in so doing, the ceramic crystallites remain superconducting).

Discontinuities in the IC lead to a voltage drop across the sample,

$$U(x) \propto j(x)\frac{dR(x)}{dT}\Delta T(x),$$

where $j(x)$ is the local density of the transport current and $dR(x)/dT$ and $\Delta T(x)$ denote local changes of resistance and temperature of the sample at the point of heating, respectively.

The expression for $U(x)$ may have a simpler form if the nonuniformity of the IC is ignored (assuming that the network of weak couplings has a regular periodic structure), and if it is assumed that the correlation between the voltage drop on a weak coupling and the current flowing through it in a normal state is defined by Ohm's law (this is justified by the fact that the behavior of Josephson contacts in the vicinity of T_c is well described by the resistive model of [1]). In this case, the voltage drop across the sample may be expressed as

$$U(x) = J\rho(l)/s, \quad (1)$$

where J is the current through the sample, ρ is the sample resistivity in a resistive state, l is the width of discontinuity of the IC, and s is the IC section in a plane perpendicular to the direction of the current J.

Therefore, by measuring the variations of the voltage drop $U(x)$, which arise during the scanning of the sample surface by a focused laser beam, one can investigate the parameters of the IC and determine its spatial localization in the sample.

The investigations were performed with samples of $YBa_2Cu_3O_{7-x}$ ceramic prepared by the conventional

1063-7842/00/4505-0623$20.00

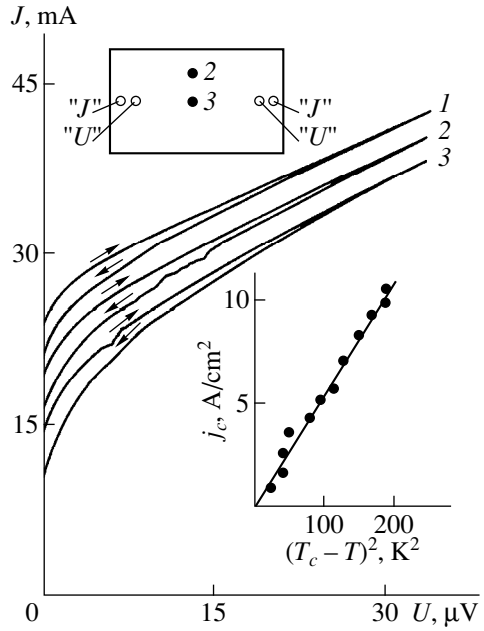

Fig. 1. The current–voltage characteristics of the investigated sample: (*1*) without illumination; (*2* and *3*) with local heating of the periphery and central part of the sample (the time of current sweep, ~5 s); (●, *2*, *3*) positions of the light spot on the sample surface, shown in the top drawing. The inset gives the temperature dependence of the critical current density of the investigated ceramic.

technology of sintering powders of $BaCO_3$, Y_2O_3, and CuO in the solid phase. As was revealed by X-ray analysis, the synthesized samples were uniform and single-phase in composition. The samples were characterized by a density of ≈4.7 g/cm^3; a resistivity at room temperature $\rho \approx 1.5 \times 10^{-3}$ Ω cm; and a critical current density $j_c(T = 78\ \text{K}) \approx 10$ A/cm^2, with the characteristic crystallite size of about 10 μm. The critical temperature of the samples, determined by the minimum detected voltage drop (see below), was approximately 92 K. The samples being investigated were processed to plates sized ~(6 × 4 × 0.2) mm and, to avoid breakage, glued (with epoxy resin) to a sapphire substrate approximately 0.5 mm thick.

All investigations were performed with a 330 Hz alternating current using the standard four-point probe method and the technique of synchronous detection of useful signal. The minimum detected voltage drop amounted to ~10^{-9} V (with the integration time constant of about 0.1 s). In order to ensure the optimum electric contact, a layer of conducting In–Ga paste was applied to the sample surface at points of contact with the electrodes. The local heating of a sample was accomplished by radiation of a He–Ne laser (λ = 0.63 μm) with a power of about 15 mW, which was focused by a microscope to a point ~15 μm in diameter on the sample surface. The sample was placed on the refrigerant line of an optical cryostat capable of automatic XY-displacement in the focal plane of the microscope at a rate of ~2 mm/min. With liquid nitrogen used as the refrigerant, the cryostat design enabled one to perform measurements at T = 84 K.

EXPERIMENTAL RESULTS

Five similar samples were investigated with similar results. At the same time, the electrical characteristics of the same sample varied markedly depending on the number of cooling–warming to room temperature–cooling cycles, which may be associated with the emergence of microcracks between crystallites, because, as a rule, the sample cracked after eight to ten such cycles. The results given below were obtained in one of the investigated samples after its first cooling to T = 84 K.

Figure 1 gives the current–voltage characteristics of an investigated sample measured without (curve *1*) and with (curves *2*, *3*) illumination of its surface by a focused laser beam. One can well see that the local heating considerably affects the value of the critical current: in the case without illumination of the sample, $J_c \approx 24$ mA, with this value decreasing to ≈14.5 mA when the light spot hits the sample center (Fig. 1).

The obtained values of J_c enable one to estimate the "effective" value of local heating ΔT. We use the data on the temperature dependence of the critical current density j_c (see the inset in Fig. 1, where the values of j_c are given as functions of $(T_c - T)^2$, which is characteristic of $YBa_2Cu_3O_{7-x}$ ceramic [1]) to find that, in the central zone of the temperature field of the concentrated heat source, $\Delta T \sim 3$ K. The observed hysteresis of the current–voltage characteristic is apparently associate with heating due to released heat of microregions between the crystallites of the ceramic, i.e., weak couplings , during their transition to a normal state.

The variations of the signal of voltage drop $U(x)$ observed at different distances from the current contacts when the sample surface is scanned by a laser beam perpendicular to the direction of current at $J \approx J_c$ are given in Fig. 2. It follows from the obtained $U(x)$ curves that the zone sensitive to point heating is localized in a fairly narrow region of the sample; i.e., in the vicinity of the critical state, the electrical conductivity of the sample is substantially nonuniform throughout its volume. It is within this region, through which almost all of the macrocurrent J is transported, that the superconducting cluster is confined. Consequently, the IC is a current filament of little-varying cross section, extending from one current contact to another.

Figure 3 gives the results of measurement, for different values of current, of the variations of voltage drop $U(x)$ in the region of the peak of the signal shown at *1* in Fig. 2. The absence of a signal indicates that, with a current J = 14 mA, the local heating does not result in disintegration of the IC. With the subsequent value of current J = 15 mA, a signal $U \approx 0.5$ μV appears on the sample, when the focus is at a distance of about

1.5 mm from the sample edge. The emergence of the signal indicates that the maximum of the temperature of local heating coincides with a superconducting IC which, in so doing, suffers a discontinuity. A further increase in the current leads to an extension of the sensitive zone. This occurs as a result of the IC approaching its critical state (or, using the nomenclature of the percolation theory, as J increases, the fraction of unbroken weak couplings approaches the percolation threshold P_c [6]); because of this, a lower heating temperature is sufficient for the IC discontinuity. This means that the IC discontinuity is not caused by the central part of the region of local heating where ΔT is maximum, but is rather caused by its periphery, thereby increasing the observed width of the cluster. The emergence of a second plateau on the first plateau of the $U(x)$ curve and, with a further increase in current, of a third one, implies that the IC suffers second and third discontinuities, respectively (for $J > 15.3$ mA, the stepped structure of variation of the $U(x)$ signal almost ceases to be observed). Note that a qualitatively similar behavior of the $U(x)$ signal was observed in superconducting $BaPb_{1-x}Bi_xO_3$ ceramic in [4].

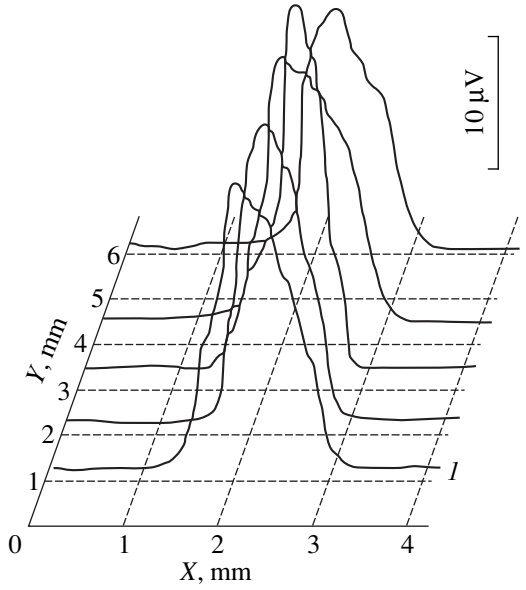

Fig. 2. Variations of the voltage drop, observed when the sample surface is scanned by a laser beam (J = 23 mA, T = 84 K).

DISCUSSION OF THE RESULTS

The transition of a Josephson contact to a superconducting state (or from superconducting to normal) in a real HTSC ceramic with a preassigned value of J is defined by three main factors, namely, its critical current, the local current density, and the intrinsic magnetic field of current at the location of the contact. Proceeding from this, we will analyze the foregoing experimental results.

It is remarkable that, for low currents, the IC discontinuities under conditions of local heating are discrete (Fig. 3). This means that the breaking of one weak coupling (or of a small number of such couplings) leads to an increase in the local current density to its critical value, as a result of which all weak couplings of this portion of the IC that are parallel to the broken one change to a normal state. The latter fact indicates that, in the vicinity of the critical state, the network of weak couplings forms Josephson contacts characterized by a slight scatter of their critical currents.

The height of steps on the $U(x)$ curves (Fig. 3) enables one to determine the width of the elementary discontinuity of the IC, which may be naturally identified with the cell size of the network of weak couplings (with a correlation radius L). We use the value of resistivity of the sample in a resistive state $\rho \approx 1.5^{-5}$ Ω cm found from the linear portions of the current–voltage characteristic (Fig. 1), as well as the values of U and J given in Fig. 3, to derive, from equation (1), $L \approx 40$ μm. In view of the fact that the characteristic crystallite size of the investigated ceramic is ~10 μm, one can conclude that an IC forms (or disintegrates) when the fraction of superconducting weak couplings amounts to ~0.25 of

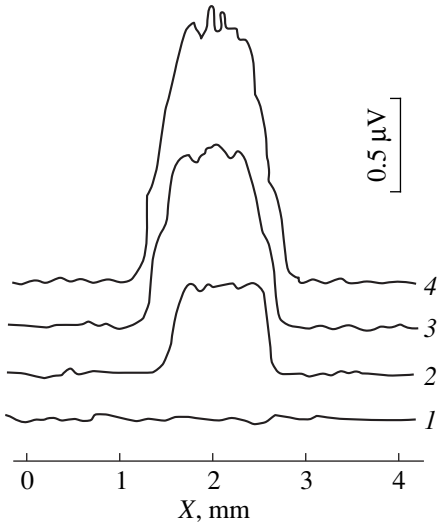

Fig. 3. Variations of the voltage drop across the sample observed when the sample surface is illuminated in the region of a peak of signal *1* at (*1*) J = 14.0, (*2*) 15.0, (*3*) 15.1, (*4*) 15.2 mA.

their total number. This figure proves to be much less than the predicted (within the percolation theory) values of the percolation threshold of a three-dimensional lattice of identical Josephson contacts $P_c = 0.37$ [7] and of the percolation threshold of an infinite cubic lattice $P_c = 0.31$ [6].

It is known (see, for example, [8]) that a decrease in P_c compared to its value following from the classical percolation theory implies that, in the process of IC formation, the current-carrying couplings are arranged in

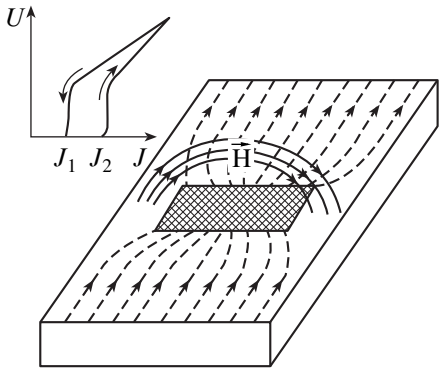

Fig. 4. The spatial distribution of transport current in the sample (broken lines) during formation of a single finite superconducting cluster in this sample (cross-hatched region). The solid lines are the lines of force of magnetic field H of the transport current. The inset gives the voltage drop across a Josephson contact as a function of flowing current; J_1 and J_2 respectively denote the critical currents of a contact during its transition from normal to superconducting and from superconducting to normal states.

the lattice in a correlated manner. Consequently, in our case, the transition of a weak coupling to a superconducting state depends on whether another superconducting weak coupling is available in the vicinity of the former weak coupling. This correlation may be explained if we take into consideration the fact that, during transition to a superconducting state, the temperature and, as a consequence, the resistance of a Josephson contact decrease (see the inset in Fig. 4, which gives the presumed current–voltage characteristic of an individual Josephson contact).[1] This, in turn, brings about a redistribution of the currents flowing through adjacent Josephson contacts, with a decrease in the currents in the nearest parallel contacts and their increase in the nearest sequence contacts. In view of the above-identified slight scatter of the critical currents of Josephson contacts which form an IC in the vicinity of its critical state, such a redistribution of currents will result in a higher probability of superconducting weak couplings emerging in parallel to one another than in series with one another. Hence, one can conclude that, in the vicinity of transition to a superconducting state, finite superconducting clusters exist in ceramics which are shaped like bands extending perpendicular to the direction of transport current, with an IC formed at the confluence of those bands.

As is known [9], it is the intrinsic magnetic field of the current that restricts the value of the critical current density in $YBa_2Cu_3O_{7-x}$ ceramic (which, in the final analysis, is due to a strong magnetic-field dependence of Josephson current); therefore, it is obviously the same factor that will define the transverse dimensions of the IC. In order to illustrate the above-described behavior of the electrical conductivity of an HTSC ceramic in the vicinity of the critical state, Fig. 4 shows diagrammatically the distribution of transport current in the sample during formation of a single finite superconducting cluster in this sample.

Note in conclusion that the model of formation of a superconducting IC treated above is largely qualitative. Obviously, more unambiguous and rigorous conclusions would require additional detailed investigations directed primarily toward studying the correlation between the electrical conductivity of an HTSC ceramic and elements of its structure (size of granules, presence of texture, properties of intergranular layers, etc.). Nevertheless, we believe that the obtained results may serve as a basis both for further experimental investigations and for theoretical models describing more adequately the electromagnetic properties of ceramic superconductors.

[1] The fact that the heating (cooling) of Josephson contacts during their transition to a normal (superconducting) state has a substantial effect on the electrical conductivity of an HTSC ceramic follows directly from the hysteresis of the current-voltage characteristics shown in Fig. 1.

REFERENCES

1. E. Z. Meĭlikhov, Usp. Fiz. Nauk **163** (3), 27 (1993) [Phys. Usp. **36**, 129 (1993)].
2. E. L. Hinrichsen, S. Roux, and A. Hansen, Physica C (Amsterdam) **167**, 433 (1990).
3. P. L. Leath and W. Tang, Phys. Rev. B **39** (10), 6485 (1989).
4. A. P. Perov, Pis'ma Zh. Éksp. Teor. Fiz. **43** (7), 327 (1986) [JETP Lett. **43**, 422 (1986)].
5. Yu. Ya. Divin, F. Ya. Nad', V. Ya. Pokrovski, and P. M. Shadrin, IEEE Trans. Magn. **27** (2), 1101 (1991).
6. D. Stauffer, *Introduction to Percolation Theory* (London, 1985).
7. K. H. Lee and D. Stroud, Phys. Rev. B **45** (45), 2417 (1992).
8. B. I. Shklovskiĭ and A. A. Éfros, *Electronic Properties of Doped Semiconductors* (Nauka, Moscow, 1979; Springer-Verlag, New York, 1984).
9. H. Dersch and G. Blatter, Phys. Rev. B **38** (16), 11391 (1988).

Translated by Henri A. Bronstein

Technical Physics, Vol. 45, No. 5, 2000, pp. 627–629. Translated from Zhurnal Tekhnicheskoĭ Fiziki, Vol. 70, No. 5, 2000, pp. 106–108.

BRIEF COMMUNICATIONS

On the Mechanism of Explosive Etching of PMDA–ODA Film in Nonequilibrium Oxygen Plasmas

I. I. Amirov

Institute of Microelectronics, Russian Academy of Sciences, ul. Universitetskaya 21, Yaroslavl, 150007 Russia

Received March 30, 1999

Abstract—The explosive acceleration of PMDA–ODA film etching in the oxygen plasma generated by a high-frequency inductive discharge at a low pressure (P = 0.2 Pa) is described. The peak in the etch rate is shown to depend on the energy of bombarding ions and film thickness. The explosive kinetics of PMDA–ODA film etching is controlled by the cyclodehydration reaction transforming it into a polyimide film. The imidization is accelerated by the exothermic effect of oxidation reactions that take place on the film surface. As a result, the two reactions form a positive feedback loop, which promotes the ion-induced chain process of PMDA–ODA film etching and imidization. © *2000 MAIK "Nauka/Interperiodica".*

The etching of organic polymer films in the oxygen plasmas generated by radio-frequency and microwave discharges are widely applied in microelectronics technologies [1, 2]. To perform etching in the anisotropic mode, the process is conducted at a low pressure (P < 1 Pa) with intense ion bombardment. Under these conditions, the ions initiate an interaction between adsorbed oxygen molecules and polymer molecules. The rate of ion-induced etching is constant in time and is independent of the specimen temperature and gas pressure [2, 3]. However, pyromellitic-dianhydride–oxydianiline (PMDA–ODA) film etching was found to be an unsteady process [4]. The rate of film etching sharply increased at an initial stage and then decreased to a certain steady-state value. The magnitude and half-width of the peak in the etch rate depended on the energy and/or energy flux carried by the ions impinging on the surface. These dynamic characteristics of film etching were attributed to the cyclodehydration reaction simultaneously taking place inside the film and resulting in its transformation into a polyimide (PI) film. At the final stage of film etching, when the etch rate has a constant value, the process was interpreted as the etching of the newly formed polyimide layer [4]. However, the mechanism of accelerated PMDA–ODA film etching still remained obscure. In this paper, it is shown that the film etching kinetics are determined by the film thickness. The peak rate of PMDA–ODA film etching is almost 100 times higher than the rate of PI film etching. The explosive film etching is explained by a positive feedback loop formed by the oxidation and cyclodehydration reactions, which promotes the ion-induced chain process of PMDA–ODA film etching and imidization.

Experiments were conducted in a reactor of the design described in detail in [4, 5]. It consisted of two vertical cylindrical chambers: a discharge chamber and a reactor. RF inductive discharge was ignited in the quartz discharge chamber (10 cm in diameter and 15 cm long) by means of an RF generator (f = 40.68 MHz). The discharge chamber was placed in a nonuniform magnetic field generated by two solenoids. At its center, the peak magnetic induction reached 10^{-2} T. The chamber was filled with oxygen and argon. The generated plasma diffused into the metal reactor (30 cm in diameter and 35 cm long), which contained a water-cooled aluminum electrode (15 cm in diameter), where the specimens to be tested were placed on an aluminum holder plate (16 cm in diameter and 3 mm thick). The distance between the bottom edge of the discharge chamber and the electrode was 30 cm. The required inductive wattage was supplied to the electrode by a separate RF generator (f = 13.56 MHz). By applying the RF bias, a constant negative self-bias potential was set at the electrode to control the energy E_i of impinging ions. It was determined as $E_i = e(U_s - U_p)$, where e is the electron charge, U_s is the surface potential, and U_p is the plasma potential. Probe measurements showed that U_p = 30 V relative to the grounded reactor walls.

The tested specimens were 3.8-, 6.0-, 9.6-, and 15-μm-thick PMDA–ODA pyromellitic-dianhydride–diaminodiphenyl-oxide-based (AD-9103 lacquer) films deposited by a centrifugal method on 400-μm-thick silicon wafers. The specimen area was 1 cm^2. The etch rate was measured by means of laser interferometry with the use of a 633-nm He–Ne laser and a MULTISEM 440 diagnostic system. After a certain time interval the film thickness was measured by a TALYSTEP profilometer.

The experiments were conducted at oxygen pressure 0.2 Pa, RF discharge power 500 W, gas flow rate 30 sccm, and RF wattage put in the wafer holder (W_s) up to 50 W.

The etching kinetics of the 15-μm-thick PMDA–ODA film substantially varied as the self-bias potential

1063-7842/00/4505-0627$20.00

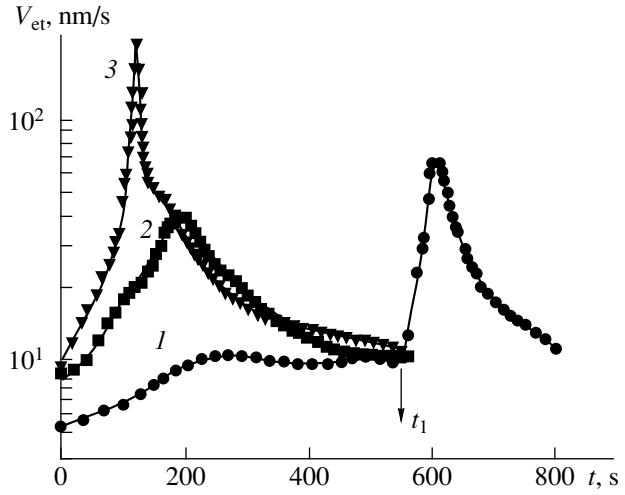

Fig. 1. Etch rate versus time for a PMDA–ODA film (h = 15.0 μm) in an oxygen plasma for various bias potentials: (*1*) $U_s = U_f$, W_s = 0 W; (*2*) U_s = –60 V, W_s = 20 W; (*3*) U_s = –105 V, W_s = 30 W; P = 0.2 Pa; Q = 30 sccm: W = 500 W.

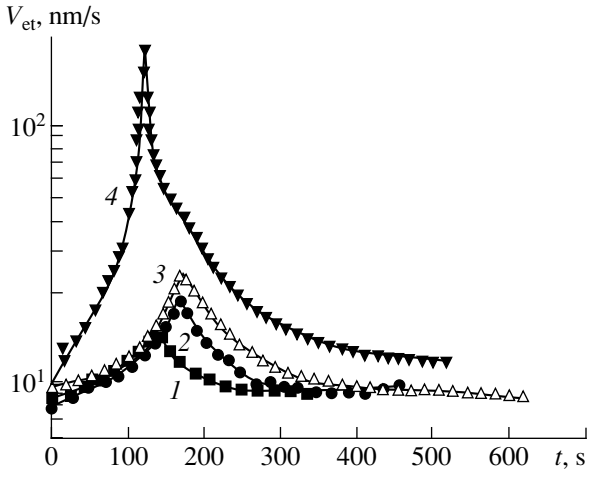

Fig. 2. Etch rate versus time for a PMDA–ODA film in an oxygen plasma for various film thicknesses at U_s = –105 V (W_s = 30 W): (*1*) 3.8, (*2*) 6.0, (*3*) 9.6, and (*4*) 15.0 μm; P = 0.2 Pa; Q = 30 sccm: W = 500 W.

was increased (Fig. 1). Without any RF wattage put in the wafer (when the surface potential was equal to the floating potential U_f), a slight increase in the etch rate with time was observed. When the bias potential was –60 V (W_s = 20 W), the etch rate sharply increased with time. When the energy of bombarding ions was increased at t_1 (U_s = –160 V, W_s = 50 W), another explosive increase in the etch rate was observed (curve *1* in Fig. 1), albeit the peak etch rate was lower than that observed for U_s = –105 V. When the bias potential was –160 V (W_s = 50 W), the peak PMDA–ODA etch rate was higher than 600 nm/s, which is almost 100 times higher than the initial etch rate. Note that the film etching would continue for ~30 s after the plasma generation was disrupted when this peak etch rate was attained.

The dependence of PMDA–ODA etching kinetics on the bias potential (Fig. 1) was much stronger as compared to that observed in [4]. This disparity is obviously due to a difference in film thickness. In [4], the film was 6.0 μm thick. An analysis of PMDA–ODA film etching kinetics in an oxygen plasma depending on the film thickness showed that the magnitude and half-width of the etching-rate peak increases with film thickness (Fig. 2). Note that when relatively thick PMDA–ODA films were etched (h = 9.6, 15, and 22 μm), the etching interferograms exhibited an initial stage of slow increase in the etch rate. This induction period, which may be as long as 60 s, is not shown in the figures. Thus, the plots presented here suggest that the PMDA–ODA film etching kinetics depends on the energy of the impinging ions and film thickness.

The explosive character of PMDA–ODA film etching is attributed to the accelerating cyclodehydration reaction taking place inside the film. The mechanism of the influence of the cyclodehydration reaction on polymer-film oxidation reactions is obscure. Since water is produced in the reaction, one may conjecture that when the water forming in the bulk of the film reaches its surface, the surface is brought into a state similar to that induced by ion bombardment. The transient PMDA–ODA film etching observed after the discharge was switched off at the moment when a high imidization rate was reached indicates that the film imidization initiates oxidation reactions. The acceleration of the cyclodehydration reaction is explained by the fast growth of film temperature caused by exothermic reactions on the film surface (the activation energy of the cyclodehydration reaction is 23–30 kcal/mol [6]). The temperature of a 10-μm-thick polymer film, estimated with the heat of reaction (5 kJ/g [2]) taken into account, can be as high as 600 K, whereas the temperature of a specimen without a film in a plasma environment did not exceed 450 K [4].

The results shown in Fig. 1 suggest that explosive etching develops only when a certain ion energy flux is reached. When the energy of impinging ions is low (i.e., etching is conducted at the floating potential), the etch rate is constant in time for films of thickness less than 9.6 μm. The oxygen ion bombardment of the surface appears to initiate not only oxidation reactions, but also imidization. In experiments on film etching in a low-oxygen O_2 + Ar (20 : 80) plasma, the etch rate did not exhibit explosive behavior, even though the specimen was heated to a high temperature. Thus, the cyclodehydration and oxidation reactions form a positive feedback loop, which promotes a chain process of etching and imidization.

ACKNOWLEDGMENTS

I thank L.A. Tsvetkova for the preparation of PMDA–ODA film specimens.

REFERENCES

1. M. A. Hartney, D. W. Hess, and D. S. Soane, J. Vac. Sci. Technol. B **7**, 1 (1989).
2. J. A. G. Baggerman, R. J. Visser, and J. H. Collart, J. Appl. Phys. **75**, 758 (1994).
3. J. H. Collart, J. A. G. Baggerman, and R. J. Visser, J. Appl. Phys. **78**, 47 (1995).
4. I. I. Amirov and P. G. Buyanovskaya, Khim. Vys. Énerg. **32**, 422 (1998).
5. I. I. Amirov, A. E. Brednikov, and M. O. Izyumov, Mikroélektronika **27**, 22 (1998).
6. N. A. Andronova, M. I. Bessonov, L. A. Laus, and A. P. Rudakov, *Polyimides: A New Class of Thermally Stable Polymers* [in Russian] (Nauka, Leningrad, 1968).

Translated by A. S. Betev

Technical Physics, Vol. 45, No. 5, 2000, pp. 630–632. Translated from Zhurnal Tekhnicheskoĭ Fiziki, Vol. 70, No. 5, 2000, pp. 109–111.

BRIEF COMMUNICATIONS

Determination of the Supercooling Dependence of the (211) Facet of BGO Crystal on Growth Rate from the Temporal Dependence of Supercooling at a Prescribed Melt-Cooling Rate

Ya. V. Vasiliev, V. D. Golyshev, M. A. Gonik, É. N. Kolesnikova, V. B. Tsvetovskiĭ, V. N. Shlegel', and V. S. Yuferev

All-Russia Scientific Research Institute of the Synthesis of Mineral Raw Materials, Aleksandrov, Vladimir oblast, 601600 Russia

Received March 30, 1999

Abstract—The results of determination of the supercooling dependence at the interphase boundary on the rate of growth from melt of the monocrystal $Bi_4Ge_3O_{12}$ in the [211] direction are presented. Determination of supercooling was based on optical pyrometer measurements of the intensity of heat emission from the interphase boundary through the growing crystal. The crystal was grown by the AHF method (axial heat flux near the front of crystallization) by cooling the AHF heater at a specified rate. The growth rate corresponding to the measured supercooling value was determined by calculations. The study has shown that the supercooling is high and varies nonlinearly with the growth rate. © *2000 MAIK "Nauka/Interperiodica".*

INTRODUCTION

To determine the features of interphase kinetics in the layer-by-layer growth mode data on supercooling at the facet as a function of growth rate, impurity species, their concentrations, and crystallographic direction are needed. However, up till now, descriptions of the processes of interphase kinetics in the growth of monocrystals of dielectrics from high-temperature melts were based upon indirect estimations of supercooling obtained from data on the temperature gradient and size of the facet, whereas direct measurements have not yet been carried out.

In [1], the method and the setup for measuring interphase boundary supercooling during the growth of $Bi_4Ge_3O_{12}$ (BGO) are described. The method is based on the peculiar optical properties of BGO. The optical absorption coefficient of the BGO monocrystal is small, while that of BGO melt is high [2]. Therefore, it can be assumed that in the wavelength range 0.65-4 μm, the crystal is transparent and the melt is not. Such optical properties allow for the measurement of the heat radiation of the interphase boundary proper through the growing crystal. The setup for supercooling measurements is made on the basis of the setup for monocrystal growth under conditions of axial heat flux near the crystallization front (AHF growth method) [3]. Tests of the method for supercooling measurements have shown that the influence of extraneous radiation is weak and does not contribute to the error of the supercooling measurement [4].

The schematic of the method of measurement is presented in Fig. 1a. The temperature of the interphase boundary is measured during the growth run by an optical pyrometer LOP-72. Its sensitivity is ±0.3°C. The area viewed by the pyrometer (∅8 mm) was in the central part of the sample. The sample was 25 mm in diameter and 50 mm in height. In the present study, the object chosen for investigation was a BGO monocrystal grown by the low-gradient Czochralski method [5] after double recrystallization. The crystal was melted by the AHF heater and grown using the same AHF heater by lowering the temperature at point T_1 at a specified rate a_1. In the experiment, temperature values at points T_1–T_3 and readings of the optical pyrometer were recorded simultaneously.

Supercooling was determined as the difference $\Delta T = U_m - U_i$, where U_m is the pyrometer reading corresponding to the melting temperature and U_i is the pyrometer reading in the course of the growth. Once the crystallization stage was finished, the sample was melted again until the initial temperature conditions and the initial melt thickness of 4 mm were achieved. After that a new crystallization cycle with a new cooling rate at point T_1 was carried out, and the variation with time of the supercooling was measured. In Fig. 1b, the obtained temporal dependences of supercooling for different cooling rates a_1 are shown.

In the last experiment of this series, after part of the molten layer had crystallized at the specified rate, crystallization was discontinued for some time and then the setup was switched off. In this way, the molten layer thickness at the moment of switching off the setup could be determined. From the recorded temperatures T_1–T_3 and the melt layer thickness, the temperature gradient in the melt was determined. Using these data, the parameters were determined for the thermal model

1063-7842/00/4505-0630$20.00

used for calculating the temporal dependence of the growth rate at different cooling rates. By comparing the temporal dependence of supercooling (Fig. 1b) approximated by a polynomial with the calculated temporal dependence of the growth rate for specified values of a_1, the dependence of the supercooling on the growth rate was determined.

Crystallization of the BGO melt was calculated using a one-dimensional approximation. The melt was treated as opaque, and the crystal as semitransparent. The heat transfer in the crystal by heat conductivity was ignored. On calculating the heat flux radiated from the crystallization front, the crystal temperature was assumed to be constant and equal to some effective temperature, which was determined from the heat balance conditions. The length of the crystal was also considered constant, since it was much larger than the initial molten layer thickness. The above assumptions allowed for the obtaining of an analytical expression for the resulting radiation flux from the crystallization front and thereby reduced the problem to the calculation of the temperature distribution in the melt. According to experimental conditions, the hot boundary of the melt contacted the air gap, which separated the melt from the heater. The distribution of the temperature in the melt was described by the equation

$$c\rho\frac{\partial T}{\partial t} = \lambda\frac{\partial^2 T}{\partial z^2}, \qquad (1)$$

where λ, ρ, and c are the heat-transfer coefficient, density, and thermal capacity of the melt, respectively.

Initial and boundary conditions for equation (1) were set in the following way: at zero time ($t = 0$) the temperature distribution in the melt was assumed to be linear:

$$T = T_{B0} - \frac{T_{B0} - T_{m0}}{h_0}z, \quad 0 \le z \le h_0, \qquad (2)$$

where h_0 is the initial melt thickness and T_{m0} is the melting temperature.

At the hot boundary of the melt at $z = 0$,

$$-\lambda\frac{\partial T}{\partial z} = \lambda_{air}\frac{T_1 - T}{d} + \varepsilon_1^{\text{eff}}\sigma(T_1^4 - T^4), \qquad (3)$$

where T_1 is the temperature of the heater; d is the air gap thickness; λ_{air} is the thermal conductivity of air; and

$$\varepsilon_1^{\text{eff}} = \frac{\varepsilon_1\varepsilon_m}{\varepsilon_1 + \varepsilon_m - \varepsilon_1\varepsilon_m},$$

where ε_1 and ε_m are the emissivity factors of the heater and the melt, respectively.

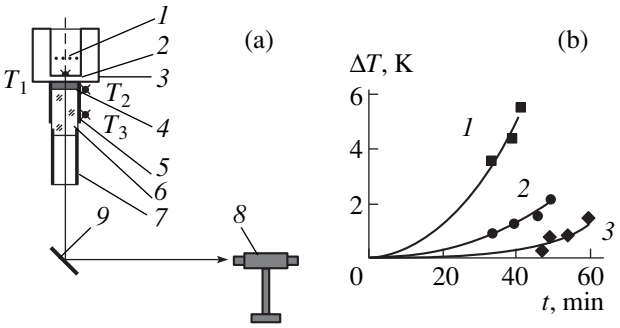

Fig. 1. Experimental layout (a) and measured curves (b) of the dependence of interphase boundary supercooling on the cooling rate (a): *1*—AHF heater; *2*—melt; *3*—platinum crucible; *4*—melt–crystal boundary; *5*—thermocouples; *6*—crystal; *7*—platinum tube; *8*—pyrometer; *9*—mirror. (b): *1*—heater cooling rate 40; *2*—30; *3*—20 K/h.

At the crystallization front at $z = h(t)$,

$$-\lambda\frac{\partial T}{\partial z} + Q\frac{\partial h}{\partial t} = \varepsilon_2^{\text{eff}}\sigma(T^4 - T_t^4), \qquad T = T_{m0} - \Delta T_m, \qquad (4)$$

where

$$\varepsilon_2^{\text{eff}} = \frac{\varepsilon_3}{1 + (1-\alpha)\beta}; \quad \varepsilon_3 = \frac{(1-r)\varepsilon_t}{1 - r(1-\varepsilon_t)};$$

$$\beta = \frac{\varepsilon_3}{n^2(1 + 2E_3 kl)}; \quad \alpha = \exp\left(-\frac{2kl}{1+\mu_0}\right);$$

where Q is the heat of phase transition; ΔT_m is the supercooling at the crystallization front; r is an average mirror reflection coefficient at the air–crystal boundary; ε_t is the effective emissivity factor of the tube receiving radiation from the crystal; T_t is the temperature of the tube; n and k are the refraction and absorption coefficients of the crystal; l is the crystal length; and μ_0 is the cosine of the angle of total internal reflection of the crystal,

$$E_3(x) = \int_0^\infty \exp(-xt)t^{-3}dt.$$

In solving the system (1)–(4), the temperatures T_1, T_t, and ΔT_m were assumed to be known functions of time, and the temperature distribution in the melt, molten layer thickness, and the crystallization rate were calculated. In this calculation, the variation with time of supercooling at the crystallization front was taken from the experiment, while the corresponding expressions for the heater and tube temperatures were taken in the form $T_1 = T_{1,0} - a_1 t$ and $T_t = T_{t,0} - a_2 t$, where the coefficient a_1 determining the heater cooling rate was taken from the experiment as well, and the values of $T_{1,0}$, a_2, and T_t were determined from the best fit of calculation

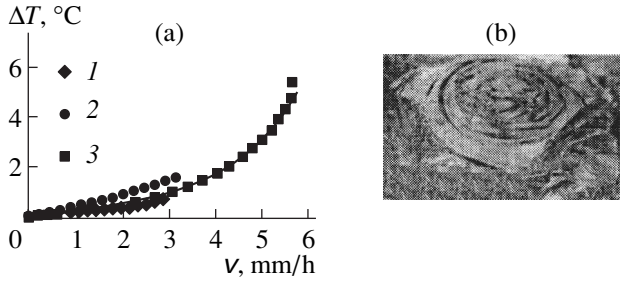

Fig. 2. The dependence of supercooling on the growth rate (a) and the morphology of the interphase surface (b). (a): *1*—cooling rate 40; *2*—30; *3*—20 K/h; solid line is the averaged curve.

results to the experimental data. The temperature T_{B0} defining the distribution (2) of the temperature at the start of crystallization, as well as the initial melt thickness, were calculated from the condition that distribution (2) satisfied boundary conditions (3), (4) where $dh/dt = 0$.

In the calculations, the following values of the parameters involved in the problem were used: T_{m0} = 1323 K, λ = 0.001 W/cm K, Q = 991 J/cm^3, λ_{air} = 0.0008 W/cm K, $c\rho$ = 2.727 J/cm^3 K, ε_t = 0.5, r = 0.15, n = 2.15, k = 0.03 cm^{-1}, l = 4 cm, and d = 0.05 cm.

The obtained curves of supercooling as a function of the growth rate for three values of the cooling rate, as well as the averaged curve plotted using data of these three experiments, are shown in Fig. 2. It is seen that the data for different cooling rates are close and fall within the experimental error. Thus, the conclusion can be drawn that the presented approach to determination of the dependence of supercooling on the growth rate, based upon the measurement of the temporal dependence of supercooling at a specified cooling rate and the calculation of the temporal dependence of the growth rate, allows for the obtaining of a set of data in the course of one experiment for a given cooling rate. Such an approach results in a considerable saving of time compared with the approach proposed in [4], which requires that a set of experiments with different cooling rates be carried out.

Data presented in Fig. 2a cannot be approximated by quadratic or exponential curves. This is presumably due to the fact that the growth step formation is a combination of two mechanisms. In Fig. 2b, the morphology of the interphase surface is shown. It is seen that the largest macrosteps occur in the form of spiral ribbons. This demonstrates the dislocation mechanism of step generation having quadratic dependence on supercooling. On the other hand, at the surface of the ribbons, a system of macrosteps can be seen aligned along the ribbons. This may be evidence of two-dimensional nucleation of steps on the ribbons. This step generation mechanism is characterized by an exponential dependence of supercooling on the growth rate. The complex character of the experimental dependence of supercooling on the growth rate can be explained by the fact that, in the area of the interphase surface seen by the pyrometer, both mechanisms of the step growth were in effect. To verify the supposition of the simultaneous occurrence of the two mechanisms of step generation in the course of BGO crystal growth from the melt in the [211] direction, additional studies are required with a substantially smaller pyrometer field of vision and a possibility of studying the dependence of supercooling at particular points at the growing interphase surface.

The study was supported by the Russian Foundation for Basic Research (project no. 97-03-32980).

REFERENCES

1. V. D. Golyshev, M. A. Gonik, and V. B. Tsvetkovskiĭ, Prib. Tekh. Éksp., No. 5, 153 (1998).
2. V. D. Golyshev and M. A. Gonik, High Temp. High Pressures. **26**, 595 (1994).
3. V. D. Golyshev and M. A. Gonik, Cryst. Prop. Prep. **36–38**, 623 (1991).
4. V. D. Golyshev, M. A. Gonik, V. B. Tsvetkovskiĭ, *et al.*, Izv. Akad. Nauk, Ser. Neorg. Mater. **35**, 715 (1995).
5. Ya. V. Vasiliev, R. R. Akhmetshin, B. N. Borovlev, *et al.*, Nucl. Instrum. Methods Phys. Res. A **379A**, 533 (1996).

Translated by M. Lebedev

Technical Physics, Vol. 45, No. 5, 2000, pp. 633–635. Translated from Zhurnal Tekhnicheskoĭ Fiziki, Vol. 70, No. 5, 2000, pp. 112–114.

BRIEF COMMUNICATIONS

Sensitivity to Initial Conditions and Lyapunov Exponent of a Quasiperiodic System

I. A. Khovanov, N. A. Khovanova, V. S. Anishchenko, and P. W. E. McClintock

Chernyshevsky State University, ul. Astrakhanskaya 83, Saratov, 410026 Russia

Received April 7, 1999

Abstract—The dynamics of a quasiperiodic map is analyzed both in the presence and in the absence of weak noise. It is shown that, in the presence of weak noise, a strange chaotic attractor with a negative Lyapunov exponent and sensitive dependence of trajectories on the initial conditions can exist in the system. This means that the types of motion of a fluctuating system cannot be classified only by the sign of the leading Lyapunov exponent. © *2000 MAIK "Nauka/Interperiodica".*

In recent years, scientists have been paying much attention to the behavior of quasiperiodic oscillatory systems which are excited by two harmonic signals having frequencies with an irrational quotient. This is explained by the fact that new dynamical effects have been discovered in quasiperiodic systems, such as the occurrence of a strange nonchaotic attractor (SNA) [1, 2]. The SNA is usually observed as an intermediate state between the regular quasiperiodic attractor (torus) and the chaotic attractor [3–5]. The diagnostics of the attractor type (chaotic or nonchaotic) are performed by analyzing the sensitivity of trajectories to initial conditions. Being equivalent to the existence or absence of an exponential divergence of close trajectories of the system, this property is generally characterized by the sign of the leading Lyapunov exponent (LLE) [6, 7]: a nonchaotic attractor has a negative LLE, and its trajectories are insensitive to initial conditions; conversely, a chaotic attractor is characterized by a positive LLE and sensitivity to initial conditions. However, we believe that this property of trajectories of quasiperiodic systems does not always correlate with the sign of the LLE. We demonstrate this by analyzing a quasiperiodic system without fluctuations and then the same system subjected to weak noise.

We consider the following logistic map:

$$\begin{aligned} x_{n+1} &= \alpha(1+\varepsilon\cos\phi_n)x_n(1-x_n) + \sqrt{D}\xi_n, \\ \phi_{n+1} &= \phi_n + \rho \bmod 2\pi, \end{aligned} \qquad (1)$$

where $x_n \in [0, 1]$, $\rho = 2\pi\omega$; ξ_n represents white noise of intensity D; and α, ε, and ω are parameters.

The map in (1) describes the dynamics of a quasiperiodically excited flow system. Without the noise term, it is the classical model for studying the SNA. The SNA of this map was analyzed in detail in [8]. Following [8], we set $\varepsilon = 0.1$ and $\omega = (\sqrt{5} - 1)/2$ and treat α as a control parameter.

First, we analyze the map dynamics without noise. Figure 1a shows the LLE Λ as a function of α by symbols (○). According to [8], a torus is observed when $\alpha < 3.2714$. At $\alpha \approx 3.2714$, the attractor goes through a crisis: the torus-repeller comes in contact with the stable torus, which gives rise to a fractal structure

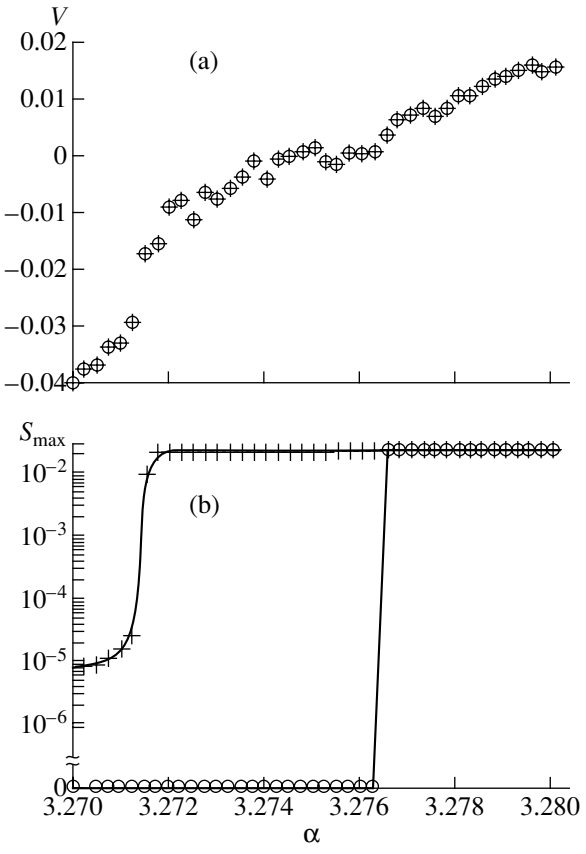

Fig. 1. Dependence of (a) Lyapunov exponent and (b) maximum dispersion S_{max} on parameter α in the presence (○) and the absence (+) of noise in the system.

1063-7842/00/4505-0633$20.00 © 2000 MAIK "Nauka/Interperiodica"

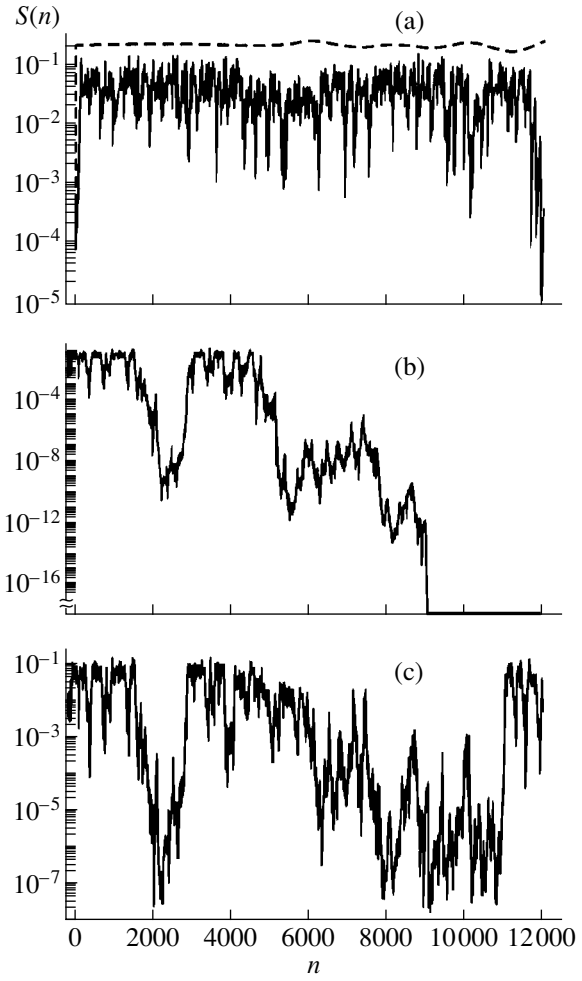

Fig. 2. Evolution of trajectory dispersion for various values of α and noise intensity *D*: (a, solid curve) α = 3.277 and *D* = 0; (b) α = 3.274 and *D* = 0; (c) α = 3.274 and *D* = 1.E–08. The dashed curve in (a) illustrates the evolution of trajectories dispersion in the nonquasiperiodic regime (α = 3.7 and ε = 0).

("strangeness"). When α > 3.2714, the attractor is a strange one. Figure 1a shows that the Lyapunov exponent is negative when α < 3.2762 everywhere, with the exception of a small interval of α in the neighborhood of α ≈ 3.2750. Conclusions made in [6–8] and the results shown in Fig. 1a suggest that (1) exponentially divergent trajectories must not exist and therefore an SNA must be observed when 3.2714 < α < 3.2762 and (2) when α > 3.2762 and in the neighborhood of α ≈ 3.2750, a strange chaotic attractor must be observed.

Let us check this inference by analyzing the sensitivity to initial conditions. To do this, we consider the time evolution of an ensemble of close initial trajectories [9, 10] of map (1): keeping the phase ϕ_m constant, we take a set of points $\{x_m^i\}$ uniformly filling an interval of length $e = 0.0001$ centered at a point in the attractor and monitor the evolution of the points. If the points scatter about the attractor and, hence, the interval length increases to the attractor dimensions, this will manifest a sensitivity to initial conditions. Conversely, if the interval length reduces to zero, there will be no sensitivity.

To describe the evolution of an ensemble of trajectories, we consider the standard deviation $S(n)$ of the trajectories of points in the interval, which is calculated as

$$S(n) = \left[\frac{1}{N}\sum_{i=1}^{N}(x_n^i - \langle x_n^i\rangle)^2\right]^{1/2}, \qquad (2)$$

where N is the number of trajectories in the ensemble and $\langle\rangle$ denotes an ensemble average [9, 10]. The quantity $S(n)$ characterizes the length of the interval where the ensemble trajectories gather. The sensitivity to initial conditions as a function of α is characterized, for example, by the maximum standard deviation S_{max} of the trajectories. It was calculated during 10^6 iteration cycles after a relaxation period of the same duration. Figure 1b shows the graph of S_{max} as a function of α. It demonstrates that the maximum standard deviation is not zero for α > 3.2762. Therefore, the system is sensitive to initial conditions and the attractor is chaotic. When α < 3.2762, there is no sensitivity, because $S_{max} = 0$. An analysis of Fig. 1b and results presented in [8] show that (1) an SNA exists when 3.2714 < α < 3.2762 and in the neighborhood of α ≈ 3.2750 and (2) the attractor is a strange chaotic one when α > 3.2762.

Thus, behavior of the LLE and sensitivity to initial conditions correlate in a quasiperiodic system without noise: both manifest the existence of an SNA or a chaotic attractor in certain domains of α. The exception is a small domain in the neighborhood of α ≈ 3.2750: the LLE is positive here, yet there is no sensitivity to initial conditions.

Let us consider the evolution of an ensemble of trajectories in more detail. We monitored the evolution of the standard deviations of chaotic-attractor trajectories (Fig. 2a) and SNA trajectories (Fig. 2b). For the chaotic attractor, dispersion S strongly fluctuates, demonstrating that the trajectories scatter about the entire attractor and gather again within a very small interval. Thus, in a quasiperiodically excited system, the divergence of close chaotic-attractor trajectories and their convergence alternate. Note that this behavior differs from the evolution of an ensemble of chaotic-attractor trajectories in nonquasiperiodic systems, for which S increases from an initial value to some maximum and then varies with time within a small interval (dashed curve in Fig. 2a) [11]. The behavior of the standard deviations of SNA trajectories (Fig. 2b) demonstrates that, after a certain relaxation period, when both scattering and gathering of trajectories is observed (as in the case of a chaotic attractor), the trajectories converge and then evolve in a similar manner. Indeed, it was shown in [9, 12] that both chaotic attractor and SNA contain

domains of scattering and gathering trajectories. The difference between these attractors is that domains of the former type dominate in a chaotic attractor, whereas domains of the latter type dominate in an SNA. This explains why, after some relaxation time, the trajectories of an SNA begin to evolve as a single trajectory despite the existence of domains with divergence. When perturbed after the relaxation time, the trajectories of the ensemble scatter again. Perturbation will definitely occur in real systems, which always fluctuate. Thus, the scattering of trajectories of noisy systems (in other words, the sensitivity to initial conditions) must be observed in the domains where strange attractors exist.

To validate this inference, let us analyze the evolution of an ensemble of trajectories and the behavior of the LLE in the case of weak Gaussian noise of intensity $D = 1.e - 08$. Figure 1a (symbols +) demonstrates that value of the LLE does not depend on whether or not the map is perturbed by weak noise. The maximum dispersion (symbols + in Fig. 1b) of a noisy system is not zero everywhere and is comparable to the attractor dimensions when $\alpha > 3.2714$. The latter property points to a sensitive dependence of trajectories on initial conditions, i.e., a chaotic state of the attractor. Recall that, a map without noise in this domain ($\alpha > 3.2714$) exhibits both an SNA ($3.2714 < \alpha < 3.2762$) and a strange chaotic attractor ($\alpha > 3.2762$). The evolution of an ensemble of trajectories for $3.2714 < \alpha < 3.2762$ shown in Fig. 2c does not qualitatively differ from that shown in Fig. 2a.

Thus, without affecting the fractal state ("strangeness") of an attractor, weak noise turns an SNA of a quasiperiodic system into an attractor that is sensitive to initial conditions (i.e., into a strange chaotic attractor) but is characterized by a negative LLE. This means that in a noisy quasiperiodic system classification of the types of motion cannot be based on the LLE and other characteristics must be used for that purpose. Moreover, one may conjecture that the transition from torus to chaos in real (fluctuating) quasiperiodic systems does not involve any intermediate period, i.e., the development of an SNA.

Similar results have been obtained for a flow systems, namely, a Duffing oscillator excited by quasiperiodic signal.

ACKNOWLEDGMENTS

This work was supported by the international foundations INTAS (grant no. 96-0305) and EPSRC (United Kingdom) and by the Royal Society of London.

One of the authors (I.A. Khovanov) thanks the Max-Planck-Institute (Dresden, Germany) for their hospitality .

REFERENCES

1. C. Grebogi, E. Ott, and J. A. Yorke, Physica D (Amsterdam) **13**, 261 (1984).
2. V. S. Anishchenko, Izv. Vyssh. Uchebn. Zaved. PND **5** (1), 109 (1997).
3. A. Bondeson, E. Ott, and T. M. Antonsen, Phys. Rev. Lett. **55**, 2103 (1985).
4. A. S. Pikovsky and U. Feudel, Chaos **5**, 253 (1995).
5. V. S. Anishchenko, T. E. Vadivasova, and O. Sosnovtseva, Phys. Rev. E **53**, 4451 (1996).
6. A. J. Lichtenberg and M. A. Lieberman, *Regular and Stochastic Motion* (Springer-Verlag, New York, 1982; Mir, Moscow, 1984).
7. H. Haken, *Advanced Synergetics: Instability Hierarchies of Self-Organizing Systems and Devices* (Springer-Verlag, New York, 1983; Mir, Moscow, 1985).
8. J. F. Heagy and S. M. Hammel, Physica D (Amsterdam) **70**, 140 (1994).
9. Y.-C. Lai, U. Feudel, and C. Grebogi, Phys. Rev. E **54**, 6070 (1996).
10. F. J. Romeiras, C. Grebogi, and E. Ott, Phys. Rev. A **41**, 784 (1990).
11. C. Nicolis and G. Nicolis, Phys. Rev. A **43**, 5720 (1991).
12. Y.-C. Lai, Phys. Rev. E **53**, 57 (1996).

Translated by V. Gurskiĭ

Technical Physics, Vol. 45, No. 5, 2000, pp. 636–640. Translated from Zhurnal Tekhnicheskoĭ Fiziki, Vol. 70, No. 5, 2000, pp. 115–118.

BRIEF COMMUNICATIONS

Optimization of a Semiconductor Lidar for Detecting Atmospheric Molecular Iodine and Hydrogen

R. N. Verem'ev, V. E. Privalov, and V. G. Shemanin

Baltic State Technical University, St. Petersburg, 198005 Russia

Received September 17, 1998; in final form, October 25, 1999

Abstract—A lidar equation for Raman backscattering of semiconductor laser radiation by I_2 and H_2 molecules is solved. The obtained results allow laser wavelength optimization for probing atmospheric I_2 and H_2 molecules at a distance up to 2 km. © *2000 MAIK "Nauka/Interperiodica".*

In this work, we extend our previous discussion [1, 2] and numerically simulate a semiconductor Raman lidar designed for the remote detection of molecular iodine and hydrogen in the atmosphere. The possibility of semiconductor lasers being used in remote detection systems stems from their spectroscopic applications [3, 4], and the development of a blue laser diode [5, 6] opens up a promising opportunity in this field. The quasi-continuous-wave power of the diode is 135 mW at a wavelength of 419 nm and a pulse repetition rate of 20 kHz, and its pulse power is 5 W for a pulse duration of 10 ns. Thus, 100-ns laser pulses with a repetition rate to 200 kHz and peak powers of 5 and 10 W can be obtained at wavelengths of 419, 678, 780, and 820 nm. High pulse repetition rates decrease the time of signal collection during the detection of lidar signals, with the detection distance at which the effective power is at a reasonable level remaining unchanged. According to [7], the effective power is determined as $PN^{1/2}$.

The goal of this work was to numerically solve a lidar equation for Raman backscattering from I_2 and H_2

Table 1. Raman scattering cross sections and wavelengths for molecular hydrogen, its isotopes, and molecular iodine calculated for the wavelengths of semiconductor lasers

Molecule		H_2	D_2	T_2	HD	HT	DT	$\left(\frac{d\sigma}{d\Omega}\right)\times 10^{30}$, cm^2/sr
ν, cm^{-1}		4160	2951	2402	3604	3398	2686	
λ, nm		λ_R, nm						
Laser	419	507.45	478.12	465.89	493.53	488.56	472.14	0.64068215
	678	944.35	847.58	809.9	897.24	880.96	828.96	0.53103125
	780	1154.7	1013.2	959.83	1085	1061.3	986.73	0.30315201
	820	1244.5	1081.8	1021.1	1164	1136.7	1051.6	0.24818952
Experiment	337	391.95	374.22	366.68	383.59	380.58	370.54	8.7

Molecule		$^{127}I_2$		N_2	
ν, cm^{-1}		213	$\left(\frac{d\sigma}{d\Omega}\right)\times 10^{30}$, cm^2/sr	2330	$\left(\frac{d\sigma}{d\Omega}\right)\times 10^{30}$, cm^2/sr
λ_0, nm		λ_R, nm		λ_R, nm	
Laser	419	422.77	8.09610017	464.33	1.46464224
	678	687.93	1.18090018	805.2	0.21363326
	780	793.18	0.64714537	953.24	0.1219577
	820	834.58	0.55192054	1013.7	0.09984636
Experiment	337			365.72	3.5
	514.4			584.45	0.43
	546	552.42	17000		
	488	493.13	4.4		

1063-7842/00/4505-0636$20.00

molecules and their isotopes. The solution was sought for semiconductor lasers with the above characteristics in order to optimize a lidar system. In accordance with [8], a lidar equation for Raman backscattering can be written as

$$P(\lambda, R) = P_0(\lambda_0)K_1\Delta R A_2 T(\lambda_0)T(\lambda)\left(\frac{d\sigma}{d\Omega}\right)N_a/R^2, \quad (1)$$

where $P(\lambda, R)$ is the Raman scattered power at a wavelength λ coming to a photodetector from a distance R; $P_0(\lambda_0)$ is the laser power at its wavelength; K_1 is the lidar constant; ΔR is the space step; A_2 is the receiver aperture; $T(\lambda_0)$ and $T(\lambda)$ are the atmosphere transmittances at the laser and backscattered wavelengths, respectively; $(d\sigma/d\Omega)$ is the Raman backscattering differential cross section of a molecule; N_A is the molecule concentration; and R is the distance to a scattering object.

The Raman wavelengths for I_2, H_2, D_2, T_2, HD, HT, and DT molecules are calculated from the formula

$$\lambda_{RH} = 1/\left(\frac{1}{\lambda_0} - \tilde{\nu}\right), \quad (2)$$

where $\tilde{\nu}$ is the eigenfrequency of the molecules. For I_2, H_2, and D_2, these frequencies were taken from [9]; for T_2, HD, HT, and DT, they were calculated according to the rule of sum of squares [10] (Table 1, second row). The calculated Raman wavelengths are also listed in Table 1.

The differential cross section for vibration Raman backscattering of linearly polarized laser radiation (both polarizations of scattered radiation are detected) can be determined from the equation [8]

$$\left(\frac{d\sigma}{d\Omega}\right)_j = \frac{16\pi^4 b_j^2 g_j}{\lambda^4[1-\exp(-hc/\lambda kT)]}\left\{\bar{\alpha}_j^2 + \frac{7}{45}\bar{\gamma}_j^2\right\}, \quad (3)$$

where b_j is the amplitude of zero-point vibrations of the jth mode; g_j is the degree of its degeneracy; $3\bar{\alpha}_j$ and $\bar{\gamma}_j$ are the trace and anisotropy of the tensor of the polarizability derivative with respect to the normal coordinate q_j, respectively; T is the vibrational temperature of molecules; k is the Boltzmann constant; h is Planck's constant; and c is the velocity of light.

If all variables but λ are omitted, equation (3) can be recast as

$$\left(\frac{d\sigma}{d\Omega}\right)_j \approx A/\lambda^4, \quad (4)$$

where the constant A is determined from the known cross section for a nitrogen laser with a wavelength $\lambda_0 = 337.1$ nm ($\left(\frac{d\sigma}{d\Omega}\right)_j = 8.7 \times 10^{-30}$ cm^2/sr [8]; Table 1, the last row). The constant A is equal to 1.122×10^{-19} cm^{2}nm^4/sr. The Raman backscattering cross sections for the selected laser wavelengths are given in the last column of Table 1.

Table 2. Atmospheric attenuation, the relative spectral sensitivity of the photocathodes, and the spectral brightness of background solar radiation calculated for the wavelengths of the semiconductor lasers and Raman backscattering from the molecules under study

λ, nm	k_0, km^{-1}		
419	0.217		
678	0.145		
780	0.1346		
820	0.132		
λ, nm	k_0, km^{-1}	ξ_p, (λ)	S_b, W/m^2 sr nm
507.5	0.1685	0.89	15.1
944.4	0.1237	0.54	5
1154.7	0.1154	0.71	3.4
1244.5	0.1127	0.79	2.6
478.1	0.18	0.98	13.9
847.6	0.13	0.45	7.1
1013.2	0.1197	0.6	4.9
1081.8	0.1175	0.66	4.2
465.9	0.189	1	13.7
809.9	0.1327	0.42	8.8
959.8	0.1226	0.55	5
1021.1	0.1193	0.61	4.8
493.5	0.17	0.95	14.8
897.2	0.1269	0.5	5.2
1085.0	0.1175	0.66	4.1
1164.0	0.1151	0.72	3.4
488.6	0.1723	0.96	14.4
881.0	0.1279	0.48	8.1
1061.3	0.1182	0.64	4.4
1136.7	0.1159	0.7	3.5
472.1	0.1845	0.99	13.4
829.0	0.1314	0.44	7.3
986.7	0.1202	0.58	5
1051.6	0.1184	0.63	4.6
422.8	0.224	0.82	11.2
687.9	0.1419	0.25	11.7
793.2	0.1338	0.41	9.1
834.6	0.131	0.44	6.9
464.3	0.19	1	13.1
805.2	0.133	0.415	8.8
953.2	0.1231	0.55	5
1013.7	0.1196	0.6	4.8

Table 3. Calculated Raman backscattering power for four wavelengths of the 10-W semiconductor lasers in the range from 0.1 to 2.0 km at a molecule concentration of 10^{19} cm^{-3}

R, km		H_2	D_2	T_2	HD	HT	DT	I_2	N_2
	N_a, nm	1E + 19	1E + 19	1E + 19	1E + 19	1E + 19	1E + 19	1E + 19	1E + 19
	P_0, W	10	10	10	10	10	10	10	10
0.1	λ_0, nm	$P(\lambda, R)$ pW	$P(\lambda, R)$ pW	$P(\lambda, R)$ pW	$P(\lambda, R)$ pW	$P(\lambda, R)$ pW	$P(\lambda, R)$ pW	$P(\lambda, R)$ pW	$P(\lambda, R)$ pW
	419	0.1852	0.2037	0.2077	0.1976	0.1997	0.2057	0.3773	0.0835
	678	0.0166	0.0138	0.0129	0.0153	0.0147	0.0135	0.017	0.0051
	780	0.0125	0.0105	0.0097	0.0116	0.0112	0.0102	0.016	0.0039
	820	0.0114	0.0095	0.0088	0.0104	0.0101	0.0091	0.0141	0.0035
0.5	λ_0, nm	$P(\lambda, R)$ fW	$P(\lambda, R)$ fW	$P(\lambda, R)$ fW	$P(\lambda, R)$ fW	$P(\lambda, R)$ fW	$P(\lambda, R)$ fW	$P(\lambda, R)$ fW	$P(\lambda, R)$ fW
	419	6.3491	6.951	7.061	6.772	6.8354	7.0062	12.652	2.8392
	678	0.5957	0.4915	0.4612	0.5507	0.5284	0.4835	0.6077	0.1833
	780	0.4513	0.3806	0.3484	0.4191	0.4062	0.3678	0.5743	0.1402
	820	0.4122	0.3436	0.3172	0.3752	0.3647	0.3278	0.5059	0.1255
1	λ_0, nm	$P(\lambda, R)$ fW	$P(\lambda, R)$ fW	$P(\lambda, R)$ fW	$P(\lambda, R)$ fW	$P(\lambda, R)$ fW	$P(\lambda, R)$ fW	$P(\lambda, R)$ fW	$P(\lambda, R)$ fW
	419	1.309	1.4249	1.4409	1.3951	1.4066	1.433	2.5372	0.5791
	678	0.1302	0.1078	0.1004	0.1202	0.1152	0.1053	0.1316	0.0399
	780	0.0996	0.0838	0.0766	0.0924	0.0895	0.0809	0.1255	0.0308
	820	0.0912	0.0758	0.0699	0.0829	0.0805	0.0723	0.1109	0.0277
2	λ_0, nm	$P(\lambda, R)$ fW	$P(\lambda, R)$ fW	$P(\lambda, R)$ fW	$P(\lambda, R)$ fW	$P(\lambda, R)$ fW	$P(\lambda, R)$ fW	$P(\lambda, R)$ fW	$P(\lambda, R)$ fW
	419	0.2226	0.2395	0.24	0.2369	0.2383	0.2398	0.4081	0.0964
	678	0.0249	0.0205	0.019	0.0229	0.0219	0.02	0.0247	0.0076
	780	0.0194	0.0162	0.0148	0.0179	0.0174	0.0157	0.024	0.0059
	820	0.0178	0.0148	0.0136	0.0162	0.0157	0.0141	0.0213	0.0054

The other parameters of equation (1) have the following values: ΔR = 15 m for a time of measurement t_d = 100 ns; A_2 = 0.008 m^2; K_2 = 0.495 for a wavelength of 532 nm [11]; peak powers of laser pulses P_0 = 1 and 10 W; probing distance R = 0.1, 0.5, 1.0, and 2.0 km; and concentration of molecules 10^{19} and 10^{16} cm^{-3}. The spectral sensitivity of photocathodes of an FEU-79 photomultiplier and an LFD-1A avalanche photodiode were taken from [12]. Their relative values are given in the third column of Table 2. As in [8], the atmosphere transmittance was calculated from the values of the attenuation coefficient k taken from [13] (see the second column of Table 2).

The above parameters were substituted into equation (1) to determine the Raman scattered power for two values of the concentration of the molecules and the selected wavelengths and peak powers of the semiconductor lasers. The probing distance ranged from 0.1 to 2.0 km. This allowed us to determine optimum parameters of the lidar system. The results of calculation for all of the molecules are given in Table 3. For comparison, the last column of Table 3 contains the results of calculation for N_2 molecules. It can be seen that an increase in the laser power causes a proportional increase in the Raman scattered power, whereas a decrease in the concentration of the molecules causes a proportional decrease in the Raman power. The spectral dependences of the factors in equation (1) remain the same. As the probing distance increases from 0.1 to 1 km, the Raman signal is reduced by two orders of magnitude; as the distance increases from 1 to 2 km, it is reduced still an order of magnitude more. It seems from these results that a blue laser with a wavelength of 419 nm is best suited for detecting the molecules in our system. Such a laser provides the maximum Raman power for all of the molecules in the range from 0.1 to 2.0 km.

However, these calculations are valid only in the absence of background illumination, i.e., for night mea-

Table 4. Calculated minimum power detectable by the lidar for the wavelengths of Raman backscattering from the molecules in the range from 0.1 to 2.0 km

Molecule	R, k	0.1	0.5	1.0	2.0
	λ_0, nm	P_b, fW	P_b, fW	P_b, fW	P_b, fW
H_2	507.5	41.86338	1565.391	359.7274	75.98623
	944.4	8.448444	321.6235	75.58345	16.69723
	1154.7	7.559807	288.7511	68.14043	15.17844
	1244.5	6.434149	246.0215	58.13539	12.98481
D_2	478.1	42.38466	1577.61	360.4566	75.26968
	847.6	9.991029	379.3909	88.87871	19.511
	1013.2	9.203097	350.9134	82.63185	18.32747
	1081.8	8.679115	331.2254	78.08162	17.35638
T_2	465.9	42.58901	1579.519	359.2726	74.35025
	809.9	11.55458	438.2901	102.5383	22.44892
	959.8	8.605843	327.7597	77.06787	17.0439
	1021.1	9.1659	349.551	82.3275	18.26727
HD	493.5	43.79126	1636.498	375.7859	79.25933
	897.2	8.132935	309.2164	72.55153	15.97624
	1085.0	8.472469	323.339	76.22253	16.94313
	1164.0	7.666513	292.8619	69.12089	15.40146
HT	488.6	43.04632	1607.18	368.6294	77.57129
	881.0	12.16065	462.1663	108.384	23.84289
	1061.3	8.816261	336.3652	79.2655	17.60721
	1136.7	7.672162	292.984	69.12204	15.3894
DT	472.1	41.2584	1532.927	349.4603	72.6458
	829.0	10.04278	381.1427	89.22661	19.55997
	986.7	9.077431	346.0526	81.46686	18.06004
	1051.6	9.072804	346.1253	81.55735	18.11268
I_2	422.8	28.45043	1040.486	232.56	46.47219
	687.9	9.135838	345.2692	80.4053	17.44208
	793.2	11.66271	442.1973	103.3955	22.6117
	834.6	9.492873	360.3302	84.37123	18.50298
N_2	464.3	40.71973	1509.588	343.1947	70.95199
	805.2	11.41668	433.0074	101.2872	22.16836
	953.2	8.605413	327.6778	77.02935	17.02686
	1013.7	9.015369	343.7691	80.95358	17.95703

surements. Background solar light has a significant effect on the Raman power received by the lidar. To take into account this effect, the background power $P_b(\lambda, R)$ at the photodetector input was calculated, and the effect of background illumination on the lidar performance was studied. Conditions of a bright sunny day were taken, for they are the most severe for lidar operation. Because of the uncertainty of the receiver axis position relative to the direction to the sun, the spectral distribution of the background radiation $S_b(\lambda)$ (the last column of Table 2) was determined with data presented in [14, 15]. The background power $P_b(\lambda, R)$ for our case was calculated by the equation

$$P_b(\lambda, R) = 1.5 S_b(\lambda) T(\lambda, R) K_2 \xi_p(\lambda) A_2 \Omega(R) \Delta\lambda, \quad (5)$$

where $\Omega(R)$ is the solid field-of-vision angle of the receiver and $\Delta\lambda$ is the spectral width of the receiver [15]. The minimum permissible signal-to-noise ratio is taken to be 1.5 [8]. The results of calculation are presented in Table 4. A comparison between these results and data in Table 3 shows that the Raman power does not exceed the background level at any of the wave-

lengths or distances. Thus, useful information will be gained only after accumulating 200 or 300 pulses. The lidar detectivity can be further improved by increasing the receiver aperture. However, this results in a considerable increase in the weight and overall dimensions of the lidar system.

Thus, the results of this work suggest that the optimization of the laser wavelength for atmospheric probing of the molecules of interest at a given distance is a possibility.

REFERENCES

1. V. E. Privalov and V. G. Shemanin, Opt. Spektrosk. **82**, 700 (1997) [Opt. Spectrosc. **82**, 650 (1997)].
2. G. V. Laktyushkin, V. E. Privalov, and V. G. Shemanin, Zh. Tekh. Fiz. **68** (1), 20 (1998) [Tech. Phys. **43**, 16 (1998)].
3. G. Schmidtke, W. Kohn, U. Klocke, *et al.*, Appl. Opt. **28**, 3665 (1989).
4. A. I. Kuznetsov, A. P. Logachev, and E. V. Stepanov, Izv. Akad. Nauk SSSR, Ser. Fiz. **54**, 1909 (1990).
5. T. S. Kalacheva, Lazer. Tekh. Optoélektron., Ser. 11, No. 6, 1629 (1991).
6. R. W. Hardin, Photonics Spectra, April, 110 (1998).
7. E. K. Ivanov, V. A. Kolbenkov, L. A. Konopel'ko, *et al.*, Izmer. Tekh., No. 5, 56 (1986).
8. R. M. Measures, *Laser Remote Sensing: Fundamentals and Applications* (Wiley, New York, 1984; Mir, Moscow, 1987).
9. W. Y. Murphy, W. Holzer, and H. J. Bernstein, Appl. Spectrosc. **23**, 211 (1969).
10. M. V. Vol'kenshteĭn, L. A. Gribov, M. A. El'yashevich, *et al.*, *Molecular Vibrations* (Nauka, Moscow, 1972).
11. T. V. Antipina *et al.*, in *Proceedings of International Aerosol Symposium Vol. Technologies, Moscow, 1994*, p. 123.
12. *Handbook on Lasers*, Ed. by A. M. Prokhorov (Sov. Radio, Moscow, 1978), Vol. II.
13. *Handbook on Lasers*, Ed. by A. M. Prokhorov (Sov. Radio, Moscow, 1978), Vol. I.
14. H. Rosen, P. Robrish, and O. Chamberlain, Appl. Opt. **14**, 2703 (1975).
15. H. Inaba and T. Kobayasi, Opto-Electronics **4**, 101 (1972).

Translated by K. Chamorovskiĭ

Technical Physics, Vol. 45, No. 5, 2000, pp. 641–643. Translated from Zhurnal Tekhnicheskoĭ Fiziki, Vol. 70, No. 5, 2000, pp. 119–121.

BRIEF COMMUNICATIONS

Chromium as an Antidiffusion Interlayer in Higher Manganese Silicide–Nickel Contacts

L. I. Petrova[1], L. D. Dudkin[1], V. S. Khlomov[1], M. I. Fedorov[2], V. K. Zaĭtsev[2], and F. Yu. Solomkin[2]

[1] *Baĭkov Institute of Metallurgy, Russian Academy of Sciences, Leninskiĭ pr. 49, Moscow, 117334 Russia*

[2] *Ioffe Physicotechnical Institute, Russian Academy of Sciences, Politekhnicheskaya 26, St. Petersburg, 194021 Russia*

Received October 21, 1998

Abstract—The interaction of higher manganese silicide ($MnSi_{1.71–1.75}$) with nickel and chromium was investigated. A chromium layer was shown to inhibit nickel diffusion into silicide more than four times. The use of the chromium layer made it possible to improve the mechanical and electrical properties of silicide–nickel contacts. *© 2000 MAIK "Nauka/Interperiodica".*

Higher chromium silicide $MnSi_{1.71–1.75}$ (HMS) is known as an anisotropic thermoelectric and can be applied in conventional and anisotropic thermoelectric devices [1]. The preparation of reliable electrical contacts that retain their properties under temperature-gradient conditions at high temperatures is a vital issue in the development of thermoelectric generators. Nickel is among materials best suited to such contacts and can be used as the short-circuited branch of a thermoelectric element [2].

Diffusion processes at the HMS–nickel interface have been studied in [3]. It has been found that HMS and nickel reactively diffuse into each other with a high rate to form Mn–Ni–Si intermetallic interlayers [4]; their thickness grows exponentially with heat treatment temperature and time. Moreover, pores and cracks appear at the interface due to the different partial diffusion coefficients of the components and interphase brittleness. With this taken into account, the use of a diffusion-inhibiting interlayer providing long-term efficiency of HMS–Ni contacts seems to be imperative. In this paper, we tested the antidiffusion properties of a chromium layer placed between HMS and Ni.

The effect of chromium was studied with samples prepared by *in vacuo* diffusion welding. Polycrystalline HMS was coated first by a 5- to 10-μm-thick galvanically deposited chromium layer and then a nickel layer. To the latter, a nickel plate was attached by diffusion welding at 1123 K for 3 h [5]. The contacts featured high mechanical strength and stable properties. At temperatures up to 1000 K, the contact resistance increased by about 10% for several hours and then remained unaltered for about 1000 h ($<1 \times 10^{-5}\ \Omega\ cm^2$).

After diffusion welding, HMS–Cr–Ni samples were investigated by metallography and electron microprobe analysis (EMPA). The chemical composition of the phases was determined by an MS-46 Cameca electron probe microanalyzer. The X-ray relative intensities were converted into the Mn, Cr, Si, and Ni contents with corrections taken from [6].

The examination of the microstructure revealed that chromium almost entirely suppresses the formation of pores in the near-contact area of HMS, which correlates well with data in [7]. Yet, in spite of the chromium spacing, interdiffusion of the contacting materials took place, resulting in the formation of interlayers. The

EMPA results for HMS–Cr–Ni contacts after diffusion welding

Layer	Phase composition	Concentration of elements, wt %			
		Mn	Ni	Si	Cr
1	HMS	52	–	48	–
2	MnSi–Ni–Si solid solution	57–50	10–20	33–30	–
3	Solid solution of Cr in MnNiSi	38–40	40–37	22–20	0–2
4	Solid solution of Cr in $Mn_6Ni_{16}Si_7$	24–26	58–50	16–12	2–12
5	Solid solution of Ni in Cr	–	2–4	–	98–96
6	Solid solution of Cr in Ni	–	65–100	–	35–0

1063-7842/00/4505-0641$20.00 © 2000 MAIK "Nauka/Interperiodica"

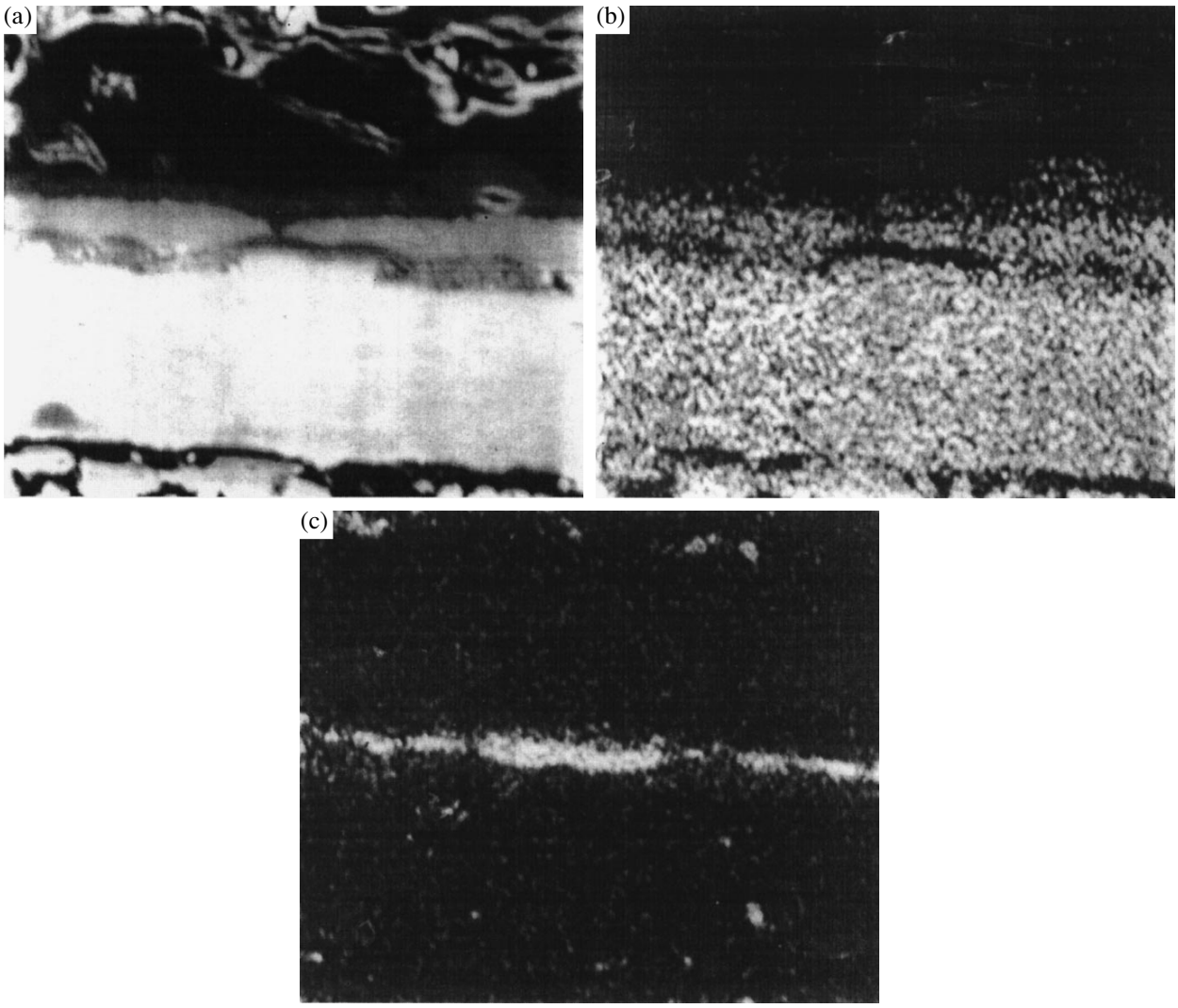

Fig. 1. HMS–Cr–Ni-contact region after diffusion welding at 1123 K: (a) absorbed-electron image and images obtained with (b) Ni K_{α_1} and (c) Cr K_{α_1} characteristic radiations.

scanned contact region of the HMS–Cr–Ni sample after diffusion welding is presented in Fig. 1.

Figure 1a shows the presence of layers that differ from the starting substances in composition. The distribution of Ni and Cr at the interfaces suggests that the former penetrates through the chromium layer into HMS and the latter is present in the HMS and nickel that are in contact with the chromium layer (Figs. 1b, 1c).

Discontinuities were observed in concentration curves for manganese, nickel, and silicon taken from the diffusion zone between HMS and chromium; this points to the reactive character of diffusion. Both on the side of HMS and on the side of nickel, the chromium profiles are typical of solid solutions. The composition's of the phases in the diffusion zone were evaluated with consideration for AZF correction [6] (see table). As follows from the table, solid solutions between the Ni and Cr layers formed due to interdiffusion; their compositions are in agreement with [7]. The chromium interlayer has a nonzero nickel concentration: it falls to 2 wt % at a depth of 1–3 μm and remains the same up to the chromium–HMS interface. Nickel penetrates through the chromium interlayer and interacts with HMS to yield several Mn–Ni–Si intermediates. We observed these phases in the diffusion zone of HMS–Ni contacts after the samples had been heat treated in the absence of chromium [3]. However, in our case, the concentration of nickel in these phases is lower.

The additional effect of chromium is that the intermetallic phases become much thinner. The thickness of the total diffusion layer between HMS and chromium varied in inverse proportion to the thickness of the antidiffusion spacing. In this study, the total thickness of the Mn–Ni–Si diffusion layer between HMS and the 6.1-μm-thick chromium layer was 32 μm. At the same time, the diffusion layer including all the intermediates

formed under heat treatment at 1123 K for 3 h near the HMS–Ni contacts without chromium was found to be as thick as 83 μm. A comparison of the growth rate constants for the diffusion layers in the vicinity of the HMS–Cr–Ni contacts shows that a 10-μm-thick chromium interlayer decreases the rate of nickel diffusion into HMS more than four times.

Thus, the application of a diffusion-inhibiting chromium layer makes it possible to produce reliable HMS–Ni contacts that offer high stability and small contact resistance.

REFERENCES

1. V. K. Zaĭtsev, in *CRC Handbook of Thermoelectrics*, Ed. by D. M. Rowe (CRC, 1995), pp. 299–309.
2. M. I. Fedorov, V. K. Zaĭtsev, F. Yu. Solomkin, *et al.*, Pis'ma Zh. Tekh. Fiz. **23** (15), 64 (1997) [Tech. Phys. Lett. **23**, 602 (1997)].
3. L. I. Petrova, L. D. Dudkin, and V. S. Khlomov, Neorg. Mater. **31**, 1216 (1995).
4. E. I. Gladyshevskiĭ, *Crystal Chemistry of Silicides and Germanides* (Metallurgiya, Moscow, 1971).
5. M. I. Fedorov, A. E. Engalychev, V. K. Zaĭtsev, *et al.*, in *Proceedings of XIII International Conference on Thermoelectric Energy Conversion, Kansas City, 1994.*
6. V. I. Rydnik and I. B. Borovskiĭ, Zavod. Lab., No. 8, 955 (1967).
7. Yu. É. Ugaste, Fiz. Metal. Metalloved. **24**, 442 (1967).

Translated by B.A. Malyukov

Technical Physics, Vol. 45, No. 5, 2000, pp. 644–645. Translated from Zhurnal Tekhnicheskoĭ Fiziki, Vol. 70, No. 5, 2000, pp. 122–123.

BRIEF COMMUNICATIONS

A Stability Criterion for an Electroslag Process

D. A. Dudko, A. M. Pal'ti, V. A. Sevryukov, and A. A. Snarskiĭ

Paton Institute of Electric Welding, National Academy of Sciences of Ukraine, 252650 Kiev, Ukraine

Received October 27, 1998

Abstract—A changeover from purely resistive slag conditions to electric arc conditions for an electroslag process is explained. A process stability criterion *Wd* is introduced. *© 2000 MAIK "Nauka/Interperiodica".*

An electroslag process means electrothermic treatment of a molten metal. When a current passes through a bath with a highly resistive molten slag, the heat being released is either spent on electrode melting and thermal treatment of edges and welds or it heats an ingot [1]. In a typical electroslag process, a steady flow of the slag melt is set. Under the electrode, the melt flows down, and heat evolution is most extensive in a truncated cone located between the electrode being spent and the molten bath (see the figure). The electrode feed is assumed to be constant (quasi-steady-state process), and effects due to drop fall are not taken into consideration (such a situation takes place, for example, during electroslag heating). Consider the case when a power source has a stiff characteristic (U = const = U_0, where U_0 is the effective interelectrode voltage) [1]. The stability of a process with such power sources has been examined experimentally [2]. At the same time, even simple theoretical considerations (see, e.g., [3]) allow us to obtain fresh data for process stability.

Let heat $P = U_0^2/R(T)$ evolve in the active cone of a slag bath. Then, under quasi-steady-state conditions, it must be removed from the lateral area F_s of the active cone via heat exchange; i.e.,

$$P = U_0^2/R(T) \cong \alpha(T - T_0)F_s = Q. \qquad (1)$$

Here, $R(T) \cong R[1 - \gamma(T - T_n)]$, γ is the temperature resistance coefficient (for typical operating temperatures, $R(T)$ is taken to be a linear function), T_n is some known temperature from the operating range, and α is the coefficient of heat exchange between the active region and the slag environment. We assume for simplicity that the active region is uniformly heated to a temperature T and that the mean temperature of the surrounding slag is T_0. Note that the actual mechanism of heat exchange is much more involved. Namely, heat-and-mass transfer due to electrohydrodynamic conditions in a slag bath takes place, the temperature field being essentially nonuniform. However, filming and photographing of actual molten slags through a quartz window have revealed the presence of the active region [4], which justifies the simplifications adopted in our model. Introducing the designation $x \equiv \gamma(T - T_n)$, we rewrite (1) in the form

$$\frac{1}{1-x} \cong \frac{\alpha(x)F_s}{\gamma P_0}(x - x_0), \qquad (2)$$

where $F_s = 2\pi rh$ is the lateral area of the active region, whose mean radius is r; $P_0 \equiv U_0^2/R_n$; $x_0 = \gamma(T_0 - T_n)$; and $\alpha(x)$ is the heat transfer coefficient, which, according to the known criteria relationship [5, 6], is given by

$$\alpha(x) = 0.664\frac{\lambda}{h}\left(\frac{v(x)h}{\nu}\right)^{1/2}\left(\frac{\nu}{a}\right)^{1/3}, \qquad (3)$$

Here, λ, ν and a are the heat conductivity, kinematic viscosity, and diffusivity of a molten slag, respectively, and h is the active-cone height.

It is also convenient to derive a relationship between the slag flow velocity v, operating current I, and bath radius r. It readily follows from dimensional considerations that

$$v \cong \frac{I(x)}{r}\sqrt{\frac{\mu_0}{\rho}}, \qquad (4)$$

where ρ and μ_0 are the density and the magnetic permeability of the molten slag, respectively.

Written as

$$\frac{1}{\sqrt{1-x}} = Wd(x - x_0), \qquad (5)$$

expression (2) involves a criterion *Wd*, which characterizes an electroslag process:

$$Wd = 2\left(\frac{rhR_n}{\nu}\right)^{1/2}\left(\frac{\nu}{a}\right)^{1/3}\left(\frac{\mu_0}{\rho}\right)^{1/4}\frac{\lambda}{\gamma U_0^{3/2}}. \qquad (6)$$

Here, the physical constants are taken at the active-cone temperature. As follows from (5), the stability of an electroslag process depends on the dimensionless parameter *Wd*, which is the ratio of the heat powers released within and removed from the active region. The graphic solution of this equation is given in the figure.

1063-7842/00/4505-0644$20.00 © 2000 MAIK "Nauka/Interperiodica"

Consider equation (5) in detail. At $Wd < 1/[2(1 - x_0)^{3/2}] = Wd_{\min}$, the line of removed heat does no longer intersect the heat release hyperbola and the process is unstable. This may indicate the transition to the arc process or heat-removal mechanism changeover (for example, radiative heat transfer is dominant at the arc process). At $Wd > Wd_{\min}$, the equation has two roots: x_1 (stable equilibrium point) and x_2 (unstable equilibrium point). Let us elucidate the meaning of the (x_1, x_2) interval. The process is assumed to be steady, but the temperature parameter is actually time-dependent and can be represented as $x(t) = x_{st} + \delta x$. At $\delta x > x_2 - x_1$, the process becomes unstable (the active cone begins to heat up unlimitedly). Thus, the more extended the temperature interval (x_1, x_2), the more stable the process. Obviously, this interval extends with increasing Wd. The extension is possible when the voltage (current) decreases or the active-cone height–mean radius product grows, as follows from (6).

Of interest is the effect of the power source characteristic on the process stability. Assume that the characteristic slightly falls; i.e., $U = U_0 - aI$, where a is a constant such that $a/R_n \ll 1$. Then,

$$I = \frac{U}{R} = \frac{U_0}{R} - \frac{a}{R}I; \quad \text{therefore,} \quad I = \frac{U_0}{R + a}. \qquad (7)$$

Here again, $R \cong R_n[1 - \gamma(T - T_n)]$. With (7), we obtain for the released heat

$$P = IU \approx \frac{U_0^2}{R}\left(1 - \frac{2a}{R}\right).$$

In terms of the introduced designations, equation (5) for the case under consideration takes the form

$$\frac{1}{\sqrt{1-x}}\left[1 - \frac{(2a/R_n)}{1-x}\right] \cong Wd(x - x_0). \qquad (8)$$

It is seen that the heat release curve (P) moves down, extending the stability interval (x_1, x_2). Conversely, for a slightly rising characteristic, the interval will shrink (expression (8) will take the plus sign in the brackets).

The above model allows an understanding of the mechanism behind the transition, for example, from purely resistive to resistive–arc process conditions. It qualitatively and, to a first approximation, quantitatively characterizes the electroslag process stability dynamics when the power source has a stiff characteristic. The stability depends on (1) the slag bath dimensions (r and h), (2) slag physical parameters (temperature resistance coefficient γ, viscosity ν, heat conductivity λ, density ρ, and diffusivity a), and (3) process conditions (voltage amplitude across the bath). Given the process parameters, the length of the (x_1, x_2) interval can be optimized. This is useful in choosing the electrical regime and also the slag properties and amount. The stability of an electroslag process is defined by the criterion Wd.

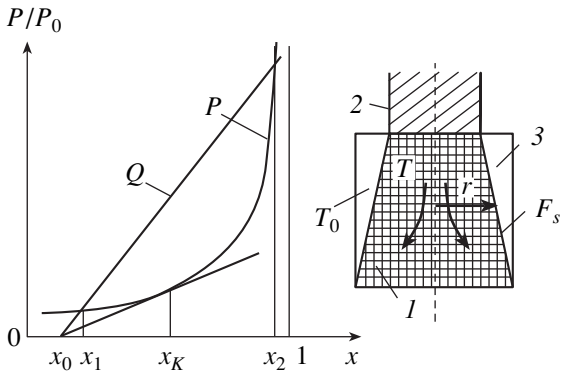

P and *Q* stand for the heat release and heat removal curves, respectively. *1*, active cone of an electroslag bath (dark background; arrows indicate the slag flow direction); *2*, electrode; and *3*, slag bath zone outside the active cone.

REFERENCES

1. *Electroslag Welding and Hard-Surfacing*, Ed. by B. E. Paton (Mashinostroenie, Moscow, 1980).
2. G. Z. Voloshkevich, Avtom. Svarka, No. 4, 19 (1962).
3. G. I. Abramov, A. V. Gurevich, S. I. Zakharchenko, *et al.*, Fiz. Tverd. Tela (Leningrad) 27, 2250 (1985) [Sov. Phys.–Solid State 27, 1350 (1985)].
4. D. A. Dudko, G. Z. Voloshkevich, I. I. Sushchuk-Slyusarenko, and I. I. Lychko, Avtom. Svarka, No. 2, 19 (1971).
5. H. Y. Wong, *Handbook of Essential Formulae and Data on Heat Transfer for Engineers* (Longman, London, 1977; Atomizdat, Moscow, 1979).
6. D. A. Dudko and A. M. Pal'ti, Avtom. Svarka, No. 9, 19 (1997).

Translated by V. Isaakyan

Technical Physics, Vol. 45, No. 5, 2000, pp. 646–649. Translated from Zhurnal Tekhnicheskoĭ Fiziki, Vol. 70, No. 5, 2000, pp. 124–127.

BRIEF COMMUNICATIONS

A Multifrequency Gyrotron

S. N. Vlasov

Institute of Applied Physics, Russian Academy of Sciences,
ul. Ul'yanova 46, Nizhni Novgorod, 603600 Russia

Received January 28, 1999

Abstract—A theory of a gyrotron that generates at frequencies that are multiples of the cyclotron frequency is considered. In the steady-state regime, this radiation appears as a nonsinusoidal electromagnetic oscillation whose waveform depends on the amplitudes of its harmonics. The theory is developed for the weakly relativistic case and is based on known transverse momentum equations for electrons moving in an electromagnetic field. Under optimal conditions, the single-harmonic emission of a multifrequency gyrotron is more efficient than that of a single-frequency device. © *2000 MAIK "Nauka/Interperiodica".*

Millimeter-wave high-power sources usually produce monochromatic radiation. The best known of them are gyrotrons, where electrons rotating in a static magnetic field are used as an active medium. An important component of a gyrotron is its cavity, whose spectrum has a mode with a close-to-cyclotron frequency. The field structure and Q-factor of this mode provide efficient generation of electromagnetic radiation. Along with the operating-mode frequency, the gyrotron spectrum contains low-level harmonics with frequencies close to multiples of the cyclotron frequency. Thus, a gyrotron can be used as a source of both monochromatic and multifrequency radiations. This property occurs, because the active medium of a gyrotron—electrons in a magnetic field—is capable of simultaneously radiating several harmonics of the cyclotron frequency. Therefore, gyrotrons can generate several harmonics with frequencies that are multiples of the cyclotron frequency. The resulting radiation appears as nonsinusoidal electromagnetic oscillations whose waveform depends on the amplitudes of its constituents.

To excite this mode, the cavity spectrum must contain modes that have multiple cyclotron frequencies, as well as an appropriate field structure and *Q*-factor. The intensity of each of the harmonics will depend on the efficiency of its interaction with the electron beam. All the modes will be in phase. This paper theoretically studies the simplest multifrequency gyrotron—a two-frequency gyrotron with the lowest order harmonics $n = 1$ and 2. The theory is developed for the weakly relativistic case and is based on known transverse momentum equations for electrons moving in an electromagnetic field [1, 2]. The space charge and electron velocity spread are ignored.

Consider the interaction between a helical electron beam typical of a gyrotron and the electromagnetic field of the cavity. The electron beam travels in the uniform magnetic field $\mathbf{H}_0$, which is directed along the *z*-coordinate and is azimuthally symmetric about the center of electron cyclotron orbits with a radius R_b in the cylindrical coordinate system (r, φ, z). The cavity is a section of a circular waveguide with a slowly varying diameter according to the theory of gyrotron cavities [3]. We will also assume the surface of the cavity to be such that the frequencies of two of its modes are sufficiently close to those of the cyclotron harmonics. This is achieved, for example, when the waveguide walls are transversely corrugated with a period that is smaller than the wavelength of the lower order harmonic but slightly larger than the half-wavelength of the higher order one. The field structure in such a cavity at the resonance frequencies is very similar to that at the cutoff frequencies in the corresponding waveguide. The electron beam will efficiently interact only with the *H*-waves which have the transverse electric field component. The operation of such a multifrequency gyrotron can be analyzed in terms of the theory developed in [1, 2] for a single-frequency gyrotron.

Consider mode interaction when one mode has a frequency ω_1 at the first harmonic and depends on the azimuth angle φ as $\sim\exp(-im\varphi)$, where *m* is the azimuth index. Let the other mode at the *n*th harmonic have a frequency $n\omega_1$ and depend on the azimuth angle as $\sim\exp(-imn\varphi)$ with the index *mn*. Then, the φ dependence of the transverse momentum of an electron $\tilde{p}$ can be described by only one harmonic and $\tilde{p} \sim \exp[-i(m-1)\varphi]$. Thereafter, we drop the azimuthal dependences when describing fields and electron motion. According to [1, 2], the normalized transverse momentum obeys the equation

$$\frac{dp}{d\zeta} + ip(\Delta + |p|^2 - 1) = \sum_{n=1}^{2} p^{*(n-1)} f_n(\zeta), \qquad (1)$$

1063-7842/00/4505-0646$20.00

where

$$p = \frac{(p_x + ip_y)\exp[-i\omega_1 t]}{|p_{\perp 0}|},$$

$\mathbf{p}_\perp = m_0\mathbf{v}_\perp$ is the transverse momentum, m_0 is the rest mass of an electron, $\mathbf{v}_\perp$ is its transverse velocity,

$$\Delta = \frac{2}{\beta_{\perp 0}^2}\frac{\omega_1 - \omega_{H0}}{\omega_1}$$

is the normalized frequency offset with respect to the resonance frequency, ω_1 is the frequency of the first harmonic,

$$\omega_{H0} = -\frac{eH_0}{m_0 c}\left(1 - \frac{\beta_{\perp 0}^2}{2} - \frac{\beta_{\| 0}^2}{2}\right)$$

is the electron cyclotron frequency at the entrance to the interaction space, n is the harmonic index, e is the electron charge,

$$\beta_{\perp 0} = \frac{|\mathbf{v}_{\perp 0}|}{c}, \quad \beta_{\| 0} = \frac{|v_{\| 0}|}{c},$$

c is the velocity of light, $\mathbf{p}_{\perp 0}$ is the amplitude of the transverse momentum, $\mathbf{v}_{\perp 0}$ and $v_{\| 0}$ are the transverse and longitudinal velocities at the entrance to the interaction space, and

$$\zeta = \frac{\beta_{\perp 0}^2}{2}\frac{\omega_{H0} z}{v_{\| 0}}$$

is the normalized longitudinal coordinate.

The functions $f_n(\zeta)$ are related to the field amplitudes $\mathbf{E}_n$ in the interaction space as [2, 4]

$$f_n = \beta_{\perp 0}^{n-4}\left(\frac{n^n}{2^{n-1}n!}\right)J_{mn-n}(k_n R_b)F_n,$$

$$\mathbf{E}_n(\mathbf{r}, t) = \mathrm{Re}[\exp(i\omega_n t)F_n(z)\mathbf{E}_{n0}(\mathbf{r}_\perp)],$$

$$\mathbf{E}_{n0} = \frac{H}{k_n}[\nabla\Psi_n \mathbf{z}_0],$$

$$\Psi_n = J_{mn}(k_n R_n)\exp(-imn\varphi).$$

Unlike the equations given in [2], (1) describes an electron beam affected by the fields of two harmonics. According to [2], the fields $f_n(\zeta)$ satisfy the set of equations

$$\frac{d^2 f_n}{d\zeta^2} + \gamma_1^2 f_n = iI_n\frac{1}{2\pi}\int_0^{2\pi} p^n d\theta_0, \qquad (2)$$

where

$$\gamma_n^2 = \frac{8\beta_{\| 0}^2}{\beta_{\perp 0}^4}\frac{(\omega_n - \omega_{crn})}{\omega_n},$$

ω_{crn} are the cutoff frequencies of the modes interacting with the electron beam,

$$I_n = 64\frac{eI_0}{m_0 c^3}n^3\beta_{\| 0}\beta_{\perp 0}^{2(n-4)}\left(\frac{n^n}{2^n n!}\right)^2\frac{J_{m-n}^2(k_n R_b)}{(k_n^2 R_p^2 - m^2)J_m^2(k_n R_n)},$$

$k_n = (\omega_1 n)/c$, I_0 is the beam current, $J_q(x)$ is Bessel functions, and θ_0 is the phase with which electrons enter the interaction space.

Since the cavity walls are corrugated, the values of R_n are different. Suppose that the Q-factors Q_1 and Q_n of the modes are sufficiently high and the field structures of the modes are described by the same Gaussian functions

$$f_n = A_n\exp\left[-\frac{(\zeta - \zeta_0)^2}{2L^2}\right] = A_n\varphi_n$$

with an extent L and amplitudes A_n; ζ_0 is the position of the cavity center. Consider steady-state generation. In this case, the amplitudes A_n are time-independent and complex. Since the zero-time reference is arbitrary, one of them, say, A_1, can be taken as real. After substituting the functions $f_n(\zeta)$ into equations (1) and (2), they take the form

$$\frac{dp}{d\zeta} + ip(\Delta + |p|^2 - 1) = \sum_{n=1}^{2} A_n p^{*(n-1)}\varphi_n(\zeta), \qquad (3)$$

$$\frac{d^2\varphi_n}{d\zeta^2} + \gamma_n^2\varphi_n = \frac{iI_n}{2\pi A_n}\int_0^{2\pi} p^n d\theta_0. \qquad (4)$$

Following [1], we multiply (4) by p^*, add the product to its complex conjugate, and integrate the result over the longitudinal coordinate ζ and the phase θ_0 with which electrons enter the interaction space. Eventually, we obtain the equation for the efficiency $\eta_\perp$,

$$\eta_\perp = -\int_0^{\zeta_k}\left[\frac{1}{2\pi}\int_0^{2\pi}\sum_{n=1}^{2}(A_n\varphi_n p^{*n} + A_n^*\varphi_n^* p^n)d\theta_0\right]d\zeta$$

$$= -\sum_{n=1}^{2}\eta_{\perp n},$$

where ζ_k is the position where electrons stop interacting with the electromagnetic field and

$$\eta_{\perp n} = -\int_0^{\zeta_k}\left[\frac{1}{2\pi}\int_0^{2\pi}(A_n\varphi_n p^{*n} + A_n^*\varphi_n^* p^n)d\theta_0\right]d\zeta \qquad (5)$$

characterize the relative powers lost by the electron beam to the modes at the first and nth harmonics. Clearly, the necessary condition for the two-frequency regime to be stationary is that $\eta_{\perp n}$ be positive.

To find the conditions for the existence of the two-frequency regime, following [2], we use equations (5) and (6) and also those for the cavity modes in the absence of the electron beam:

$$\frac{d^2\varphi_n}{d\zeta^2} + \gamma_{10}^2\varphi_n = 0. \tag{6}$$

The quantities γ_{n0}^2 are complex, their imaginary parts being nonzero because the Q-factors of the modes are finite:

$$\operatorname{Im}\gamma_{n0}^2 = \frac{\omega_n^2 l^2}{c^2 Q_n}, \quad l = \frac{2v_{\parallel 0}}{\beta_{\perp 0}^2 \omega_{H0}}. \tag{7}$$

Using equations (4) and (6), one can obtain the equalities characterizing the operation of a two-frequency gyrotron:

$$\gamma_n^2 - \operatorname{Re}\gamma_{n0}^2 = -\frac{I_n}{|A_n|^2 N_n}\operatorname{Im}\left[\int_0^{\zeta_k}\left(\frac{1}{2\pi}\int_0^{2\pi} p^n d\theta_0\right)A_n^*\varphi_n^* d\zeta\right], \tag{8}$$

$$\operatorname{Im}\gamma_{n0}^2 = -\frac{I_n}{|A_n|^2 N_2}\operatorname{Re}\left[\int_0^{\zeta_k}\left(\frac{1}{2\pi}\int_0^{2\pi} p^n d\theta_0\right)A_n^*\varphi_n^* d\zeta\right] = \frac{I_n\eta_{\perp n}}{2|A_n|^2 N_n}, \tag{9}$$

where

$$N_n = \int_0^{\zeta_k}|\varphi_n|^2 d\zeta.$$

Equalities (8) yield the offset of oscillation frequencies with respect to the cavity modes in the absence of the electron beam. Equalities (9) complement equalities (5): they relate the pump amplitude I_n to the amplitudes of steady-state oscillations. Using (7) and (9), we rewrite offset formula (8) in the form that is more convenient for representing results of a simulation:

$$\Delta_n = \frac{\operatorname{Im}\frac{1}{2\pi}\int_0^{\zeta_k}\left\{\int_0^{2\pi} p^{*n}A_n d\theta_0\right\}d\zeta}{\eta_{\perp n}} = \frac{(\gamma_n^2 - \operatorname{Re}\gamma_{0n}^2)Q_n\beta_{\perp 0}^4}{8n^2\beta_{\parallel 0}^2}. \tag{10}$$

It is known that the coordinate ζ_k at which electrons stop interacting with the electromagnetic field is of great importance in designing gyrotrons [4, 5]. In order to compare our results with the known ones, we assume that, for both modes, the rf field is maximum at the center of the cavity ($\zeta_0 = \zeta_k/2$) and decreases by a factor of $\exp(-3) \approx 1/20$ toward its edges.

Operating conditions of a two-frequency gyrotron are defined by frequency offset Δ, field extent L, and pump intensity (dimensionless currents I_n). Upon numerically simulating a two-frequency gyrotron, it is useful to specify the amplitudes A_n and then calculate the eigenfrequencies and Q-factors of the empty cavity from equations (8)–(10) with regard for the amplitudes of the dimensionless currents. Below, we present results of the numerical analysis of a two-frequency gyrotron operating in the steady-state regime.

Figures 1 and 2 plot the efficiencies $\eta_\perp$, $\eta_{\perp 1}$, and $\eta_{\perp 2}$ as a function of $|A_2|$ for phases $\alpha = -0.02$ and -0.64. As a starting device, we employed a single-frequency first-

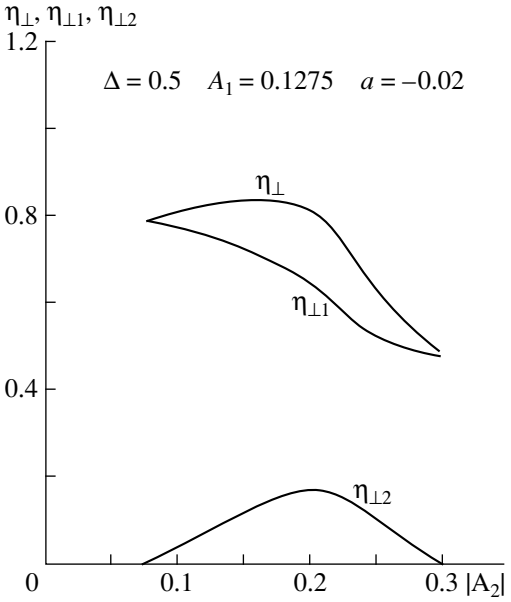

Fig. 1. Efficiency of the two-frequency gyrotron against the amplitude of the second harmonic at $\Delta = 0.5$, $L = 6$, $A_1 = 0.124$, and $\alpha = -0.02$.

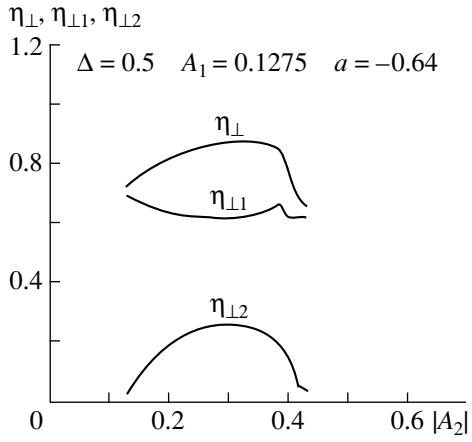

Fig. 2. Same as in Fig. 1 at $\alpha = -0.64$.

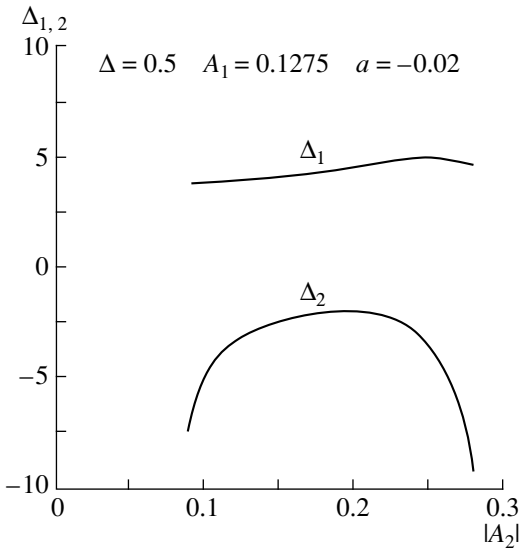

Fig. 3. Relative frequency offsets of the two-frequency gyrotron modes against the amplitude of the second harmonic at $\Delta = 0.5$, $L = 6$, $A_1 = 0.124$, and $\alpha = -0.02$.

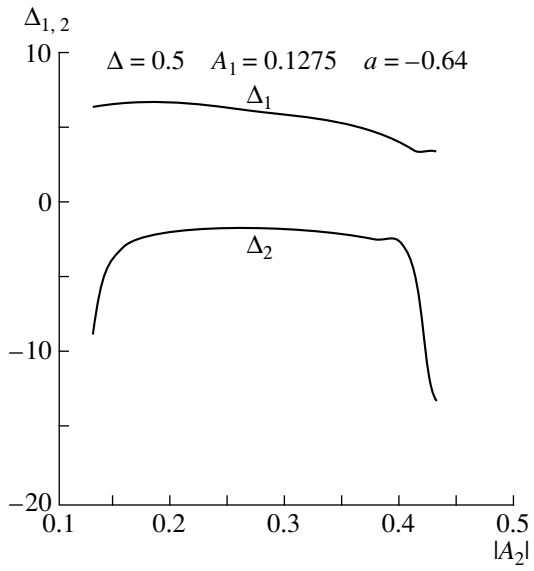

Fig. 4. Same as in Fig. 3 at $\alpha = -0.64$.

harmonic gyrotron operating with parameters providing the maximum efficiency [5] ($\Delta = 0.5$, $L = 6$, $A_1 = 0.124$, and $\eta_\perp = 0.71$). The plots were constructed in the interval of $|A_2|$ where $\eta_{\perp 1}$ and $\eta_{\perp n}$ are positive. The figures show that there exist the optimal $|A_2|$ and α at which the gyrotron efficiency attains the maximum. The maximum efficiency of the total two-harmonic radiation ($\eta_\perp \sim 0.87$ at $|A_2| \approx 0.35$ and $\alpha = -0.64$ in Fig. 2) is higher than that of the one-harmonic radiation at a certain ratio of the harmonic intensities. At particular $|A_2|$ and α, the efficiency of the two-harmonic device emitting the first harmonic alone can be higher than the efficiency of the single-frequency gyrotron ($\eta_\perp > 0.79$ at $|A_2| \approx 0.08$ and $\alpha = -0.02$ in Fig. 1). The higher efficiency of the two-frequency gyrotron means that the second harmonic rather efficiently picks up energy from the electrons bunched by the field of the first harmonic; however, the field of the first harmonic still remains higher. If the starting gyrotron has the optimal parameters for the second harmonic [5] ($\Delta = 0.55$, $L = 2.9$, $|A_2| = 0.124$, and $\eta_\perp = 0.71$), the addition of the first harmonic does not improve the efficiency, because the cavity is not sufficiently long.

Figures 3 and 4 plot normalized frequency offsets $\Delta_{1,2}$ vs. second-harmonic field for the same gyrotron parameters. The presence of the interval of $|A_2|$ where the difference between Δ_1 and Δ_2 varies not too rapidly shows that, at fixed cavity parameters, the two-frequency regime can exist in a certain range of the pump amplitude.

REFERENCES

1. V. K. Yulpatov, in *Gyrotron*, Ed. by A. V. Gaponov-Grekhov (Inst. Prik. Fiz. Akad. Nauk SSSR, Gorki, 1981), pp. 26–40.
2. V. L. Bratman, M. A. Moiseev, and M. I. Petelin, in *Gyrotron*, Ed. by A. V. Gaponov-Grekhov (Inst. Prik. Fiz. Akad. Nauk SSSR, Gorki, 1981), pp. 122–145.
3. S. N. Vlasov, G. M. Zhislin, I. M. Orlova, *et al.*, Izv. Vyssh. Uchebn. Zaved. Radiofiz. **12**, 1236 (1969).
4. V. L. Bratman, M. A. Moiseev, M. I. Petelin, *et al.*, Izv. Vyssh. Uchebn. Zaved. Radiofiz. **16**, 622 (1973).
5. V. I. Belousov, V. S. Ergakov, and M. A. Moiseev, Élektron. Tekh., Ser. 1: Élektron. SVCh, No. 9, 41 (1978).

Translated by A. D. Khzmalyan

Technical Physics, Vol. 45, No. 5, 2000, pp. 650–652. Translated from Zhurnal Tekhnicheskoĭ Fiziki, Vol. 70, No. 5, 2000, pp. 128–129.

BRIEF COMMUNICATIONS

Porous Gallium Arsenide with Arsenic Clusters

Yu. N. Buzynin, S. A. Gusev, Yu. N. Drozdov, and A. V. Murel

Institute of Physics of Microstructures, Russian Academy of Sciences, Nizhni Novgorod, 603600 Russia

Received March 30, 1999

Abstract—It is for the first time that the possibility is demonstrated of preparing gallium arsenide with arsenic clusters under conditions of annealing of its porous layers obtained by electrochemical etching. It is found that the clusters are concentrated in porous layer barriers, their size ranges from 1 to 10 nm, and the density reaches 4×10^{18} cm^{-3}. Under conditions of annealing in the temperature range from 400 to 600°C, an improvement in the structure quality of the porous layer is observed, and the lattice parameter (reduced for this layer) increases to approach a value characteristic of a single crystal. When highly alloyed substrates of the *n*-type are used, the inversion of the type of conductivity is observed in the surface part of the porous layer, which is due to the emergence of deep-lying acceptor centers. Thermal annealing leads to a narrowing of the inversion layer and to a more uniform distribution of electrically active centers over the porous layer thickness. © *2000 MAIK "Nauka/Interperiodica".*

Owing to its unique electronic and optical properties, gallium arsenide containing arsenic clusters has recently been attracting researchers' attention [1]. This material is characterized by a high resistivity and an anomalously short lifetime of charge carriers. These properties make the material promising from the standpoint of developing buffer layers in manufacturing integral circuits and extrafast photodetectors. Up to now, gallium arsenide with arsenic clusters has been prepared by molecular-beam epitaxy at a low growth temperature or by ion implantation with subsequent annealing.

In this study, we have demonstrated for the first time the possibility of preparing gallium arsenide with arsenic clusters under conditions of thermal annealing of porous gallium arsenide. Layers of porous gallium arsenide with an excess of arsenic atoms (up to 10%) were prepared by electrochemical etching on highly alloyed substrates of *n*-type conductivity [2]. Then, samples of porous gallium arsenide were placed "face to face" on a single-crystal gallium arsenide substrate in order to reduce the loss of arsenic from the layer surface and annealed in a flow of helium in the temperature range from 400 to 700°C for a period of 3–30 min. The samples thus treated were investigated using the electron microscopy, X-ray diffractometry, electrochemical C–V profiling, and probe methods.

A study of angle laps of thermally treated samples by transmission electron microscopy using a JEM-2000 EX microscope has revealed that layers of porous gallium arsenide contain arsenic clusters (dark dots in Fig. 1) in column barriers. The average cluster size ranges from 1 to 10 nm, and their density reaches a value of 4×10^{18} cm^{-3}.

The lattice parameter and the structure perfection of the layers of porous gallium arsenide were estimated by X-ray diffractometry using the scheme of a double-crystal spectrometer with a (400) GaAs monochromator. Figure 2 gives the rocking curves taken for the initial samples and after annealing at different temperatures. In addition to a sharp peak of GaAs, a broadened peak of low intensity is present, which corresponds to a

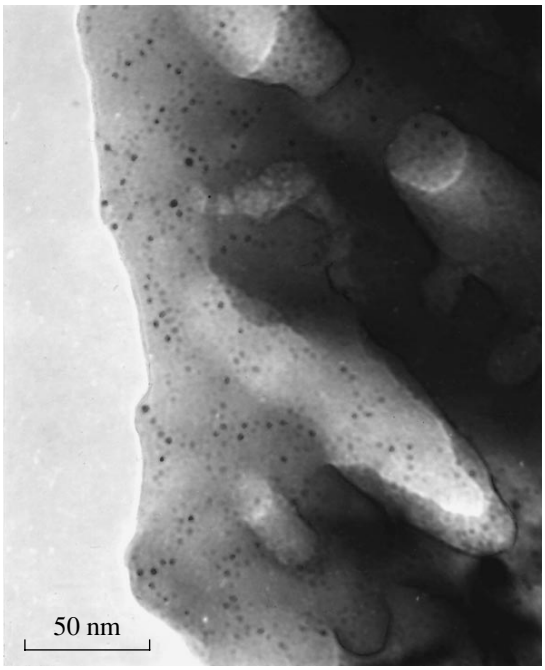

Fig. 1. Arsenic clusters in a layer of porous gallium arsenide.

1063-7842/00/4505-0650$20.00

porous layer. A shift of this peak is indicative of a variation of the lattice parameter of the porous layer. The initial layer has a reduced lattice parameter. The estimates indicate that the variation of the lattice parameter on a normal to the substrate surface is $\Delta\alpha/\alpha_\perp = -2.5 \times 10^{-4}$. It follows from the foregoing data that the additional maximum associated with the porous layer narrows up to annealing at 600°C and approaches the peak of (400) GaAs matrix. Then, the peak broadens again and moves away from (400) GaAs. This result indicates that the structure quality of the porous layer improves as a result of annealing in the temperature range from 400 to 600°C, and the degree of compression on a normal to the surface decreases. It may be assumed that one of the reasons for the reduced lattice parameter of the initial samples of porous GaAs is the compression of column barriers bounded by surfaces of high curvature due to the forces of surface tension. This effect was observed recently for porous silicon [3]. The increase in the lattice parameter of porous GaAs observed during annealing may be associated with the transition of excess As from the pore surface to tetrahedral interstices whose size in the case of GaAs is less than the tetrahedral radius for arsenic.

The distribution of electrically active defects over the layer thickness was studied using the method of electrochemical C–V profiling. This method includes alternate etching of the layer with the depth estimated by Faraday's law and C–V measurements of the depletion layer of the semiconductor–electrolyte interface with subsequent estimation of concentration by the known formulas [4]. Figure 3 gives the results of such profiling for layers of porous gallium arsenide on a highly alloyed single-crystal substrate ($n = 2 \times 10^{18}$ cm^{-3}). The results of a formal calculation by the formulas of the volt–farad method point to the presence on the surface of a layer with a high concentration of acceptors which, in all probability, are deep-lying, because a strong frequency dispersion of capacitance is observed, and the results of conductivity measurements fail to prove the presence of a high concentration of charge carriers. A change of the conductivity type occurs at some depth; this apparently implies the arrival at the substrate. However, the value of the concentration is very overestimated, which may be also associated with the extremely disturbed surface structure after etching the layer of porous gallium arsenide. The true thickness of the layer of porous gallium arsenide must differ from the calculated value as a result of a strong indeterminacy of the true area of the electrolyte–semiconductor contact because of the highly developed surface of porous material. However, as revealed by comparison with the results of measurements on a cleaved sample in an electron microscope, these values may be used for rough estimation. The temperature annealing in the temperature range from 400 to 700°C leads to a narrowing of the inversion layer up to its complete disappearance and to a leveling of the concentration of electrically active centers over the layer thickness (Fig. 3a). As the time of annealing of the porous layer increases, the uniformity of distribution of electrically active defects over its thickness likewise increases (Fig. 3b).

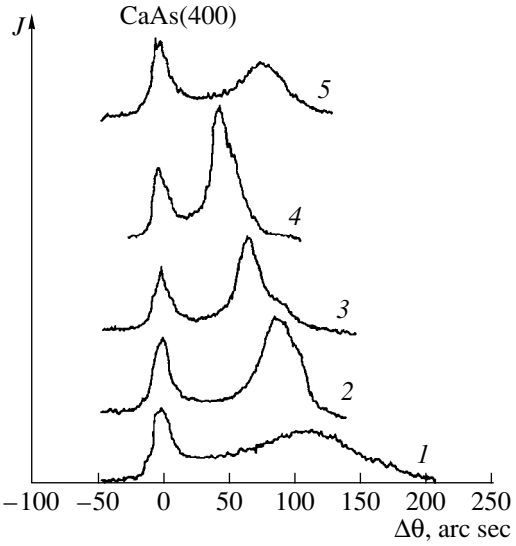

Fig. 2. X-ray diffraction rocking curves in the neighborhood of (400) GaAs, taken (*1*) in the initial state and after annealing at (*2*) 400, (*3*) 500, (*4*) 600, and (*5*) 700°C.

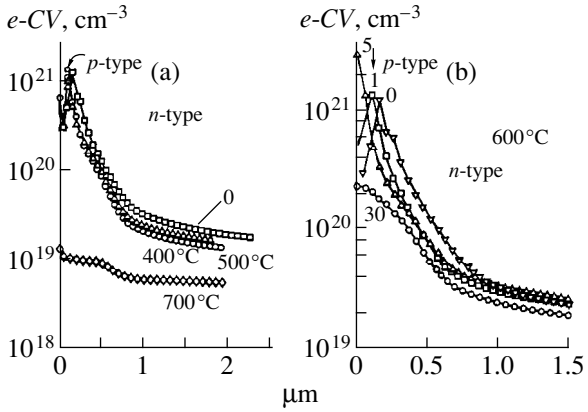

Fig. 3. The electrochemical C–V profile of layers of porous gallium arsenide after high-temperature treatment: (a) isochoric annealing (annealing time, 15 min), (b) isothermal annealing (numerals by the curves indicate the annealing time in min).

The estimates made as a result of probe measurements demonstrate that the resistivity of the material increases strongly upon formation of porous gallium arsenide and its subsequent thermal annealing. This may be associated with the formation of depletion regions at the boundaries of As clusters and the GaAs matrix [5]. It is difficult to perform accurate measurements of the resistivity of porous GaAs because of the shunting substrate.

ACKNOWLEDGMENTS

This study received support from the Russian Foundation for Basic Research (project no. 96-02-18843) and from the International Science and Technology Program on the Physics of Solid-State Nanostructures (project no. 97-1070).

REFERENCES

1. N. A. Bert, A. N. Veĭnger, M. D. Vilisova, *et al.*, Fiz. Tverd. Tela (St. Petersburg) **35**, 2909 (1993) [Phys. Solid State **35**, 1289 (1993)].
2. Yu. Buzynin, S. Gusev, Yu. Drozdov, *et al.*, in *Proceedings of ALT'95 International Symposium, 1995* [Proc. SPIE **2777**, 43 (1995)].
3. M. E. Kopman, E. G. Kuz'minov, and V. B. Kulik, Pis'ma Zh. Éksp. Teor. Fiz. **64**, 696 (1996).
4. I. V. Irin and A. V. Murel, Prib. Tekh. Éksp., No. 6, 150 (1993).
5. A. V. Warren and J. L. Woodal, Appl. Phys. Lett. **57**, 1331 (1990).

Translated by Henri A. Bronstein

Technical Physics, Vol. 45, No. 5, 2000, pp. 653–655. Translated from Zhurnal Tekhnicheskoĭ Fiziki, Vol. 70, No. 5, 2000, pp. 130–132.

BRIEF COMMUNICATIONS

Ferrite and High-Temperature Superconductor Targets for Sputtering

A. A. Lepeshev[2], V. N. Saunin[2], S. V. Telegin[1], K. P. Polyakova[1], V. A. Seredkin[1], and A. I. Polsky[1]

[1] *Kirenskiĭ Institute of Physics, Siberian Division, Russian Academy of Sciences, Akademgorodok, Krasnoyarsk, 660036 Russia*

[2] *Siberian Aerospace Academy, Krasnoyarsk, 660014 Russia*

Received March 30, 1999
Final version of October 25, 1999

Abstract—A method is described of preparing targets for sputtering, which involves the use of plasma deposition of respective powders onto a cooled metal plate. It is demonstrated that the use of plasma technology enables one to produce, in a controlled atmosphere, intricately shaped ceramic targets characterized by a highly uniform composition and by reliable mechanical and thermal contact of the resultant coating with the holder plate. Experiments are performed on the sputtering of targets to prepare polycrystalline ferrite films for magnetooptical applications and epitaxial films of high-temperature superconductors. © *2000 MAIK "Nauka/Interperiodica".*

The development of computer equipment, control systems, and means of communication stimulated investigations in the field of thin-film technologies from the standpoint of both the development of relevant equipment and improvements in the manufacturing technology, as well as of the practical utilization of thin metal, dielectric, magnetic, and other film coatings. Depending on the function and desired characteristics, thin films may be deposited by a variety of systems, including sputtering ones such as diode, triode, magnetron, and other dc systems or systems involving the use of RF discharge. Along with the choice of the type of sputtering system, special attention should be given to the technology of manufacturing the cathode assembly, in particular, the methods of preparing targets and the methods of securing and cooling these targets. A great variety of methods exist for preparing targets. The main methods of preparing nonmetallic targets include pressing with subsequent sintering or hot pressing. In this case, however, one often fails to solve the problem of joining a target and a cooled holder plate.

This paper deals with an ingenious method of preparing targets on a cooled holder plate, which we believe to be promising and quite universal, namely, a method involving the use of plasma deposition. In the case of plasma deposition, a gas–powder mixture is injected into a flow of low-temperature plasma where the particles are accelerated, heated to a preassigned mass-average temperature, melted, and subsequently cooled on the surface being deposited. The use of plasma technology enables one to produce, in a controlled atmosphere, intricately shaped targets of both metal and ceramic materials characterized by reliable thermal contact of the coating with the holder plate.

The plasma deposition was accomplished using the equipment developed by us [1]. The functional diagram

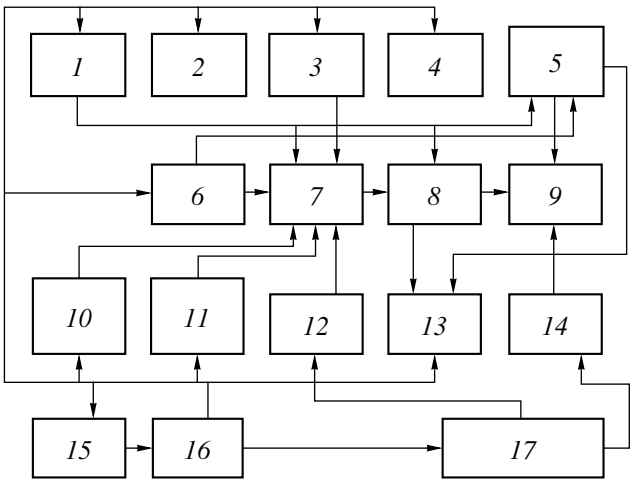

Fig. 1. The functional block diagram of the facility: (*1*) working gas delivery system, (*2*) transporting gas delivery system, (*3*) powder feeder, (*4*) feeder control unit, (*5*) device of generator mode of coating, (*6*) cooling system, (*7*) Vulkan-type plasma generator, (*8*) deposition chamber, (*9*) part subjected to deposition, (*10*) electric supply system of the plasma generator, (*11*) system for ignition of the plasma generator arc, (*12*) plasma generator-positioning mechanism, (*13*) exhaust and utilization system, (*14*) feed mechanism, (*15*) parameter measurement system, (*16*) control system of the facility, (*17*) system of control of relative positioning.

1063-7842/00/4505-0653$20.00 © 2000 MAIK "Nauka/Interperiodica"

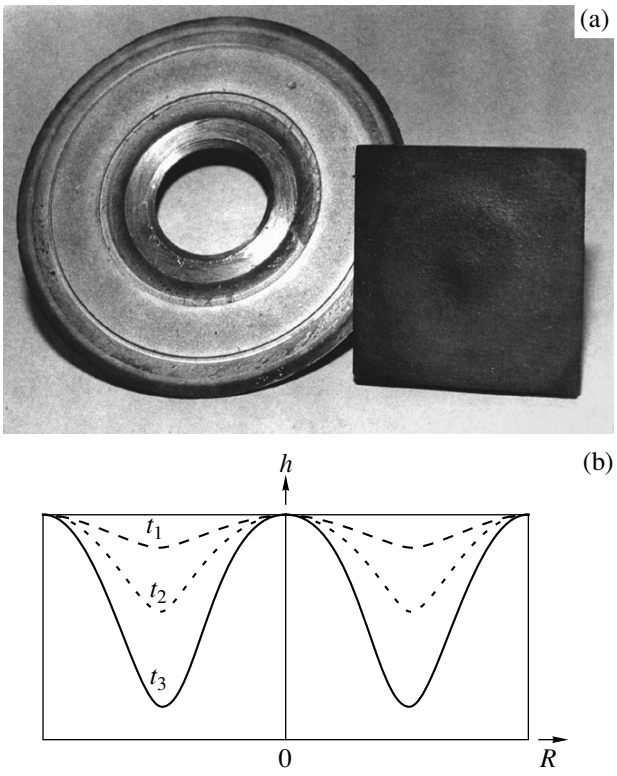

Fig. 2. (a) Exterior view of targets prepared by plasma deposition and (b) the formation of the erosion zone of a round target for different operation times t ($t_1 < t_2 < t_3$).

of the facility is given in Fig. 1. The main component of the facility is an electric-arc plasma generator with coaxial feed of powder designed to develop a flow of dispersed particles of preassigned density, temperature, and velocity.

Figure 2a illustrates plane targets of magnetic materials prepared by plasma deposition. In spite of fairly large dimensions (circular target diameter, 18 cm; thickness, 4 mm), the deposited coating is uniform, without visible cracks, spallation, or peeling off the plate (plate material, copper).

The metallographic studies of the coatings have revealed that their microstructure is typical of plasma deposition, with a characteristic form anisotropy of pores, which are, as a rule, oriented in parallel with the surface being deposited and have a depth of ~3 μm. The porosity of the coating, as well as its other properties, may be controlled by the process conditions of deposition, the optimum values of whose parameters for a number of oxide targets are given in the table.

It is known that materials of high resistivity, in particular, ferrites (10^3–10^6 Ω m), are usually sputtered in facilities with RF generators [2]. For sputtering of dielectrics in dc facilities, which are more efficient energetically, alloying additions are introduced into the composition of a target with a view to reducing its electric resistance (such additions may affect the quality of thin-film coating) [3].

The plasma deposition of a number of ferrite targets may be accomplished without alloying additions. It is known that the processing of ferrites in a reduction medium leads to a variation of the ferrite composition, loss of oxygen, an increase in the fraction of bivalent iron, and, as a result of this, to an increase in the electrical conductivity [4]. Analogous processes are observed when sputtering ferrites in a flow of low-temperature plasma. This makes possible the control of electrical conductivity within a fairly wide range owing to the choice of deposition conditions.

Note an important fact which is associated with the efficiency of utilization of the target material and largely defines the design and process singularities of manufacturing the cathode assembly. Because the intensity of sputtering of a material on a surface is nonuniform and the rate of sputtering is maximum along the axis of the discharge zone and decreases toward its periphery, an erosion zone is formed in the target in the course of operation, with the shape of that zone replicating the discharge shape (band, ring, ellipse, etc., Fig. 2b). As the erosion zone goes deeper, the angular distribution of bombarding ions varies, as a result of which the deposition rate decreases. The high efficiency of utilization of resulting targets was attained in our case by shaping their working surface, namely, by varying the thickness of the material being deposited in accordance with the profile of the erosion zone (Fig. 2b). The use of shaped targets of this type makes it possible to raise the utilization factor of the target material to 50%.

Table

Material of the target	Dispersion of powder, μm	Sputtering distance, mm	Power, kW	Plasma-forming gas		Transporting gas		Powder flow rate, kg/h
				composition	G, m^3/h	composition	gas flow rate, G, m^3/h	
$(BiY)_3(GaFe)_5O_{12}$	50–80	100	12–14	Ar	1.1	$Ar + H_2$	0.2 + 2	0.9
$BiDy_2Ga_{1.2}Fe_{3.8}O_{12}$	50–80	100	14	Ar	1.1	$Ar + H_2$	0.2 + 2	0.9
$CoFe_2O_4$	50–80	100	14	Ar	1.1	$Ar + H_2$	0.2 + 2	0.9
$xCoFe_2O_4(1-x)P_2O_5$	50–80	100	12	Ar	1.2	$Ar + H_2$	0.2 + 1.8	0.8
$YBa_2Cu_3O_7$	50–80	100	12	Ar	1.1	$Ar + H_2$	0.2 + 2	0.8

The above-described method was used to prepare conducting targets of ferrites $(BiY)_3(GaFe)_5O_{12}$, $Bi_{1.7}Y_{1.3}Al_{1.2}Fe_{3.8}O_{12}$, $BiDy_2Ga_{1.2}Fe_{3.8}O_{12}$, $CoFe_2O_4$, and $xCoFe_2O_4(1 - x)P_2O_5$, as well as of a high-temperature superconductor $YBa_2Cu_3O_7$. The material of the targets was synthesized by the ceramic technology.

The above-identified targets were used to prepare, by sputtering, polycrystalline ferrite films and epitaxial films of high-temperature superconductors. The sputtering of the target material was performed in a standard URMZ.279.050 provided with a dc sputtering source (triode system), in an argon atmosphere onto different substrates at a temperature of the latter of ~50°C and deposition rate of 2 A/s. The films thus prepared were in an amorphous state. The crystallization was effected by way of annealing the deposited films in air for a period of 3 h at a temperature from 600 to 900°C depending on the film composition. According to the data of X-ray spectral fluorescence analysis, the chemical composition of the prepared films is close to that of the targets used. The results of electron-microscopic and Auger-spectroscopic studies have revealed that oxide films are characterized by a uniform distribution of the components in the bulk of the film.

As was revealed by the results of studies of, for example, the magnetic and magnetooptical properties of ferrite films, the use of targets prepared by plasma sputtering proved quite efficient in developing magneto-optical storage media based on the use of polycrystalline ferrite films [5, 6].

REFERENCES

1. V. N. Saunin and A. A. Lepeshev, Preprint No. 675, IF SO RAN (Institute of Physics, Siberian Division, Russian Academy of Sciences, Krasnoyarsk, 1990).
2. V. S. Danilin and V. K. Syrchin, *Magnetron Sputtering Systems* (Radio i Svyaz', Moscow, 1982).
3. T. D. Shermergor and N. N. Strel'tsova, *Film Piezoelectrics* (Radio i Svyaz', Moscow, 1986).
4. Yu. D. Tret'yakov, *Ferrite Thermodynamics* (Khimiya, Leningrad, 1967).
5. A. A. Lepeshev, V. F. Pavlov, K. P. Polyakova, *et al.*, Avtometriya, No. 3, 50 (1995).
6. K. P. Polyakova, V. A. Seredkin, A. A. Lepeshev, *et al.*, Neorg. Mater. **34**, 970 (1998).

Translated by Henri A. Bronstein

Technical Physics, Vol. 45, No. 5, 2000, pp. 656–658. Translated from Zhurnal Tekhnicheskoĭ Fiziki, Vol. 70, No. 5, 2000, pp. 133–135.

BRIEF COMMUNICATIONS

Effect of Technological Parameters on the Structure and Surface Morphology of Carbon Films

A. N. Gladkiĭ, S. Yu. Suzdal'tsev, and R. K. Yafarov

Institute of Radio Engineering and Electronics, Saratov Branch, Russian Academy of Sciences, 410019 Saratov, Russia

Received March 30, 1999

Abstract—Technological parameters and conditions providing control over the process of surface morphology formation in the films of the various allotropic carbon phases are established. Using these conditions, it is possible to obtain carbon films with preset properties, in particular, the values of surface density and the size of diamond-like or graphite nano- and microcrystallite. © *2000 MAIK "Nauka/Interperiodica".*

Study of the conditions and mechanisms of the chemical synthesis of thin nano- and microcrystalline carbon films of various structural modifications at low pressures and temperatures is important from practical and scientific standpoints. The significance of the problem is connected to the active search for new ways of creating stable low-voltage cold electron emitters for flat-panel displays and SHF vacuum microelectronic devices. It is known that topographic enhancement of the electric field on the film surface plays an important part in decreasing the electron emission threshold. Relationships between the morphology of particles and their growth mechanism and the surface topography, conductivity, and field emission characteristics of the films are extensively studied. In connection with this, our aim was to tablish technological conditions for obtaining diamond-like nano- and microcrystalline films with developed surface morphology.

Carbon films were deposited onto glass substrates in a plasma of ethanol vapor in a microwave gas discharge with electron cyclotron resonance (ECR) using on experimental setup described in [1]. The process temperature in the steady-state regime was measured with an accuracy of 5 K by a calibrated thermoresistor fixed in the substrate holder. After deposition, the film thicknesses were determined using an ellipsometric laser microscope. The film microtopography was studied in detail using a scanning atomic force microscope (SAFM), and the film structure was investigated by X-ray diffraction analysis using a DRON-3.0 diffractometer.

Figure 1 shows the plots of the film thickness, surface density, and the size of microcrystallites formed during deposition of carbon films on the flow rate of ethanol vapor at a fixed pressure of 1 Pa, a substrate holder temperature of 300°C, and an SHF power of 250 W supplied to the microwave plasma source. The flow rate of ethanol vapor through the chamber is given in the relative units V/V_m, where V_m is the flow rate of ethanol vapor corresponding to the maximum deposition rate and the maximum microcrystallite number density of the film (reaching the extremum values of 10–15 nm/min and 4–5 μm^{-2}, respectively). Apart from the coinciding maxima and a general correlation between the film thickness and microcrystallite density as functions of the flow rate of ethanol vapor, special attention in Fig. 1 must be given to the noncorrelated nonlinear monotonic decrease in the crystallite sizes from 100 nm to 10–15 nm with increasing vapor flow rate. SAFM images showing the surface morphology of carbon films obtained in the microwave discharge plasma for different flow rates of ethanol vapor are presented in Fig. 2.

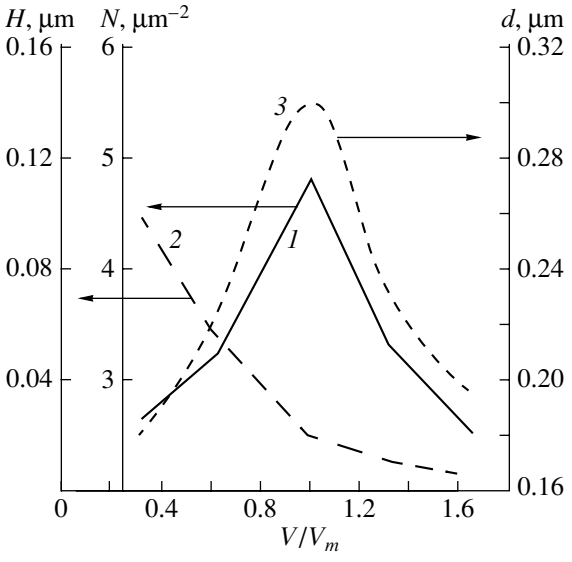

Fig. 1. The plots of (*1*) surface density, (*2*) microcrystallite size, and (*3*) thickness of a diamond-like film versus the ethanol vapor flow rate in the plasma of microwave gas discharge with ECR.

1063-7842/00/4505-0656$20.00 © 2000 MAIK "Nauka/Interperiodica"

Figure 3 shows dependences of the film thickness, size, and surface number density of microcrystallites on the value and sign of the accelerating potential applied to the substrate holder during the film deposition. It was found that the most pronounced qualitative changes in the structure, deposition rate, and film morphology (for otherwise equal parameters of the deposition process) occurred upon changing the potential sign on the substrate holder, which resulted in the reverse run of some curves. For example, at negative potentials the dependences of the surface density and the thickness (deposition rate) of films exhibit the same trends (as in Fig. 1), whereas almost opposite behavior is observed on changing the value and sign of the accelerating potential to positive. In the range from –300 V to 0, the microcrystallite size was about 30 nm at concentrations of up to 3–5 μm^{-2}, both values being almost independent of the substrate potential. With a voltage increase from 0 to + 300 V, the crystallite size drastically increases up to 220 nm and their concentration on the surface decreases to 0.1 μm^{-2} and below. As the positive potential rises, a correlation between the deposition rate (film thickness) and the crystallite size is observed, rather than between the rate and the crystallite concentration.

At negative bias voltages on the substrate holder, as well as under all the experimental conditions given in Fig. 1, "light" diamond-like films with a transmission coefficient > 85% were deposited. X-ray analysis of these films showed that they mainly contain diamond-like carbon phases with a hexagonal lattice of three different structural modifications (lonsdaleite, C(20H), etc.), include a cubic diamond phase with the lattice orientation (111), and contain small inclusions of a finely crystalline graphite phase (002). These films had a low conductivity (or high resistivity up to 10^7 Ω m).

X-ray analysis of the films deposited on to the substrate holder at positive potentials confirmed the predominant formation of a fine crystalline phase of graphite with an interplanar distance of $d = 3.36$ Å [2]. These films had a transmission coefficient from 60 to 75%, which decreased at higher positive potentials. Specific resistances of these films did not exceed several tens of Ω m.

An increase in the flow rate of gases through a plasmatron leads, on the one hand, to increasing consumption of a substance in the form of excited and neutral particles (including those favorable for the formation of a diamond-like phase of carbon) and, on the other hand, to a decreasing ionization degree of the plasma and lower adsorption of particles on the surface. At very large flow rates, the latter circumstance hinders the nucleation and growth of crystallites and film formation. With the flow rate V/V_m decreased from 1 to 0.32, the ionization degree of the plasma increases and, hence, the ion bombardment density of the surface grows. This results firstly in a nonlinear increase in the growth rate of microcrystallites, with their size reaching 100 nm even under the conditions of decreasing flow of the "building" material in the form of excited and neutral carbon particles of certain types. At $V/V_{m1} \longrightarrow 1$, the optimum relationships between the flows of ionized and neutral particles for the formation of a diamond-like phase and for the maximum film deposition rates are realized.

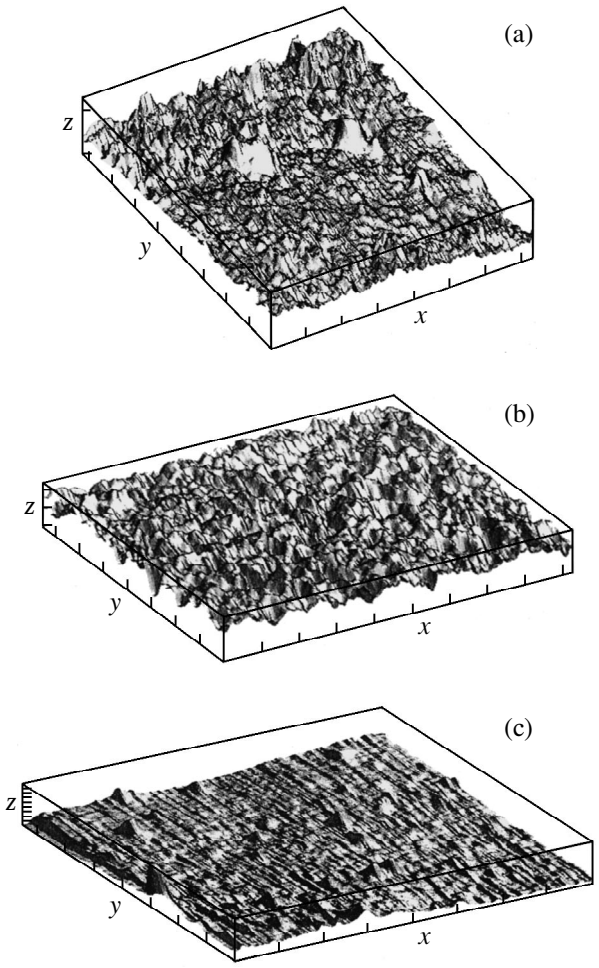

Fig. 2. SAFM images of a diamond-like carbon film surface for the samples obtained at various values of the ethanol vapor flow rate in the plasma of microwave gas discharge with ECR: $V/V_m = 0.32$ (a), 1.0 (b), 1.64 (c). Scale: (a, b) *x*, 1 μm; *y*, 1 μm; *z*, 0.01 μm; (c) *x*, 1 μm; *y*, 1 μm; *z*, 0.001 μm.

Application of an electric field stimulates the crystallite growth during deposition from the ionized gas phase by intensifying the mass transfer and by activating processes on the growth surface [3]. The electric field separates ions (positive and negative, depending on the potential sign on the substrate holder) coming to the substrate upon the dissociation and subsequent ionization of ethanol molecules. As is known, an excess of negative oxygen ions and a lack of positive hydrogen ions are beneficial to the growth of a graphite phase. In addition, the electric field produces polarization of molecules of the gas phase and the chemisorbed layer,

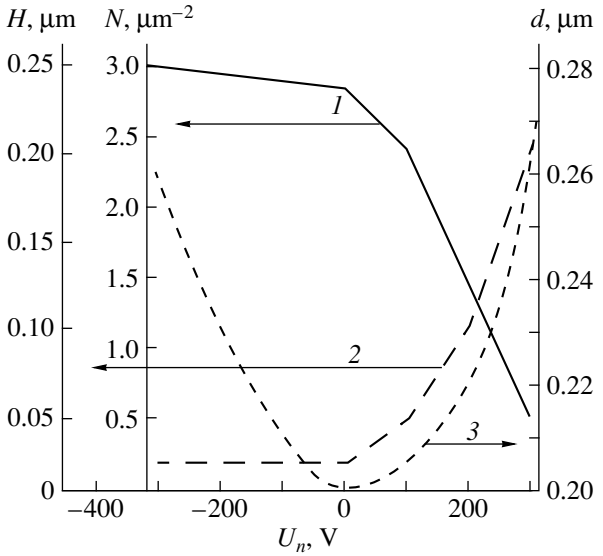

Fig. 3. The plots of (*1*) surface density, (*2*) microcrystallite size, and (*3*) thickness of carbon films of the different phase compositions versus the substrate bias potential.

which, in turn, stimulates processes of substance transfer to the growing faces of microcrystals, as well as on their surface. Deformation of the adsorbed complexes in the electric field during crystal growth by chemical deposition from the gas phase may change the activation energy of their dissociation and thus intensify the "building" process on the growing surface of the given crystallographic structure.

From the reported results it follows that the presence of a positive ion component on the substrate is the most critical factor determining the process of nucleation and growth of nano- and microcrystallites, as well as the deposition rate of a diamond-like film. Thus, the dominating formation of diamond-like microcrystallites at a negative voltage on the substrate holder may be caused by the following two mechanisms: first, by ion-chemical etching of the graphite phase by hydrogen ions in the absence of interaction between the growing diamond-like phase and negative oxygen ions and, second, by stimulation of chemisorption and crystallization of excited and ionized carbon particles of certain types responsible for the diamond-like crystal structure formation.

Thus, the results of our surface morphology studies and ellipsometric measurements of the thickness of carbon films obtained using different regimes of microwave gas discharge generation with ECR lead to the following conclusions.

1. A correlation between the deposition rate (film thickness) and the surface number density (nucleation frequency) of diamond-like nano- and microcrystallites takes place, rather than between the rate and the crystallite sizes. The surface concentration and size of the diamond-like crystallites are almost independent of the applied negative potential.

2. Low supply rates of ethanol vapor to the chamber at a negative potential on the substrate holder stimulate mainly the process of diamond-like crystallite growth; however, these conditions are not optimum for the maximum film growth rate. Increasing in the supply rate of ethanol vapor above the optimum level results in a decrease in the concentration and typical size of crystallites, as well as in the deposition rate of the diamond-like carbon film. Only a definite relationship between the flows of charged and neutral particles provides for the optimum conditions favoring the formation of a diamond-like phase at a maximum film deposition rate.

3. A positive potential on the substrate holder leads to preferential formation of a graphite phase in the carbon films. For graphite films, unlike the diamond-like ones, a correlation between the deposition rate and the microcrystallite size is typical. The microcrystallites increase in size with increasing positive potential, while the dependence of the surface concentration of graphite microcrystallites on this parameter has a reverse character.

4. The technological parameters and conditions that control the processes of surface morphology formation in films of allotropic carbon phases are established, which makes it possible to obtain carbon films with preset properties, in particular, the values of surface density and the size of diamond-like and graphite nano- or microcrystallites.

REFERENCES

1. N. N. Bylinkina, S. P. Mushtakova, V. A. Oleĭnik, *et al.*, Pis'ma Zh. Tekh. Fiz. **22** (6), 43 (1996) [Tech. Phys. Lett. **22**, 245 (1996)].
2. A. R. Ubbelohde and F. A. Lewis, *Graphite and its Crystal Compounds* (Clarendon Press, Oxford, 1960; Mir, Moscow, 1965).
3. Yu. M. Tairov and V. F. Tsvetkov, *Technology of Semiconductor and Dielectric Materials* (Vysshaya Shkola, Moscow, 1990).

Translated by M. Astrov

Technical Physics, Vol. 45, No. 5, 2000, pp. 659–661. Translated from Zhurnal Tekhnicheskoĭ Fiziki, Vol. 70, No. 5, 2000, pp. 136–138.

BRIEF COMMUNICATIONS

Anomalous Thermal Electromotive Force in Samarium Monosulfide

M. M. Kazanin, V. V. Kaminskiĭ, and S. M. Solov'ev

Ioffe Physicotechnical Institute, Russian Academy of Sciences, Politekhnicheskaya ul. 26, St. Petersburg, 194021 Russia

Received March 30, 1999

Abstract—The thermal emf in samarium monosulfide was investigated at temperatures between 300 and 530 K. At T = 435–455 K, an anomalous increase in the emf was found. This effect is explained by a noncoherent change in the valency of samarium ions. *© 2000 MAIK "Nauka/Interperiodica".*

In [1, 2], a change in the energy of activation of electrical conductance in samarium monosulfide (SmS) at $T \sim 450$ K was discovered. It is believed that, at $T > 450$ K, current carriers are activated from the 4*f* levels of samarium ions ($E_f = 0.23$ eV), and at $T < 450$ K, from some uncontrollable impurities. It has been assumed [3] that these impurity levels ($\Delta E = 0.045 \pm 0.015$ eV) are due to interstitial Sm^{2+} ions rather than to those occupying lattice sites (of NaCl type). It has also been shown [4] that the semiconductor-to-metal phase transition under hydrostatic pressure takes place when the conduction electron concentration in SmS reaches $n_k = (8 \pm 1) \times 10^{19}$ cm^{-3}. It is therefore tempting to induce this transition by thermally activating carriers to the concentration n_k and trace the phase modification from changes in the electrical performance of the material. Four-probe dc conductivity measurements proved to be unreliable because of the instability of the output signal in the temperature range of 400–500 K. It appears that such difficulties were also encountered in earlier works concerned with kinetic phenomena in SmS. Such a judgement follows from the fact that data for conductivity and thermal emf in this temperature interval are lacking [2, 5]. In connection with this, the temperature dependence of thermal emf between 300 and 530 K has been given careful study.

Samples used were cleaved SmS(100) single crystals measuring $8 \times 2 \times 2$ mm. At T = 300 K, the carrier concentration and the thermal emf were, respectively, $n_k \sim 6 \times 10^{18}$ cm^{-3} and 300 μV/K. During heating and cooling the samples in a vacuum, the temperature and the thermal emf were continuously recorded with two copper/constantan thermocouples. They were either in direct contact with the samples or attached to evaporated nickel contacts. The distance between them was from 6 to 8 mm. To be certain that an effect does exist and to avoid uncontrollable temperature gradients, a series of experiments was performed by heating samples immersed in VM-1 vacuum oil.

The measured temperature dependence of the thermal emf is given in Fig. 1. The temperature dependence of the differential thermal emf obtained from this curve is presented in Fig. 2. The sharp peak of the emf at T = 435–455 K is noteworthy. Its magnitude (more than 10 mV) exceeds the background value (0.2–0.4 mV) by almost two orders and has the opposite sign. This suggests that an emf mechanism near the peak is other than that in the rest of the temperature interval under study.

It is natural to relate this effect to the semiconductor-to-metal phase transition observed in SmS under hydrostatic pressing [6]. The transition proceeds in two stages: (1) a change in the electron subsystem and, hence, a change in the samarium ion valency ($Sm^{2+} \longrightarrow Sm^{3+} + \bar{e}$) in the defect system and (2) a similar change in the system of samarium ions occupying lattice sites with a subsequent change in the lattice parameter. In both cases, the valency changes because of screening of the electrical potential of the ions by conduction electrons. Note that stage 1 provides conditions (supplies a sufficient quantity of electrons to the conduction band) for stage 2. In our case, stage 1 alone is likely to take place. Without pressing, the 4*f* levels of Sm^{2+} ions at lattice sites are 0.23 eV away from the conduction-band bottom. For the phase transition under a hydrostatic pressure P_k = 650 MPa, the 4*f* levels shift 0.1 eV closer to the conduction-band bottom (the baric shift of the 4*f* levels is ~0.16 meV/MPa [3]). In this case, electrons are more weakly confined by the potential than at $P = 0$. Thus, we can suppose that, without hydrostatic pressing, the screening effect of electrons that fall into the conduction band after stage 1 is insufficient for stage 2 to take place. In other words, SmS remains in the semiconducting state, as observed in [1, 2, 5]. However, impurity samarium ions are distributed over the sample nonuniformly and, in addition, may occupy nonequivalent interstitial positions. As a result, we observe a noncoherent change in the valency of these samarium ions in time and space in response to a temperature variation. Extra electrons that result in the conduction band

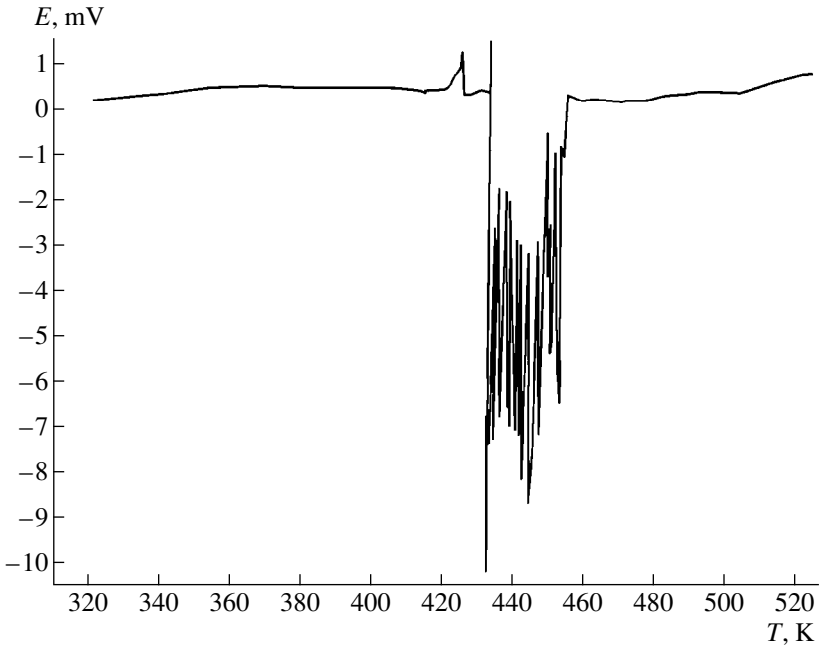

Fig. 1. Temperature dependence of the emf signal for the SmS sample.

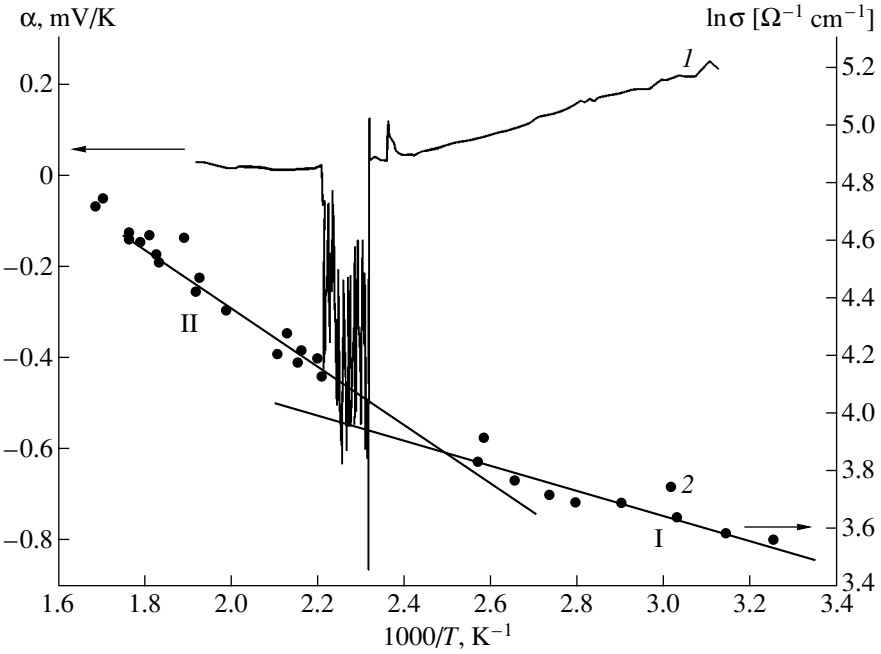

Fig. 2. Temperature dependence of the (*1*) differential thermal emf and (*2*) conductivity σ [5] for the SmS sample. Energy of activation is (I) 0.056 and (II) 0.18 eV.

produce a concentration gradient and the related emf that are measured in experiments. Thus, the observed anomalous emf is associated not with a temperature gradient but rather with a conduction-electron concentration gradient due to intrinsic processes occurring in the sample. To put it otherwise, it is not an emf in the conventional meaning of this term. This conclusion was verified in the oil experiments, where an external temperature gradient was absent but the emf was recorded.

The thermal emf and the conductivity of SmS in the given temperature interval were also studied earlier. Curve *2* in Fig. 2 was taken from the SmS sample similar to ours in parameters (α = 315 μV/K and $n = 7 \times 10^{18}$ cm^{-3} at T = 300 K) [5]. We were the first to

observe the occurrence of emf due to a noncoherent valency change. This has been made possible by the use of continuous, rather than discrete, recording.

The reproducible features of the effect are as follows: (1) The occurrence of emf is accompanied by spontaneous heating of the sample. (2) The emf peaks can be as high as 50–80 mV. (3) The effect shows up at temperatures between 400 and 500 K.

Consider the differential thermal emf in the rest of the given temperature range (beyond the observed anomaly). At $T < 435$ K, α drops with increasing T, which is common in semiconductors. At $T > 455$ K, α remains constant or even grows slightly with T. Such behavior is inconsistent with an increase in σ (Fig. 2) observed in [5] if one adheres to the conventional band theory of electrical conduction in SmS. If, however, it is assumed that, at $T = 435$–455 K, Sm^{3+} ions with a concentration of $\sim 10^{20}$ cm^{-3} (which is the concentration of interstitial samarium ions [3]) appear in the sample, which means that about 1% of the samarium ions became trivalent, the hopping conduction mechanism may come into play. Such a situation was observed in SmS thin films [7]. Under these conditions, the behavior of α is hard to predict and calls for further investigation. Thermally activated hops might take place between the $4f$ levels of Sm^{2+} ions and holes on impurity levels. The energy of activation of this process is $E_f - \Delta E \sim 0.185 \pm 0.015$ eV. It is this energy value that is found from the conductivity data at $T > 455$ K (Fig. 2).

ACKNOWLEDGMENTS

The authors thank M. I. Fedorov for fruitful discussions.

REFERENCES

1. A. V. Golubkov, B. V. Goncharova, V. P. Zhuze, *et al.*, *Physical Properties of Rare-Earth Element Chalcogenides* (Nauka, Leningrad, 1973).
2. V. P. Zhuze, E. V. Goncharova, N. F. Kartenko, *et al.*, Phys. Status Solidi A **18** (1), 63 (1973).
3. L. N. Vasil'ev and V. V. Kaminskiĭ, Fiz. Tverd. Tela (St. Petersburg) **32**, 1173 (1994) [Phys. Solid State **36**, 640 (1994)].
4. S. I. Grebinskiĭ, V. V. Kaminskiĭ, A. V. Ryabov, and N. N. Stepanov, Fiz. Tverd. Tela (Leningrad) **24**, 1874 (1982) [Sov. Phys. Solid State **24**, 1069 (1982)].
5. E. V. Shadrichev, L. S. Parfen'eva, V. I. Tamarchenko, *et al.*, Fiz. Tverd. Tela (Leningrad) **18**, 2380 (1976) [Sov. Phys. Solid State **18**, 1388 (1976)].
6. V. V. Kaminskiĭ, V. A. Kapustin, and I. A. Smirnov, Fiz. Tverd. Tela (Leningrad) **22**, 3568 (1980) [Sov. Phys. Solid State **22**, 2091 (1980)].
7. L. N. Vasil'ev, V. V. Kaminskiĭ, Yu. M. Kurapov, *et al.*, Fiz. Tverd. Tela (St. Petersburg) **38**, 779 (1996) [Phys. Solid State **38**, 430 (1996)].

Translated by V. Isaakyan

Technical Physics, Vol. 45, No. 5, 2000, pp. 662–666. Translated from Zhurnal Tekhnicheskoĭ Fiziki, Vol. 70, No. 5, 2000, pp. 139–142.

BRIEF COMMUNICATIONS

Interaction between Microwave Oscillation and a Photoionized Semiconductor Plasma in a Two-Layer Waveguide

V. V. Antonov and S. V. Ivanov

Saratov State Technical University, Saratov, 410054 Russia

Received April 6, 1999

Abstract—Theoretical studies are performed on the interaction between microwave electromagnetic radiation and a photoionized semiconductor plasma in a two-layer waveguide. The interaction between the characteristic wave types of oscillation and a photoexcited semiconductor plasma is investigated. The dependences of the reflection coefficient and phase of the microwave-frequency wave on the optical radiation intensity are obtained; the effect of the surface and of the geometric dimensions of semiconductor elements on these parameters is investigated. *© 2000 MAIK "Nauka/Interperiodica".*

The coefficient of reflection of microwave radiation from an inhomogeneous semiconductor placed in a waveguide system depends considerably on the electromagnetic field frequency and distribution of dielectric permittivity $\varepsilon(x, y, z, \omega)$ over the sample cross section. In a conducting medium, the dielectric permittivity is defined by the concentration of charge carriers at each point, so that the variation of the conductivity of a semiconductor structure under the effect of optical radiation in the region of plasma resonance of microwave oscillation may be used to measure the intensity of a laser beam with a short pulse duration.

The relatively small cross-sectional dimensions of the channeling system of microwave radiation in the millimeter wavelength range enable one to use semiconductor plates with a thickness of the order of the diffusion length for measuring the reflection coefficient of oscillation. In this case, the process of distribution of concentration over the cross section is affected considerably by the states of semiconductor surfaces.

The investigation of the interaction between microwave radiation and an inhomogeneous photoionized plasma is based on the following model. A semiconductor plate is arranged along the narrow wall in a waveguide whose geometry is given in Fig. 1. An electromagnetic wave of frequency ω propagates along the z-axis. Because the microwave-frequency techniques involve the use of standard waveguides rated for the wave of dominant mode H_{01}, the wave in the irregular part of the waveguide system *II* will be a wave of the *LE* type [1]. The photogeneration of charge carriers under the effect of a laser beam occurs on the surface $y = d$.

We will determine the distribution of electron and hole concentration on the coordinate y in the superconductor plate *I* from the balance equation for charge carriers

$$\operatorname{div} \mathbf{j}_{n,p} = \mp e(G - R_{n,p}), \qquad (1)$$

where $G = G_0 e^{\alpha(y-d)}$ is the rate of carrier generation, α is the coefficient of light absorption in the crystal, $G_0 = \eta\alpha(I_0/\hbar\omega_0)$, η is the quantum yield, ω_0 is the light frequency, I_0 is the laser beam intensity, $R_n = (n - n_0)/\tau_{rec}$, $R_p = (p - p_0)/\tau_{rec}$, n_0 and p_0 respectively denote the equilibrium concentration of electrons and holes, and τ_{rec} is the recombination time.

Under conditions of high generation, the nonequilibrium concentration $n \gg n_0, p_0$, so that $\delta n = n - n_0 \approx \delta p = p - p_0$ (the condition of quasineutrality is valid at every point of the sample). In order to determine the density of electron and hole currents $\mathbf{j}_n$ and $\mathbf{j}_p$, we use the equation of motion in the diffusion approximation,

$$\mp e\mathbf{E} - \nu_{n,p} m_{n,p} \mathbf{v}_{n,p} - \frac{kT}{n} \operatorname{grad} n = 0, \qquad (2)$$

where $\nu_{n,p}$ denotes the frequency of collisions of electrons and holes with lattice points and $m_{n,p}$ denotes the effective mass of electrons and holes.

We substitute the values of $\mathbf{j}_{n,p} = \mp e n \mathbf{v}_{n,p}$ into equation (1) and, in view of the equality to zero of the y projection of total current, derive the equation for determining the distribution of concentration on the y axis,

$$D\frac{d^2(\delta n)}{dy^2} - \frac{\delta n}{\tau_{rec}} + G_0 e^{\alpha(y-d)} = 0, \qquad (3)$$

where

$$D = \frac{\mu_n D_n + \mu_p D_p}{\mu_n + \mu_p}$$

is the coefficient of bipolar diffusion, μ_n and μ_p denote the electron and hole mobility, and D_n and D_p are diffusion coefficients.

1063-7842/00/4505-0662$20.00 © 2000 MAIK "Nauka/Interperiodica"

We will write the general solution of equation (3) in the form

$$\delta n = Ae^{\frac{d-y}{L}} + Be^{-\frac{d-y}{L}} + Ce^{-\alpha(d-y)}, \quad (4)$$

where $L = \sqrt{D\tau_{rec}}$, and $C = G_0\tau_{rec}/(1 - \alpha^2L^2)$.

We determine the integration constants A and B from the boundary conditions

$$\begin{aligned} j_n(y = 0) &= e\delta n(0)S_1, \\ j_n(y = d) &= -e\delta n(d)S_2, \end{aligned} \quad (5)$$

where S_1 and S_2 denote the rate of surface recombination on the faces $y = 0, d$.

We introduce the notation

$$a_0 = -\frac{D}{L} - S, \quad a_1 = \frac{D}{L} - S,$$

$$b_0 = (D\alpha - S)C, \quad b_1 = (D\alpha + S)C,$$

to derive the following expressions for the constants A and B:

$$A = \frac{b_1e^{d/L} - b_0e^{-\alpha d}}{a_0(e^{-d/L} - e^{d/L})} + \frac{b_1}{a_0}, \quad B = -\frac{b_1e^{d/L} + b_0e^{-\alpha d}}{a_1(e^{-d/L} - e^{d/L})}.$$

We will represent the electromagnetic field before the irregular portion of the waveguide system in the form of a superposition of the incident wave H_{01}, the reflected wave of the same type, and waves H_{0m} $(m \geq 2)$ of higher types whose amplitudes decrease away from the superconductor layer on the z-axis. The respective components of the electric and magnetic fields are defined by the expressions

$$E_x^0 = jk_{z1}\sin(k_{y1}y)(A_4e^{jk_{z1}z} - A_5e^{-jk_{z1}z}) + j\sum_{m=2}^{\infty} a_m\sin(k_{ym}y)e^{jk_{zm}z},$$

$$E_y^0 = E_z^0 = 0, \quad H_x^0 = 0,$$

$$H_y^0 = \frac{k_{z1}^2}{j\omega\mu_0}\sin(k_{y1}y)(A_4e^{jk_{z1}z} + A_5e^{-jk_{z1}z}) + \sum_{m=2}^{\infty} \frac{a_mk_{zm}}{j\omega\mu_0}\sin(k_{ym}y)e^{jk_{zm}z},$$

$$H_z^0 = \frac{k_{z1}k_{y1}}{\omega\mu_0}\cos(k_{y1}y)(A_4e^{jk_{z1}z} - A_5e^{-jk_{z1}z}) + \sum_{m=2}^{\infty} a_m\frac{k_{zm}k_{ym}}{\omega\mu_0}\cos(k_{y1}y)e^{jk_{zm}z},$$

where $k_{ym}^2 + k_{zm}^2 = k_0^2$; $k_{ym} = m\pi/a$; $m = 1, 2, \ldots, n$.

In order to determine the field in the region *II*, we introduce the electric vector potential $\mathbf{F}(0, F, 0)$ directed on the axis y (*LE*-wave) [2–4],

$$\mathbf{E} = -\mathbf{curl}\mathbf{F}. \quad (6)$$

The vector potential $\mathbf{F}$ satisfies the homogeneous Helmholtz equation

$$\Delta\mathbf{F} + k^2\mathbf{F} = 0, \quad (7)$$

where $k_0^2 = \omega^2\varepsilon_0\mu_0$.

The solution of equation (7) with the boundary conditions $E_x(y = d) = 0$ defines the field structure in the following form:

$$E_x^1 = jk_z\sin(k_y(a - y))(A_4'e^{jk_{z1}z} - A_5'e^{-jk_{z1}z}),$$

$$E_y^1 = E_z^1 = 0, \quad H_x^1 = 0,$$

$$H_y^1 = \frac{k_z^2}{j\omega\mu_0}\sin(k_y(a - y))(A_4'e^{jk_{z1}z} + A_5'e^{-jk_{z1}z}),$$

$$H_z^1 = -\frac{k_zk_y}{\omega\mu_0}\cos(k_y(a - y))(A_4'e^{jk_{z1}z} - A_5'e^{-jk_{z1}z}),$$

where $k_y^2 + k_z^2 = k_0^2$.

The equality of the tangential components at the interface $y = d$ enables one to derive from the Maxwell equations the wave equation for determining the amplitude of the electric component of the field inside the semiconductor layer,

$$\frac{\partial^2E_x}{\partial y^2} + (k_1^2 - k_z^2 - j\omega\mu_0\sigma)E_x = 0, \quad (8)$$

where $k_1^2 = \omega^2\varepsilon_0\mu_0\varepsilon_p$, ε_p is the dielectric permittivity of the lattice,

$$\sigma = \frac{e^2(m_p\nu_p + m_n\nu_n + j\omega(m_p + m_n))n}{m_pm_n(\nu_n + j\omega)(\nu_p + j\omega)}$$

is the coefficient of electrical conductivity of electrons and holes at a frequency ω, m_p and m_n respectively denote the effective hole and electron mass, ν_p and ν_n respectively denote the frequency of collisions of holes and electrons with lattice points, and n is the concentration of charge carriers per unit volume.

We introduce the notation

$$\begin{aligned} \varepsilon &= \varepsilon_p - \frac{k_z^2}{\varepsilon_0\mu_0\omega^2} - \frac{j\sigma}{j\omega\mu_0}, \\ \psi(y) &= \omega\sqrt{\varepsilon_0\mu_0}\int\sqrt{\varepsilon}dy \end{aligned} \quad (9)$$

and use the Wentzel–Kramers–Brillouin (WKB) approximation method to derive the solution of equa-

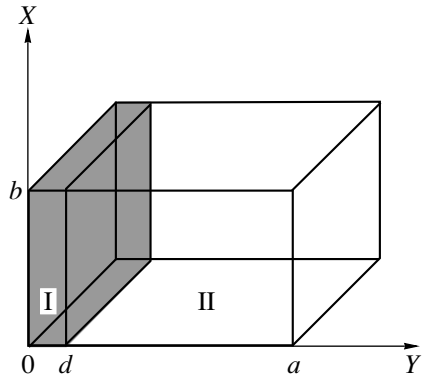

Fig. 1. A waveguide along whose narrow wall a semiconductor plate is arranged: (*I*) part of the waveguide system with a semiconductor plate; (*II*) part of the waveguide system without a semiconductor.

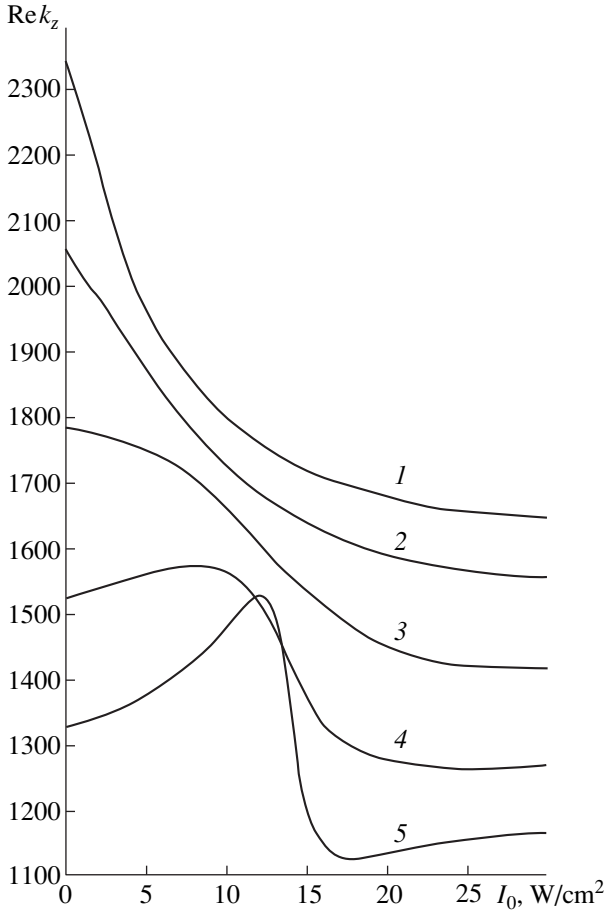

Fig. 2. The real part of k_z as a function of the light intensity I_0, with the surface recombination rate S = 10 m/s and with d = (*1*) 400, (*2*) 420, (*3*) 450, (*4*) 480, and (*5*) 500 μm.

tion (8) in the form

$$E_x = \frac{C_1 e^{j\psi} + C_2 e^{-j\psi}}{\sqrt[4]{\varepsilon}}(F_3 e^{k_z z} - F_4 e^{-k_z z}). \qquad (10)$$

On the wall of the $y = 0$ waveguide, the tangential component of the field $E_x(0) = 0$, which enables one to determine the correlation between the constants C_1 and C_2. The electromagnetic field in this case may be expressed in the form

$$E_x = \frac{\sin(\psi(0) - \psi(y))}{\sqrt[4]{\varepsilon}}(F_3 e^{jk_z z} + F_4 e^{-jk_z z}),$$

$$H_y = -\frac{k_z}{\omega\mu_0}\frac{\sin(\psi(0) - \psi(y))}{\sqrt[4]{\varepsilon}}(F_3 e^{jk_z z} - F_4 e^{-jk_z z}),$$

$$H_z = -\frac{1}{\omega\mu_0}\left(\frac{\cos(\psi(0) - \psi(d))\psi'}{\sqrt[4]{\varepsilon}}\right. \qquad (11)$$

$$\left. - \frac{\sin(\psi(0) - \psi(d))\varepsilon'}{4\varepsilon^{5/4}}\right)(F_3 e^{jk_z z} + F_4 e^{-jk_z z}),$$

where $\psi' = d\psi/dy$, $\varepsilon' = d\varepsilon/dy$.

From the equation of the equality of impedances on the sample boundary $y = d$,

$$\frac{E_x}{H_z} = \frac{E_x^{(1)}}{H_z^{(1)}}$$

follows the equation for determining the constant k_y,

$$\frac{\tan[k_y(a-d)]}{k_y} = \frac{\tan(\psi(0) - \psi(d))}{\psi'(d) + \tan(\psi(0) - \psi(d))/4\varepsilon(d)\varepsilon'(d)}. \qquad (12)$$

We will equate the tangential components of the fields on the boundaries $z = 0$, l, multiply the obtained equalities by $\sin(\pi/a)y$, and then integrate for the variable y going from 0 to a. The integration yields the equations

$$jk_{z1}(A_4 - A_5) = 2(\psi_1 + \psi_2)(A_4' - A_5'),$$

$$k_{z1}^2(A_4 + A_5) = 2jk_z(\psi_1 + \psi_2)(A_4' + A_5'),$$

$$jk_{z1}A_5 e^{-jk_z l} = 2(\psi_1 + \psi_2)(A_4' e^{jk_z l} - A_5' e^{-jk_z l}), \qquad (13)$$

$$k_{z1}^2 A_5 e^{-jk_{z1} l} = -2jk_z(\psi_1 + \psi_2)(A_4' e^{jk_z l} - A_5' e^{-jk_z l}),$$

where the notation

$$\int_0^d \frac{\sin(\psi(0) - \psi(y))}{\sqrt[4]{\varepsilon}} \sin\left(\frac{\pi}{a}y\right)dy = \psi_1,$$

$$jk_z \int_0^d \sin(k_y(a-y)) \sin\left(\frac{\pi}{a}y\right)dy = \psi_2$$

is introduced.

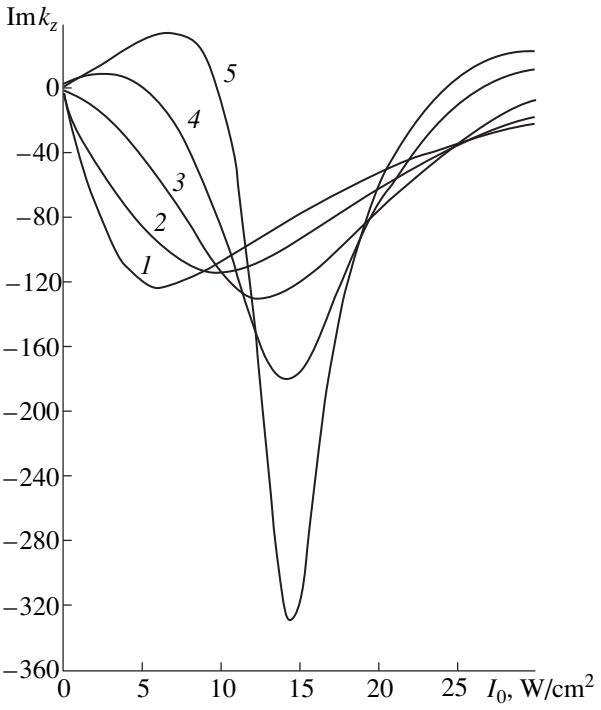

Fig. 3. The same as in Fig. 2 for the imaginary part of k_z.

The set of algebraic equations (13) gives the following expression for the coefficient R of wave reflection from an irregular layer:

$$R = \frac{A_4}{A_5} = \frac{(k_{z1} + k_z)R_1 + k_z - k_{z1}}{(k_{z1} - k_z)R_1 + k_z + k_{z1}}, \qquad (14)$$

where

$$\frac{A_4'}{A_5'} = R_1 = \frac{(k_{z1} - k_z)}{(k_{z1} + k_z)} e^{-2k_z l}$$

is the coefficient of reflection of a microwave-frequency wave from the boundary $z = 1$.

Solutions of equation (12) for the real, Rek_z, and imaginary, Imk_z, parts of k_z as functions of intensity I are given in Figs. 2 and 3. Minima of the function Rek_z, which become more pronounced as the sample thickness d increases, are realized in the limits of $0.48 \le d \le 0.5$ mm. The values of intensity at the minimum points correspond to the conditions of plasma resonance ($\omega = \omega_p$). As the sample thickness increases, the effect of the surface recombination rate decreases, and the maximum of the concentration is observed in the vicinity of the surface $y = d$. Analogous correlations are observed in the case of Imk_z.

Figure 4 gives the modulus of the reflection coefficient of a microwave-frequency wave as a function of light intensity I for different values of the semiconductor plate thickness. The derived correlations are nonmonotonic, with the increase in d causing the minima of $|R|$ to shift toward higher values of intensity. Under conditions of plasma resonance, the energy of microwave oscillation is absorbed, as a result of which the reflection from the layer increases.

The respective dependences of the phase ϕ of the reflection coefficient on the intensity are given in Fig. 5. Quantitative estimates for the dependences of Rek_z, Imk_z, $|R|$, and ϕ are given for the electromagnetic

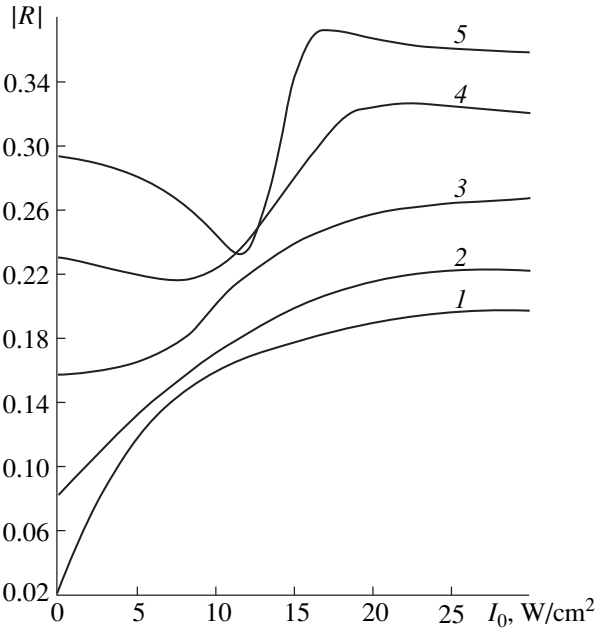

Fig. 4. The same as in Fig. 2 for the modulus $|R|$ of the reflection coefficient.

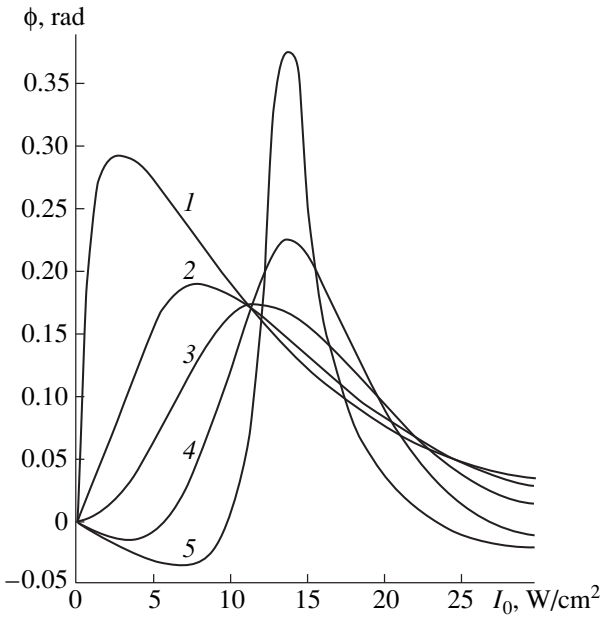

Fig. 5. The same as in Fig. 2 for the phase φ of the reflection coefficient.

field frequency $\omega = 9.42 \times 10^{11}$ Hz and the waveguide system channel cross section of 0.8×1.6 mm. The semiconductor insert was made of CdSe with the basic parameters of $\mu_n = 0.01$ m^2/(V s), $\mu_p = 0.005$ m^2/(V s), $n_0 = 10^5$ m^{-3}, $S = 10$ m/s, and $\tau_{rec} = 10^{-6}$ s.

As a result of theoretical studies, the dependence of the modulus and phase of the reflection coefficient on the laser radiation intensity was determined. The foregoing characteristics define the possibility of using the effect of interaction between microwave radiation in the millimeter range and photoionized plasma for measuring the basic parameters of laser pulses in the infrared and optical wavelength ranges.

REFERENCES

1. V. L. Ginzburg, *The Propagation of Electromagnetic Waves in Plasmas* (Nauka, Moscow, 1967; Pergamon, Oxford, 1970).
2. Yu. V. Egorov, *The Physics of Semiconductors* (Sov. Radio, Moscow, 1967).
3. P. S. Kireev, *Partially Filled Rectangular Waveguides* (Vysshaya Shkola, Moscow, 1975).
4. V. V. Antonov, S. V. Ivanov, V. P. Tsarev, and V. N. Chupis, Zh. Tekh. Fiz. **68** (11), 94 (1998) [Tech. Phys. **43**, 1358 (1998)].

Translated by Henri A. Bronstein